Research Activities

Design Study of an 1 GeV Storage Ring for UVSOR-II Project

Hiroyuki HAMA and Masahito HOSAKA

UVSOR Facility, Institute for Molecular Science, Okazaki 444 Japan

Experimental research activity with synchrotron radiation (SR) in various fields has been steadily getting prosperously at the UVSOR facility since the first SR emitted from the UVSOR storage ring in 1983. The UVSOR storage ring was designed as a second generation light source, and after commissioning the storage ring itself and injector accelerators has been continuously developed, so that three insertion devices have become to be available. However the progress of SR technology and accelerator physics is so fast, then it may be concluded the light source accelerator always becomes less competitive due to progress in the world, not worn-out hardware. It will directly connect with less opportunity for unique or advanced studies.

Number of third generation light sources has been constructed and a couple of them are already operational. The so-called ultra low emittance beam has been already achieved. For instance, an emittance of less than 5 *nmrad* is realized on the 1.5 GeV machine at ALS, Berkeley. High brilliant radiation from such a low emittance beam is definitely important for the progress of SR experiments. However the low emittance machine requires a very large circumference. It is not suitable for capacity of the UVSOR facility. For the design work of UVSOR-II, here we may have some restrictions; 1) spectral range of SR is from far infrared to soft X-ray, 2) not so large circumference (less than 130 m) because available land space is expected to be 80 m × 100 m, 3) unique but multi-purpose ring, 4) relatively low emittance, 5) not so expensive and 6) do not compete with other rings and projects in Japan. Moreover based on our research works on the UVSOR, the new ring will be hopefully optimized for free electron laser (FEL) in short wavelength region and production of very short bunch length of electron beam.

A nominal beam energy of 1 GeV has been chosen by considering continuation of research activity at the present UVSOR. The basic concept of new ring is that the momentum compaction factor α_p is very low to reduce the electron bunch length, and nominally negative to have an advantage against correction of both chromaticity and higher order momentum compaction. To reduce α_p efficiently, an inverted dipole is introduced in an unit cell], and then the cell basically consists of triple bend achromat (TBA) lattice. Figure 1 shows the lattice of a basic unit cell. Because

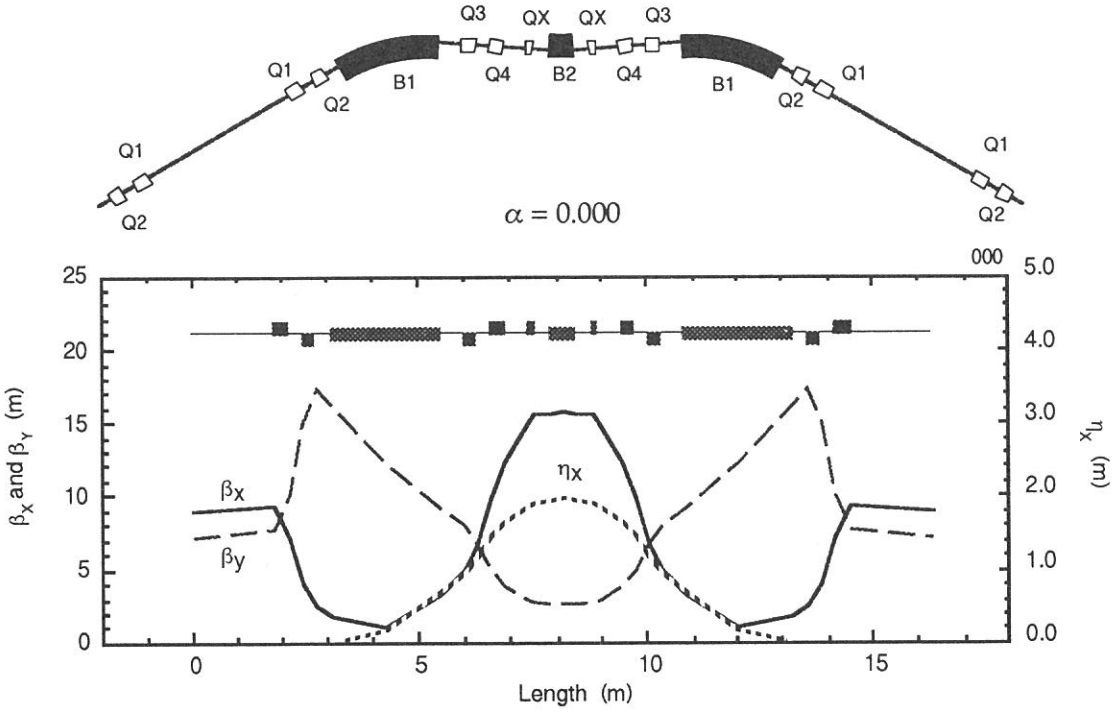

Fig. 1 The basic lattice and lattice functions of UVSOR-II storage ring.

of existence of inverted dipole, the bending angle of normal dipole is so large that the natural emittance is not much reduced. Additional focusing quadrupoles put on just sides of the inverted dipole assist variation of α_p from negative to positive without big change of the beta functions as shown in Fig. 2.

To obtain high effective gain of FEL, we considered a racetrack type ring including 10 m-long straight sections and 6 basic unit cells. There are some important points to produce high power FEL. Particularly a degree of transverse overlapping between the laser pulse and the electron bunch directly affects the effective FEL gain. Moreover high electron density of the bunch in the undulator section is required. These requirements prevent large beta functions at straight section. Generally high betatron tune number brings low emittance beam, but makes large beta functions at straight sections in case of TBA or DBA lattice normally. The beam size at the straight section is determined by compromise between emittance and beta functions. In this design work, the beta function is subdued under 10 m, then emittance became to be around 24 *nmrad*.

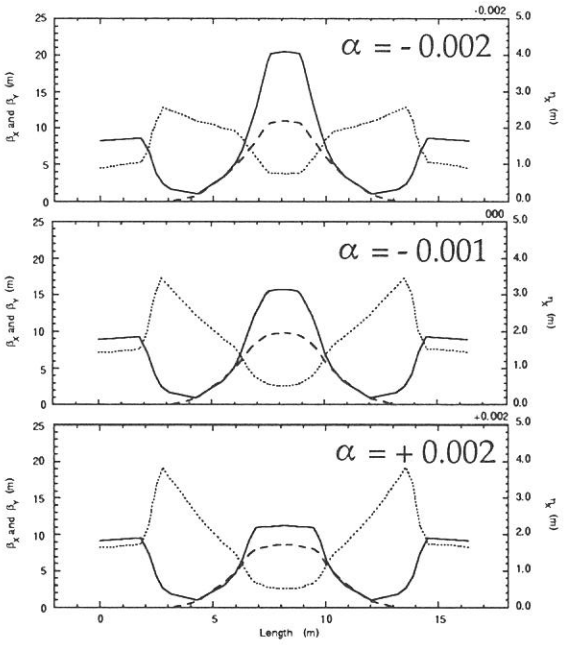

Fig. 2 Lattice functions for various momentum compaction factor α_p.

Figure 3 shows a possible layout of experimental hall with the racetrack type ring that has 118 m -long circumference. There are 4 short straight sections of 3.6 m-long and 2 long straight sections of 10 m-long. Since an RF cavity and pulse magnet for beam injection occupy at least one short straight

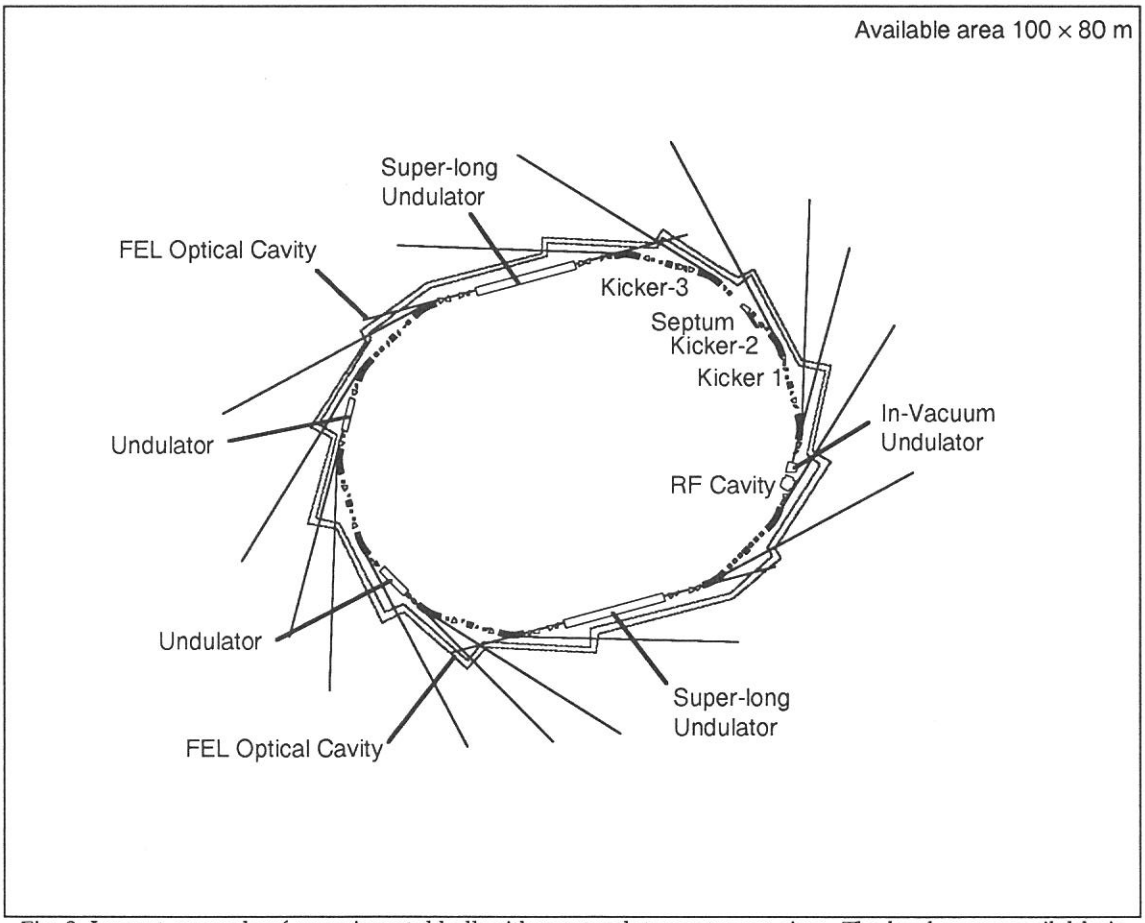

Fig. 3 Layout example of experimental hall with racetrack type storage ring. The land space available is expected to be 80 m × 100 m.

section, 4 or 5 insertion devices may be available. Although the figure is just sketch of UVSOR-II, one can see enough space for beam-line stations. We have not considered about injector accelerators. According to a case of the DELTA facility, which has almost same size as shown in Fig. 3, a linac and a booster synchrotron are able to be placed inside the storage ring. Another possible way of beam supply is to use present injectors of the UVSOR.

The lattice functions of the racetrack type are shown in Fig. 4. To modify the ring into the racetrack, additional 4 families of quadrupoles are required. However the beta functions in the long straight section can be widely varied. Parameters and properties of the designed storage ring and present UVSOR are summarized in Table 1. Here we have to write that this proposed new storage ring is just a starting point of the new project and surely preliminary design. More precise calculations such as dynamic aperture and higher order effect are under developing. We have thought very optimistic for design work right now. However the progress of the light sources is very rapid, thus the most important work for future UVSOR is conclude to be that we always learn from advanced facilities in the world.

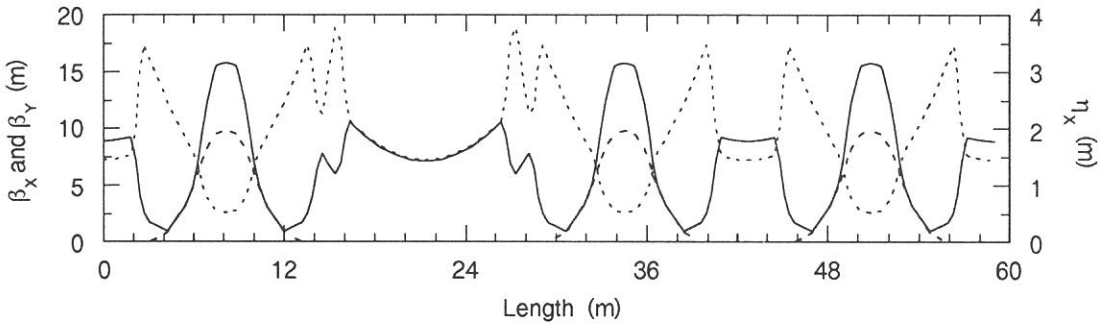

Fig. 4 Lattice functions for racetrack type ring (one superperiod).

Table 1 Parameters of the UVSOR and designed storage ring

UVSOR		*Designed Ring*
53.2 m	Circumference	118.0 m Racetrack
Double-bend Achromat	Lattice Type	Modified Triple-bend Achromat
	Number of Super-cells	2
4	Number of Unit-cells	6
750 MeV (430 ~ 800 MeV)	Beam Energy	1 GeV (0.6 ~ 1.5 GeV)
2.2 m	Bending Radius	4 m (34° normal dipole)
		- 4m (-8° inverted dipole)
8	Number of Dipoles	12 (normal dipole)
		6 (inverted dipole)
28 (4 families)	Number of Quadrupoles	68 (9 families)
3.16 (horizontal)	Betatron Number	5.73 (horizontal)
2.62 (vertical)		2.60 (vertical)
-4.524 (horizontal)	Natural Chromaticity	- 8.588 (horizontal)
-4.800 (vertical)		- 7.272 (vertical)
0.033	Momentum Compaction α_p	~ 0 (- 0.002 ~ + 0.002)
113 π nm rad (at 750 MeV)	Natural Emittance	24.1 π nm rad (at 1 GeV)
4.01×10^{-4}	Natural Energy Spread	3.81×10^{-4}
11.6 keV/turn (dipoles only)	Radiation Loss	28.1 keV/turn (dipoles only)
26 ms (horizontal)	Betatron Damping Time	28 ms (horizontal)
23 ms (vertical)		28 ms (vertical)
11 ms	Synchrotron Damping Time	14 ms
90.115 MHz	RF Frequency	508.123 MHz
50 kV	RF Peak Voltage	500 kV
16	Harmonic Number	200
13.2 kHz	Synchrotron Frequency	0 kHz (max 14.3 kHz)
48 mm - 160 ps	Natural Bunch Length (σ)	~ 0(?) mm (max 2.5 mm - 8.5 ps)
	Beam Size (10 % coupling assumed)	
0.41 mm (horizontal)	Dipole center	0.15 mm (horizontal)
0.28 mm (vertical)		0.17 mm (vertical)
1.05 mm (horizontal)	3.6 m-long straight section	0.46 mm (horizontal)
0.20 mm (vertical)		0.13 mm (vertical)
	10 m-long straight section	0.43 mm (horizontal)
		0.13 mm (vertical)

Synchrotron Radiation Profile Monitor

Shiro TAKANO*, Jun-ichiro YAMAZAKI, Kazuhiko KIMURA,
Hiroyuki HAMA, Toshio KINOSHITA and Masato HOSAKA

**SPring-8, Kamigori, Ako-gun, Hyogo 678 - 12*
UVSOR Facility, Institute for Molecular Science, Myodaiji, Okazaki 444

A new synchrotron radiation profile monitor (SRPM) has been installed on the UVSOR storage ring to quantitatively measure the transverse two-dimensional profile and to deduce transverse emittance of the electron beam.

Schematic layout of the SRPM is shown in fig. 1. The synchrotron radiation emitted by an electron beam moving in magnetic field of a bending magnet (BM3) is deflected upwards by a copper mirror. It is transported into the atmosphere through a glass window. Three mirrors steer the optical beam towards a digital CCD camera (Hamamatsu Photonics C4742). A plano convex spherical single lens with a focal length of 1000 mm makes an image of an electron beam on the CCD sensor. A bandpass filter centered at 500 nm is used to reduce the image enlargement caused by chromatic aberration. The enlargement of observed image caused by chromatic aberration and spherical aberration has been analyzed by a ray-tracing method. The pass band of the bandpass filter has been chosen to be 0.8 nm (FWHM) so that the enlargement is less than 5 μm of the electron beam size, which is negligibly small for the present measurement. A dove prism is put in front of the CCD camera to rotate the image of an electron beam and to align its major and minor axes to the horizontal and vertical axes of the CCD camera, respectively. The CCD camera outputs a 10 bits digital video signal, which is captured by a Macintosh^{TM} personal computer. Parameters of optical components of the SRPM are listed in table 1.

Table 1. Optical Components of the SRPM

lens	
location (nominal)	1490 mm from the source point
focal length	996 mm @ 500 nm
bandpass filter	
center wavelength	500.4 nm
bandwidth	0.8 nm (FWHM)
CCD camera	
location (nominal)	4520 mm from the source point
pixel size	12 μm × 12 μm
number of pixels	1000 (H) × 1018 (V)

The intrinsic beam size of the electron beam σ_x and σ_y are related to the observed sizes Σ_x and Σ_y as,

$$\Sigma_x^2 = \sigma_x^2 + \sigma_{diff}^2 + \sigma_{dof}^2 + \sigma_c^2, \quad (1)$$

$$\Sigma_y^2 = \sigma_y^2 + \sigma_{diff}^2 + \sigma_{dof}^2. \quad (2)$$

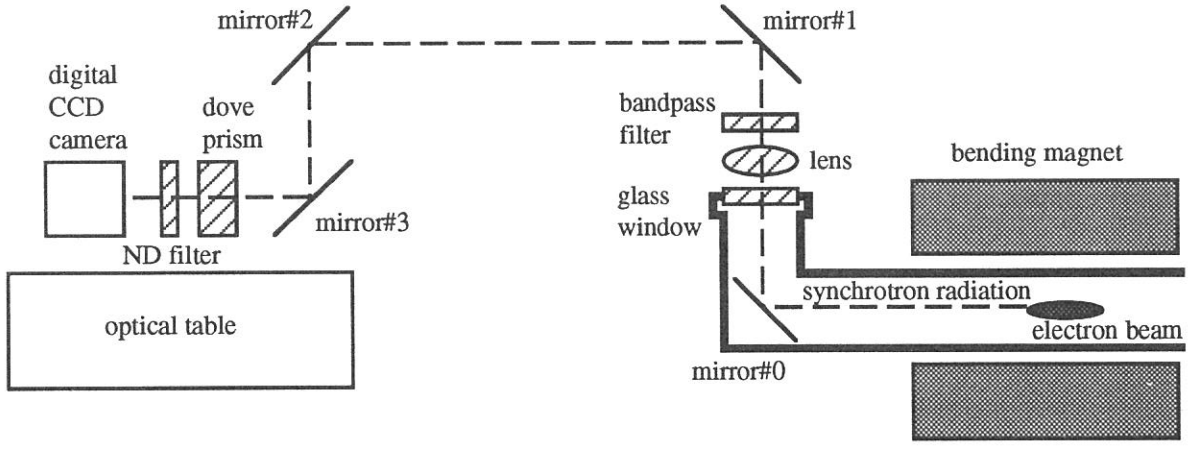

Fig. 1. Synchrotron Radiation Profile Monitor (SRPM)

The half width of the lens aperture $\Delta\theta$ is 8.7 mrad, while the r.m.s. angular spread of synchrotron radiation $\sigma_{r'}$ is 4 mrad at the wavelength λ of 500 nm. The enlargement caused by diffraction σ_{diff} is estimated to be $\sigma_{diff} = \lambda/4\pi\sigma_{r'} = 10\ \mu m$. The depth of field of the source is $R\Delta\theta$, where R is the bending radius or the curvature radius of the electron orbit. The finite depth of field produces an enlargement σ_{dof}, which is estimated as $\sigma_{dof} = R\ \Delta\theta\ \sigma_{r'} / 4 = 77\ \mu m$. The curved electron orbit introduces another enlargement σ_c in the horizontal direction, which is estimated to be $\sigma_c = R\ \Delta\theta^2 = 42\ \mu m$.

Figure 2 shows a typical transverse two-dimensional intensity distribution of the electron beam observed by the SRPM. The energy of the electron beam is 750 MeV. The distribution is consistent with a two-dimensional Gaussian distribution. The one-dimensional profile of the electron beam projected on the horizontal and vertical axes are shown in figures 3. The widths Σ_x and Σ_y of the observed profile are determined by fitting a Gaussian curve to the data. By using equations (1) and (2) the intrinsic electron beam sizes are calculated to be $\sigma_x = 0.380 \pm 0.020$ mm and $\sigma_y = 0.116 \pm 0.010$ mm. The errors quoted are dominated by the uncertainty in the magnification of optics 2.0 ± 0.1.

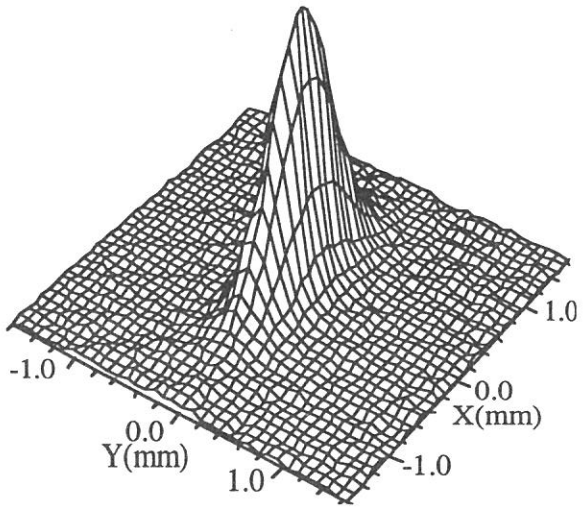

Fig. 2. Surface plot of the observed two-dimensional profile of the electron beam. X and Y denote the horizontal and vertical directions, respectively. The beam energy is 750 MeV.

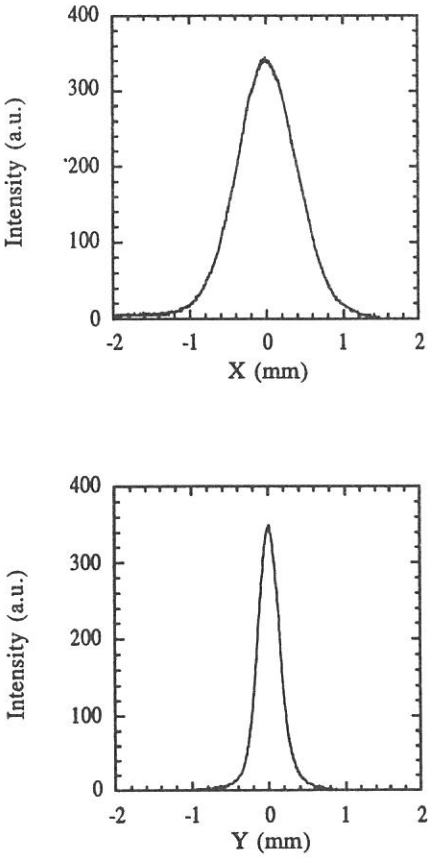

Fig. 3. One-dimensional profiles of the electron beam projected on the horizontal direction (upper) and vertical direction (lower). The beam energy is 750 MeV.

The electron beam sizes σ_x and σ_y are related to emittances ε_x and ε_y as,

$$\sigma_x^2 = \varepsilon_x \beta_x + \eta^2 (\sigma_E/E)^2, \quad (3)$$

$$\sigma_y^2 = \varepsilon_y \beta_y, \quad (4)$$

where βx and βy are the horizontal and vertical beta functions and η is the dispersion function. The nominal source point of synchrotron radiation for the observation with SRPM is 140 mm downstream of the entrance edge of the bending magnet. The calculated beta functions βx and βy and the dispersion function η at the nominal source point are βx=1.21 m, βy = 5.29 m and η = 0.58 m, respectively. The relative energy spread is calculated to be $\sigma_E/E = 4.1 \times 10^{-4}$. According to equations (3) and (4), the horizontal and vertical emittances are deduced to be $\varepsilon_x = 73.2 \pm 12.6\ \pi$ nm rad and $\varepsilon_y = 2.6 \pm 0.4\ \pi$ nm rad, respectively. The total transverse emittance ε_{tot} and the emittance coupling ratio κ are $\varepsilon_{tot} = \varepsilon_x + \varepsilon_y = 75.8 \pm 13.0\ \pi$ nm rad and $\kappa = \varepsilon_y/\varepsilon_{tot} = 3.8 \pm 1.2$ %, respectively. Taking into account of uncertainties of lattice functions introduced by uncertainty of location of the source point, the deduced total emittance is marginally consistent with the calculated natural emittance $\varepsilon_{h,0} = 104.4\ \pi$ nm rad.

Developement of New Operating Points on the UVSOR Storage Ring

Masahito HOSAKA, Hiroyuki HAMA, Jun-ichiro YAMAZAKI, Toshio KINOSHITA and Kazuhiko KIMURA*

UVSOR Facility, Institute for Molecular Science, Myodaiji Okazaki 444
**The Graduated University for Advanced Studies, Myodaiji, Okazaki 444*

Control of operation points on the UVSOR storage ring will enable various usage of it, i. e., a low emittance operation which has an advantage for high brilliance of synchrotoron radiation and a negative alpha operation from which we will learn for our future project UVSOR II. One of the way to vary the operation point is that the electron beam is injected into the storage ring at the regular operation point, and then it is moved to a particular one by changing excitation current of the quadrupole magnets. However this method is not valid in case the betatron tune or the synchrotron tune much changes in the process because the electron beam tends to be lost by the stop bands. It is preferred if the electron beam is able to be injected at a target operation point, we have therefore investigated to develop new injection points for low emittance operation as our first goal.

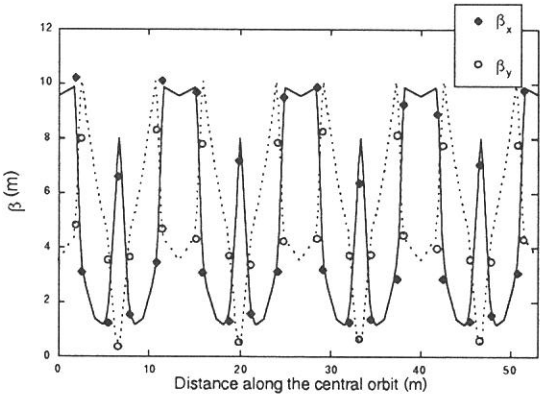

Fig. 1 . Comparison of the measured and calculated betatron functions at the regular operation point.

To develop this study, a suitable lattice calculation is necessary. However lattice characteristics of the UVSOR calculated using the designed values of the field strength do not agree well with experimental ones normally. Therefore we have investigated new correction parameters considering the effect of fringing fields and the non-linear excitation current dependence of magnets. Using the correction parameters, the characteristics of the UVSOR have become to be well reproduced by the calculations. For example, a comparison of measured and calculated beta functions for normal operation point at electron energy of 750 MeV is shown in figure 1. The beta functions were measured with changing field strengths of the qudarupole magnets by 1% using individual correction coils. One can see a good agreement between the experiment and the calculation. We also measured dispersion functions at the location of position monitorsand found them to be consistent with calculations. As a result, we made sure that our new correction parameters are mostly valid.

The experiments for low emittance operation were carried out at an electron energy of 600 MeV, which is the energy for the ordinal injection. Decreasing the field strength of one of defocusing quadrupole magnets (Q3 in fig. 2) in each unit cell, then the horizontal tune is increased, and a beam emittance may become lower.

Table 1. Parameters at the ordinal and low emittance operation at the electron energy of 600MeV. β_x , β_y and η_x mean the horizontal , vertical betatoron functions and the dispersion function at the center of the straight section, respectivly.

	emittance (nmrad)	β_x (m)	β_y (m)	η_x (m)
ordinal	67.1	9.56	3.32	0.41
low emittance (D)	36.2	11.66	11.23	0.30

Furthermore with zero field strength of the defocusing quadrupole magnet, an emittance about 1/2 of the regular operation point can be achieved (Table 1). At the same time, field strength of other quadrupole magnets should be changed in order to keep the betatron amplitude of the electron beam stable. Figure 2 shows betatron and dispersion functions of a quarter lattice at the low emittance operation point.

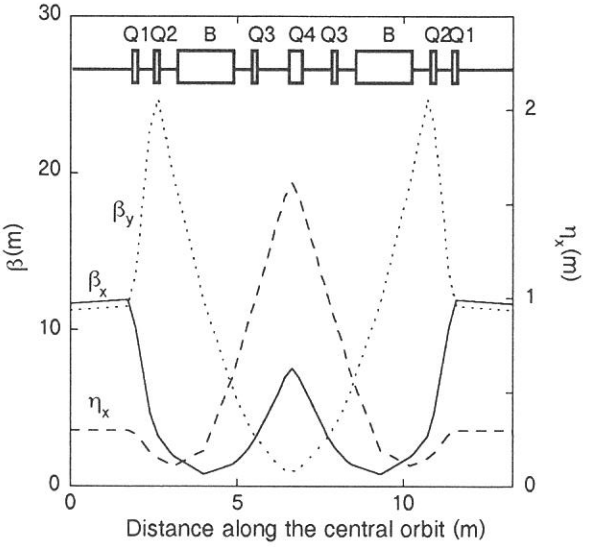

Fig. 2. The betatron and dispersion functions at the low emittance operation point (D in fig. 3)

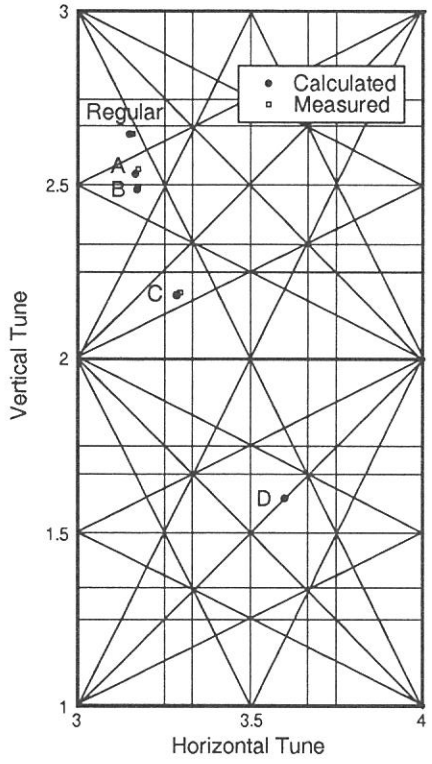

Fig. 3. Tune diagram for the UVSOR storage ring showing the ordinary operation point and new operation points. The lines show stop band up to third order (thicker lines: the integer stop bands).

Prior to the injection at new operation points, we injected the electron beam at the regular point and then changed the operation point decreasing the field strength of the defocusing quadrupole magnet until it reached to C indicated in figure 3. At this operation point the field strength of the defocusing quadrupole magnet is about 67% of that at the normal injection point. At each operation points, we measured the horizontal and vertical tunes and made sure that these values are agree with calculated ones. This calculation was performed using the correction parameters mentioned earlier. At the operation point C, we measured the beam orbit by position monitors located entrances and exits of bending magnets and made it to be almost the same as that at the normal injection point by using steering magnets.

After that, the electron beam was successfully injected at the operation point C, by adjusting the transport and the bump orbit changing. As the next step, we tried to inject the electron beam at the low emittance operation point (D in figure 3). In this case, the observation of the beam orbit prior to the injection is impossible since we can not vary the operation point from the ordinal one to D without passing the strong stop band (integer resonance with vertical tune: $\nu_y = 2$ in figure 2) which will destroy the stored beam completely. We changed the orbit of the electron beam for injection with various way. We, however, have not observed the electron beam stored in the storage ring. This fact indicates that the bump orbit of the electron beam changes greatly at the operation point D. Hence we are now developing new sensitive and fast monitors to observe a trajectory of the electron beam in the storage ring, even it is lost in a single turn.

Gain Narrowing of Spectral and Temporal Widths in the UVSOR-FEL

Kazuhiko KIMURA [a], Jun-ichiro YAMAZAKI [b], Shiro TAKANO [c], Toshio KINOSHITA [b], Masahito HOSAKA [b] and Hiroyuki HAMA [a,b]

[a] *The Graduate University for Advanced Studies, Myodaiji, Okazaki 444*
[b] *UVSOR Facility, Institute for Molecular Science, Myodaiji, Okazaki 444*
[c] *SPring-8, JASRI-JAERI-RIKEN Project Team, Kamigori, Ako-gun, Hyogo 678-12*

Oscillation dynamics of storage ring free electron laser (SRFEL) has been studied experimentally. For utilization of the SRFEL, such as a two-color experiment performed with the Super-ACO FEL (LURE), it is necessary to understand spectral and temporal characteristics of the SRFEL. Since there have been a few operational SRFELs so far, experimental studies are not sufficient to give general descriptions for behavior of the linewidths and the pulsewidths in the SRFEL. The spectral widths of the UVSOR-FEL had not been measured precisely yet since the first achievement of laser oscillation. We have developed measurement system based on a streak camera in order to observe the time-dependent evolution of the temporal and the spectral distributions. Micro-macro temporal distributions have been measured by the streak camera with a dual-sweep [1]. A time-resolving spectrometer consisting of a Fabry-Perot etalon and slow sweep function of the streak camera have been employed for the spectral width measurement [2].

It was observed that the spectral distribution of the UVSOR-FEL has considerable internal substructures. However, the overall widths of the distributions have decreased with the ring currents. The spectral width versus the ring current measured in the gain-switching mode are shown in Fig. 1a. The ring current dependence of the spectral width was discussed by comparing with a model calculation according to a general concept of *gain narrowing*.

A single-pass (small signal) gain of FEL has spectral profile which is proportional to derivative of spontaneous radiation spectrum. As a consequence of exponential amplification, the intensity amplified at the top of the gain profile grows up much more rapidly than that at wings of the profile. Therefore the linewidth of the laser becomes narrower than its gain bandwidth (gain narrowing). Here we introduce a total gain G defined as an integrated value of a single-pass gain over the interaction number. Ratio of the linewidth of the laser σ to that of the gain profile σ_0 is analytically evaluated to be $\sigma / \sigma_0 = \sqrt{1/G}$. Temporal distribution of the single-pass gain is linked to the electron bunch and the temporal development of FEL is in the same

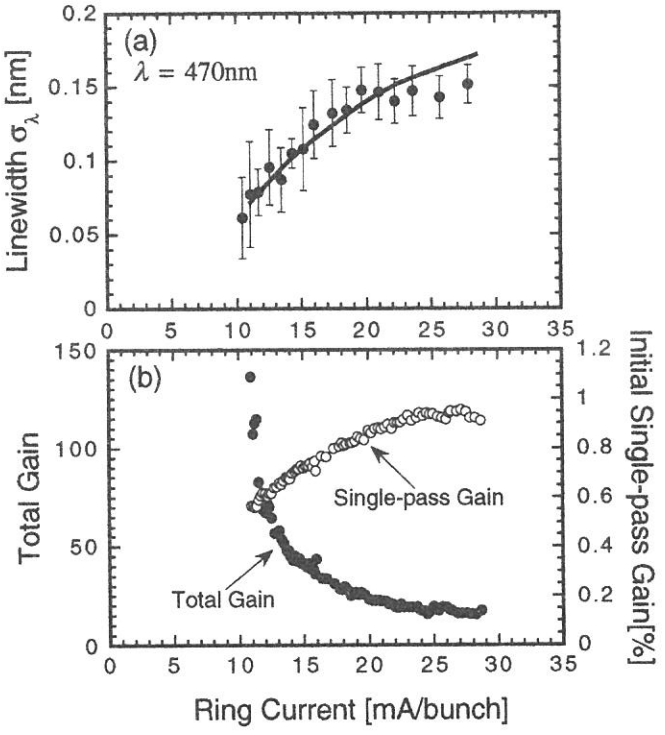

Fig. 1 Measured linewidth versus the ring current (a). The solid line represents the calculations of the gain narrowing model. The initial single-pass gain and the total gain obtained from the macropulse shape are also shown (b).

manner as the spectral narrowing.

A ring current dependence of the initial single-pass gain and the total gain are shown in Fig. 1b. The single-pass gain was deduced from the temporal variation of the laser intensity measured with a photodiode. The initial single-pass gain decreases with the ring current, while the total gain increases conversely. The gain narrowing model predicts that the spectral width decreases with increasing the total gain. The solid line in Fig. 1a represents the spectral widths calculated using the measured total gains, which is in good agreement with the experimental result.

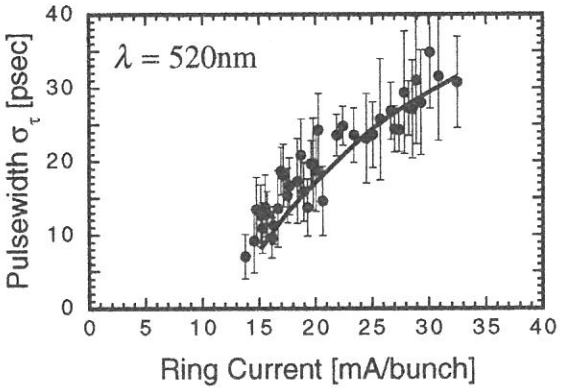

Fig.2 Measured pulsewidth versus the ring current.The solid line represents the calculations of the gain narrowing model.

Figure 2 shows the temporal width measured near the peak intensity of the macropulse plotted as a function of the ring current, which was obtained in a separated experiment. The temporal width of the laser becomes shorter as the ring current decays. The experimental results can be explained by the gain narrowing model as well. The temporal width calculated using the experimentally obtained total gains is also shown in Fig. 2.

In the above results, both the spectral and the temporal widths have decreased with the ring current. This suggests that their widths does not reach the Fourier transform-limit within the range of lasing ring current. Figure 3 shows spectral width versus temporal width in the gain-switching operation calculated using the experimentally obtained total gain shown in Fig. 1b. The shading indicates the Fourier transform-limit region for a laser pulse at 470 nm. Using typical values of the spectral gain bandwidth and the bunch length of the UVSOR-FEL, it is estimated that the total gain of about 3700 is required for the laser development to reach the Fourier transform-limit. Namely the laser should be amplified for ~66 ms in a steady-state when single-pass gain is 0.5% that is a typical gain in the UVSOR-FEL. Extremely stable storage ring and optical cavity are, therefore, required for utilization of high quality SRFEL.

In the analysis, the total gain used for the calculation was deduced from the experimental data. The gain saturation mechanism may play an important role to provide the total gains. Further experimental and theoretical studies are required to discuss the total gain and the saturation mechanism of the SRFEL quantitatively.

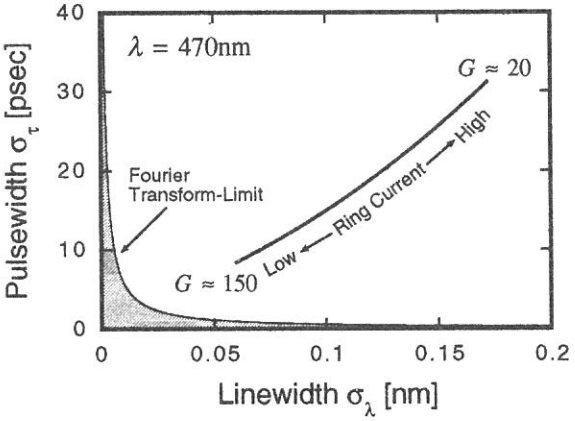

Fig. 3 Linewidth versus pulsewidth calculated from the experimentally obtained total gain. The shaded portion indicates the Fourier transform-limit region for a laser pulse at 470nm.

References

[1] H. Hama, J. Yamazaki, T. Kinoshita, K. Kimura and G. Isoyama, Nucl. Instr. and Meth. A358 (1995) 365.

[2] K. Kimura, J. Yamazaki, S. Takano, T. Kinoshita and H. Hama, submitted to Proc. of 17th Int. Free Electron Laser Conf., New York City (1995).

Free Electron Laser Oscillation around 270nm on the UVSOR Storage Ring

Kazuhiko KIMURA [a], Shiro TAKANO [b], Jun-ichiro YAMAZAKI [c]
Toshio KINOSHITA [c], Masahito HOSAKA [c] and Hiroyuki HAMA [a,c]

[a] *The Graduate University for Advanced Studies, Myodaiji, Okazaki 444*
[b] *SPring-8, JASRI-JAERI-RIKEN Project Team, Kamigori, Ako-gun, Hyogo 678-12*
[c] *UVSOR Facility, Institute for Molecular Science, Myodaiji, Okazaki 444*

Extension to shorter lasing wavelengths is a very important work for a utilization of storage ring free electron laser (SRFEL). Though there is no limitation on the FEL tunability in principle, it is difficult to obtain lasing at short wavelength such as the UV region because both the FEL gain and reflectivity of cavity mirrors decrease as the wavelength becomes shorter. The shortest FEL wavelength achieved so far has been 240 nm operated on the VEPP-3 (Novosibirsk) installed a bypass for accommodating long optical klystron (OK) in 1989. Some projects for lasing in the VUV region using new dedicated storage ring are under way.

On the UVSOR, the first oscillation in the UV region around 300 nm was achieved in 1993 [1]. Further wavelength shortening to 270 nm has been investigated along with other research work on the SRFEL dynamics. The OK of the UVSOR-FEL is scheduled to be replaced by a helical optical klystron in spring of 1996. The FEL gain of the helical OK is expected to be much higher than the present OK [2], and the FEL operation below 240 nm seems to be possible if high reflectance mirror for such wavelength region is available. Experimental study of FEL oscillation at 270 nm in advance of installation of the new helical OK has a significant meaning to investigate both the decreasing tendency and degradation of the mirror reflectance in the UV, the optical performances and the SRFEL dynamics at shorter wavelengths

In order to overcome the increase of cavity losses at shorter wavelength, some gain-enhancement technique are necessary because the UVSOR is not a dedicated ring to FEL and then the length of a straight section for the OK is short. The FEL gain is directly proportional to the electron density which is inversely proportional to the bunch length and the transverse beam size. Reduction of the bunch length using a higher harmonic cavity was employed for the lasing at 300 nm [1]. The beam energy E is a possible factor to enhance the UVSOR-FEL gain. The UVSOR-FEL has been ordinarily operated at the energy of 500 MeV. The FEL gain is a decreasing function scaled as E^{-3}, so that higher gain can be obtained at lower beam energy. In addition to that, the electron density increases as the beam energy becomes lower because the emittance of the storage ring scales as E^2 and the bunch length scales as $E^{1.5}$. Figure 1 shows the relative FEL gain to that at 500 MeV as a function of beam energy. Below 280 MeV, the gain decreases with the energy since the K value of the undulator becomes less than 1. The emission of the resonant wavelength of 270 nm is prohibited at the energy of the shaded portion because of the constraint on the magnet gap of the present OK. Although the FEL gain increases with decreasing the beam energy as shown in Fig. 1, another problem arises, that is, a beam lifetime becomes considerably shorter as the energy

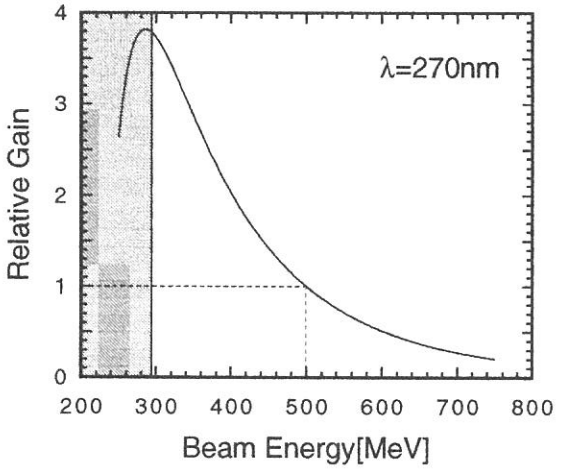

Fig. 1 Relative gain at 270 nm as a function of the beam energy. The emission at 270 nm cannot be obtained at the beam energy of the shaded portion due to the limitation of the magnet gap.

decreases due to Touschek effect scaled as $E^{4.5}$. For a given injection system, the Touschek lifetime determines the maximum beam current stored in the ring. From compromise with the FEL gain and the injection speed of the UVSOR, the energy of 430 MeV has been chosen. It can be expected that the gain at 430 MeV is 1.6 times higher than the gain at 500 MeV.

Since the FEL gain is very small, the mirror reflectance is a critical problem for lasing at shorter wavelengths. In the visible and the UV region, a multilayer dielectric mirror composed of alternate layers of a high index material (HfO2) and a low index material (SiO2) is employed to obtain a very low loss reflector. Although SiO2 is transparent down to 150 nm, the increase in the absorption of the high index coating below 300 nm results in the decrease of mirror reflectivity. In addition, scattering losses due to the surface roughness increases as the wavelength becomes shorter. Normally it is difficult to obtain high reflectance in the UV region. The multilayer mirror is mostly deposited by e-beam evaporation (EBE) or ion beam sputtering (IBS). Figure 2 shows the wavelength dependence of maximum reflectivity of the HfO2/SiO2 multilayer calculated using the extinction coefficient of HfO2 film measured by A. Starke et al. [3]. The calculated reflectivity of EBE and IBS deposited multilayers are represented by the solid and the dotted lines respectively. Since the extinction coefficient of the IBS-HfO2 film in Ref. [3] is 5 to 20 times larger than that of the EBE film, the reflectivity of IBS mirror is expected to be lower. The measured reflectances using a cavity detuning method are also shown in Fig. 2. The reflectance of EBE mirror is close to the calculated value even in the UV range and higher than the IBS mirror.

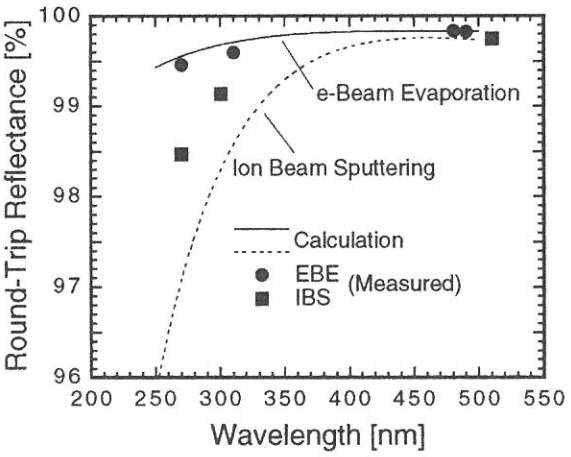

Fig. 2 Round-trip reflectivity of the HfO2/SiO2 multilayer mirror calculated using the extinction coefficient of HfO2 film in Ref. [3]. The reflectivity of EBE and IBS mirrors are represented by the solid and the dotted lines respectively. Measured values on the UVSOR are also shown.

Using the EBE mirror* for the optical cavity, we obtained the first FEL oscillation around 270 nm on January 29, 1996 with the initial beam current of 30 mA/bunch. Figure 3 shows the spectrum of the shortest wavelength laser in the experiment measured by a monochromator with the undulator gap of 53.6 mm. The threshold current was about 13 mA/bunch. Further experimental studies such as the measurement of the average power and the macro-temporal structure of the UV laser are in progress. The achievement of UV laser oscillation may encourage a development of shorter wavelengths FEL on the UVSOR using the new helical OK.

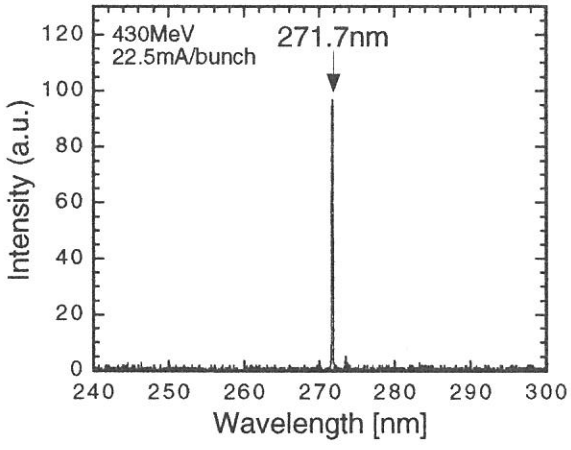

Fig. 3 Spectrum of the shortest wavelength laser measured by a monochromator. The beam energy and the current were 430 MeV and 22.5 mA/bunch respectively.

References

[1] H. Hama, J. Yamazaki and G. Isoyama, Nucl. Instr. and Meth. A341 (1994) 12.
[2] H. Hama, Nucl. Instr. and Meth. A (in press).
[3] A. Starke, H. Schink, J. Kolbe and J. Ebert, SPIE vol. 1270 (1990) 299.

* produced by Showa Optronics Co., Ltd. 22-1, Hakusan 1 chome, Midori-ku, Yokohama 226

Study of Gain Saturation Mechanism in a Storage Ring Free Electron Laser

Hiroyuki HAMA[a], Kazuhiko KIMURA[b], Jun-IchiroYAMAZAKI[a], Shiro TAKANO[c], Toshio KINOSHITA[a] and Marie-Emmanuelle COUPRIE[d]

[a] *UVSOR Facility, Institute for Molecular Science, Okazaki 444 Japan*
[b] *The Graduate University for Advanced Studies, Okazaki 444 Japan*
[c] *SPring-8, JASRI-JAERI-RIKEN Project Team, Kamigohri, Akoh-gun, Hyogo 678-12 Japan*
[d] *LURE CNRS/CEA/MEN, Bat 209D Univ. de Paris Sud,91405 Orsay France*

Gain of the free electron laser (FEL) is steeply decreasing as the electron energy increases, and much sensitive to the beam quality such as the energy spread and instabilities like collective synchrotron oscillations. Although lasing in the UV region has been already achieved on a couple of the storage rings, many difficulties and unknown dynamic behavior remain in the storage ring FELs.

A gain-switching (G-switching) operation seems to be one of reasonable ways to provide the high power pulse-laser [1]. Since, on the storage rings, the laser photons are produced by the interaction with the *same* electron bunch turn-by-turn, the beam quality such as the energy spread becomes no longer same as an initial condition. It is generally so called "bunch-heating". However the longitudinal motion of the electrons in a bunch recovers their quality after taking the time longer than the synchrotron damping time without the FEL interaction. The G-switching technique secures enough time for cooling-down of the electrons by off-synchronism between optical and electron bunches after saturation of the laser. However an effective gain is already decreesed just after the G-switched macropulse developed as shown in Fig. 1. To undertand the bunch-heating process during laser macropulse evolution in the G-switching mode, we analyzed the gain variation with a simple empirical formura

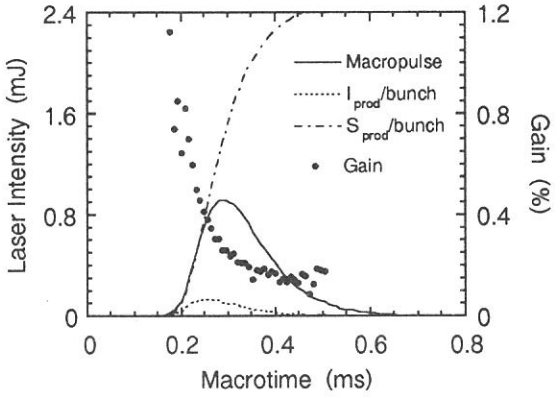

Fig. 1 Deduced time dependent variation of the G-switched macropulse and the effective gain in the cavity.

$$g = g_0 / \left(1 + S_{prod} / S_{sat}\right), \tag{1}$$

where $S_{prod} = \int i_{prod}\, dt$ is an integration of produced laser intensity i_{prod} and g_0 is an initial gain without laser oscillation, and g_0 and S_{sat} are fitting parameters. The saturation energy S_{sat}, which gives half of the initial gain, was obtained at various beam currents. As shown in Fig. 2, S_{sat} devided by number of electrons in a electron bunch was found to be almost constant. From the physical point of view, validity of eq. (1) is not clear at the moment. We can, however, draw a simple picture of that an ability of the electron bunch for photon production is diminished as the photons are emitted, which is analogous to the population inversion in conventional lasers. The result essentially agrees with a theoretical consideration by Dattoli et al. [2].

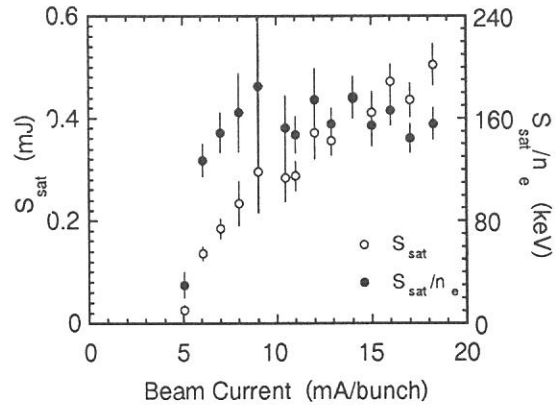

Fig. 2 Deduced saturation energies S_{sat} (open circle) against the beam current. Those per one electron S_{sat} / n_e (closed circle) are also shown.

The FEL gain is proportional to the modulation factor f of the spontaneous radiation, then the temporal gain can be written as

$$g = g_0 f(\sigma_\gamma{}^2) = g_0 / \exp\left[8\pi^2 (N + N_d)^2 \Delta\sigma_\gamma{}^2\right], \tag{2}$$

where $\sigma_{\gamma 0}^2$ is the natural energy spread, and $\Delta\sigma_\gamma^2$ is the additional energy spread $\sigma_\gamma^2 - \sigma_{\gamma 0}^2$. Constant N is the number of periods of the undulator, and $N + N_d$, which represents the interference order between two undulators in the OK, is ~ 90 for the present experiment. Let us assume most part of the gain reduction is induced by the increase of the energy spread. The first order expansion of the denominator in eq. (2) is same as the form of eq. (1), and leads to $S_{prod} / S_{sat} \sim 8\pi^2 (N + N_d)^2 \Delta\sigma_\gamma^2$, then we can roughly estimate the laser intensity in the natural lasing for an equilibrated state of which $S_{prod} / S_{sat} < 1$ is satisfied. Taking account the bunch-cooling due to the synchrotron damping, we obtain the growth rate of the energy spread for one beam bunch as

$$\frac{d\sigma_\gamma^2}{dt} \approx -\frac{2}{\tau_s}\Delta\sigma_\gamma^2 + \frac{d\Delta\sigma_\gamma^2}{dt} = -\frac{2}{\tau_s}\Delta\sigma_\gamma^2 + \frac{i_{prod}}{8\pi^2 (N + N_d)^2 S_{sat}}, \tag{3}$$

where τ_s denotes the synchrotron damping time, and $i_{prod} = dS_{prod}/dt$ is the laser production rate. Let us assume conditions of the equilibrated state as $g = \alpha$ and $d\sigma_\gamma^2 / dt = 0$. One obtains the output power from the optical cavity at the two-bunch operation,

$$P_L = \frac{T}{\alpha} 2\, i_{prod} = \frac{T}{\alpha} \frac{4}{\tau_s} \log\left(\frac{g_0}{\alpha}\right) S_{sat}. \tag{4}$$

Calculated power P_L = 1.2 mW, which is obtained using α = 0.3 %, $T = 5 \times 10^{-5}$, and τ_s =30 ms, g_0=1% and S_{sat} ~ 0.5 mJ, agrees well with the data at the beam current of 18 mA/bunch in shown in Fig. 3. Consequently, the empirical formula of eq. (4) has been in good agreement with the experimental data at various conditions of the mirror and the beam current.

Since synchrotron radiation power is written as $P_{SR} = n_e U_0 / T$ and the damping time is calculated from $\tau_s = E\,T / U_0$, eq. (4) but for one electron bunch P_L' can be written in terms of P_{SR} as

$$P_L' = \frac{T}{\alpha} 16\pi^2 (N + N_d)^2 \Delta\sigma_\gamma^2 \frac{S_{sat} / n_e}{E} P_{SR}, \tag{5}$$

where n_e, U_0, and T denote number of electrons in one bunch, energy loss per turn and the revolution time, respectively. While P. Elleaume derived the average laser power from the optical klystron based on well-known Renieri's limit as [3],

$$P_L = \frac{T}{\alpha} 8\pi (N + N_d)\, f\, \Delta\sigma_\gamma^2 P_{SR}. \tag{6}$$

By comparing with eqs. (5) and (6), we deduced the relative saturation energy as

$$S_{sat} / n_e = E\, f \left[2\pi (N + N_d)\right]^{-1}. \tag{7}$$

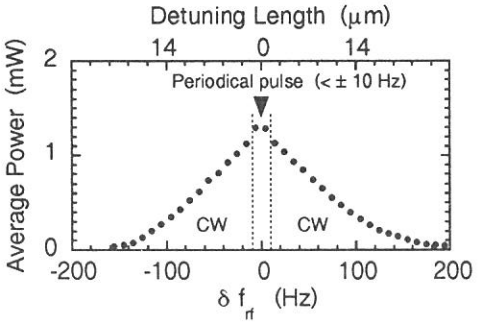

Fig. 3 Measured typical detuning curve of average power in the natural lasing mode at the beam current of 18 mA/bunch.

For the UVSOR FEL, the right hand term of eq. (7) is approximately 700 keV. On the other hand the derived value of S_{sat} / n_e of 160 keV is much smaller than the calculation. That means the average power has not reached Renieri's limit. We do not have an answer for the discrepancy at the moment. It may be difficult to experimentally find out whether the saturation energy is reduced by other factors of the ring such as growth of beam emittance. However to gather experimental data at various lasing conditions including different beam energies will be worth.

References

[1] P. Elleaume, J. Phys. 45 (1984) 997.
[2] G. Dattoli, S. Cabrini and L. Giannessi, Phys. Rev. A44 (1991) 8433.
[3] P. Elleaume, These de doctorat d'Etat (1984) Rapport CEA-R-5270.

Design of a Helical Undulator

Shin-ichi KIMURA, Masao KAMADA, Hiroyuki HAMA,
X. M. Maréchal[1], Takatsugu TANAKA[2] and Hideo KITAMURA[1]

UVSOR Facility, Institute for Molecular Science, Okazaki 444
[1] JAERI-RIKEN SPring-8 Project Team, The Institute of Physical and Chemical Research (RIKEN), Wako 351-01
[2] Faculty of Engineering, Kyoto University, Kyoto 606-01

Circularly polarized light in the vacuum-ultraviolet region is a powerful source for the investigation of the electronic structure of materials. The light can be obtained by off-axis synchrotron radiation from bending magnets and also by insertion devices such as a helical undulator and a helical wiggler. Since the light intensity of the latter is some orders greater than that of the former, insertion devices have been installed in storage rings.

We plan to install a helical undulator in 0.75 GeV electron storage ring, UVSOR, of the Institute for Molecular Science. The main purpose is to investigate the electronic structure of magnetic and non-magnetic materials by spin resolved photoelectron spectroscopy.

A monochromator for the helical undulator, which is named SGM-TRAIN, has already been designed and it is currently under construction [1]. The monochromator covers the energy range of 5 - 250 eV using two glancing incidence and one normal incidence mounts. The energy range of the light from the undulator is therefore required to be in the range of 5 - 250 eV.

Several kinds of helical undulators and wigglers have been installed in other storage rings. They have some disadvantages for our purpose. The main reason is the low acceleration energy of UVSOR. Hence we adopt a new type which is planned for the SPring-8 of JAERI-RIKEN at Nishi-Harima [2]. The advantage compared to other helical undulators or other helical wigglers is follows; (1) the undulator is retractable from the storage ring, (2) the peak energy of the helical undulator radiation can be changed with keeping the degree of helical polarization. The undulator for the UVSOR storage ring becomes not only a helical undulator but also a multipole planar wiggler because of the strong remanent field and the small period length of the permanent magnet. In the following, the design concept and the expected performance of the undulator are reported.

The helical undulator was designed with the following requirements; (1) The perfectly circularly polarized light is obtained in the energy range above 5 eV, (2) the elliptic light is obtained below 250 eV, (3) the throughput photon flux after the post-mirror at the photon energy of 100 eV is 10^{12} photons/sec with the resolving power $E/\Delta E \sim 10^3$, and (4) the length of the straight section in which the undulator is inserted is about 2.9 m and the energy of the electron beam is 0.75 GeV.

The designed alignment and the dimension of permanent magnets are shown in Fig. 1. Fundamentally, the

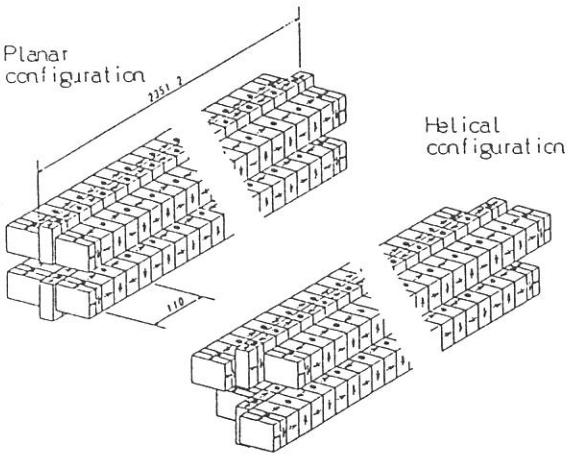

Figure 1. Schematic figure of the helical undulator for the UVSOR storage ring in the planar and the helical configurations.

Number of periods	21
Period length, λ_u	110 mm
Total length	2351.2 mm
Permanent magnet	Nd-Fe-B
Remanent field, Br	1.3 T
Width of magnet pole for vertical field	21 mm
Width of magnet pole for horizontal field	50 mm
Gap between upper and lower magnets	30 - 150 mm
Magnetic field of helical mode	0.007 - 0.45 T
Magnetic field of planar mode	0.015 - 0.83 T
Deflection parameter, $K_{x, y}$, of helical mode	0.07 - 4.6
Deflection parameter, K, of planar mode	0.15 - 8.5

Table 1 Parameters of the helical undulator.

undulator has planar configuration of magnets with 21 periods. It looks like a planar undulator but each magnet array consists with three lanes. Center lane and side lanes provide vertical and horizontal magnet fields, respectively. The phase between the horizontal and the vertical fields can be changed by shifting the side lanes. Hence the direction and the degree of circular polarization can be changed. The detailed parameters of the magnet array are given in Table 1. Since the form of the undulator is like a planar one, the undulator is retractable from the storage ring. Hence the undulator can be removed when the undulator is not used.

The value of λ_u is 0.11 m and the total length of the undulator including the orbital correction magnet is 2.3512 m. The remanent field of the permanent magnet (B_r) is assumed to be 1.3 T. The expected photon energy range of the perfectly circularly polarized undulator radiation is 2 - 45 eV. The higher order radiation in the operation of the elliptic undulator radiation is obtained up to 200 eV. The expected maximum deflection parameter, K, is 8.5 in the planar configuration. The critical photon energy of the planar multipole wiggler operation is about 310 eV. The expected brilliance spectra of some operations compared with the bending radiation are shown in Fig. 2 [3].

In the helical configuration, the K_x and the K_y values can be changed without changing the ratio K_x / K_y. Here K_x and K_y are the parallel and perpendicular components, respectively, of the K of the undulator with respect to the horizontal plane. The magnetic field and the K value as a function of the magnet gap are plotted in Fig. 3. The figure shows that the decreasing rates of K_x and K_y are almost equal to each other. This means that the peak energy of the helical undulator radiation can be changed with keeping the degree of helical polarization only by changing the distance between the upper and the lower permanent magnet arrays.

The design concept of a helical undulator for UVSOR 0.75 GeV storage ring was reported. The expected spectral features are as follows; (1) the helical undulator light is obtained in the energy range of 2 - 45 eV, (2) the intensity is about 400 times stronger than the bending radiation, (3) the peak energy of the helical undulator can be swept by changing only the magnet gap.

REFERENCES

1. M. Kamada, K. Sakai, S. Tanaka, S. Ohara, S. Kimura, A. Hiraya, M. Hasumoto, K. Nakagawa, K. Ichikawa, K. Soda, K. Fukui, Y. Fujii and E. Ishiguro, Rev. Sci, Instrum. **66** (1995) 1537.
2. X. M. Maréchal, T. Tanaka and H. Kitamura, Rev. Sci. Instrum. **66** (1995) 1937.
3. The spectra were calculated using the Synchrotron Radiation Calculation Program, SPECTRA, written by Kitamura and using our original program.

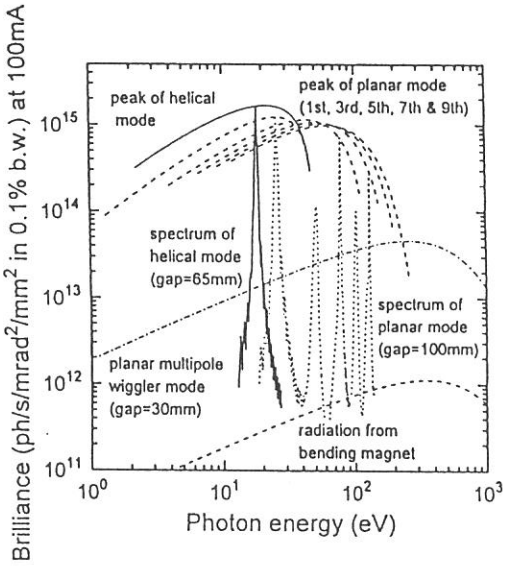

Figure 2. The expected brilliance spectra of the helical undulator for the UVSOR storage ring.

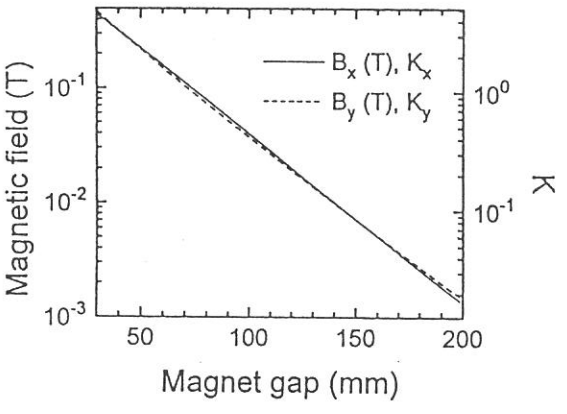

Figure 3. The calculated magnetic field (B_x and B_y) and the K value of the helical configuration parallel (x-direction) to and perpendicular (y-direction) to the horizontal plane as a function of the gap size between upper and lower magnetic arrays.

A helical optical klystron for an UV-FEL project at the UVSOR

Hiroyuki HAMA

UVSOR Facility, Institute for Molecular Science, Okazaki 444 Japan

Most of existing storage ring free electron lasers (SRFEL) are, at present, strongly restricted those performances by degradation of mirrors for optical cavities. Although degradation rate may depend on material, substrate, coating fabrication and so on, some aspects of mirror degradation become clear. First of all, residual hydrocarbon gasses interacting with the XUV radiation from the undulator is considered to be an origin of surface damage even under ultra-high vacuum. Furthermore the XUV radiation may produce defects inside upper layer of coating. Heating of the mirrors due to absorption of laser power also destroys the layers. Recently they have reported that oxygen plasma cleaning certainly removes the surface carbon contamination, and annealing with appropriate temperature effectively cures degradation due to defects inside layer [1]. As far as employing a planar (transverse) optical klystron (POK), on-axis emission of higher harmonic photons is inevitable. Particularly high K undulator is required for short wavelength FELs, then the number of higher harmonics increases and those intensities dominate whole radiation from the POK. On the other hand, an OK employing helical undulators seems to be an attractive solution to reduce the degradation rate of intracavity mirrors because the on-axis radiation is concentrated to be the fundamental radiation. Although the higher harmonics appear in off-axis area, if those opening angles are larger enough than laser spot size, the mirror degradation may be evaded.

The present UVSOR-FEL dedicated for basic research of the SRFEL has been scheduled to be shutdown in 1994, and a new helical undulator for user programs will occupy the straight section of the storage ring. To continue research works of the SRFEL and develop to provide the FEL beam to user experiments, we have investigated to modify the undulator into a helical optical klystron (HOK) by replacing magnets configuration at the center part of the undulator. Based on calculated magnetic fields for a possible HOK configuration, spatial and energy distributions of the radiation and the FEL gain are numerically evaluated.

Here the K number is defined as $K^2 = K_x^2 + K_y^2$, where $K_{x,y} = 0.934 B_{x,y} \lambda_u$, $B_{x,y}$ is the peak magnetic field [T] for the horizontal or the vertical axis and λ_u is a period length of the undulator. For the perfect planar and helical undulators, $K = K_y$ and $K = \sqrt{2}K$, respectively. Dimensions and configuration of magnets for the HOK were optimized to keep a condition of $B_x = B_y$ for whole available gap range. Calculated magnetic fields and beam trajectories in the HOK are shown in Fig. 1, where thickness of the magnets at the dispersive section has been chosen to be same as that at the undulator sections.

The critical frequency of synchrotron radiation ω_c with a bending radius ϱ is generally written as $3c\gamma^3 / 2\varrho$. From this formula, we estimate that the higher harmonics with appreciable photon density may exist up to $e_c[eV] = 712E[GeV]^2 K / \lambda_u[cm]$. Taking several hundreds MeV for the beam energy, the K number of 3 ~ 4 and λ_u of 10 cm into account for the general SRFEL experiment, the critical energy e_c is estimated to be ~ 100 eV, while the FEL wavelength at the region of UV or visible is less than 10 eV. It is obvious that considerable part of radiated power from the OK is consumed as higher harmonic radiations. The higher harmonic radiation must to be less to maintain initial reflectivity of mirrors. The Mirror diameter should be large enough to capture whole the laser intensity spreading by the laser transverse mode, which is, however, not so wide. For example, mirrors of 2" diameter and 1" diameter are used for the UVSOR FEL and the Super-ACO FEL,

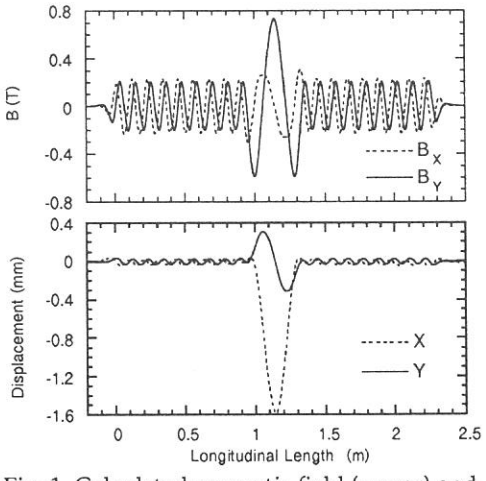

Fig. 1 Calculated magnetic field (upper) and beam trajectory (lower) in the HOK.

respectively. Since spreading angles for the OK radiation are order of *mrad* for both cases, those mirror sizes are comparable to or a bit less than half angles of the undulator radiation given by $(1+K^2/2)/\gamma$. Therefore the irradiation power onto the mirror is influenced by the angular distribution of radiation. Double differential intensity of radiation from a moving charge is evaluated from the integrals of Lienard-Wiechert potential,

$$\frac{d^2\mathbf{I}}{d\omega d\Omega} = \frac{e^2}{4\pi^2 c}\left|\int_{-\infty}^{\infty} e^{i\omega[t+R(t)/c]}\frac{\mathbf{n}\times[(\mathbf{n}-\beta)\times\dot{\beta}]}{(1-\beta\cdot\mathbf{n})^2}\right|^2 dt, \qquad (1)$$

where R is the distance between the charge and the observation point and $\mathbf{n}$ is its unit vector. In actual calculations of radiation, velocity β and acceleration $\dot{\beta}$ of the electron passing through the HOK have been calculated by the relativistic equation of motion in the calculated magnetic field shown in Fig. 1, while a measured magnetic field was used for the present UVSOR FEL with the POK.

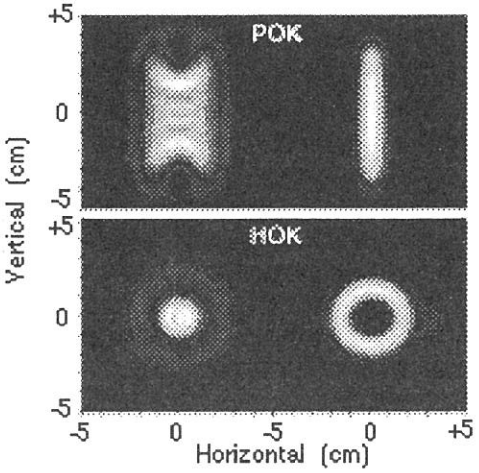

Fig. 2 Calculated spacial distributions of radiation power for POK and HOK.

Calculated spatial power distributions at the position of the front mirror for the low energy region (ε_{photon} < 10 eV; left) and the high energy region (10 < ε_{photon} < 200 eV; right) are shown in Fig. 2. Difference of radiation patterns between the planar and the helical undulator is obvious. A ring-shape spatial distribution of the high energy photons from the HOK is quite favorable because the most of radiation might be out of the front mirror if an 1" mirror is used. Laser spot size on the mirror is determined by a configuration of the optical cavity. For the fundamental mode of TEM_{00} on the UVSOR FEL, the spot size on the front mirror is around 2 mm (*rms*) for the UV and visible laser. Therefore an area of the on-axis 1 cm^2 receives about 95 % of the laser intensity. Beside the heating problem of the mirror, incoming photon number on this area is very important factor for the degradation of the multilayer coating. Although the numbers of photons from the OKs are almost comparable to each other at the low energy region, the photon number from the HOK at high energy region above 10 eV is reduced to less than 20 % of that from the POK.

Using Madey's theorem [2], the calculated peak gain for the POK is 1.7 % at the beam current of 10 mA/bunch with a beam energy of 500 MeV. Meanwhile the experimental value with the present POK at the wavelength around 500 nm was 0.7 %. Taking reduction factors such as a modulation factor and filling factor into account, the measured gain is in good agreement with the calculated value. For the HOK, the calculated peak gain at a wavelength of 235 nm at 10 mA/bunch with a beam energy of 600 MeV is 3.4 %. Although the gain will be reduced to be 1.4 % due to the reduction factors, it is still twice as large as the gain of the present UVSOR FEL.

The spatial and the energy distributions of the spontaneous radiation are calculated based on Lienard-Wiechert potential. For the front mirror aperture, radiation power of higher energy photons emitted from the HOK is significantly reduced. These results of calculation are quite favorable to make less degradation rate for the mirrors. Estimated effective gain at the laser wavelength of 235 nm is 2 times higher than that at the visible laser in the present FEL. We can conclude that the new designed HOK has enough performance not only to obtain a UV lasing but also to utilize the SRFEL in actual synchrotron radiation experiments. In addition, the polarization of the radiation from the HOK is able to be changed, so that a new aspect of utilization of the SRFEL is also hopefully attained.

Author is grateful to Dr. Shin-ichi Kimura for his calculation of the magnetic fields in the optical klystrons with various conditions, and also thank Prof. Hideo Kitamura for his suggestions to the helical undulator.

References

[1] K. Yamada et al., Nucl. Instr. and Meth. A358 (1995) 392.
[2] J.M.J. Madey, Nuovo Cimento B50 (1979) 64.

Tune Shift and Lattice Distortion in Excitation of Superconducting Wiggler

Hiroyuki HAMA, Masahito HOSAKA, Jun-ichiro YAMAZAKI, Toshio KINOSHITA
and Kazuhiko KIMURA*)

UVSOR Facility, Institute for Molecular Science, Okazaki 444 Japan
**)The Graduate University for Advanced Studies, Okazaki 444 Japan*

The UVSOR storage ring equipped a high magnetic field superconducting wiggle , which has become routinely operational in these years. The superconducting wiggler is a wavelength shifter type, and maximum magnetic field is 4 T to supply high intensity soft X-rays. Helium leakage from a refrigerator, used to trouble frequently, was almost fixed, then a total operation time of the wiggler reached 800 hours in 1994, and it was almost one-third of beam times for user experiments. Correction of the closed orbit distortion due to the excitation of the wiggle was also fairly achieved.

Operation of the storage ring with the superconducting wiggler has been apparently established already. However corrections for effects of insertion devices with high magnetic field are usually very significant for reasonable operation of the storage ring, and particularly an low energy storage ring is much sensitive to effects of insertion devices. It must be an important work to investigate what the wiggler field changes the beam properties in the storage ring.

Generally vertical wiggling field in the insertion device causes vertical tune shift. Field gradient $g_y l$ in a half pole of the wiggler with peak magnetic fields B_0 and period length λ_p is written as

$$g_y l = \frac{e}{cp}^2 B_0 \int_0^{\lambda_p/4} \sin^2 2\pi\lambda_p z dz = -\frac{e}{cp}\frac{1}{8} B_0{}^2 \lambda_p . \tag{1}$$

Using a relation of $cp = eB_0\varrho_0$, a focusing strength $k_y l$ is expressed as

$$k_y l = g_y l / B_0\varrho_0 = -\frac{\lambda_p}{8\varrho_0{}^2}, \tag{2}$$

where $B_0\varrho_0$ is the beam rigidity. It may be easier to understand the vertical focusing forth by rewriting eq. (2) using a relation of $p \sim E[GeV] = 0.3B_0[T]\varrho_0[m]$ as

$$k_y l = -\frac{0.3^2}{8E^2} B_0{}^2 \lambda_p . \tag{3}$$

A measured magnetic field in the wiggler is shown in Fig. 1. The wiggler field is basically one period wiggling field. However because correction fields induced sub-coils are required to cancel an integral of magnetic field, the actual distribution of the wiggling field is a bit complicate. Therefore the magnetic field is replaced with a half period of main part and two half periods of sub-parts as shown in Fig. 1. From measured field, period lengths of main part and sub part are estimated to be 0.325 m and 0.26 m, respectively. Peak magnetic field in the sub field is obtained to be $(5/8)B_0$. Since the focusing strength expressed by eq. (3)

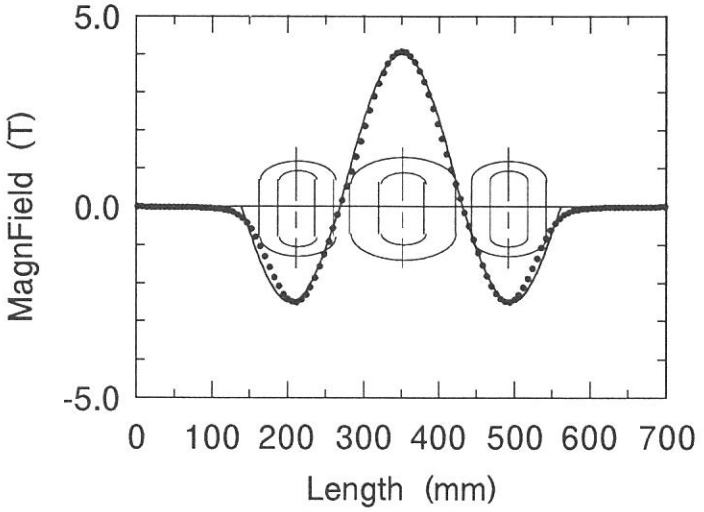

Fig. 1 Measured magnetic field in the superconducting wiggler (solid circle). Configuration of coils is also shown. Solid line indicates a model distribution of the magnetic field for calculations of tune shift and lattice function.

is for *one half pole* of the magnetic field and the total vertical focusing strength is summation of these part, then we have obtained

$$k_y l = -\frac{0.3^2}{8E^2} B_0{}^2 \left[2 \times 0.325 + 4 \times 0.26 \cdot \left(\frac{5}{8} \right)^2 \right] = -0.0119 \frac{B_0[T]^2}{E[GeV]^2}. \quad (4)$$

This is a very important result. The effect of the high magnetic field wiggler is inversely proportional to square of the beam energy and proportional to square of the peak magnetic field. That is the reason why it is very difficult to operate the superconducting wiggler on low energy machines such as the UVSOR. That is also the reason why we could not inject the beam with reasonable injection rate at the injection energy of 600 MeV with the 4 T excitation. It should be noted that there is different situation on the UVSOR with the superconducting wiggler from that at the Photon Factory and other facility with high energy machines.

The tune shift due to the wiggler effect is written as

$$\Delta \nu_y = \frac{\beta_y}{4\pi} k_y l, \quad (5)$$

where β_y is the beta function at the wiggler. We have estimated β_y at the wiggler position is approximately 3.3 m in a normal operation with 600 MeV, then we estimate a very large vertical tune sift of ~ 0.14 at the 4 T wiggler excitation of 4 T.

It is of course very difficult to measure the tune shift with a wide range of the wiggler excitation because the betatron tune may hit stop bands due to the tune shift. In the normal operating point of the UVSOR is surrounded by many resonance lines. Particularly a strong stop band of $\nu_y = 2/3+2$ is very close to the normal operating point. Therefore we changed the operating point a bit in a experiment of measurement of tune shifts. Results of experiment and calculation using eq. (5) for the beam energy of 600 MeV are shown in Fig. 2. Because the formula eq. (5) of the tune shift is valid for only the case of small deviation, and in case of large tune shift, the change of the beta function itself becomes to be not negligible, the theoretical estimation is not always correct. However one can see a very good agreement between the experiment and the calculation. We have also observed the horizontal tune shift. Although we cannot tell exactly, it may be due to multipole components in the wiggler magnetic field.

One can see how the vertical tune shift is large in Fig. 3. In the actual operation in both the beam injection and the 750 MeV operation, the tune has been globally corrected by changing strengths of Q1 and Q2 quadrupole families.

Although we are able to apply a global correction for the tune shift, it seems to be very

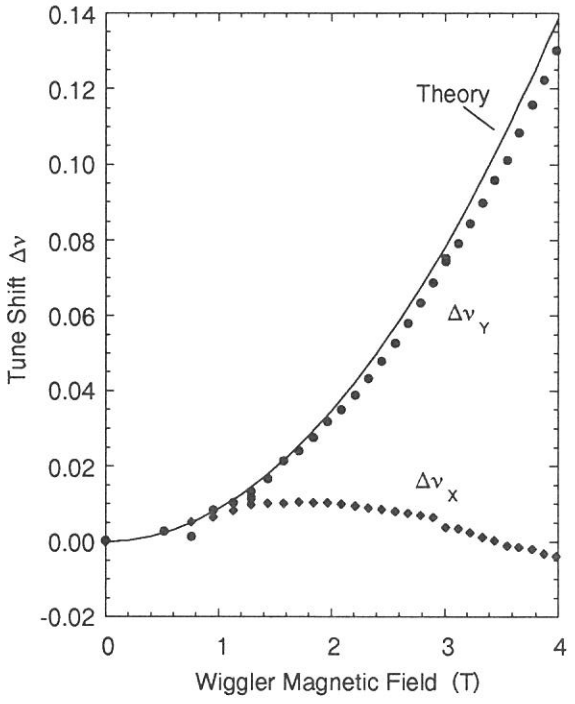

Fig. 2 Measured tune shift due to wiggler excitation at the beam energy of 600 MeV. The solid line indicates theoretical prediction of the vertical tune shift.

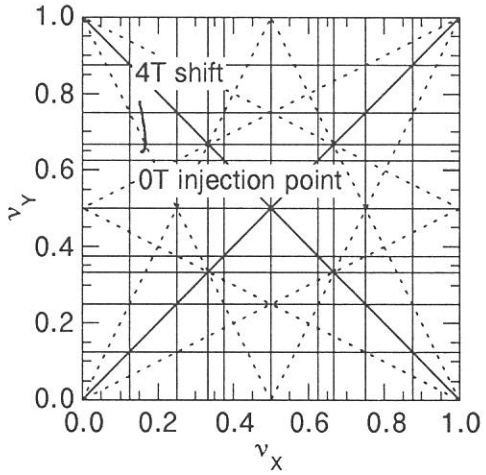

Fig. 3 Tune shift due to the wiggler excitation from 0 T to 4 T with the beam energy of 600 MeV plotted in tune diagram.

much difficult to correct distortions of the lattice function. For future development of the storage ring, we have measured local beta functions for the whole ring by excitation of correction coils of each quadrupole magnet. Figures 4a and 4b show distortion of the beta functions for the horizontal plane and the vertical plane, respectively. A linear lattice calculation for the 4 T wiggler excitation was performed by adding edge focusings of dipoles with a proper magnetic field strength onto the location of the wiggler. The measured values are in good agreement with the calculation. As one can see in the figures, the beta functions are much distorted and the order of symmetry became to be one. Unfortunately the wiggler was not put at the center of the long straight section to avoid a conflict between the main RF cavity. That is a reason of the large distortion of the beta functions along with the high magnetic field. Although we have one quadrupole magnet for the correction of the wiggler effect, that is not located properly. Consequently we have no means to correct the beta functions completely. It has been found out that at least 3 additional quadrupoles are required to correct the

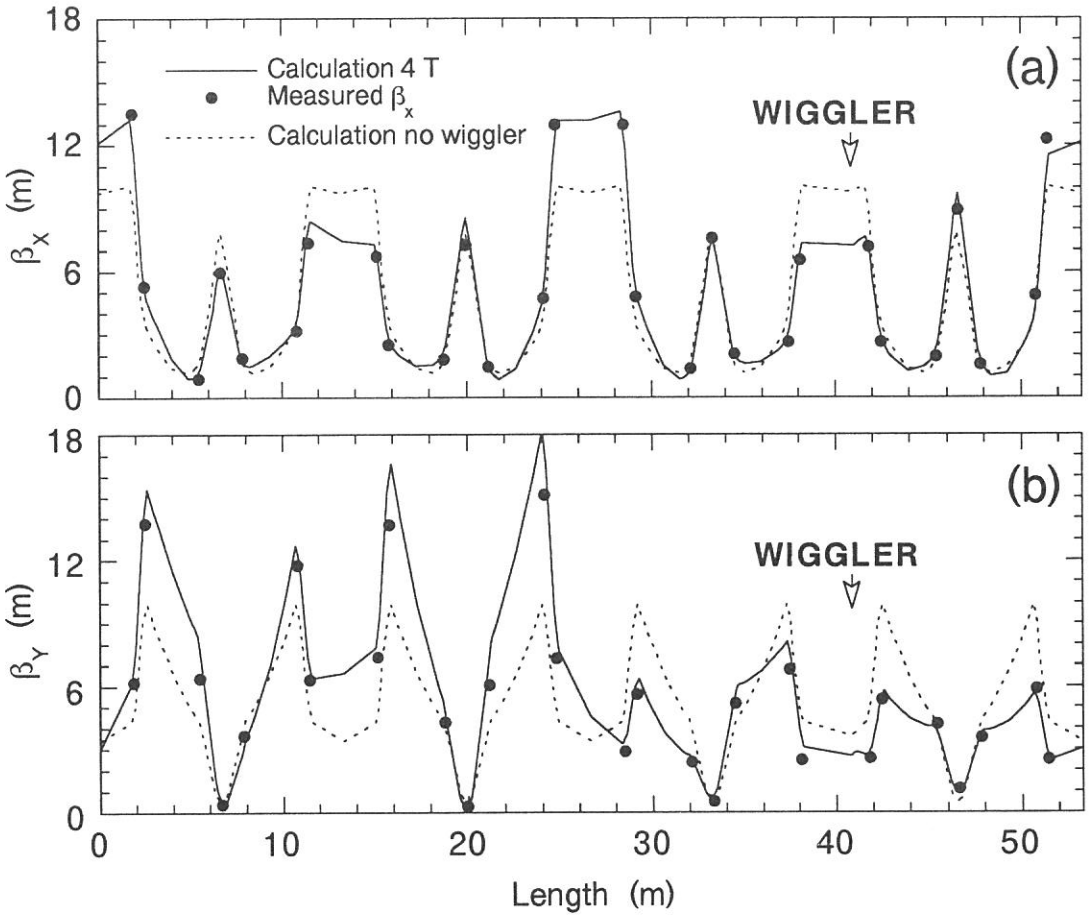

Fig. 4 Measured beta functions for the horizontal (a) and the vertical (b) planes at the beam energy of 750 MeV. Dashed lines show the calculated beta functions without a wiggler excitation (nominal beta functions). Solid lines show the beta functions with the 4 T wiggler excitation.

beta function. However there is no space to put those quadrupoles because of the very small ring. Another possible way is that 3 quadrupolse near the wiggler would be separated from families of serial lines of power supplier, and one introduce independent power suppliers for each quadrupole.

In conclusion, although the superconductiong wiggler has been successfully operated with a very high magnetic field of 4 T, the lattice function is much distorted. That probably spoils the quality of the electron beam and reduces the lifetime. Reduction of the dynamic aperture reduction due to the sextupole field in the wiggler excitation is also important problem. We have learned how the wiggler operation is difficult on the small and low energy machine. Further experimental and theoretical studies are highly desired to improve the wiggler operation.

Construction of a Photoelectron spectroscopy and microscopy system

Toyohiko KINOSHITA, Shinya YAGI, and Shinichi KIMURA

UVSOR Facility, Institute for Molecular Science, Okazaki 444

In order to investigate the surfaces and interfaces of solids, we are constructing an experimental system for photoelectron spectroscopy and photoelectron microscopy. Two types of photoelectron microscopy have been developed so far to achieve micro-analysis. One combines a micro-photon beam with a conventional photoelectron analyzer. The other uses a special electron energy analyzer and an electrostatic lens element to obtain magnified image of the photoelectrons, in which light with normal beam size (several mm ϕ) can be used. Since it is rather difficult to obtain micro- photon beam with enough intensity at UVSOR, we have chosen the latter system. It consists a hemispherical electron analyzer with 150 mm radius, an electrostatic lens system, a magneto lens system for further magnification of the photoelectron image, a X-ray tube (Mg K α, Al K α) for photoexcitation, a sputtering gun, and so on. Ultra high vacuum of less than 2×10^{-10} mbar can be achieved. The schematic diagram of the apparatus is shown in Fig. 1. It is expected that spatial resolution of 2 μm for the imaging mode and 20 μm for the spectroscopic mode respectively, can be achieved.

In conjunction with monochromatized synchrotron radiation light from UVSOR storage ring, we plan to undertake the following studies with this apparatus.

(1) Observation of magnetic domains of ferro- and antiferromagnetic surfaces by means of magnetic dichroism effects.
(2) Observation of adosorbates on metal and semiconductor surfaces.
(3) Photoelectron spectroscopy studies of very small crystals.
(4) In situ observation of photochemical reaction on surfaces.

In 1996, the experiments will be performed at BL7A and BL5B.

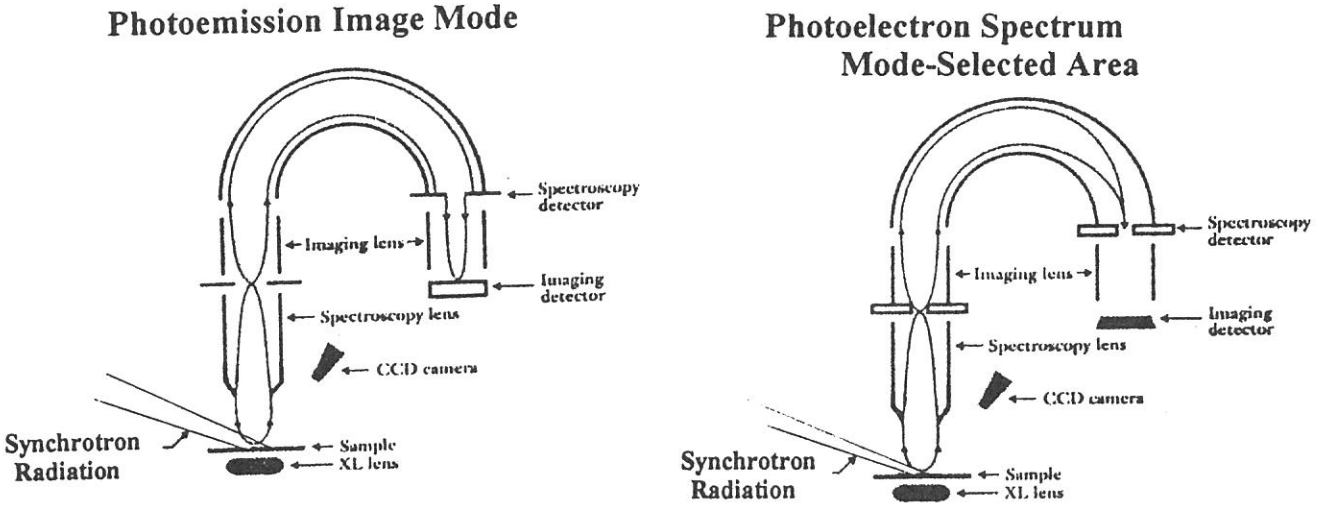

Figure 1

Photoelectron spectro-microscopy equipment.

(BL-1A)

Resonant Ni 3p and 3s Photoemission for the Ni 2p Core-Excitation in NiO

Motohiko NAKAMURA, Yasutaka TAKATA and Nobuhiro KOSUGI
Institute for Molecular Science, Myodaiji, Okazaki 444

Recently some newly-developed theoretical approaches are applied to core excitation spectra of the Ni compounds[1]. In order to obtain the information about core-excited electronic states of NiO, we have measured Ni 3p and 3s photoemission spectra in the Ni 2p core excitation region.

NiO samples were prepared by oxidation of nickel rods (99.99%, ϕ10mm × ^{t}5) at 950°C in air for 5 hours[2]. A clean surface was obtained in situ by scraping the sample with a diamond file under the pressure of ~10^{-10} Torr. Photoabsorption and photoemission spectra were measured at the soft x-ray beamline BL1A[3]. A pair of beryl crystals was used in a double crystal monochromator, and the energy resolution was 0.6 eV at 850 eV. A hemispherical electron energy analyzer (SCIENTA, SES-200) was used for the photoemission measurement. The resultant total energy resolution of the photoemission spectra was about 0.7 eV in the case of the analyzer pass energy of 300 eV. The Ni 2p x-ray absorption spectrum was measured by monitoring total electron yields. Each spectrum was normalized by the photon energy intensity measured by total electron yields from an Au mesh.

Figure 1 shows the Ni 2p XAS spectrum of NiO. Ni 3p and 3s photoemission spectra were measured at the photon energies 0-16 indicated in Fig. 1. Some of the obtained spectra are shown in Fig. 2. At the Ni $2p_{3/2} \rightarrow$ 3d resonance, strong enhancement is observed for the photoemission peaks (a-f) in Fig. 2. Above the photon energy 9 (860.5 eV) in Fig. 1, all the enhanced peaks (a-f) shift toward a higher binding energy with increase of the photon energy similarly to normal Auger peaks. In the Ni $2p_{3/2}$ photoemission spectrum (not shown here), the peak energy represented from the vacuum level is close to the photon energy 9 (860.5 eV) in the Ni $2p_{3/2}$ photoabsorption spectrum. This result indicates that the Ni $2p_{3/2}$ ionization threshold is located around 860 eV.

For the Ni $2p_{3/2} \rightarrow$ 3d resonance region between the photon energy 2 and 6, the energy positions of all the enhanced peaks except peak (b) are equal to those of the satellite peaks observed in the off resonance spectrum (PES(0)). The resonance photoemission spectrum can be interpreted by the interference between the $2p^63d^n \rightarrow 2p^53d^{n+1}$ photoexcitation with a subsequent decay to localized $2p^53d^n$ states and the direct photoemission $2p^63d^n \rightarrow 2p^53d^n + e^-$. The electronic states of the enhanced photoemission peaks at main Ni 2p → 3d resonance (PES(2)) have mainly $3d^8$ configuration because the ground state of NiO has mainly $3d^8$ configuration[5]. In PES(2-6), the spectral features are nearly the same as that in PES(2). If the Ni 2p photoexcited states have different electron configurations, different photoemission peaks should be enhanced in the Ni $2p_{3/2} \rightarrow$ 3d resonance region. This indicates that Ni 2p photoabsorption states at 4 and 6 may have the same $3d^9$ configuration as the photoabsorption state at 2. In a single configuration

approach[6], the photoabsorption states at 2 and 4 were assigned to the $3d^9$ configuration and the photoabsorption at 6 was assigned to $3d^{10}\underline{L}$, where $\underline{L}$ denotes an oxygen ligand hole. In multi-configuration approach[1], the photoabsorption states at 2, 4, and 6 were assigned to the $3d^9$ configuration. The present experimental result is consistent with the assignment by the multi-configuration approach[1].

Tanaka and Jo[7] have calculated the Ni 3d, 3p and 3s resonant photoemission spectra for NiO in the Ni 2p core excited region in the multi-configuration description. The calculated spectra is in good agreement with PES(2) and PES(4) except the intensity of the enhanced peak (b): the relative intensity of peak (b) in PES(2) is much larger than that of the calculated spectrum. They have evaluated interaction between a 3p core hole and 3d electrons for the 3p photoemission spectra and shown that peak (b) becomes strong with increase of this interaction energy. Therefore, it is probable that the 3p-3d interaction has a larger value than 8.3 eV which was the value used in their calculation.

References

[1] M.A. van Veenendaal and G.A. Sawatzky, Phys. Rev., B**50** (1994) 11326.
:M.A. van Veenendaal and G.A. Sawatzky, Phys. Rev. Lett., **70** (1993) 2459.

[2] A. Hiraya, T. Horigome, N. Okada, N. Mizutani, K. Sakai, O. Matsudo, M. Hasumoto, K. Fukui and M. Watanabe, Rev. Sci. Instrum., **63** (1992) 1264.

[3] Y. Takata, M. Nakamura and N. Kosugi, in this issue.

[4] K.S. Kim and R.E. Davis, J. Electron Spectrosc., **1** (1972) 251.

[5] S. Hufner, Advances in Physics, **43** (1994) 183.

[6] G. van der Laan, J. Zaanen, G.A. Sawatzky, R. Karnatak and J.-K. Esteva, Phys. Rev., B**50** (1994) 11326.

[7] A. Tanaka and T. Jo, J. Phys. Soc. Jpn., **63** (1994) 641.

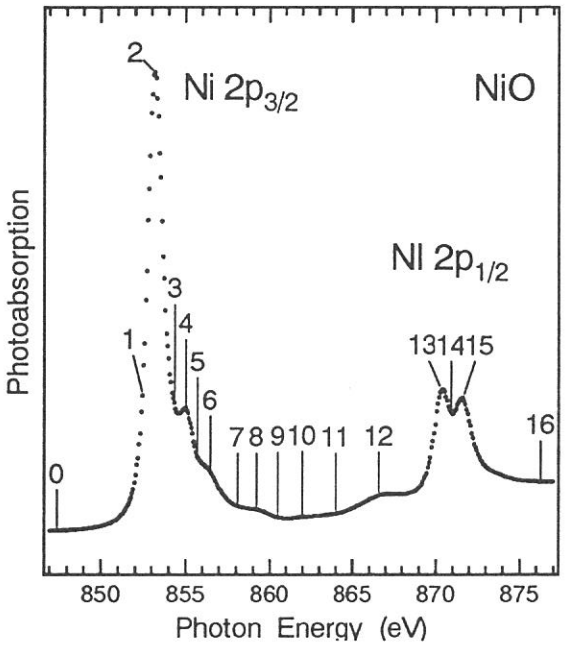

Fig. 1. Ni 2p absorption spectrum of NiO. At the photon energies marked by the vertical bars, Ni 3p and 3s photoemission spectra were measured.

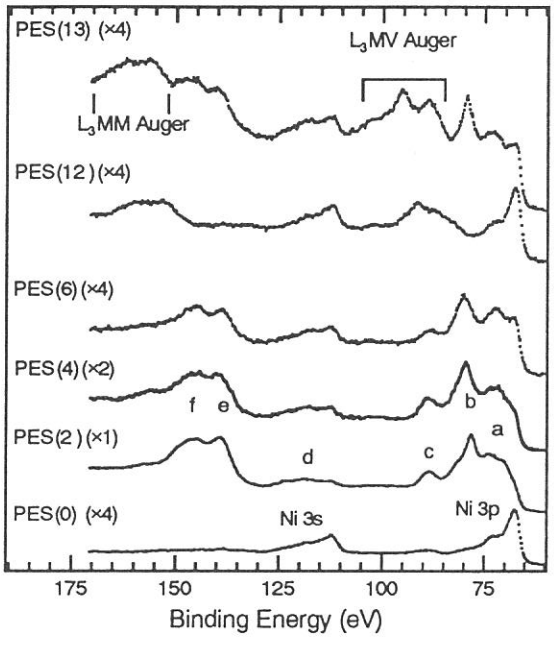

Fig. 2. Comparison of the photoemission spectra measured at the photon energies 0, 2, 4, 6, 12, and 13. Except PES (2), the intensity is multiplied by 2 and 4.

(BL1A)

Resonant Photoelectron Spectra of $K_2Ni(CN)_4$ Following the Ni 2p Excitation

Yasutaka TAKATA, Motohiko NAKAMURA and Nobuhiro KOSUGI

Institute for Molecular Science, Myodaiji, Okazaki 444

Resonant photoelectron, or resonant Auger spectroscopy is a powerful method to investigate core excited electronic states. We have studied electronic states of several 3d transition metal compounds at the 2p (L_{II}, L_{III}) edge. In the present study, we have measured resonant photoelectron spectra of the $K_2Ni(CN)_4$ salts following the Ni 2p photoabsorption, where $Ni(CN)_4^{2-}$ ion is a square-planar complex.

The experiments were performed at the soft x-ray beamline BL1A. A pair of beryl ($10\bar{1}0$) crystals was used in a double crystal monochromator and the energy spread of the incident photon is 0.6 eV around the Ni 2p edge. Ni 2p photoabsorption spectra were measured by total electron yield. Ni resonant photoelectron spectra were measured using a hemispherical electron energy analyzer (SCIENTA, SES-200). The sample of $K_2Ni(CN)_4$ was prepared by scraping the single crystal in ultra-high-vacuum. $K_2Ni(CN)_4$ is an insulator so that an electron flood gun was used to compensate the charge-up of the sample. Electron kinetic energy and intensity were calibrated by using the N 1s photoelectron peak.

Figure 1 shows the Ni 2p photoabsorption spectrum of $K_2Ni(CN)_4$. Resonant photoelectron spectra were measured at the photon energy marked in the photoabsorption spectrum and the results are shown in Fig. 2. A normal Auger spectrum was also measured at the photon energy of 1238 eV. The Ni 3p and 3s photoelectron peaks labeled (*), whose kinetic energies are shifted in proportion to the photon energy (namely, the binding energies are constant), show no resonance enhancement. If the excited electron directly take part in the Auger decay, the energies of the final states should be the same as those of single hole states created by direct photoionization and the peaks should be enhanced at the resonance. Therefore, participant Auger decay is a minor channel. On the other hand, all the peaks (a-e) enhanced by resonant photoabsorption have higher kinetic energy in comparison with the normal Auger spectrum and are shifted as converging to the normal Auger peaks. Peaks (a, b), (c), and (d, e) correspond to $\underline{2p_{3/2}}e-\underline{3p3d}e'$, $\underline{2p_{3/2}}e-\underline{3s3d}e'$ and $\underline{2p_{3/2}}e-\underline{3p3p}e'$ transitions, respectively, where under bar denotes single hole. The symbols e and e' represent that the excited electron remains in the exited orbitals as a spectator electron in the initial and final states, respectively. The kinetic energies of the most intense peak (b) and $\underline{2p_{3/2}}-\underline{3p3d}$ normal Auger peak are plotted in Fig. 3 as a function of photon energy. It is very clearly seen that the kinetic energy of the resonant Auger electron decreases with increase of the photon energy in the $2p_{3/2}$ photoexcited region. Such kinetic energy shift was observed in some atoms[1] and molecules[2]. For solid samples, similar kinetic energy shift was reported in alkali fluorides (LiF, NaF and KF), but the relation between the kinetic energy and photon energy was not clear[3]. The data points in $2p_{3/2}$ photoexcited region (2-6) were fitted by line and the energy dependence (kinetic energy vs. photon energy) was about -0.55 ± 0.05. The energy dependence can be explained qualitatively if we assume that the photoexcited spectator electron behaves like a hydrogenic exciton and the spectator electron is shaken up ($e\neq e'$, $e\rightarrow e'$). The fitted line and the extrapolated line from the normal Auger peak cross at the photon energy of 867 eV, which may correspond to the Ni $2p_{3/2}$ ionization threshold.

References

[1]for example, H. Aksela et al., Phys. Rev. **A39** (1989) 3401.
[2]for example, W. Eberhardt et al., Phys. Scr. **T41** (1992) 143.
[3]H. Aksela et al., Phys. Rev. **B49** (1994) 3116.

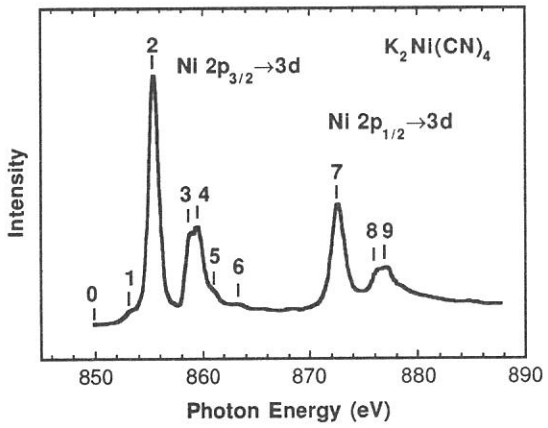

Figure 1. Ni 2p photoabsorption spectrum of $K_2Ni(CN)_4$.

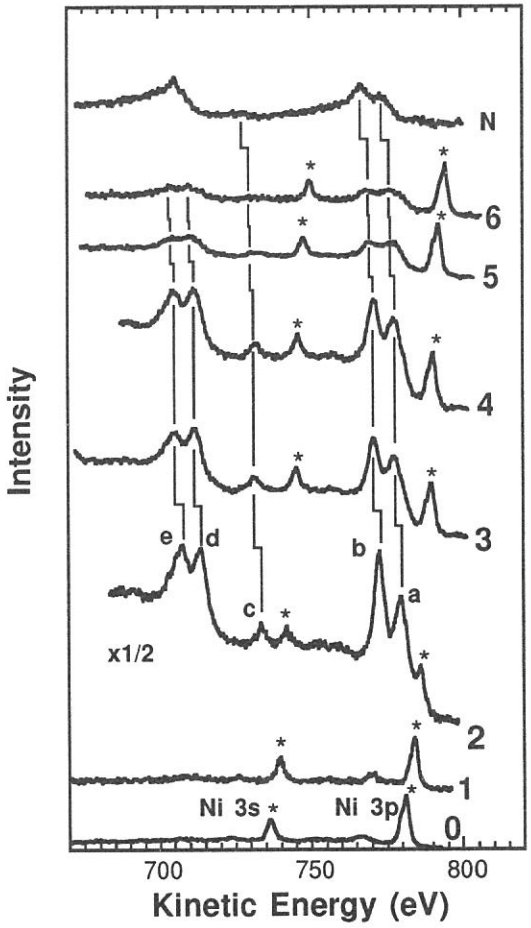

Figure 2. Resonant photoelectron spectra of $K_2Ni(CN)_4$.

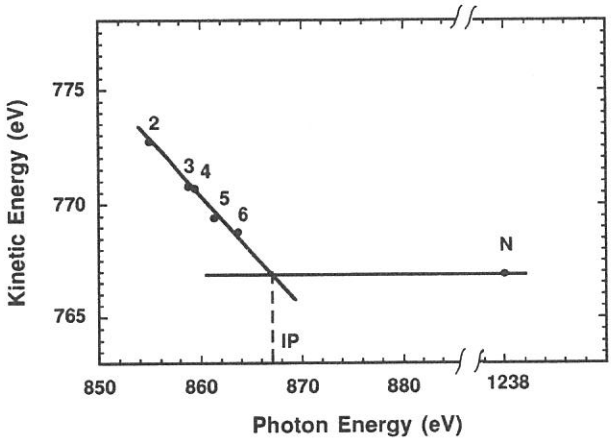

Figure 3. Kinetic energy of the spectator Auger peak (b) in Fig.2 as a function of excitation photon energy.

(BL1B)

Excitation Spectra of Excitonic Luminescence in Lead Halides

Tetsusuke HAYASHI, Masayuki WATANABE, Ping GU*, Takayuki MAKINO**
and Toru Tsujibayashi***

Department of Fundamental Sciences, Faculty of Integrated Human Studies, Kyoto University, Kyoto 606
**Department of Physics, Faculty of Science, Kyoto University, Kyoto 606*
***School of Human and Environmental Studies, Kyoto University, Kyoto 606*
****Department of Physics, Osaka Dental University, Hirakata 573*

Excitation spectra of luminescence in the high energy ultraviolet region beyond the band-gap of solids contain information on relaxation processes of initially created hot electrons. A role of excitons in the de-excitation process is of particular interest, but investigations have not been accumulated yet. Recently, Lushchik *et al.*[1] observed a significant difference in the excitation spectra between intrinsic luminescence bands of alkali halides, and suggested the excitonic process stimulated in a particular energy region. We have investigated luminescence excitation spectra in PbI_2 and $PbBr_2$ in the energy range between 2 and 13 eV with BL1B beam line of UVSOR. The lowest energy exciton state in PbI_2 is known to arise from 6s-6p intraionic transition of Pb^{2+},[2] and, presumably, it holds also in $PbBr_2$. Exciton formation through high energy excitation will be manifested by the luminescence band characteristic of the cationic exciton.

Figure 1 shows near-normal reflection spectra measured on the surface cleaved perpendicular to the crystal c-axis (upper) and the excitation spectra of luminescence bands (lower) in PbI_2 and $PbBr_2$ at 12 K. Luminescence spectrum of PbI_2 at low temperatures consists mainly of the bands due to free excitons, bound excitons and D-A pair recombination. The excitation spectrum (1) corresponds to that of free exciton band (FE), and the spectrum (2) to that of D-A pair recombination luminescence (DA). The intensity of the two spectra are normalized at 4 eV. The structures in the reflection spectrum of PbI_2 below 4 eV was assigned to excitonic transitions from the valence band top (Pb^{2+} 6s) to Pb^{2+} 6p-like conduction band states which are split by spin-orbit interaction and the crystal field.[3,4] The structures between 5 and 7 eV were assigned to excitonic ones arising from the onset of I^- 5p-like valence band, and those above 7 eV to the lower split part of the same valence band. We can see that the luminescence efficiency of FE relative to that of DA is accurately constant below 7 eV, while it starts to increase above 7 eV.

There is no report on the band structure calculation for $PbBr_2$. However, the feature of the reflection spectrum is very similar to that of PbI_2 except for a high energy shift of about 1.5 eV. Excitation in the lowest exciton band induces efficiently a luminescence band at 2.75 eV (Blue), while for excitation above the band gap the Blue band is replaced by the bands at 2.62 eV (BG) and at 1.88 eV (Red). Excitation spectra for Blue and

Red bands are shown by (1) and (2), respectively, in the figure. The intensity of the two spectra are normalized at 5 eV. The Blue band is firmly ascribed to self-trapped excitons related to the lowest cationic exciton. The origin of the Red band is not clear at present, but it is certainly an intrinsic one due to recombination of electrons with a kind of trapped holes since the band is excited only in the fundamental absorption region. (Excitation slightly below the exciton absorption edge induces a similar band, but the peak is not identical with the Red band.) The efficiency of the Blue band relative to that of Red one increases clearly above 8.5 eV.

The enhancement in the relative luminescence efficiency of FE in PbI_2 and of Blue in $PbBr_2$ can be identified with that in the exciton formation through hot electron excitation. The enhancement is seen in a similar energy range in the two crystals, namely, the onset of the lower split part of halogen valence band. Understanding on the mechanism of exciton formation yielded in the limited energy range has not yet been established.

References

1) A. Lushchik *et al.*: Phys. Rev. **B50** (1994) 6500.
2) I. Ch. Schlüter *et al.*: Phys. Rev. **B9** (1974) 1652.
3) J. Beaumont *et al.*: J. Phys. C **10** (1977) 761.
4) T. Hayashi *et al.*: J. Phys. Soc. Jpn. **57** (1988) 1861.

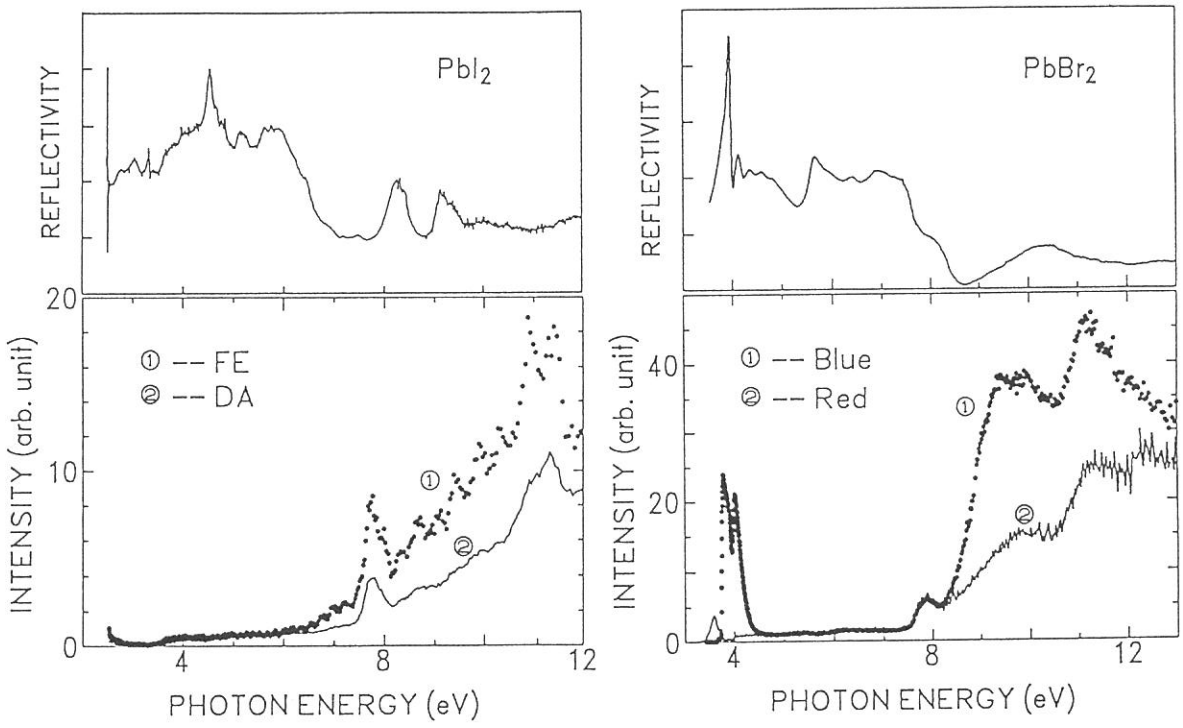

Figure 1

(BL1B)

Intrinsic nature of the 6.0-eV band appearing on the high-energy side of Auger-free luminescence in CsCl

Minoru ITOH

Faculty of Engineering, Shinshu University, Nagano 380

It has been established that Auger-free luminescence (AFL) of CsCl is ascribed to the radiative transition of electrons from the Cl^- $3p$ valence band to the Cs^+ $5p$ core band [1]. This luminescence consists of two intense bands peaking at 4.6 and 5.2 eV, with a long tail extending down to 3.0 eV. Besides these bands, a weak shoulder-like band has been reported to appear around 6.0 eV in CsCl by several researchers [2-4]. They have tentatively attributed it to Br^- impurities. This conclusion is based on the following results; (i) the AFL band of CsBr has a component around 6.0 eV, and (ii) the intensity of the 6.0-eV band in CsCl is nearly proportional to the Br^- ion concentration. However, similar weak bands have also been found on the high-energy side of the AFL in other systems such as RbF and CsF, and they have been confirmed to be of intrinsic origin. In the present work, therefore, we have made the detailed measurements of the excitation spectra and decay behaviors of the AFL in CsCl, in order to clarify the nature of the 6.0-eV band.

Figure 1 shows luminescence spectrum of a nominally pure crystal of CsCl, measured by the core-band excitation with 21.4-eV photons at 80 K. The specimen was grown from Merck suprapur-grade chemicals by the Bridgman technique under a halogen atmosphere. As clearly seen, there exists a weak structure around 6.0 eV on the high-energy side of the main AFL bands at 4.6 and 5.2 eV. The same band was also found in solution-grown CsCl crystals.

In Fig. 2 are shown excitation spectra for the 5.2 and 6.0-eV bands in CsCl. Both bands exhibit essentially the same excitation spectrum; the threshold at 14.2 eV, the fine structure between 14.5 and 17.0 eV, and the broad structure around 21.0 eV. It is worth noting that the excitation spectrum for the AFL (6.0-eV band) of CsBr is rather different from those of Fig. 2 except for the identical threshold energy [1], although this fact does not rule out completely any possibilities of a contribution

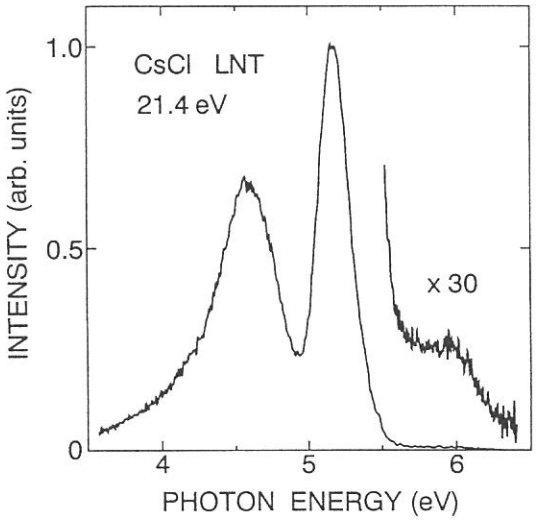

Fig. 1. Luminescence spectrum of CsCl measured under the core-band excitation with 21.4-eV photons at liquid nitrogen temperature.

of Br^- impurities.

It has been well confirmed that, at room temperature, the decay time τ of the AFL is very different between CsCl (1.2 ns) and CsBr (0.07 ns) [1,5]. Therefore, it may be promisingly important to investigate the decay behavior of the 6.0-eV band in CsCl. In Fig. 3 are shown decay curves of the 5.2- and 6.0-eV bands in CsCl, obtained at 300 K under the single-bunch operation of synchrotron radiation at 21.4 eV. The value of τ of the 5.2-eV band is estimated to be 1.2 ns, in good agreement with the previous data. From this figure, one can recognize that the 6.0-eV band shows the same decay time as the 5.2-eV band.

The above results strongly suggest that the 6.0-eV band is intrinsic feature of CsCl, arising from the Auger-free transition of electrons between the Cl^- $3p$ valence band and the Cs^+ $5p$ core band. It is interesting to mention here that the AFL spectra may have a common profile in many systems; i.e., they are composed of three parts. The main part, consisting of one or two intensive bands, appears in the energy range $E_{VC} - \Delta E_V < h\nu < E_{VC}$, where E_{VC} is the energy difference between the top of the valence band and that of the outermost-core band, and ΔE_V is the valence-band width. The second part appears on the high-energy side of the main band(s), which shows a fine structure in CsF and CsBr, and a shoulder-like structure in CsCl, RbF and BaF_2. The third part appears as a low-energy tail of the main band(s), extending to the energy region below $E_{VC} - \Delta E_V$. Theoretical studies taking lattice-relaxation effects into account are highly required to understand these characteristics of the AFL spectra.

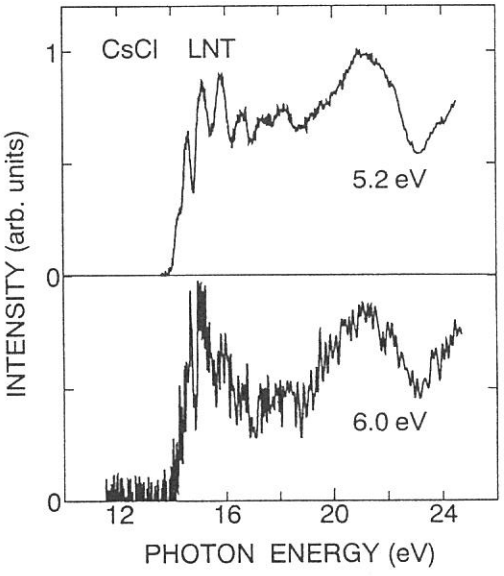

Fig. 2. Excitation spectra for the 5.2- and 6.0-eV bands in CsCl at LNT.

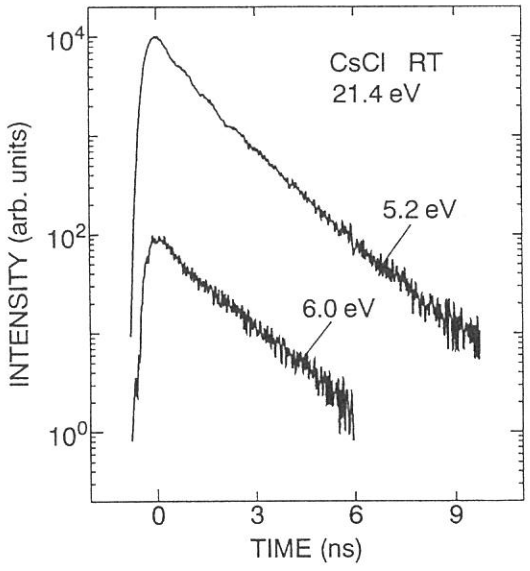

Fig. 3. Decay curves of the 5.2- and 6.0-eV bands in CsCl excited with 21.4-eV photon pulses at RT.

[1] M. Itoh, S. Kubota, J. Ruan(Gen) and S. Hashimoto; Rev. Solid State Sci., 4 (1990) 467.

[2] I. Kuusmann, T. Kloiber, W. Laasch and G. Zimmerer; Radiation Effects and Defects in Solids, 119-121 (1991) 21.

[3] Z. Rachko, J. Jansons and J. Valbis; Radiation Effects and Defects in Solids, 119-121 (1991) 93.

[4] K.U. Ibragimov and F.A. Savikhin; Phys. Solid State, 35 (1993) 744.

[5] T. Matsumoto, K. Kan'no, M. Itoh, H. Hara and N. Ohno; UVSOR Activity Report 1993, (1994) 147.

(BL1B)

Auger-free luminescence in mixed $CsF_{1-x}Cl_x$ system

M. Itoh,[a] H. Hara,[a] N. Ohno,[b] H. Yoshida,[b] S. Hashimoto,[c] K. Kan'no[d] and M. Kamada[e]

[a]*Faculty of Engineering, Shinshu University, Nagano 380*
[b]*Faculty of Engineering, Osaka Electro-Communication University, Neyagawa 572*
[c]*Department of Physics, Kyoto University of Education, Kyoto 612*
[d]*Department of Physics, Kyoto University, Kyoto 606*
[e]*Institute for Molecular Science, Okazaki 444*

The spectral shape of Auger-free luminescence (AFL) has been studied theoretically in terms of a cluster model or a band model. However, no consensus has been reached as to the validity of these approaches. The AFL transition takes place after photo-generated core holes relax to the top of the band. This suggests that the AFL spectra are not so sensitive to the density-of-states of the core band, but are influenced by the changes in the valence band. Therefore, it is meaningful to investigate the AFL in halogen-substituted alkali halides. In the present work we have studied the AFL in CsF crystals containing a small amount of Cl^- ions.

Figure 1 shows luminescence spectra of $CsF_{1-x}Cl_x$, (a) $x = 0$ and (b) $x = 0.01$, obtained by the core-band excitation with 21.4-eV photons at 80 K. In Fig. 1(a), one can see an intense band at 3.2 eV and some weak bands at 3.7 and 4.0 eV. These bands have been assigned to the AFL due to radiative transition of electrons from the F^- $2p$ valence band to the Cs^+ $5p$ core band [1]. From Fig. 1(b) it is apparent that the introduction of small amounts of Cl^- ions into CsF gives rise to a luminescence band peaking at 4.5 eV.

In Fig. 2 are shown excitation spectra for the 3.2- and 4.5-eV bands in $CsF_{1-x}Cl_x$ with $x = 0.01$. The excitation spectrum for the AFL (5.2-eV band) in CsCl is also depicted in Fig. 2. The 4.5-eV band is induced by the photo-excitation above 14.2 ± 0.2 eV, which is the same energy as the 3.2-eV band of CsF and the 5.2-eV band of CsCl.

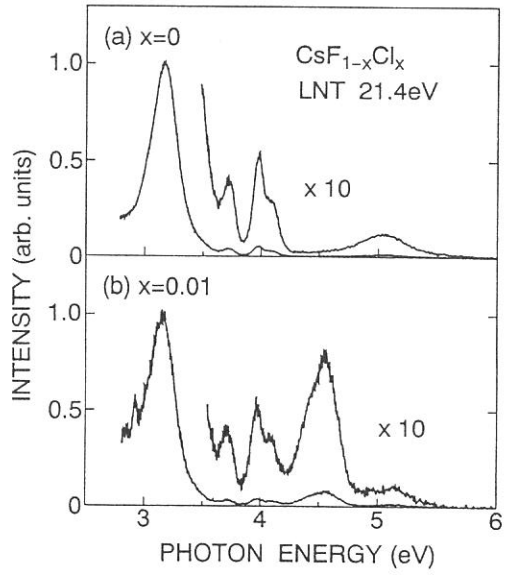

Fig.1. Luminescence spectra of $CsF_{1-x}Cl_x$ excited with 21.4-eV photons at LNT; x = 0 and 0.01.

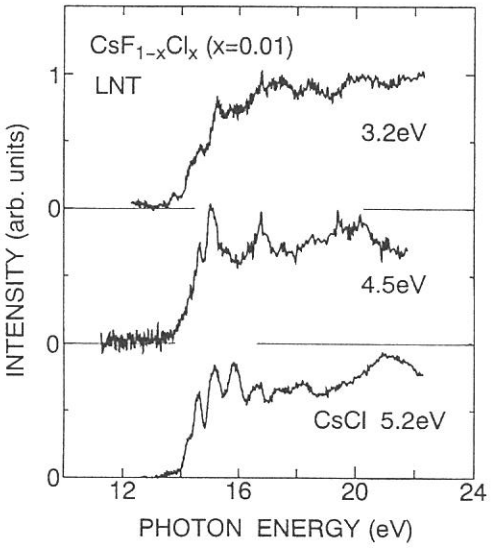

Fig.2. Excitation spectra for the 3.2- and 4.5-eV bands in $CsF_{1-x}Cl_x$ and the 5.2-eV band in CsCl.

When small amounts of Cl^- ions are added into the matrix of CsF, the Cl^- $3p$ states (localized impurity band) will be situated 1-2 eV above the top of the F^- $2p$ valence band. It is thus anticipated that an additional AFL band appears on the high-energy side of the AFL band of CsF. All the present results indicate that such a band is actually observed in the region of about 4.5 eV where pure CsF does not emit. The new band observed at 4.5-eV is attributed to the radiative electronic transition from the Cl^- $3p$ impurity level to the Cs^+ $5p$ core band.

It is of considerable interest to compare the Cl^--impurity AFL band with that of pure CsCl. To do so, we subtract the luminescence spectrum of Fig. 1(a) from that of Fig. 1(b) after normalizing their intensities around 4.0 eV. The result is shown by solid line in Fig. 3, together with the AFL spectrum (broken curve) of pure CsCl. As clearly seen, the impurity-associated band is single-peaked, in contrast to a double-peaked structure of the pure band. Since the space lattice of CsCl is simple cubic, the Cs^+ ion has eight Cl^- ions as nearest neighbors. On the other hand, in CsF crystal of face-centered cubic, each Cs^+ ion is surrounded by six nearest neighbors of F^- ions, one of them being replaced by a Cl^- ion in mixed $CsF_{1-x}Cl_x$. It is thus supposed that the spectral structure of AFL is very sensitive to the immediate anion environment around the core hole produced on a cation site.

The single-peaked AFL bands have also been observed around 4.5 eV in KCl:Cs and RbCl:Cs systems under X-ray irradiation [2]. In these systems, an alkali metal ion (K^+ or Rb^+) is replaced by a Cs^+ ion in the NaCl-type configuration, and therefore, the resultant AFL bands have been ascribed to the radiative electronic transition from the Cl^- $3p$ valence band to the Cs^+ $5p$ impurity level. The spectral width (FWHM) of the AFL bands in KCl:Cs and RbCl:Cs is about 0.45 eV at room temperature. This value is almost comparable to that (0.35 eV) of the 4.5-eV band in Fig. 3. In other words, the spectral width of AFL does not depend strongly on whether the upper filled band is derived from the valence state or the impurity state. This fact suggests that the spectral width of AFL is not connected to that of the upper filled band in a straightforward way. It may be that some lattice-relaxation effect plays a significant role for the broadening of the AFL bands.

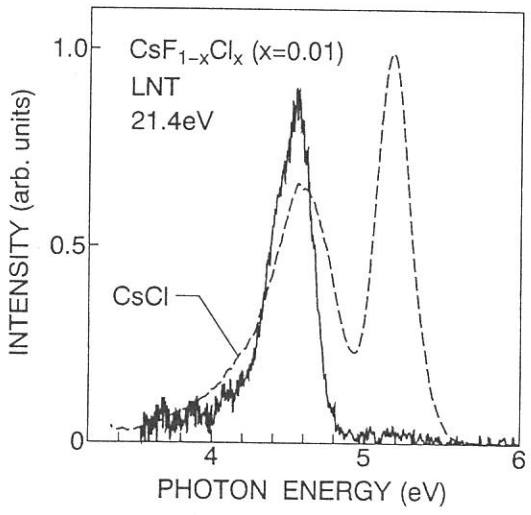

Fig.3. Comparison of the 4.5-eV band in $CsF_{1-x}Cl_x$ with the AFL band in CsCl.

[1] M. Itoh, S. Kubota, J. Ruan(Gen) and S. Hashimoto; Rev. Solid State Sci., 4 (1990) 467.
[2] A.S. Voloshinovskii, V.B. Mikhailik, S.V. Syrotyuk and P.A. Rodnyi; Sov. Phys. Solid State, 34 (1992) 1022.

(BL1B)

Luminescence due to Localized Excitons in CsCl:I and CsCl:Br

Nobuhito Ohno, Hisashi Yoshida and Minoru Itoh†

Department of Solid State Electronics,
Osaka Electro-Communication University, Neyagawa 572
†*Department of Applied Science, Shinshu University, Nagano 380*

As is well known, the crystal structure of alkali halides is classified into two groups: NaCl type and CsCl type. The luminescence properties of self-trapped excitons (STE's) in the former have been investigated experimentally and theoretically, and the STE configurations have been discussed in terms of "on-center" and "off-center" model. On the other hand, the STE's in the latter case, especially localized excitons in a halogen-doped crystal with the CsCl structure, have been little studied so far. It is of fundamental interest to investigate whether or not a difference in the crystal structure affects the relaxed configuration of excitons.[1] In present work, we have studied luminescence properties of localized excitons in dilute mixtures of CsCl:I and CsCl:Br at temperatures between 10 K and 300 K.

Figure 1 shows the luminescence (left side) and the excitation (right side) spectra of $CsCl_{1-x}I_x$ (x=0.2 mol%) measured at 10 K. Two luminescence bands peaking at 3.96 eV and 5.13 eV are observed under the excitation of VUV light at 6.89 eV. The excitation spectra for the 3.96-eV and 5.13-eV bands are presented by broken and solid curves, respectively. It is clear that they are efficiently stimulated in the energy region just below the fundamental absorption of CsCl. It is also found that the intensity of the 5.13-eV band normalized by that of the 3.96-eV band increases almost linearly with the iodine concentration. These results indicate that the 3.96-eV band is ascribed to a monomer emission from localized excitons with [ICl^- + e] configuration and the 5.13-eV band a dimer with [I_2^- + e] configuration.

In Fig. 2 are shown the luminescence (left side) and the excitation (right side) spectra of $CsCl_{1-x}Br_x$ (x=0.5 mol%). As clearly seen, there appear three luminescence bands peaking 3.84 eV, 4.34 eV and 5.27 eV under the excitation of VUV light at 7.42 eV. These luminescence bands are stimulated in the low-energy side of the fundamental absorption region of CsCl. The 4.34-eV and 5.27-eV emissions exhibit similar excitation spectra, stimulated efficiently at 7.4 eV. It is found that the intensities of these bands normalized by that of the 3.84-eV band are almost proportional to the bromine concentration. Thus, it is concluded that the 3.84-eV band is due to a Br^- monomer emission and the 4.34-eV and 5.27-eV bands originate from similar relaxed exciton states, namely, Br^- dimers.

We have measured a decay profile of each luminescence band under single-bunch operation. The decay measurements indicate that the monomer emissions consist of two decay components of a short lifetime (I^- monomer: 3.4 ns, Br^- monomer: 2.9 ns) and a fairly long lifetime (> 1 μs). On the other hand, the dimer emissions in CsCl:I and CsCl:Br exhibit a single exponential decay, as shown in Fig. 3. The I^- dimer emission decays with a long lifetime of 0.4 μs, but both of the Br^- dimer emissions decay with a short lifetime (4.34 eV: 1.5 ns, 5.27 eV: 0.6 ns). The results are different from those of localized excitons in halogen-dilute mixtures of NaCl-type alkali halides. This difference may be partly because the off-center configuration is more stable for relaxed excitons in CsCl. In cesium halide crystals of simple-cubic structure, the displacement of the halogen molecular ion along <100> axis will be easier due to "a small molecule in a large cage."

1) M. Itoh, K. Tanimura and N. Itoh: J. Phys. Soc. Jpn. **62**(1993) 2904.

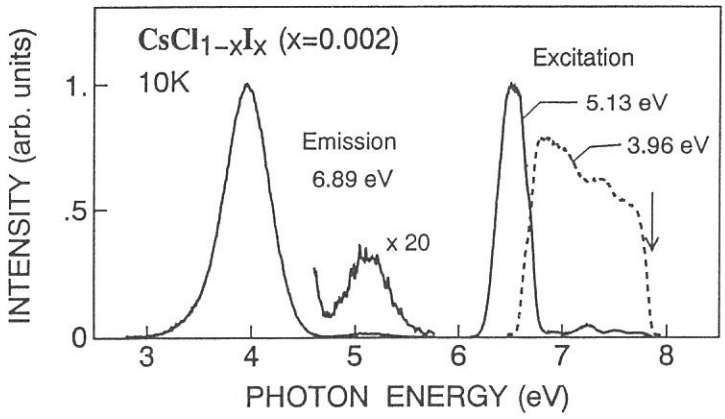

Figure 1. The luminescence spectrum (left side) and the excitation spectra (right side) of $CsCl_{1-x}I_x$ (x=0.2 mol%) at 10K. The arrow indicates the peak position of the n=1 exciton absorption band of CsCl.

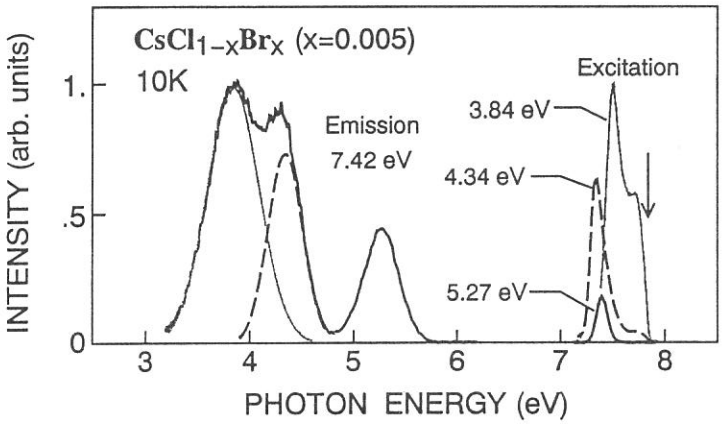

Figure 2. The luminescence spectrum (left side) and the excitation spectra (right side) of $CsCl_{1-x}Br_x$ (x=0.5 mol%) at 10K. The arrow indicates the peak position of the n=1 exciton absorption band of CsCl.

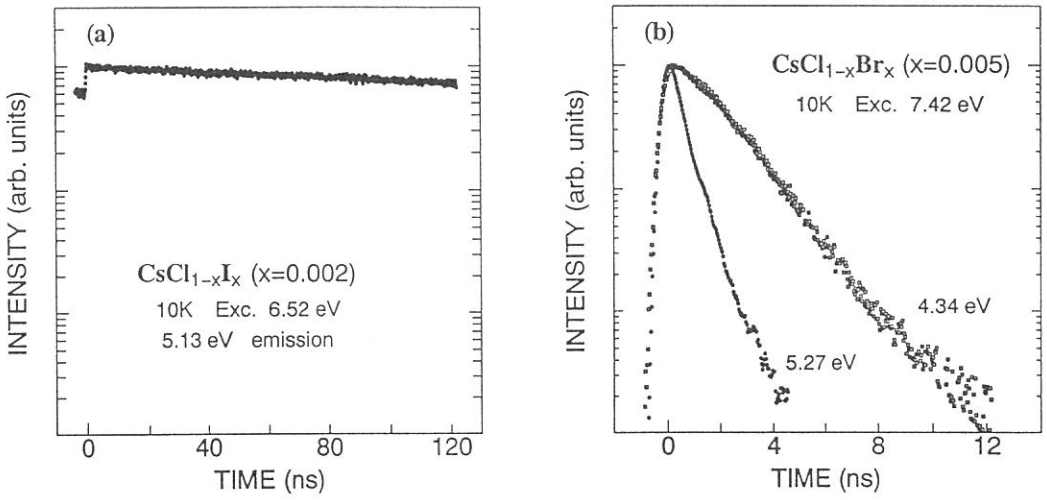

Figure 3. The decay profile of dimer emissions in (a) $CsCl_{1-x}I_x$ (x=0.2 mol%) and (b) $CsCl_{1-x}Br_x$ (x=0.5 mol%) observed at 10 K.

(BL1B)

Luminescence from Self-Trapped Excitons in $BaFCl_{1-x}Br_x$ mixed crystals

A. Ohnishi*, K. Kan'no, Y. Iwabuchi[A] and N. Mori[A]

Department of Physics, Kyoto University, Kyoto 606
[A] Fuji Photo Film Co., Ltd., Miyanodai, Kaisei-machi, Kanagawa 258

BaFX (X=Cl, Br, I) crystals are layered ionic crystals of tetragonal matlochkite (PbFCl) type [1]. In these materials, the possibility for self-trapping of excitons in a variety of different relaxed configurations has been discussed [2-5]. In the present study, luminescence spectra from BaFCl, BaFCl:Br and BaFCl-BaFBr mixed crystals have been investigated, to see the effect of changing in the crystal environment on the manner of exciton self-trapping.

Experiments were performed using synchrotron radiation from the beam line BL1B of UVSOR. BaFCl, BaFBr and their mixtures were crystallized by a horizontal Bridgmann method from the melt containing stoichiometric amounts of BaFCl and BaFBr. Luminescence was analyzed by a Spex 270M monochromator attached with a R955 photomultiplier, and corrected for the dispersion and sensitivity of the detecting system, and for the spectral distribution of the excitation light.

Two characteristic emission bands have been generally recognized in $BaFCl_{1-x}Br_x$ mixed crystals under excitation at 10.3 eV. Main results of their emission and excitation spectra are shown in Figs. 1-2, respectively. For comparison, we also measured the luminescence of BaFCl:Br, which is attributed to the radiative decay of localized excitons associated with Br^- impurities. These results are summarized in Fig. 3.

As seen in Fig.1(a), in BaFCl (x=0), two bands are observed at 5.36 eV and 3.37 eV at 11 K. The 5.36 eV band is almost quenched at 71 K. Existence of the 3.37 eV band and its enhancement upon raising temperature are in good agreement with the results reported by Radzhabov and Egranov [3], though they did not observe the 5.36 eV band. In the x=0.1 crystal, two new bands appear at 5.43 eV and 4.46 eV, in addition to the 3.37 eV band which completely disappears in the crystals of $x \geq 0.3$. They are very similar to the emission bands (5.51 eV, 4.46 eV) in BaFCl:Br, which can be stimulated by photo-excitation into the absorption bands being located around 7.5 - 8.5 eV (Fig. 3). We suppose that the 5.51 eV band in BaFCl:Br originates from localized excitons composed of the electron bound on the trapped hole of the $(ClBr)^-$ and/or Br_2^- core. With increasing x, the 5.43 eV band shifts continuously to the low energy side and is finally connected to the intrinsic luminescent band at 5.1 eV in BaFBr, as indicated by a line ("UV_1 band" series). Contrary to the UV_1 band, the 4.46 eV band is weakened to disappear for $x>0.3$, as far as temperature is low enough. This band, however, seems to be connected to the 4.25 eV band of BaFBr which is prominent at high temperatures, as indicated by another line ("UV_2 band" series).

Excitation spectra for the UV_1 bands (solid curves) and those for the UV_2 bands (broken curves) are almost similar to each other, except for the low energy part around 8 eV in the x=0.1 and x=0.3 (Fig. 2). It is suggested that localized excitons will change into band excitons around x=0.1-0.3. For x=0.6, new dips appear at 7.75 eV and 8.24 eV, being connected to the halogen doublet of BaFBr with increasing x. The present results suggest that the UV_1 and UV_2 bands should be attributed to two different STEs associated with the Br_2^- cores.

It should be noted that the spectral changes of emission and excitation in $BaFCl_{1-x}Br_x$ are somewhat similar to those in $KCl_{1-x}Br_x$ where three different types (I, II and III) of STE luminescence appear against x [6,7]. Such variations in the spectra may reflect the change in the manner of exciton self-tapping. A configuration of on-center type, like the type I STE in alkali halides, is reasonably imagined to be responsible for the UV_1 bands of the mixtures, the 5.1 eV band of BaFBr, and also for the 5.36 eV band of BaFCl. On the other hand, a configuration situating in a manner similar to that of the type II STE (a weakly off-centered configuration), will be responsible for the UV_2 band and for the 4.25 eV band of BaFBr. As for the 3.37 eV band of BaFCl, a strongly off-centered configuration, like the type III STE in alkali halides, should be assumed to explain the origin of its remarkably large Stokes-shift.

---

* Present address: *Department of Physics, Yamagata University, Yamagata 990, Japan*

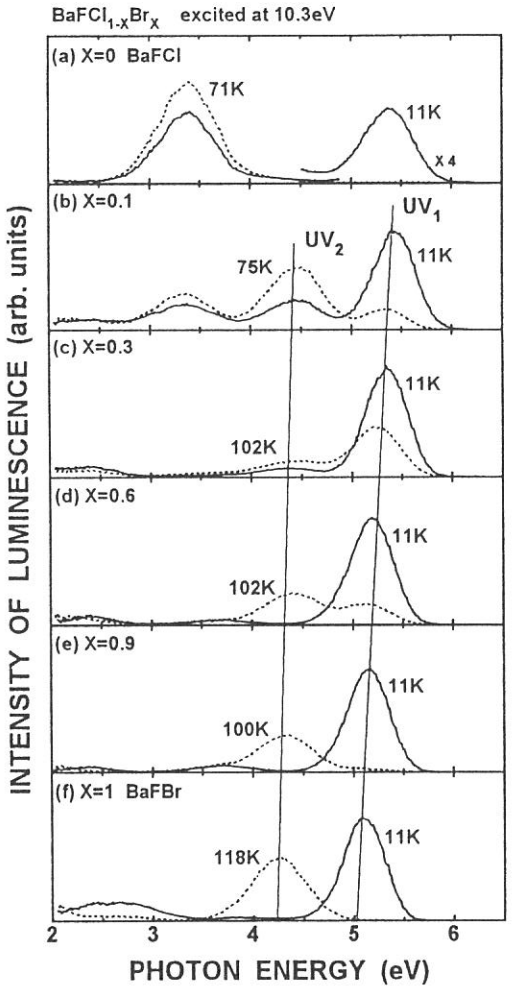

Fig. 1

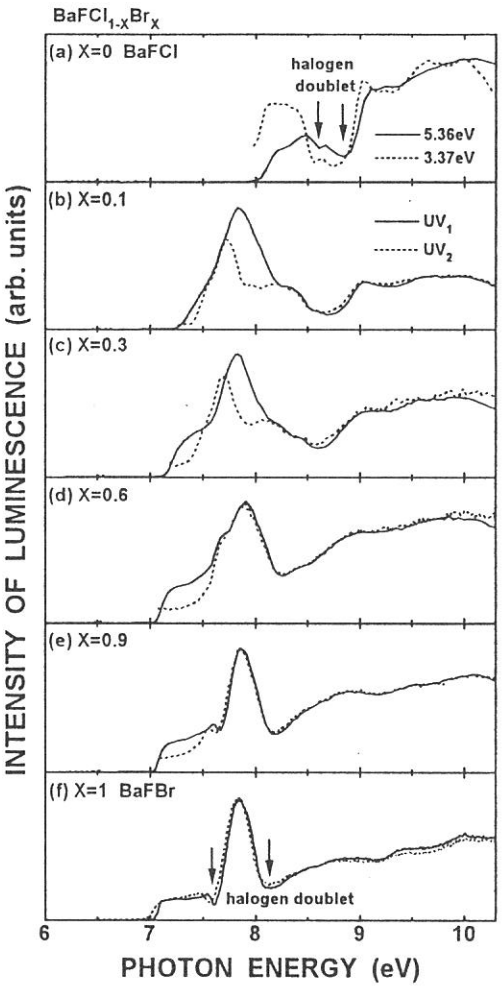

Fig. 2

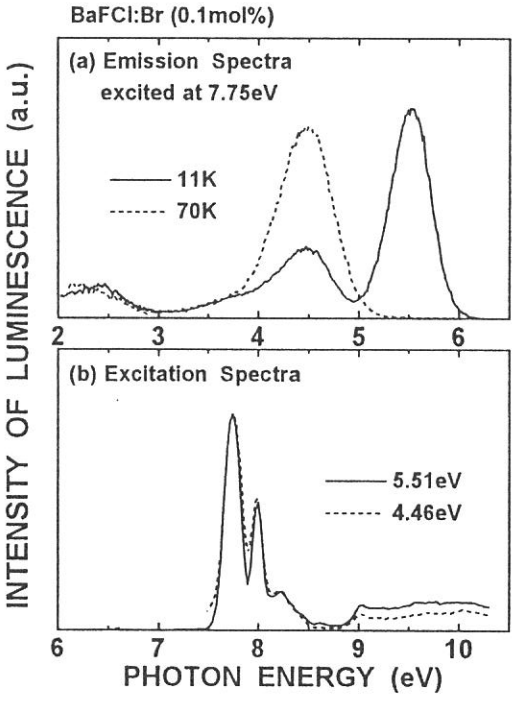

Fig. 3

REFERENCES

1. B. W. Liebich and D. Nicollin ; Acta. Cryst. B33 (1977), 2790.
2. A. Ohnishi, K. Kan'no, Y. Iwabuchi and N. Mori ; Nucl. Instr. and Meth. in Phys. Res. B91 (1994), 210.
3. R. C. Baetzold ; Phys. Rev. B40 (1989), 3246.
4. E. A. Radzhabov and A. V. Eranov ; J. Phys : Condens. Matter 6 (1994), 5639.
5. H. H. Ruter, H. v. Seggern. R. Reininger and V. Saile; Phys. Rev. Lett. 65 (1990), 2438.
6. K. Tanaka, K. Kan'no and Y. Nakai; J. Phys. Soc. Jpn. 59 (1990), 1474.
7. K. Kan'no, K. Tanaka and T. Hayashi; Rev. Solid State Science 4 (1990), 383.

(BL1B)

Emission Spectra and Decay Characteristics in Photo-Stimulated $(C_2H_5NH_3)_2CdCl_4$

A. Ohnishi[a], T. Yamada[a], T. Yoshinari[a], I. Akimoto[b] and K. Kan'no[b]

[a]*Department of Physics, Yamagata University, Yamagata 990*
[b]*Department of Physics, Kyoto University, Kyoto 606*

Alkylammonium cadmium chlorides, $(C_2H_5NH_3)_2CdCl_4$, is layered ionic crystal of perovskite-type. Metal precipitation was found to be remarkably evolved when the crystal exposed with X- or γ-rays at 77K was warmed to room temperature [1]. It was also confirmed that self-trapped hole center Cl_2^- and trapped electron center are created in the crystals X- or γ-rayed at 77K [2,3]. In this crystal, self-trapping of exciton is expected. If so, self-trapped exciton (STE) may have a structure of two-center type, which is composed of an electron and a Cl_2^- center, just like in alkali chlorides. In the present work, recombination processes of electrons and holes have been studied through luminescence from photo-stimulated $(C_2H_5NH_3)_2CdCl_4$ with VUV light.

Crystals were grown by evaporation of aqueous solution containing stoichiometric amounts of $C_2H_5NH_2$·HCl and $CdCl_2$·5/2H_2O. Experiments were performed using synchrotron radiation from the beam line BL1B of UVSOR. Luminescence was detected with a micro-channel-plate or a R955 photomultiplier through a Spex 270M monochromator. Luminescence decays and time-resolved emission spectra were measured under single bunch operation mode using a method described in ref.4.

Figure 1(a) shows emission spectra measured at 11K. When excited at the 5.90 eV, which falls into the excitonic absorption band, a largely Stokes-shifted emission band is found at 2.50 eV. When excited at 10.3 eV in the band-to-band transition range, however, another emission band appears at 2.25 eV. This band rapidly degrades during prolonged irradiation. The excitation spectrum detected at 2.50 eV is shown in Fig.1(b). Dips at 5.64 eV and 6.31 eV indicated by arrows in the figure almost coincide with the peak positions of two kinds of the excitonic absorption bands reported by Yoshinari et. al. [5]. In Fig.1(c) is shown the temperature dependence of emission intensities of the 2.50 eV (●) and 2.25 eV (○) bands. As the temperature is raised, the intensity of the 2.50 eV band increases stepwise at 20K, followed by gradual increase around 30~50K. Around 50K the band thermally quenches. The 2.25 eV band rapidly decreases until 60K.

Figure 2 shows decay profiles of (a) the 2.50 eV and (b) 2.25 eV bands at 11 K. They are composed of fast and slow decays. The decay time of the fast component observed at 2.50 eV is 3.56 ns and that observed at 2.25 eV is 2.04 ns. Figure 3 shows time-resolved emission spectra for the fast and slow components measured under excitation at 5.90 eV. Spectral shapes of both components resemble each other, though the peak of the fast component is not at 2.50 eV but at 2.62 eV. These features of decay profiles and time resolved emission spectra are very similar to those of the STE luminescence bands in NaBr and NaI crystals [4,6]. By the analogy, we tentatively suppose that two decay components in $(C_2H_5NH_3)_2CdCl_4$ come from the singlet and triplet luminescent states. On the other hand, separate measurements using an ArF (6.42 eV) or a F_2 (7.90 eV) excimer laser show that decay profiles of the slow components are approximated by power series of time.

Rapidly degradation and non-exponential decay of the 2.25eV band suggest that the band is stimulated by tunneling recombination of electrons with self-trapped holes. As for the 2.50 eV, supposedly, de-excitation of STE's with the Cl_2^- core is a plausible candidate. However the luminescence decay of slow component indicates non-exponential decay. This means that the luminescence dose not simply come from the radiative transition of a well-defined STE state but from recombination of several kinds of correlated electron-hole pairs. We speculate that the STE in this material is situated in the way of nearest neighbor F-H pairs, similar to the off-center STEs in alkali halides [7].

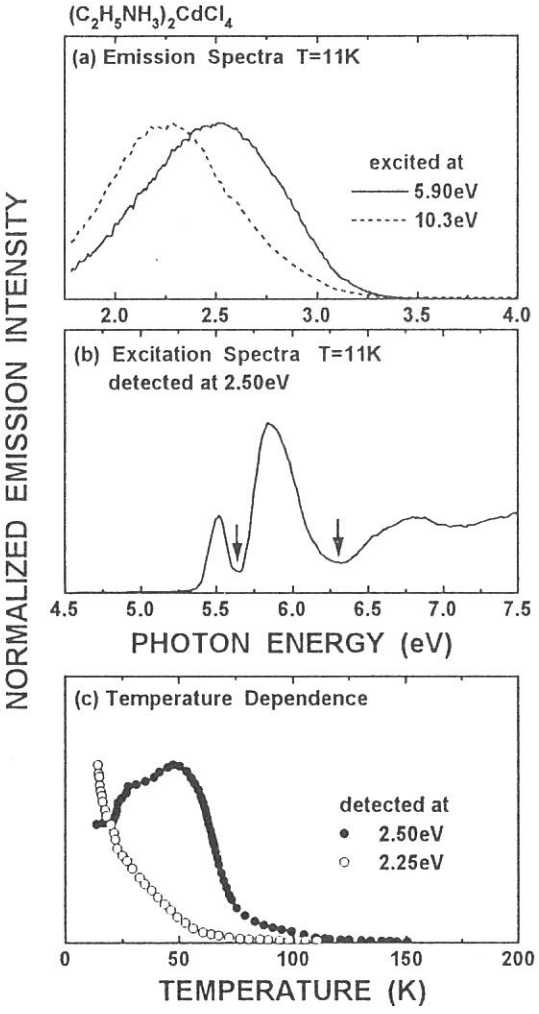

Fig. 1

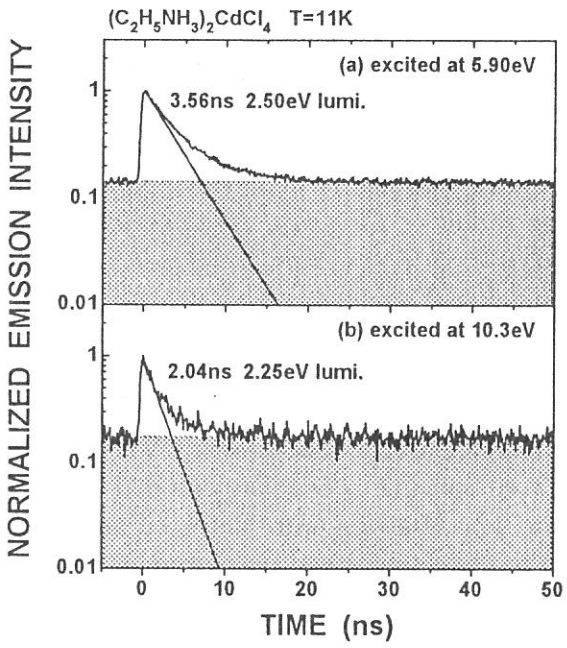

Fig. 2

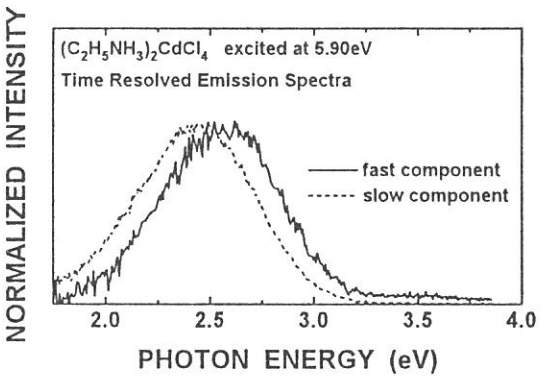

Fig. 3

REFERENCES

1. T. Yoshinari, T. Matsuyama, H. Yamaoka and K. Aoyagi, Jpn. J. Appl. Phys. 24 (1985) L720
2. T. Yoshinari, T. Matsuyama, N. Achiwa, H. Yamaoka and K. Aoyagi, J. Phys. Soc. Jpn. 56 (1987) 3354
3. T. Yoshinari, T. Matsuyama, H. Yamaoka and K. Aoyagi, J. Phys. Soc. Jpn. 58 (1989) 4222
4. T. Matsumoto, T. Kawata, A. Miyamoto and K. Kan'no, J. Phys. Soc. Jpn. 61 (1992) 4229
5. T. Yoshinari, T. Nanba, S. Shimanuki, M. Fujisawa, T. Matsuyama, M. Ikezawa and K. Aoyagi, J. Phys. Soc. Jpn. 58 (1989) 2276
6. K. Kan'no, K. Tanaka, H. Kosaka, T. Mukai, Y. Nakai, M. Itoh, T. Miyanaga, K. Fukui and M. Watanabe, Physica Scripta 41 (1990) 120
7. K. S. Song and R. T. Williams, Self-Trapped Excitons (Springer-Verlag, Berlin, Heiderberg, 1993)

Effect of Ultraviolet Light Irradiation to CVD-grown (100) Diamond Surfaces

Nobuhiro Eimori, Yusuke Mori, Akimitsu Hatta, Toshimichi Ito and Akio Hiraki
Department of Electrical Engineering, Osaka University, Osaka 565, Japan

The diamond films were deposited using the microwave plasma CVD method. The (100) diamonds synthesized in high pressure were used as substrates.

The resistivity of as-grown CVD diamond is low because of the conductive layer at the surface. Specimens were annealed at 773K in the O_2 atmosphere, to remove the conductive layer. The O atoms were detected at the surface after annealing from Auger spectra.

Photoelectron yield measurements were carried out at room temperature in 10^{-8} Torr using synchrotron radiation from the 750 MeV storage ring of the Institute for Molecular Science. Specimens were biased to −240 V to collect emitted electrons. A quartz window of 5-mm thickness was used to eliminate higher energy light of $h\nu > 8$ eV. The photoelectron yield spectra were corrected by the relative beam intensity of incident photons including the effects of wavelength-sensitive grating used and time-dependent storage ring current.

The threshold of photoelectron yield for the (100) surface after annealing in O_2 atmosphere was 6.2 eV, which is larger than the band-gap energy of diamond, 5.5 eV, as shown in Fig. 1. The origin of emitted electrons around the threshold of photoelectron yield is considered to be the maximum of the valence band or impurity levels or the surface states in the mid band gap. Therefore, the electron affinity is positive from the reason that the threshold energy of photoelectron yield is larger than the band-gap energy of diamond, as reported in our previous work [1].

When the ultraviolet (UV) light is irradiated to the specimen surface, the photoelectron yield increased. The photoelectron yield after UV irradiation for 20 minutes was 2 times larger than that before. During UV irradiation, CO and O pressures in the chamber increased and O_2 gas was not detected. These gases did not increase when the Al sample holder was irradiated by UV light. Therefore, it is sure that these gases are desorbed from the specimen surface due to UV irradiation.

After UV irradiation, the threshold of photoelectron yield shifted to lower energy of incident photon. It is considered for the reason of this shift that the O atoms at the specimen surface were desorbed by UV irradiation.

The electron affinity of O contaminated surface was positive and that of as-grown surface is negative. Therefore, the O atoms at surface lead to an increase in electron affinity (threshold of photoelectron yield curve) [1]. After desorption of O atoms, C

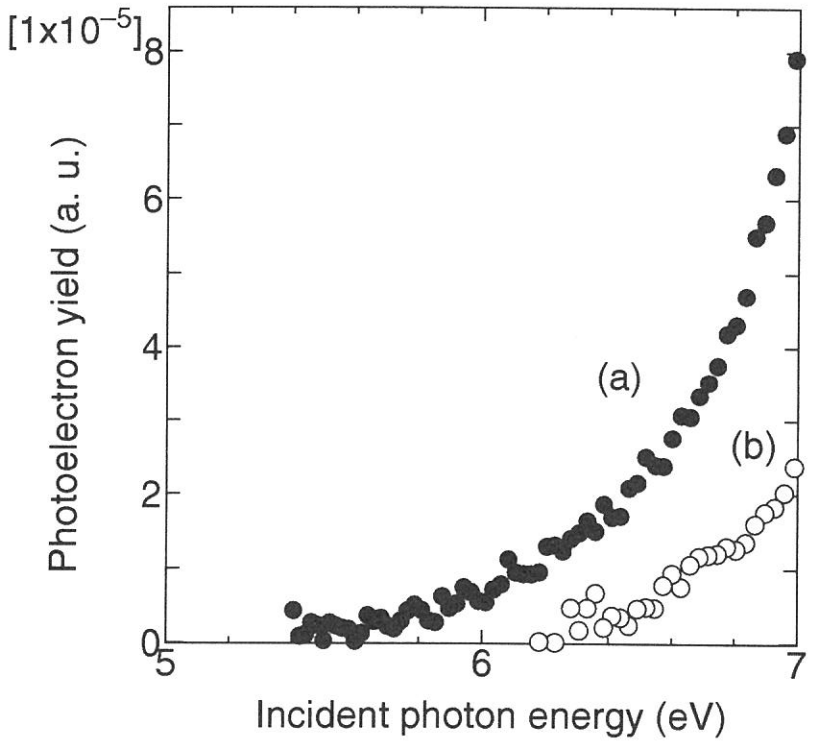

Figure 1: The photoelectron yield spectra of (100) surface (a) before and (b) after UV irradiation.

atoms on the surface adsorb H atoms in the vacuum chamber, and then the electron affinity decreased. So, the threshold of photoelectron yield after UV irradiation shifted to lower incident photon energy than that before.

References

[1] N. Eimori, A. Hatta, T. Ito and A. Hiraki, Jpn. J. Appl. Phys. 33(1994)6312.

[2] Y. Mori, H. Yagi, M. Deguchi, T. Sogi, Y. Yokota, N. Eimori, H. Yagyu, H. Ohnishi, M. Kitabatake, K. Nishimura, A. Hatta, T. Ito, T. Hirao, T. Sasaki and A. Hiraki, Jpn. J. Appl. Phys. 32(1993)4661.

(BL1B)

VUV absorption spectra in thermally poled silica glass pre-exposed to CuKα X-ray radiation

Akihiro KAMEYAMA, Atushi YOKOTANI, and Kou KOROSAWA

Department of Electric and Electronic Engineering, Miyazaki University Miyazaki, 889-21

Second harmonic generation (SHG) has been observed in fused silica glass plates, which has been applied by a high electric field of 3-5kV/mm at about 300℃[1]. Many resachers have discussed about relation bewteen origins of SHG and various impurities[2]-[6]. For example, Myer *et al.* have proposed that the movement of Na^+ ion causes the phenomenum, and Nasu *et al.* have reported that the SHG sintensity increases with increasing the concentration of hydroxyl group in the silica glass.

In general, the defects influence property of the silica glass. In silica glass, high energy photons have been found to induce a relatively high density of defects, and their behavior is well-studied[7]-[10]. Galeener *et al.* have observed that when the Suprasil-1(Heraeus-Amersil Co.,) containing high cocentrations of hydroxyl group, was exposed to CuKαX-ray radiation (λ=1.54Å), oxygen deficient defect (E'center) and non-bridging oxygen hole center (NBOHC) were induced. They also have indicated that CuKαX-ray have irradiated to Suprasil-W1 which contains hydroxyl group much less than the Suprasil-1 , E'-center and peroxy radicals (PR's) were induced[9].

We investigate a relation between the defects and the origin of SHG phase in the poled silica glass. So, to induced the defects, CuKαX-ray has been used (the operating condition : 40kV, 15mA, 20min). And then, a high electric field of 4kV/mm has applied at about 260℃ for 20min. Figure.1 shows the obseravation results of SHG signals in these samples. As far as the synthetic silica glass, a strong SHG signal has been observed only after CuKαX-ray exposure as shown in Fig.1. Furthermore, the SHG signal intensity depended on the polarity of electric field during poling. The SHG intensity when the exposed surface was set on the positive electrode, was larger than the case when set on the negative electrode. The values of χ^2 were the same as that of fused silica glass. These results indicate the defect concerns the SHG phase. It is known that the absorption peak of E'center exist around 5.5 eV, and we have measured the VUV absorption spectra of the synthetic silica glass to identify the defect. Figure.2 shows a absorption spectrum of the synthetic silica glass which has been exposed by X-ray. It is shown that the absorption edge was located in 7.8 eV, and the absorption peak of the impurities such as H_2O molecule around 7.5 eV or O around 4.8 eV[11-12] weren't strong. Although E'center is a major defect which is induced by high energy photon irradiation, such a peak wasn't observed in our sample. It is considered that the amount of the induced E'center was very small. Such a low level of E'center which isn't detected by VUV absorption, might be concerned with SHG in the poled silica glass.

In summary, we have observed the VUV absorption spectrum of poled synthetic silica glass which is exposed by X-ray. The result indicated that a small amount of E'center is concerned with SHG in the poled silica glass.

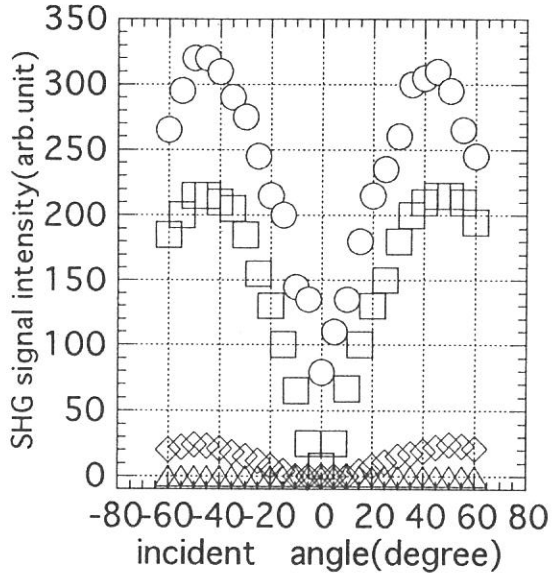

Fig. 1 The SHG signal intensities against the incident angle of YAG laser beam in these samples.
○: show that of the fused glass, △: show that of the synthetic glass without the X-ray exposure, □: show that of the synthetic glass whose exposed surface has been sat on the positive electrode, and ◇ show that of the synthetic glass whose exposed surface has been sat on the negative electrode.

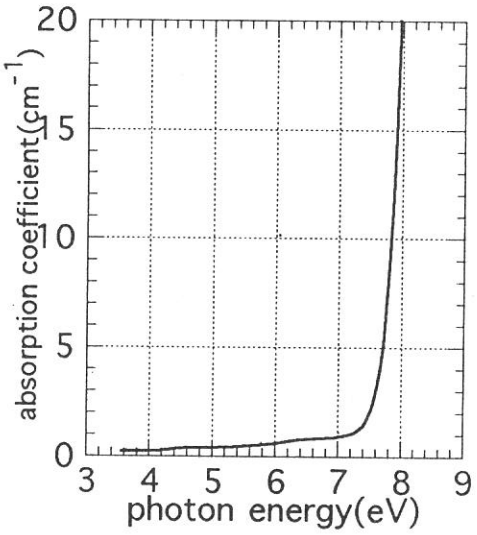

Fig. 2 The VUV absorption spectrum of poled synthetic silica glass

Reference
1 R.A Myers.*et al.* Opt.Lett. **16**, 1732(1991)
2 N.Mukherjee *et al.* J.Opt.Soc.Am.B. **11**, 665(1994)
3 P.G.Kazansky *et al.* Opt.Lett. **18**, 693(1993)
4 P.G.Kazansky *et al.* Opt.Lett. **18**, 1141(1993)
5 P.G.Kazansky *et al.* Opt.Comm. **110**, 611(1994)
6 H.Nasu *et al.* Jpn.J.Appl.Phys.**34**,L1455(1995)
7 R.A.Weeks. J.Appl.Phys.**27**,1376(1956)
8 K.Arai *et al.* Appl.Phys.Lett.**53**,1891(1988)
9 F.L.Galeener *et al.* Solid.State.Comm.**82**,271(1992)
10 H.Imai *et al.* Phys.Rev.B,**48**,3116(1993)
11 K. Awazu Bunkou-Kenkyuu,**41**,81(1992)
12 K.Nagasawa NEW GLASS,**4**,51(1989)
13 A.Kameyama *et al.* Proceeding of International Laser , Lightwave and Microwave Conference (ILLMC'95) **88** (1995)

Vacuum UV Photoluminescence of Alkali Earth Fluorides: CaF_2, SrF_2 and BaF_2.

Arisato Ejiri, Akira Hatano, * and Kunihiro Arakaki

Science Education Devision, College of Education, University of the Ryukyus, Nishihara, Okinawa 903-01.

*College of Arts and sciences, University of Tokyo, Komaba, Meguroku, Tokyo 153.

Recentry, Vacuum UV studies of alkali earth fruorides have been attracted some interests in their luminescence and photoelectric total yield with high resolution, because of competitive relation between the luninescence and the photoelectric yield. [1)]

In the present work, STE (self-trapped-exciton) luminescence spectra in CaF_2, SrF_2, and BaF_2 for exciting the valence electron and the outer-most core electron as well as excitation spectra for the luminescence in these fruolides were measured at several low temperatures down to 23K.

BL-1B was used with a 1m Seya-Namioka monochromator and a Spex spectrometer. Samples used were single crystal slabs of these fluorides. Measurements were performed in the photon energy range of 8eV-40eV for excitation and 2eV-6.2eV for luminescence.

Luminescence spectra obtained were not corrected for the spectral efficiencyof the Spex spectrometer, however, normarized by the excitation intensity. The excitaion spectra were normalized by the electron beam intensity.

In Fig. 1, luminescence spectra in BaF_2 excited at 20eV for several temperatures are shown. [1)] The 5.7eV peak which is knowen as the Auger free luminescence decreases on the cooling, whereas STE luminescence peak locating around 4eV witha doublet structure increases on the cooling. These temperature dependencies [1)] are not monotonic but complicated manners which are essentially fitted with C. Shi et al's results. [2)]

In Fig. 2(a), (b), and (c), .STE luninescence spectra are shown in CaF_2, SrF_2, and BaF_2 excited at 10eV for room temperature and 23K, respectively. In Fig. 3(a), (b), and (c), excitation spectra for the STE luminescence of these three fluorides. From these results, it is newly found that the increasing property of the STE luminescence for excitation of the valence electron upon the cooling is the most in CaF_2 and the least in SrF_2. These properties for the three fluorides agree well with temperature dependencies of their photoelectron yield which competes with the luminescence. [1)] It is also found that, in BaF_2, STE luminescence strongly increases for the excitation of $Ba^{2+}5p$ core electron, contrary to

CaF_2 and SrF_2 cases where such increases are very weak.

References

1) A. Ejiri et al; in press, Proc. 11th Int. Conf. VUV Rad. Phys. (1995, Tokyo).

2) C. Shi et al; J. Lumi. 40/41(1988) 189.

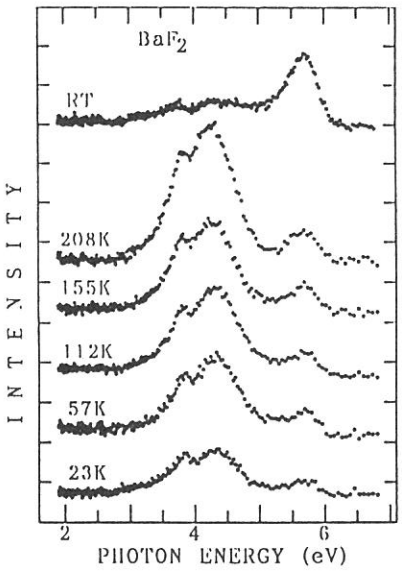

Fig. 1 Luminescence spectra in BaF_2 excited at 20eV.

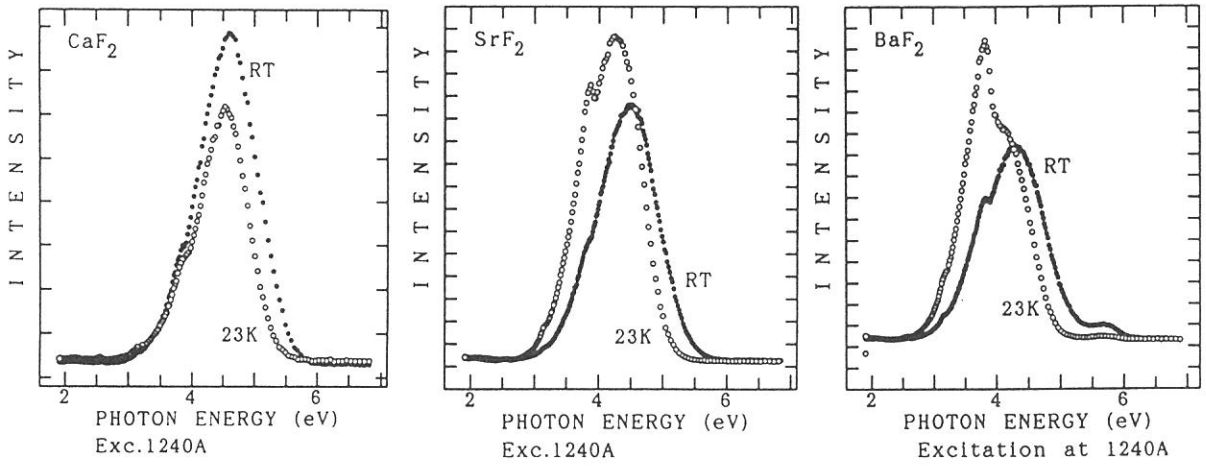

Fig. 2 STE luminescence spectra in CaF_2, SrF_2, and BaF_2 excited at 10eV.

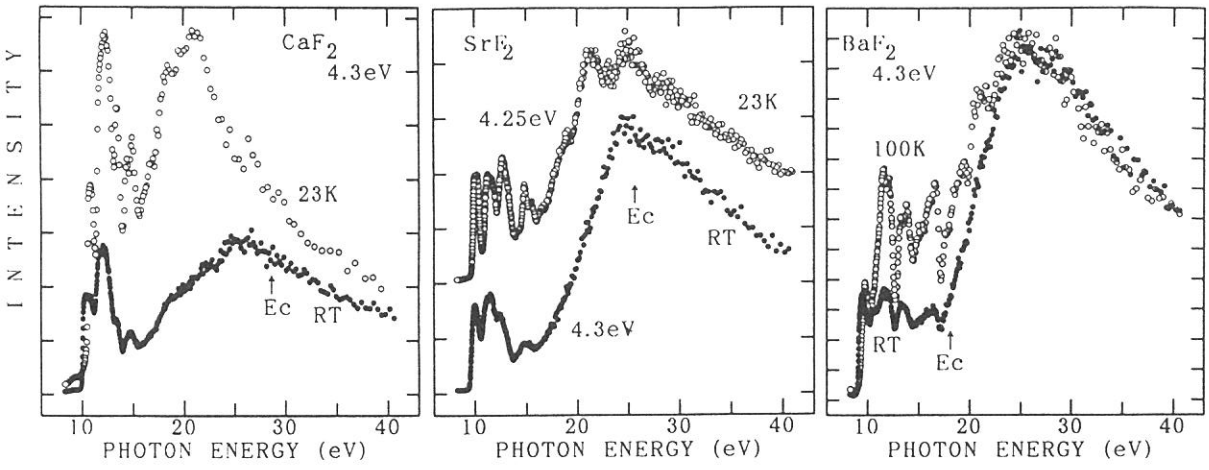

Fig. 3 Excitation spectra of STE luminescence in CaF_2, SrF_2, and BaF_2.

(BL1B)

Luminescence from Lithium Oxide at Low Temperatures

Yoshinobu ISHII, Minoru ITOH[a] and Nobuhito OHNO[b]

Japan Atomic Energy Research Institute, Tokai, Ibaraki 319-11
[a]Faculty of Engineering, Shinshu University, Nagano 380
[b]Faculty of Engineering, Osaka Electro-Communication University, Neyagawa 572

Lithium oxide(Li_2O) crystallizes in an anti-fluorite type structure and has a simple band structure. Radiation-induced defects such as F^+-centers in this material have been studied under the irradiation with high-energy ions or neutrons[1], since Li_2O is a candidate material of a blanket for a fusion reactor. The optical transition energy of F-type centers has been calculated by A.Shluger and N.Itoh[2]. However, no experimental study on luminescence has been reported in literature. To understand the origin of the emission in Li_2O, preliminary experiments of reflectivity and luminescence were conducted at BL1B-beam line.

Li_2O single crystal was grown from a sintered rod of Li_2O with a floating zone-melting method by infrared light. Specimens used in the present experiment were cleaved from the single crystal ingot, having a (111) face. Their dimensions were about 8mm in diameter and 0.3mm in thickness. Handling of the specimen was done in a dry-argon gas atmosphere to prevent the reaction with moisture. All measurements were carried out at low temperatures of 10-15K in vacuum.

Figure 1 shows reflectivity of Li_2O as a function of the photon energy. The absorbance is also added as reference. In Fig.1 one can see a sharp peak at 7.1eV and four peaks around 4.9eV, 5.6eV, 6.5eV and 8.8eV. Optical

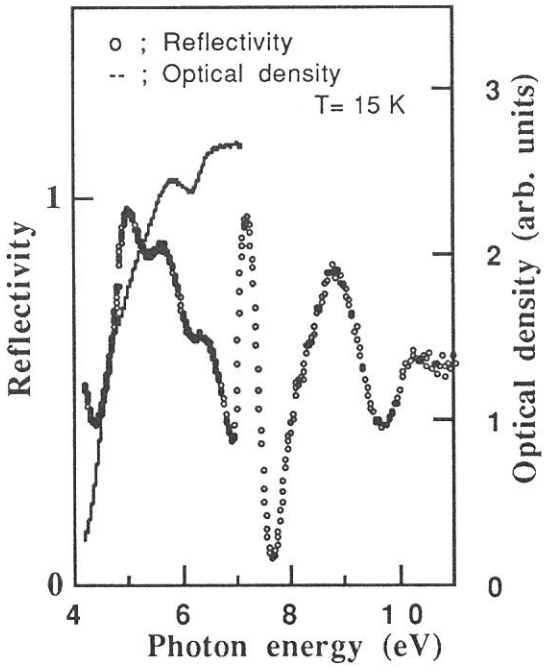

Fig.1. Reflectivity(open circles) and absorbance (solid line) of Li_2O at 15K.

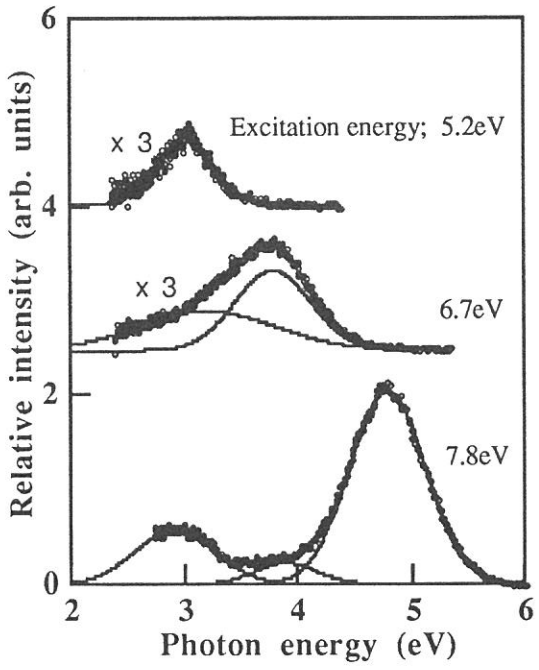

Fig. 2. Typical luminescence spectra of Li_2O at 15K. Open circle shows the experimental data and solid lines indicate the results of Gaussian fit.

density is increased with increasing photon energy up to 7eV. The sharp peak at 7.1eV is probably due to the creation of free excitons. The origin of the other peaks is not clear at present.

Luminescence spectra of Li_2O are shown in Fig.2. These spectra were fitted with Gaussian curves. There are three bands peaking at 3.0eV, 3.8eV and 4.8eV. Excitation spectra for the three bands are shown in Fig.3. The 4.8-eV band is mainly excited by 7.5-eV photons, and the others are excited with 6.8-eV photons. Fig.4 shows the emission intensity of the 3.0-eV band(solid circles) and 4.8-eV band(open circle) as a function of the temperature. Solid lines indicate the calculated results by using the Mott formula. The activation energies for 3.0-eV band and 4.8-eV band are 72meV and 340meV, respectively.

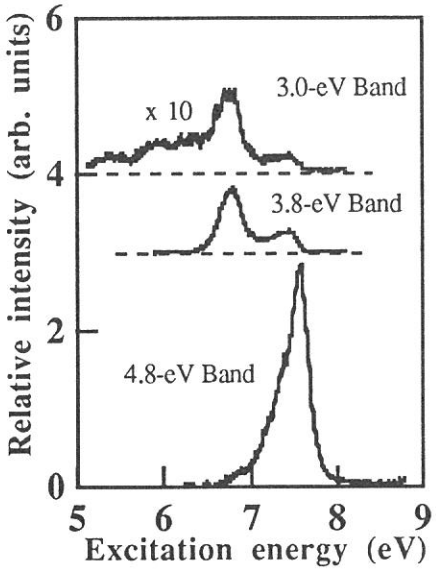

Fig.3. Excitation spectra for 3.0-, 3.8- and 4.8-eV bands of Li_2O.

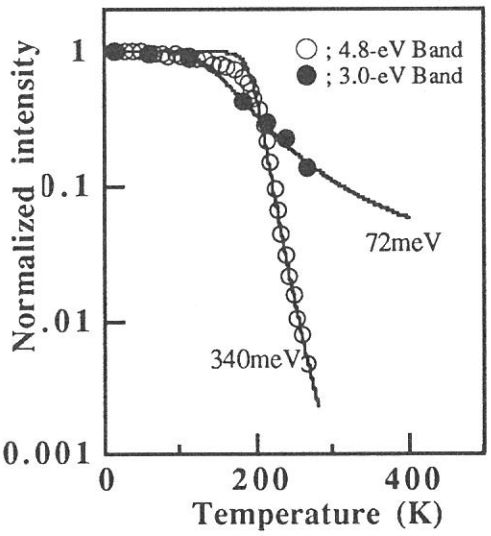

Fig.4. Temperature dependence of the emission intensity of the 3.0- and 4.8-eV bands excited by 7.6-eV photons.

In the present experiment, we found three emission bands at 4.8, 3.8 and 3.0eV. The excitation threshold of the 4.8-eV band is located around 7.0eV, which is almost the same as the sharp peak position shown in Fig.1. Therefore, the 4.8-eV band may be associated with a radiative recombination of excitons relaxed into a metastable state. The 3.0- and 3.8-eV bands are related to defects or impurities in the specimen, because they are excited with low-energy photons.

To clarify the nature of these emission bands, further experiments are being planned.

Reference

[1] K.Noda, Y.Ishii, H.Matsui and H.Watanabe; Radiat. Eff., **97** (1986) 297.

[2] A.Shluger and N.Itoh; J. Phys. Condens. Matter, **2** (1990) 4119.

(BL1B)

Luminescence study of $C_{60}F_{48}$

Masao Kamada, Sayumi Hirose, Masami Hasumoto, Masatake Ichikawa[a], Ken-ichi Kan'no[b], and V. G. Stankevitch[c]

UVSOR, Institute for Molecular Science, Myodaiji, Okazaki 444
[a]College of Engineering, Fukui University, Fukui 910
[b]Faculty of Science, Kyoto University, Kyoto 606
[c]Russian Research Center "Kurchatov" Institute, Russia

Recent years, fullerens and related materials have attracted much interest, because they are third material consisting of carbon, and because they show new functional and interesting features on electric and magnetic properties. While there have been reported many works in recent years, the optical property of fullerens needs more detailed studies.

We have investigated the luminescence spectra of C_{60} by using undulator radiation and uv laser. The temperature dependence of the luminescence intensity showed the anomalous change due to the phase transition (1). The energy position of the luminescence was in the mirror image compared to that of the absorption. This indicates that the optical transition originates from a state like an exciton of a Frenkel type. On the other hand, we observed the luminescence bands around 2.5 and 3.2 eV on $C_{60}F_{48}$ powder (2), while the absorption peak is observed around 5 eV on the $C_{60}F_{48}$ in the solution. This implies strongly that the lattice relaxation of $C_{60}F_{48}$ is very large due to a strong electron-phonon coupling. The purpose of the present study is to know the luminescence property of $C_{60}F_{48}$ in solid phase and to investigate the difference in electron-lattice interaction in fullerens.

Experiments were carried out at BL1B and BL3A1 stations in UVSOR. Refrectivity and excitation spectra of luminescence from $C_{60}F_{48}$ crystal and powder were measured at BL1B with an 1-m Seya-Namioka monochromator. Luminescence spectra were observed by using a Spex 270M uv-vis monochromator with a CCD detector (Princeton Instr.) through a quartz lens. Mass and luminescence spectra were measured at BL3A1 under the excitation with quasi-monochromatized undulator radiation. Decay time of the luminescence was also obtained by using a single-photon counting method under a single-bunch operation, where the duration and repetition were 0.4 and 178 ns, respectively. Both of crystalline and powder $C_{60}F_{48}$ were grown in Kurchatov Institute and were attached on a sample holder of a flow-type He cryostat.

Figure 1 shows the luminescence spectra of $C_{60}F_{48}$ crystal at 11 K. Two luminescence bands are seen at 2.5 and 3.2 eV. The excitation spectra of these two bands are shown in Fig. 2. A prominent peak is observed around 4 eV and a week peak is seen around 8 eV. The excitation spectrum of the 2.5-eV band is similar with that of the 3.2-eV band, but the intensity of the shoulder around 4.5 eV is stronger for the 2.5-eV band than that for 3.2-eV band. This indicates the excited states producing the 2.5-eV and 3.2-eV bands locate around 4 and 4.5 eV, respectively. The present result is very different from the spectral feature of the reflectivity, which shows a week band around 6 eV and a peak at 8 eV. Therefore, it is supposed that the luminescence may be attributed to trap states or triplet states locating below the threshold of the band-to-band transition. Mass spectrum from the powder sample irradiated with intense undulator radiation at 36 eV showed the constituent molecules such as CF and F2, and the luminescence intensity decreased with a long irradiation. These results indicate that the luminescence may be correlated with the bonding between carbon and fluoride in $C_{60}F_{48}$.

References

(1)M. A. Terekhin, N. Yu. Svechnikov, V. G. Stankevitch, A. A. Kolmakov, V. A. Stepanov, V. N. Bezmelnitsin, M. Kamada, and K. Kan'no, Optics and Spectroscopy 78, 773-780 (1995).
(2)A. Kolmakov, V. G. Stankevitch, V. Bezmelnitsin, A. Rizkov, V. Sokolov, M. Kamada, S. Hirose, K. Kan'no, I. Akimoto, and T. Matsumoto, VUV-11 Abstract W56 (1995).

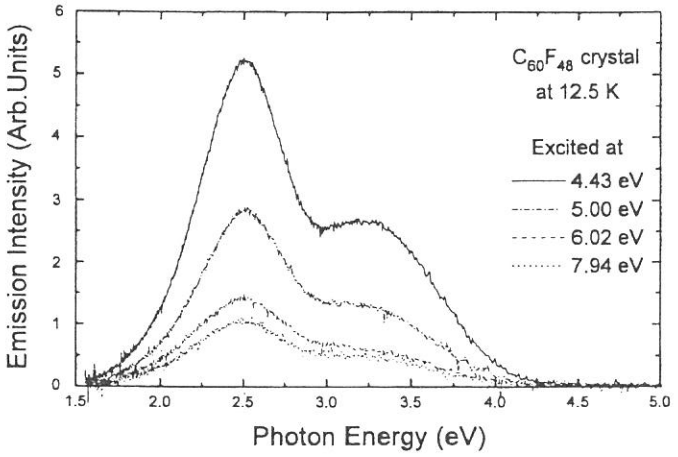

Fig. 1. Luminescence spectra of $C_{60}F_{48}$ crystal at 12.5 K.

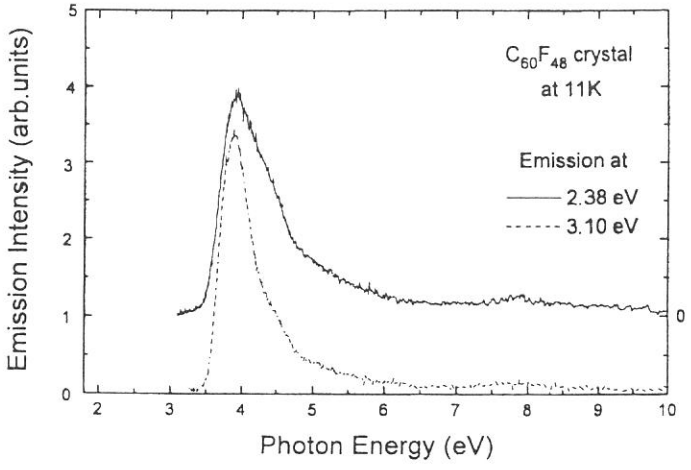

Fig. 2. Excitation spectra of $C_{60}F_{48}$ crystal at 11 K.

(BL2A)

Photochemistry of Cyanogen Iodide in the 40 - 120 nm Region

Kazuhiro KANDA, Takashi NAGATA[1], Mitsuhiko KONO[2],
Kosuke SHOBATAKE[3] and Toshio IBUKI[2]

Department of Fundamental Science, College of Science and Engineering, Iwaki Meisei University, Iwaki 970
[1] Department of Chemistry, College of Arts and Sciences, The University of Tokyo, Komaba, Meguro-ku 153
[2] Institute for Molecular Science, Myodaiji, Okazaki 444
[3] Department of Materials Chemistry, School of Engineering, Nagoya University, Chikusa-ku, Nagoya 464-01

When a cyanogen iodide (ICN) is photolyzed by a vacuum ultraviolet (VUV) radiation, a CN radical is formed in a variety of electronically excited states. The CN fragment produced in a $B^2\Sigma^+$ state immediately decays via a radiative process into the ground. Recently we have reported on the photochemistry of cyanogen iodide, ICN, in the 105-175 nm region.[1] For the wavelength range shorter than 105 nm, however, little has been known about the high-lying electronic states of ICN because of the lack of a radiation source available for the photoabsorption measurements. In the present study, by taking advantage of the window-less experimental configuration at BL2A of UVSOR, absolute cross section for the formation of CN(B) are determined in the wavelength range 40-120 nm, below the LiF cut-off. In the 90-120 nm region, the photoabsorption spectrum and photoexcitation spectrum have been measured by use of an Ar gas filter, instead of a LiF window, which was mounted in front of the absorption cell, in order to eliminate the secondary light of a incident SOR beam. Typical pressure of Ar in the gas filter was 270 mTorr. For the measurement in the 40-90 nm region, any gas was not introduced to the gas filter.

The electronic configuration of ICN in the ground electronic state is[2]

$$(1\sigma)^2(2\sigma)^2(3\sigma)^2(1\pi)^4(3\sigma)^2(2\pi)^4;\ ^1\Sigma^+.$$

The ionization potentials (IPs) of ICN are reported to be 10.93 eV (113.4 nm) and 11.46 eV (108.1 nm) for the production of ICN^+ in the $^2\Pi_{3/2}$ and $^2\Pi_{1/2}$ manifolds, respectively. The second IP associated with the $^2\Sigma^+$ ionic state is located at 13.16 eV (94.2 nm). In Fig. 1 and 2, the absolute cross section is plotted against the excitation wavelength in the range 40-90 and 90-120 nm, respectively. A broad, structureless continuum was observed below 94 nm, above the second IP. Numerous peaks have been observed in the wavelength region $\lambda >$ 94 nm. The absorption peaks, in the 94-113 nm region have been assigned to the transitions to the super-excited states. These super-excited states have been associated with the Rydberg series converging to the second IP. As a result, almost absorption bands below the second IP can be assigned to the Rydberg transitions converging to these first and second IPs or intravalence transitions. Dominant Rydberg series converging to these first and

second IPs are identified in the Fig. 2.

The absolute cross section for the production of CN(B) was determined by a comparison of the intensity of the CN(B-X) emission produced in the photodissociation of HCN.[3] The quantum yield was calculated as the ratio of the emission cross section to the absorption cross section. As shown in Fig. 3, the quantum yield for the production of CN(B) is only ~0.028 at 120 nm and increases with the excitation energy up to ~0.033 at 114 nm. It appears that the dominant photodissociation channels in the wavelength region $\lambda > 114$ nm lead to the production of CN fragments in $X^2\Sigma^+$ and/or $A^2\Pi_i$ states. The quantum yield decreases drastically down to ~0.018 around 113 nm and to ~0.008 around 108 nm, due provably to the preferential operation of ionization in the energies above the first ionization potentials.

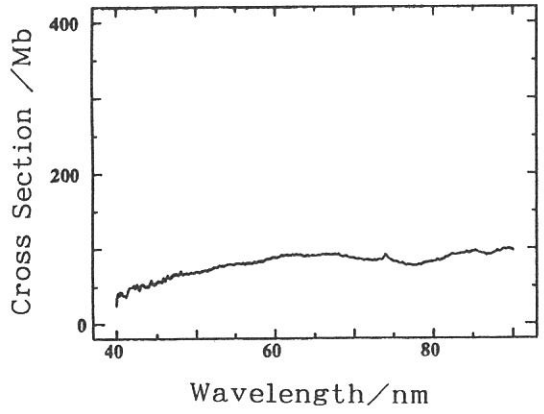

Fig.1 The absorption cross sections of ICN in the 40-90 nm region. The spectral resolution was 0.1 nm.

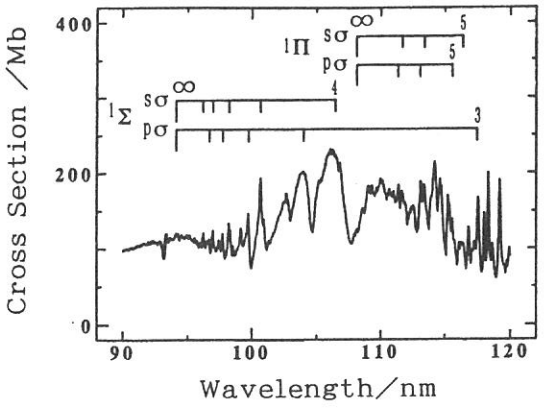

Fig.2 The absorption cross sections of ICN in the 90-120 nm region. The spectral resolution was 0.1 nm.

Reference

[1] K. Kanda, S. Katsumata, T. Nagata, T. Kondow, A. Hiraya, K. Tabayashi and K. Shobatake, UVSOR Activity Report 1992, p.15.

[2] B. Kovac, J. Phys. Chem. 91, 4231 (1987).

[3] L. C. Lee, Chem. Phys., 72, 6414 (1980).

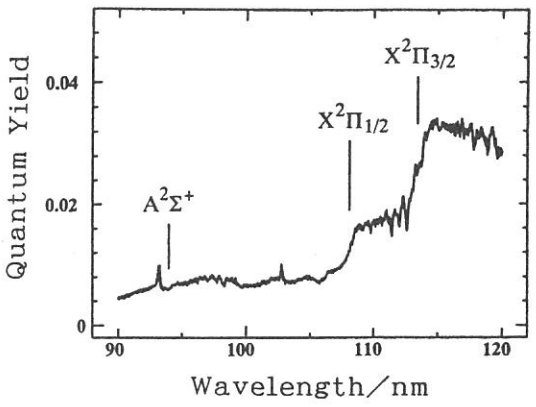

Fig.3 The quantum yield for the CN(B) formation in the photodissociation of ICN in the 90-120 nm region.

(BL2A)

Electronic Spectroscopy of Cyanamide in the VUV Energy Region.

A. INOUE, K. TABAYASHI, O. TAKAHASHI, K. SAITO,
K. YOKOYAMA*, M. KONO#, K. SHOBATAKE#+

Department of Chemistry, Hiroshima University,
Kagamiyama, Higashi-Hiroshima 739
**Advanced Science Research Center,*
Japan Atomic Energy Research Institute, Tokaimura, Ibaraki 319-11
#Institute for Molecular Science, Myodaiji, Okazaki 444
+Department of Material Chemistry, School of Engineering,
Nagoya University, Chikusa-ku, Nagoya 464-01

Cyanamide NH_2CN has been predicted the most stable molecule among a number of structual CH_2N_2 isomers by theoretical calculations. However, the spectroscopic measurements have so far encountered difficulties due to its low vapor pressures at room temperatures and fast bimolecular reactions at relatively elevated temperatures in the gas phase. Here, we have firstly measured absorption and fluorescence cross sections of NH_2CN in the energy region 105-200 nm using a newly designed gas cell with long optical pathlength.

Fig. 1. shows absorption and fluorescence excitation spectra, obtained with ~10 mTorr NH_2CN in a temperature controlled gas cell (ℓ=27.3 cm, T=70-80 °C). Absolute scale for the fluorescence excitation cross section was determined by comparing the photo-emission intensity with that of reference molecule, CH_3CN.

The ordering of the valence shell orbitals is expressed[1] as $- - - (4a')^2(5a')^2(2a")^2(6a')^2$. Outermost 6a' orbital is regarded as a lone pair n_{NH2} character, 2a" and 4a' are π_{CN} in nature, and 5a' is attributed to n_N on the terminal N atom. The observed absorption bands are found assignable in terms of excitation to Rydberg states as indicated in Fig. 1. Absorption bands appeared in the lower energy (> 140 nm) region show broad and nearly continuous. Based on the MR-CI calculation, lower Rydberg states are considered to be strongly mixed with antibonding intervalence transitions.

Rydberg transitions, R←6a', R←2a", and R←5a' in the higher energy (< 140 nm) region are found accompanied by vibrational progressions with average spacing of ~710, 1960, and 1050 cm^{-1}. They are assigned to NH_2 wagging, C=N, and N-C stretching vibrations, respectively. From the molecular geometry analysis of the relevant ions by MO calculation, the vibrational progressions are interpreted as molecular geometry changes to the excited states on the assumption of Franck-Condon principle.

Fluorescence dispersion spectrum were analyzed to have sharp CN(B-X) peaks in 340-460 nm region and broad CN(A-X) bands in the longer wavelength. Presently, no NH_n emission bands have been discernible for NH_2CN excitation. Quantum yields for the CN(A/B) formation are shown in Fig. 2.

[1] R. Combi and W. Von Niessen, Chem. Phys. 86, 389 (1984).

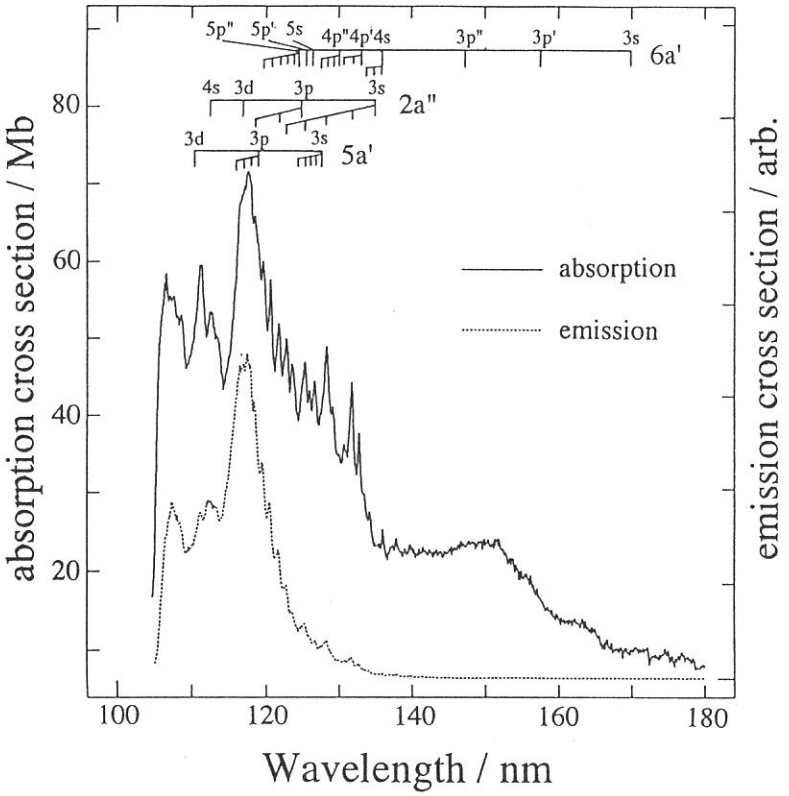

Fig. 1. Absorption and fluorescence excitation cross sections for NH_2CN in the 105 - 180 nm region. The spectral resolution was 0.3 nm. Sample pressure was 20 mTorr.

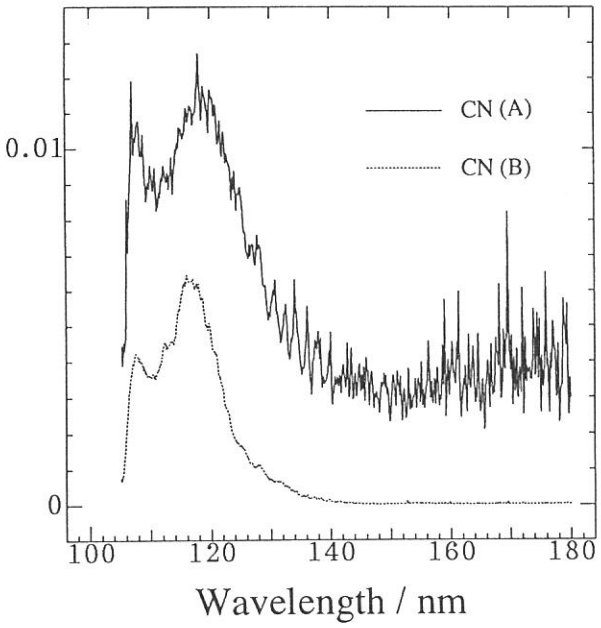

Fig. 2. Quantum yields for the CN(B) and CN(A) formation in the VUV-photodissociation of NH_2CN.

(BL2A)

Photo-Excited States of Malononitrile in the VUV Energy Region.

Shinobu Uchida, Kiyohiko TABAYASHI, Koh SAITO,
Mitsuhiko KONO*, Toshio IBUKI*

Department of Chemistry, Hiroshima University,
Kagamiyama, Higashi-Hiroshima 739
**Institute for Molecular Science,*
Myodaiji, Okazaki 444

Photochemistry of simple mono-cyanides, such as XCN, HCN, and CH_3CN has been relatively well studied in the VUV energy region, since they produce fluorescent CN(A/B) fragments from which discussions about photo-dissociation dynamics are frequently available. Here, we extended VUV spectroscopic measurements to dicyano compound, and absorption and fluorescence excitation spectra of malononitrile $CH_2(CN)_2$ have been firstly observed in the 105-200 nm energy region.

Fig. 1 shows absorption (solid line) and fluorescence excitation (dotted) cross sections, obtained with resolution of 0.2 nm at a gas cell temperature of 45 °C. The highest occupied $2b_1$ orbital in $CH_2(CN)_2$ has a π_{CN} bond character and strongly mixed with a lower π_{CN} orbital. Broad bands appeared in the 130-140 nm range are assignable to intervalence $\pi^* \leftarrow$n transitions[1]. Sharp peaks in the higher energy region < 130 nm are assigned to Rydberg transitions as indicated in Fig. 1. Rydberg transition R$\leftarrow 2b_1$ is found to be accompanied by some vibrational progressions. They are considered to be CH_2 scissors, CCC bending, and other sym. bending vibration with low frequency.

In a separate measurement for dispersed fluorescence spectra, CN(A-X) and CN(B-X) emission has been identified when $CH_2(CN)_2$ was excited at the intense absorption peak of 124.5 nm. The dissociative excitation,

$$CH_2(CN)_2 + h\nu \rightarrow CH_2CN + CN(A/B)$$

are then confirmed as prominent fluorescent decay channels following VUV excitation. The emission intensities from CN(A) and CN(B) were isolated by optical filters, the fluorescence excitation spectra for CN(A/B) formation were recorded. Each cross section was determined by comparing the photo-emission intensity with that of reference molecule, CH_3CN. The quantum yields thus obtained are compared with in Fig. 2.

Inspection of the quantum yields reveals as follows. Both quantum yields generally show monotonous decrease with a decrease in excitation energy. No prominent bands are appeared in the quantum yield to show the presence of excited states which strongly couple with the dissociative excitation channels. Similar monotonous decrease in the quantum yield for the CN(A/B) formation is also found in the photolysis of CH_3CN.

[1] R. Rianda et al., J. Chem. Phys. 80, 4035 (1984).

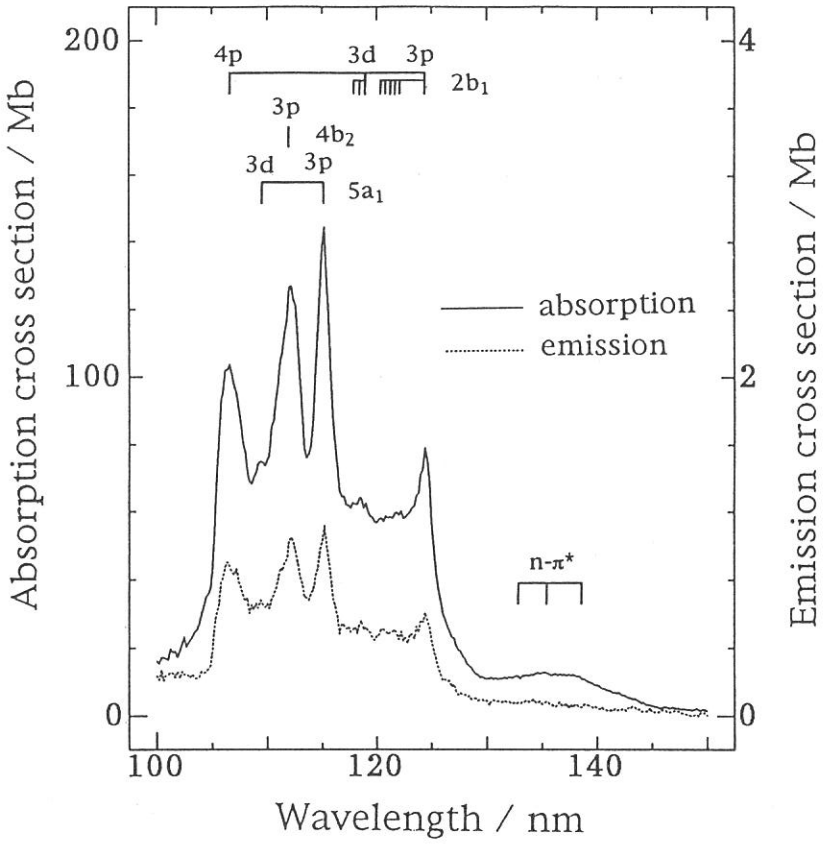

Fig. 1. Absorption and fluorescence excitation cross sections for $CH_2(CN)_2$ in the 105 - 150 nm region. The spectral resolution was 0.2 nm. Sample pressure was 15 mTorr.

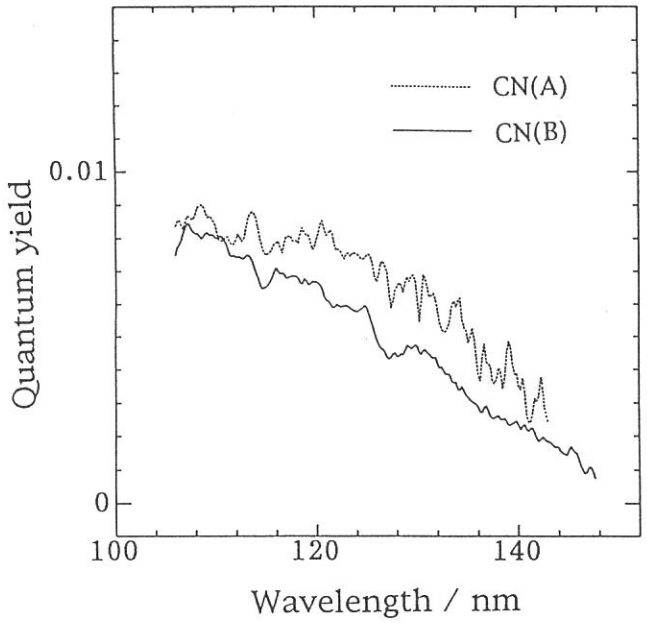

Fig. 2. Quantum yields for the CN(B) and CN(A) formation in the VUV-photodissociation of $CH_2(CN)_2$.

(BL2A)

Absolute photoabsorption cross section of $GeCl_4$ in the 6-31 eV region

Toshio IBUKI, Mituhiko KONO, and Kosuke SHOBATAKE[a]

Institute for Molecular Science, Myodaiji, Okazaki 444

[a]Department of Material Science, School of Engineering, Nagoya University, Chikusa-ku, Nagoya 464-01

Absolute cross sections for photoabsorption by $GeCl_4$ have been measured in the region 6-31 eV. Higher order light from a 1-m Seya monochromator has been suppressed by use of an Ar gas filter at the range 11.3-15.5 eV (110-80 nm) and a LiF window at $h\nu$<11.8 (105 nm). The pressure of argon gas was kept constant at 300 mTorr. The spectral resolution of the primary photon beam was about 1Å.

Figure (a) shows the general features of photoabsorption cross sections. The squares in the figure are the values obtained separately by using a double ion chamber at Ar I (16.85 eV) and He I (21.22 eV) resonance lines generated by a 2.45 GHz microwave discharge. These measurements indicate that the higher order stray light is successfully reduced by the Ar gas filter. Up to 10.7 eV molecular extinction coefficients of $GeCl_4$ have been measured by using a hydrogen discharge lamp.[1] The present cross sections in the $h\nu$>10.7 eV photon energy region are the first measurements. Figure (b) shows the details of the photoabsorption spectrum at the 6-16 eV range where discrete peaks were observed.

The valence shell electronic configuration of $GeCl_4$ molecule with T_d symmetry is $(2a_1)^2(2t^2)^6(1e)^4(3t_2)^6(1t_1)^6$. The three outermost molecular orbitals (MO's) are characteristic of Cl lone pair electrons and their ionization potentials have been reported to be 11.7, 12.4, and 12.8 eV for the $\tilde{X}\,^2T_1$, $\tilde{A}\,^2T_2$, and $\tilde{B}\,^2E$ states, respectively.[2] Since the $ns \leftarrow t_1$ transition in T_d symmetry is dipole forbidden, the broad band at 7.06 eV in fig. (b) is assigned as the first member of the $3t_2$ MO Rydberg series. The quantum defect (δ) for this $4s \leftarrow 3t_2$ transition is deduced to be 2.41. Mean δ values for the transitions assigned in fig. (b) are 2.44 ± 0.03, 1.80 ± 0.11, and 0.41 for the 4*s*, n*p*, and 4*d* Rydberg levels, respectively. These experimental δ's are close to those for the 4*s*, n*p*, and $4d \leftarrow 3p$ transitions of Cl atom with δ=2.14 ± 0.04, 1.68 ± 0.07, and 0.63 ± 0.14, respectively.[3] The first band at 7.06 eV has been assigned as the transition to the vacant σ^* MO.[1] This assignment has been supported by Robin.[4] However, we assign the peak as the 4*s*-terminating Rydberg level judging from the quantum defects deduced.

In the case of $SiCl_4$ molecule[5] with the same symmetry, the photoabsorption spectra show similar features with those of $GeCl_4$, and can be analyzed by the Rydberg concept. The results are consistent with the present ones.

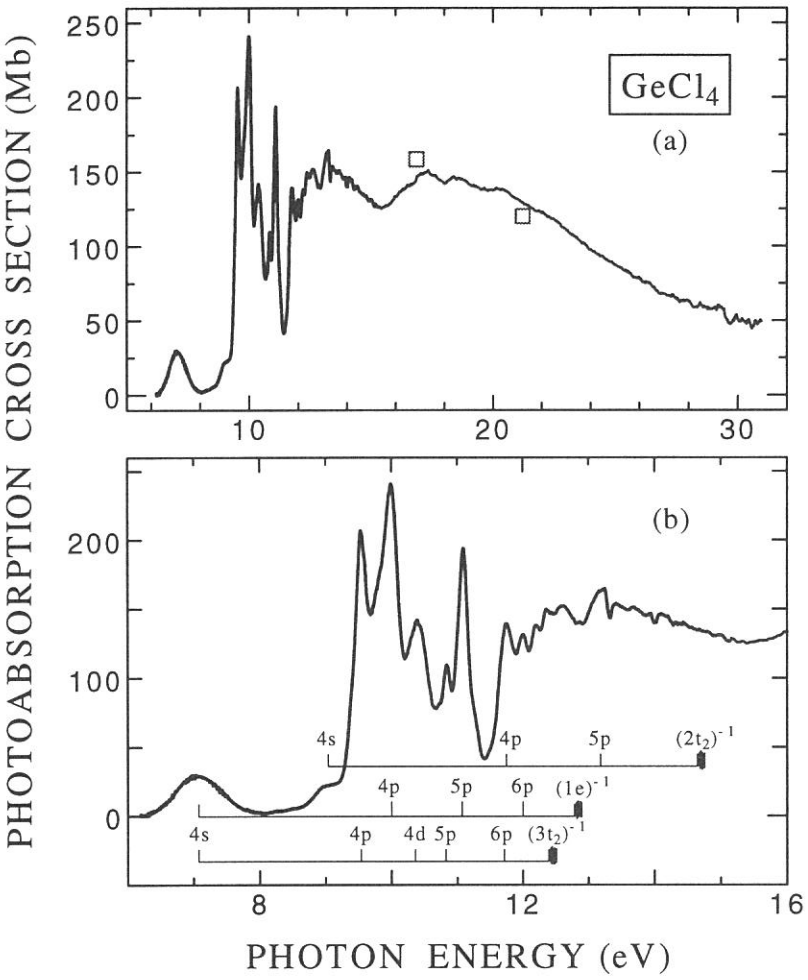

Fig. 1. Photoabsorption cross section of $GeCl_4$ in the region of 6-31 eV.

References

[1] G. C. Causley and B. R. Russell. J. Electron Spectrosc. Relat. Phenom. **11**, 383 (1977).

[2] D. M. Smith, R. P Tuckett, K. R. Yoxall, K. Codling, P. A. Hatherly, J. F. M. Aarts, and M. Stankiewicz, J. Chem. Phys. **101**, 10559 (1994).

[3] C. E. Moore, *Atomic energy levels*, Nat. Stand. Ref. Data Ser., Nat. Bur. Stand. **35** (Washington DC, GPO, 1971).

[4] M. B. Robin, *Higher excited states of polyatomic molecules*, Vol. 3 (Academic Press, New York, 1985).

[5] T. Ibuki. M. Kono, and K. Shobatake, "Photoabsorption and fluorescence cross sections of $SiCl_4$ in the region of 6.2- 31 eV", in preparation.

(BL2A) Fluorescence Excitation Spectra of $SnCl_4$ and $Sn(CH_3)_4$ in the Vacuum Ultraviolet

Ikuo TOKUE and Toshio IBUKI*

Department of Chemistry, Faculty of Science, Niigata University, Niigata 950-21
**Institute for Molecular Science, Myodaiji, Okazaki 444*

There is some information in the literature[1] on absorption and photoelectron spectra of tetrachlorides and tetramethyl compounds of the group IVA elements in the wavelength longer than 115 nm. However, very little is known about photochemistry of these chemicals below 115 nm in the gas phase. In this study, absorption cross sections and fluorescence excitation spectra of $SnCl_4$ and $Sn(CH_3)_4$ have been measured in the 40–120 nm region at the beamline BL2A of UVSOR. The intensity of incident VUV was monitored by converting into UV light, and absorption cross sections in the 40–81.5 nm have been determined by comparing the absorbance with the ionization cross section which was derived from the electric current of ions produced at gas cell. The second order light contaminated in the light source in the 80–120 nm was eliminated with argon gas filter. Fluorescences were monitored with two photomultiplier combining with several optical filters; Hamamatsu R585 for the 200–600 nm region and R955 for the 550–1000 nm region.

Figure 1 shows absorption and fluorescence cross sections of $SnCl_4$. Intense peaks longer than 100 nm are assigned to Rydberg transitions converging to the several ionization potentials, which are indicated with the arrows. The fluorescence corresponding these Rydberg transitions is mainly in the 380–550 nm, and its emitting species is arributable to $SnCl_2(^1B_1, ^3B_1)$ which appears in the 310–600 nm region .[2] The emission with a broad maximum near 60 nm appearing shorter than 90 nm in the fluorescence excitation spectrum seems to consist of several broad bands. The $SnCl(A^2\Delta–X^2\Pi)$ band at 376 nm and Sn(I) resonance lines are candidate for these fluorescences; Sn(I) resonance lines can appear in the wavelength range of 200–1000 nm.

Figure 2 shows absorption and fluorescence cross sections of $Sn(CH_3)_4$. The absorption cross section shows a structureless broad feature. Total fluorescence cross section of $Sn(CH_3)_4$ is roughly one tenth of that for $SnCl_4$, and the emission longer than 540 nm is negligible. Broad peak at 60 nm in the fluorescence excitation spectrum is attributable to Sn(I) resonance lines. However, the intensity distribution of Sn(I) resonance lines from $Sn(CH_3)_4$ seems to be very different from that for $SnCl_4$ since fluorescence longer than 540 nm is very weak.

We have a project to measure dispersed fluorescences in the 200-600 nm region from $SnCl_4$ and $Sn(CH_3)_4$.

References

1) G.C.Causley and B.R.Russell, *J.Electorn Spectrosc. Related Phenomena*, **11**, 383 (1977); A.E.Jonas, G.K.Schweitzer, F.A.Grimm, and T.A.Carlson, *ibid.*, **1**, 29 (1972/73).

2) J.H.Wang, B.S.Cheong, C.C.Fang, and J.M.Parson, *J.Chem. Phys.* 93, 7830 (1990).

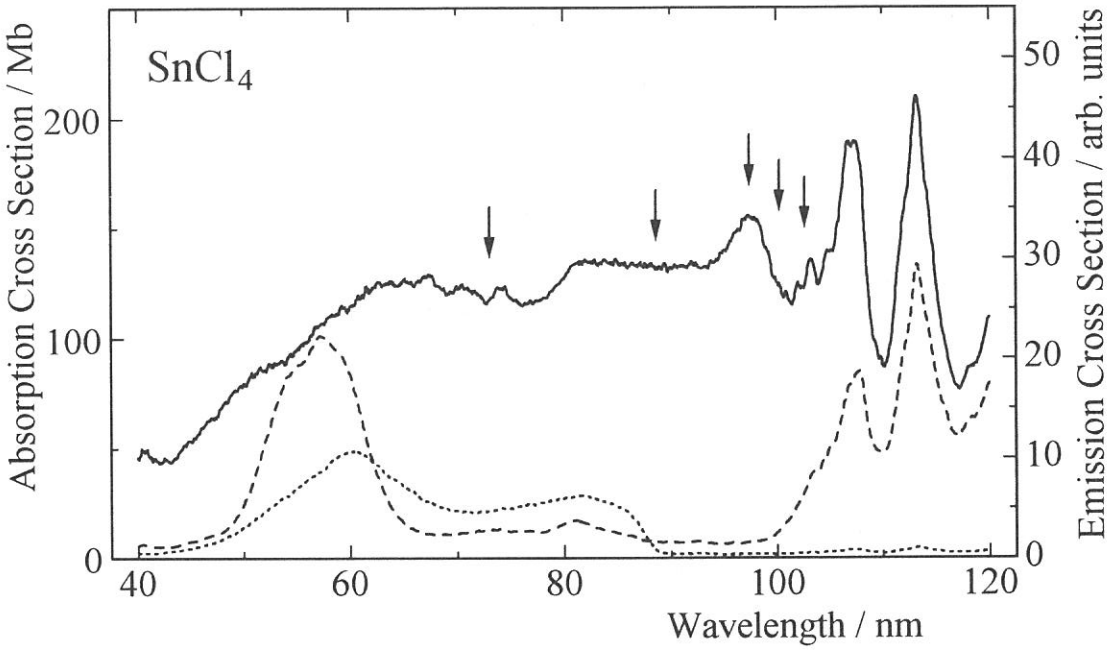

Figure 1. Absorption (solid) and fluorescence (broken and dotted) cross sections of $SnCl_4$: broken and dotted lines represent the emissions in the 200–600 and 540–1000 nm, respectively. The arrows indicate the vertical ionization potentials.

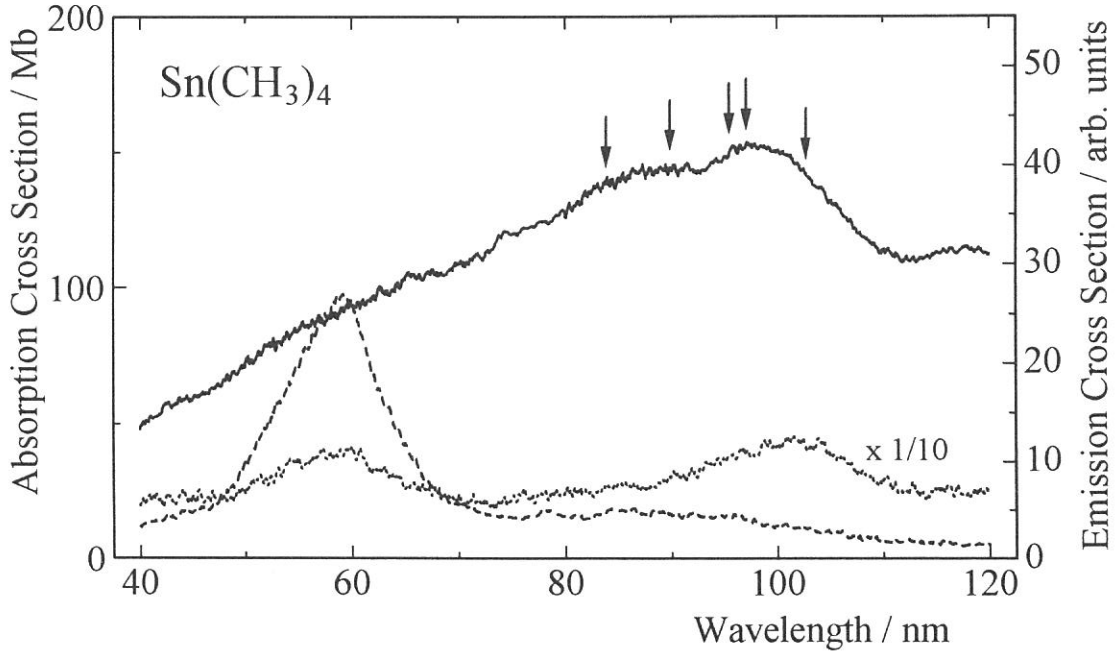

Figure 2. The same as Figure 1 but for $Sn(CH_3)_4$.

(BL2B1)

Polarization-dependent soft x-ray absorption study of Sr_2RuO_4

Takayoshi YOKOYA[1], Ashish CHAINANI[1], Takashi TAKAHASHI[1],
Hiroshi KATAYAMA-YOSHIDA[1], Masahiro KASAI[2], and Yoshinori TOKURA[2,3]

[1]*Department of Physics, Tohoku University, Sendai 980-77, Japan*
[2]*Joint Research Center for Atom Technology (JRCAT), Tsukuba 305, Japan*
[3]*Department of Applied Physics, The University of Tokyo, Tokyo 113, Japan*

Sr_2RuO_4 is a recently discovered non-cuprate layered perovskite superconductor (T_c ~1), having the same crystal structure as La_2CuO_4 but with RuO_2 layers replacing CuO_2 [1]. A comparative study between Sr_2RuO_4 and cuprate high temperature superconductors (high-T_c) would provide useful information on the role of the CuO_2 plane.

A band structure calculation of Sr_2RuO_4 [2,3] predicts that the electronic states at the Fermi level (E_F) consist of Ru $4d\varepsilon$(xy, yz, zx) - O $2p\pi$ anti-bonding bands in contrast with the cuprates where Cu $3d(x^2-y^2)$ - O $2p\sigma$ anti-bonding bands cross E_F. The specific heat γ value obtained by the band calculation is about 4 times smaller [2] than observed value [1] and correspondingly the higher Pauli susceptibility was observed [4], suggesting that strong electron-electron correlation is important to understand the electronic structure of Sr_2RuO_4. Actually, a resonant photoemission study [5] manifests the correlation induced satellite, although the x-ray photoemission spectrum is in good agreement with the band calculation. Angle-resolved photoemission spectroscopy (ARPES) shows a consistent result with the band calculation in the wide energy scale, but exhibits an extended van-Hove singularity (VHS) near E_F inconsistently with the band calculation[2].

In this activity report, we present a polarized x-ray absorption spectroscopy (XAS) of Sr_2RuO_4 to study the unoccupied electronic structure of Sr_2RuO_4.

A single crystal of Sr_2RuO_4 was prepared by a floating zone method. The structure of sample was characterized by x-ray diffraction. The magnetic susceptibility measurement confirmed the superconductivity at about 0.9 K in good agreement with the previous report [1].

The polarization-dependent x-ray absorption measurement was performed at the BL2B1. The energy resolution was 2 eV at 530 eV photon energy. The sample was cleaved *in-situ* in the preparation chamber and then transferred to the main chamber(the pressure, $1x10^{-10}$ Torr). The sample showed a flat shiny surface appropriate for angle-dependent measurements. Measurements were carried out by keeping samples at 110 K. The absorption spectra were obtained by the total-photoelectron-yield which was normalized by photon flux. The photon energy was calibrated by the absorption edge of $Bi_2Sr_2CaCu_2O_8$ with referring to a previous data[6].

Figure 1 shows the polarization dependence of the Oxygen K-absorption spectrum of Sr_2RuO_4. As found in the inset of Fig. 1, the electric vector of incident light becomes gradually parallel to the surface normal as the polar angle θ is increased. All spectra have three distinct peaks A, B, and C at 530, 534, and 538 eV photon energy, respectively. The intensity of peak B decreases monotonously as the polar angle is increased, namely the magnitude of the electric vector of incident light parallel to the surface is decreased. This indicates that peak B has a dominant $O2p_{x,y}$ (in-plane) character. On the other hand, peak A changes its position as well as its intensity with respect to the polar angle θ. In order to study this behavior in detail, we have measured the spectra with better signal-to-noise ratio and a smaller interval. The result is displayed in Fig. 2. It is noticed that the spectrum of θ=20° has two substructures A_1 and A_2 at 529.5 and 530.3 eV photon energy, respectively. While the shoulder A_1 seems to have less/no polarization-dependence, peak A_2 shows a slight sift to the higher photon energy with increasing θ. This result indicates that peak A1 is isotropic, while peak A_2 has a dominant $O2p_z$ (perpendicular to the a-b plane) character. Based on the above discussions, we assign peaks A_1, A_2, and B as the O2p orbital hybridized with the $Ru4d_{xy,yz,zx}$, $d_{3z^2-r^2}$, and $d_{x^2-y^2}$ states, respectively. The peak C is ascribed to the O2p states hybridized with Sr4d states. This

assignment is consistent with the band structure calculation[3]. Thus the polarization-dependent Oxygen K-absorption study reveals that the unoccupied density of states just above E_F consist of the Ru 4dε - O 2pπ anti-bonding band. This result is consistent with a recent ARPES study [5].

References

[1] Y. Maeno et al., Nature 372, 532 (1995).
[2] T. Oguchi, Phys. Rev. B 51, 1385 (1995).
[3] D. J. Singh, Phys. Rev. B 52, 1358 (1995).
[4] S.A. Carter et al., Phys. Rev. B 51,17184 (1995); R. J. Cava et al., Phys. Rev. B49, 11890 (1994); J. J. Neumeier et al., Phys. Rev. B 50, 17910 (1994).
[5] T. Yokoya et al., J. Phys. Chem. Solids (to be published).
[6] H. Matsuyama et al.,Physica C 160, 567 (1989).

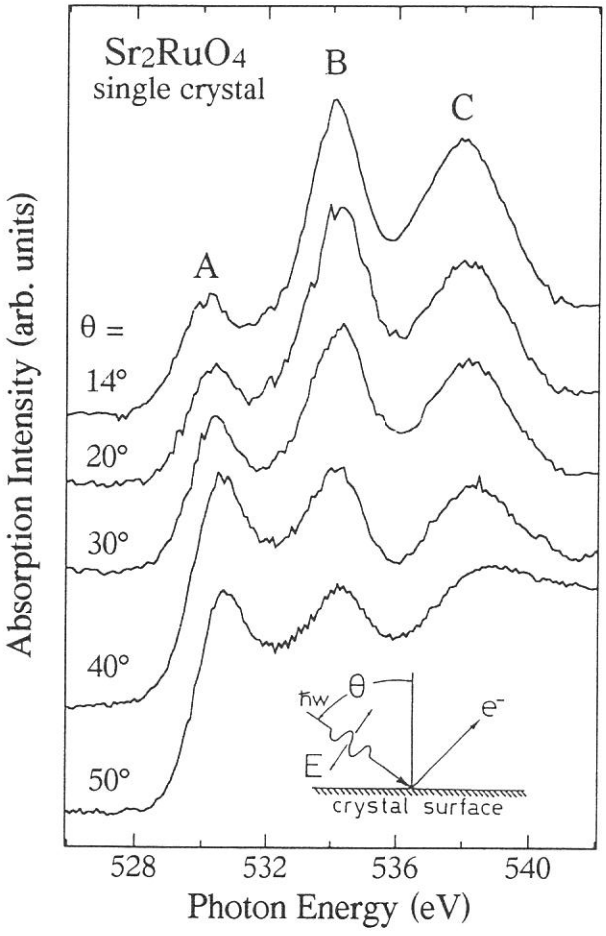

Fig. 1. Oxygen K-absorption spectra of single crystal Sr_2RuO_4 measured with linearly-polarized light by changing the incident angle (θ).

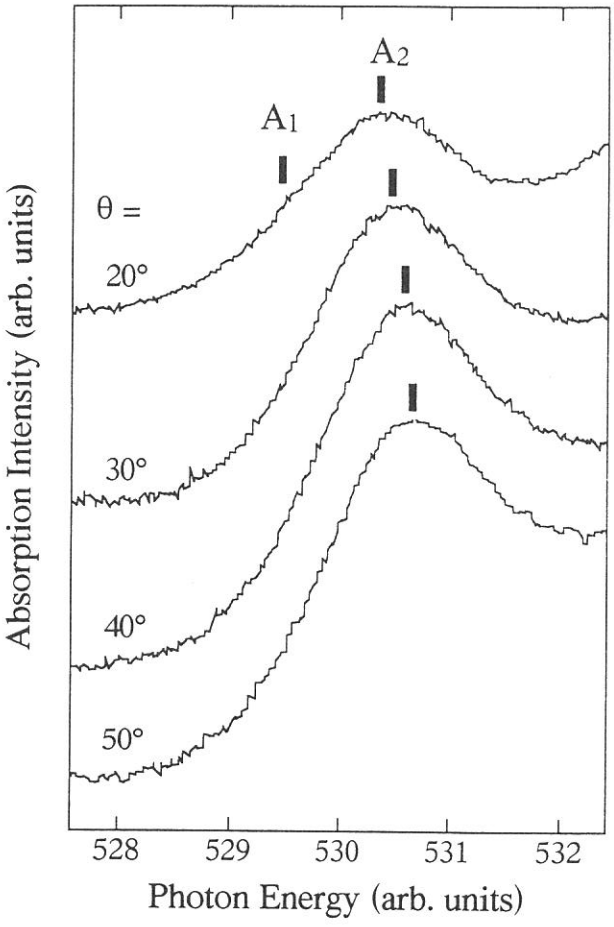

Fig. 2. Oxygen K-absorption spectra of single crystal Sr_2RuO_4 (near E_F region) measured with linearly-polarized light by changing the incident angle (θ).

(BL2B1)

Photoemission and Oxygen *K*-edge X-ray-absorption Study of $La_{2-x}Sr_xCoO_4$

Takahisa OMATA, Tatsuya MIYAJIMA, Hiroshi MIZOGUCHI* and Hiroyuki IKAWA

Department of Chemical Technology, Kanagawa Institute of Technology, Atsugi 243-02
**Reserch Laboratory of Engineering Materials, Tokyo Institute of Technology, Yokohama 227*

The electronic structure of late 3d transition-metall (TM) oxides with a K_2NiF_4 structure such as $(La,Sr)_2CuO_4$ and $(La,Sr)_2NiO_4$ has been extensively studied. Little attenstion, however, is paid to middle 3d TM oxides with a K_2NiF_4 structure[1)-3)]. The electronic structure of $La_{1.75}Sr_{0.25}CoO_4$ was studied[3)] by means of a optical reflectivity spectroscopy. The concerns of the present study is the electronic structure of $La_{2-x}Sr_xCoO_4$ ($0.2 \leqq x \leqq 1.2$), which corresponds a hole-doped La_2CoO_4.

The samples sintered were prepared at 1300~1430℃ for 12h under O_2 and N_2 flow. Photoemission and X-ray absorption (XAS) measurements were performed at the beam-line BL2B1 under a vacuum of $3\sim5 \times 10^{-8}$ Pa. The surfaces of samples were scraped with a diamond file just before measurements to avoid surface contamination under a vacuum of $3\sim5 \times 10^{-7}$ Pa. No carbon 1s absorption peak was seen in XAS after scraping. All photoemission and XAS measurements were performed at room temperature.

Figure 1 shows valence-band photoemission energy-distribution-curves (EDC) of $La_{2-x}Sr_xCoO_4$ with excitation photon-energy of 100 and 200 eV. The spectra present four major features indicated in the figures by A, B, C and D. In Fig. 1 (a) (excitation energy $h\nu$=100 eV), intensities of the feature B decrease upon Sr doping. Intensities of the feature A increase upon doping in the spectra of $h\nu$=200 eV (Fig. 1 (b)). Besides these observations, one can see that the features C and A are dominant in the spectra of $h\nu$=100 eV and 200 eV, respectively. It is refered that the photoionization cross section for subshells of Co 3d and O 2p at $h\nu$=200 eV are 2×10^0 Mb and 2×10^{-1} Mb[4)], respectively. Further, respective those at $h\nu$=100 eV are 6×10^0Mb and 1×10^0 Mb. In a first approximation, experimental photoemission spectra can be related to the one-particle removal spectral function by appropriate weighting factors. It is reasonable to discuss, by refering the data mentioned above, that the feature C in Fig. 1 is attributed to O 2p states because the intensity of this feature decreased significantly with increasing the excitation photon energy. Features A and B dominate the valence-band spectrum of $h\nu$=200eV, so these features are mainly derived from Co 3d states. Therefore, it may be concluded that the valence-band edge of heavily-doped $La_{2-x}Sr_xCoO_4$ has a strong Co 3d character.

Figure 2 shows oxygen *K*-edge X-ray-absorption spectra of $La_{2-x}Sr_xCoO_4$. Four absorption features are observed in these spectra, which are indicated by A, B, C and D. The most prominent change in the spectral

features upon Sr-doping is the intensity and the energy of the feature A. These observations suggest that a new hole band, which has a strong O 2p character, is generated around the conduction-band edge of La_2CoO_4 upon doping, further this new hole band shifts toward a lower energy side above the composition of x=0.6.

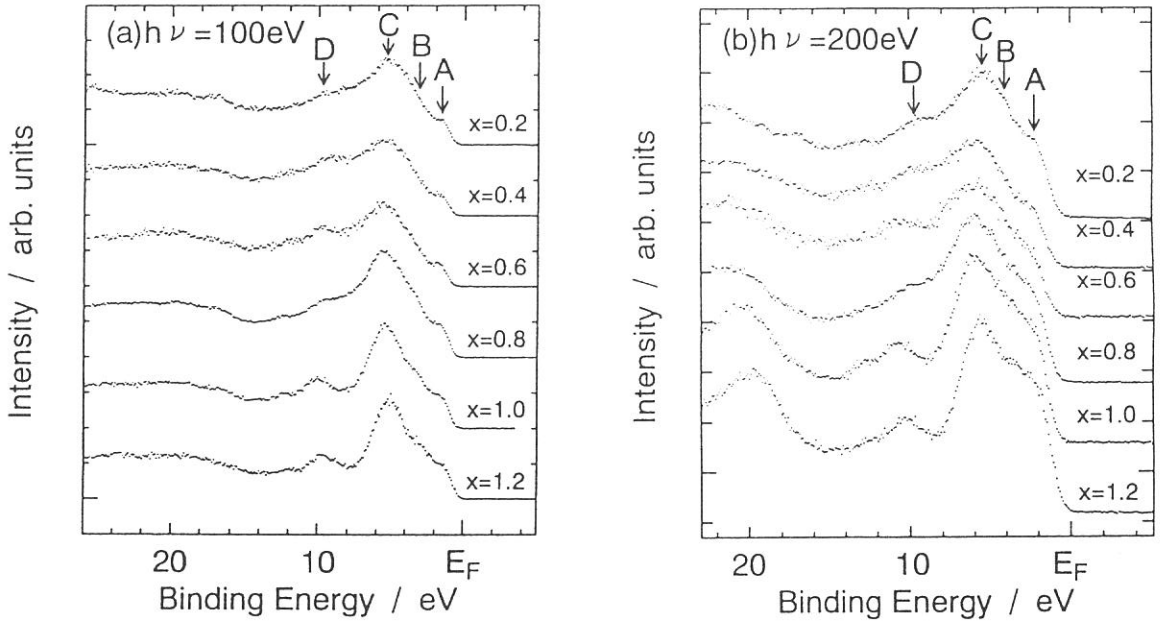

Fig. 1. Valence-band photoemission energy distribution curves (EDC) of $La_{2-x}Sr_xCoO_4$.

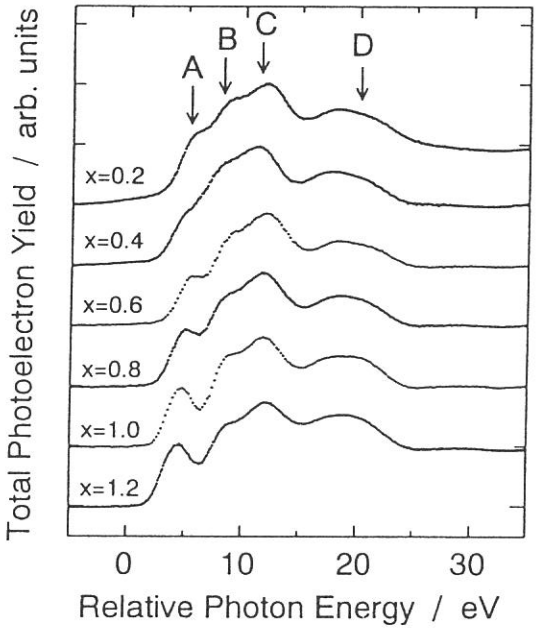

Fig. 2. Oxygen *K*-edge X-ray-absorption spectra of $La_{2-x}Sr_xCoO_4$.

References

1) Y.Moritomo, Y.Tomioka, A.Asamitsu, Y.Tokura and Y.Matsui, *Phys. Rev. B* **51**, 3297(1995).

2) T.Omata, K.Ueda, H.Hosono, T.Miyazaki, S.Hasegawa, N.Ueda and H.Kawazoe, *Phys. Rev. B* **49**, 10200(1994).

3) S.Tajima, H.Ishii, T.Nakahashi, T.Takagi, S.Uchida, M.Seki, S.Suga, Y.Hidaka, M.Suzuki, T.Murakami, K.Oka and H.Unoki, J. *Opt. Soc. Am.* **6**, 475(1989).

4) J.J.Yeh and I. Lindau, *At. Data Nucl. Data Tables* **32**, 1(1985).

(BL2B1)

POLARIZED ABSORPTION SPECTRA OF POLYETHYLENE TEREPHTHALATE AND POLYETHYLENE NAPHTHALATE FILMS IN SOFT X-RAY REGION

Isuke OUCHI, Ikuo NAKAI, Masao KAMADA * and Shin-ichiro TANAKA *

Faculty of Engineering, Tottori University, Koyama, Tottori 680
* UVSOR, Institute for Molecular Science, Myodaiji, Okazaki 444

We have examined the soft x-ray absorption spectra of polyethylene terephthalate (PET) and polyethylene naphthalate (PEN) in the shape of thin films since a few years ago. Absorption peaks at K-edges of carbon and oxygen changed their shapes with incident angle, by which we distinguished π -related peaks from σ -related ones; assignment of each peak was made [1]. These emperiments were carried out at BL-2B1 by total electron yield method by use of gratings of either 600 or 1200 mm/line. This time, we utilized same samples and same beam line but with a grating with higher resolution as 2400 mm/line.

As observed in the previous study, there are, in the carbon K-edge region, two sharp peaks "A" at 285.6 eV and "B" at 289.3 eV, which are related to C1s $\rightarrow \pi^*$ transitions, and three broad peaks "C", "D" and "E" originated from C1s $\rightarrow \sigma^*$ transition, in the higher energy region for PET and PEN films.

However, owing to a grating of higher resolution, it was revealed that peaks "A" and "B" were doublets for PET, as seen in Fig. 1. Namely, peak "A" was composed of a main peak at 285.1eV and a subpeak at 285.9 eV, and peak "B" consisted of peaks at 288.7 eV and 289.4 eV.

Moreover, one component of peak "B" at 289.4 eV behaved differently from others, as clearly seen by expanding the abscissa in Fig. 2; this peak kept its height when the film was tilted, while the other peaks increased their intensities when incident angle became larger. Since the molecular plane with aromatic rings of biaxially drawn PET film is sharply aligned parallel to the film plane with its molecular axis distributed almost evenly in the plane, the component of peak "B" at 289.4 eV is not of isotropic nature but must be of mixture of C1s $\rightarrow \pi^*$ and C1s $\rightarrow \sigma^*$ transition.

In the previous publication [1], we assigned peak "B" to three transitions related to π^* (C=O), π^* (C=C) and σ^* (C-H), based on the following reasons. First, peak "B" corresponds to the second C1s $\rightarrow \pi^*$ transition of benzene at around 288.5 eV [2] which is not as intense as first π^* peak of benzene at 285.6 eV; hence, there must be some additional contribution to the intensity of peak "B". Second,

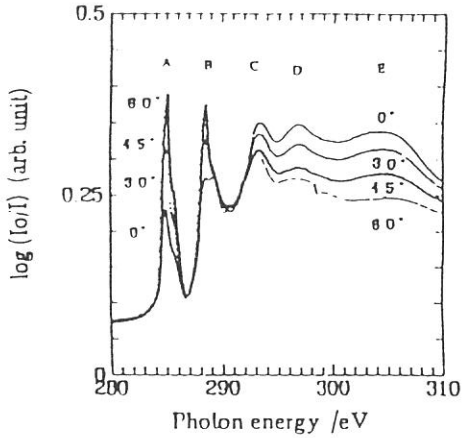

Figure 1. Total electron yield spectra near carbon K-edge of a biaxially drawn PET film 0.74 μ m thick for various incidenct angles.

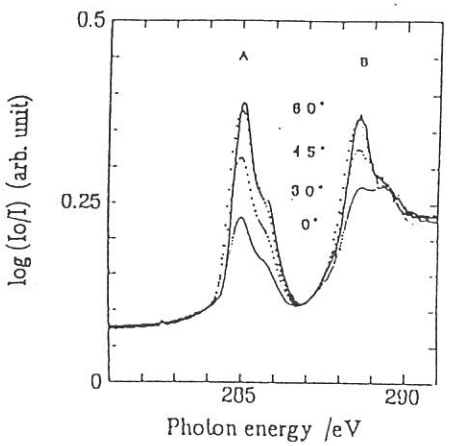

Figure 2. Enlarged view of peak "A" and "B", for various incident angles, in a biaxially oriented PET film depicted in Figure 1.

molecules having carbonyl groups show intense absorption at 288–289 eV range; polymethyl methacrylate, which has no aromatic ring but has C=O groups, reveal intense C1s → π^* peak at 288 eV [3]. Third, the C–H bond of polyethylene gives rise to C1s → σ^* transition peak at 287.4 eV, polarized perpendicular to the chain [4] and C–H bonds of benzene show σ^* transition in the 286 – 290 eV range, polarized in the ring plane[2].

These assignments which were made previously are basically consistent with present observation on the behaviour of peak "B" for oblique incidence. More specifically, the intense component of peak "B" at 288.9 eV has a nature of π^* and must be sttributed to C=O, while the other components at 289.4 eV is a mixture of C1s → π^* transition corresponding to the second π^* transition of benzene as mentioned in literature [2] and C1s → σ^* transition of methylene carbon.

The absorption spectra of biaxially drawn PEN film were slightly different with that of PET in details, but did not contradict the above interpretation. In the spectra of PEN, the higher energy component of peak "B" at 289.4 eV rather decreases its intensity with icident angle, while there is a weak shoulder at about 287.5 eV growing with incident angle. Since the number and the conformation of methylene carbons are same for both films, the peak at 289.4 eV, having σ^* nature, shall be originated in methylene carbons in PEN. Hence, the shoulder at 287.5 eV in PEN, having rather π^* nature, would be related to naphthalene carbons.

It is not unreasonable if the peak position of carbon of aromatic rings is different between PET and PEN; in fact, the absorption shape near peak "D" around 297 eV is different between these two films.

Finer structures are now found in near oxygen K–edge region of PET and PEN films as shown in Figure 3 and 4; in addition to the previously observed O1s → π^* transition at 532.3 eV, which was designated as peak "OA", there appeared smaller peak of π^* nature at 535 eV. In the previous paper[1], we argued that peak "OA" must have corresponded to the doublet at 533–555 eV in XPS. Now, it was proven indeed to be so. It is also revealed that peak "OB" at 540.5 eV has a shoulder at about 538 eV, both being of σ^* nature. Resemblance in the absorption spectra in this range between PET and PEN films is reasonable judging from the similarity of their chemical formulae and crystal structures, although slight difference of the peak ratio of "OA" to "OB" between these films in spite of their similarity is not yet explanatory.

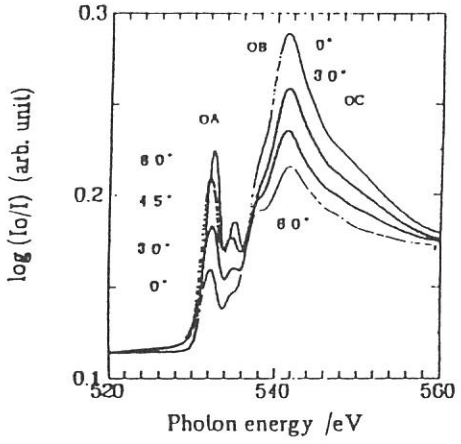

Figure 3. Total electron yield spectra near oxygen K–edge of a biaxially drawn PET film 0.74 μ m thick for various incident angle.

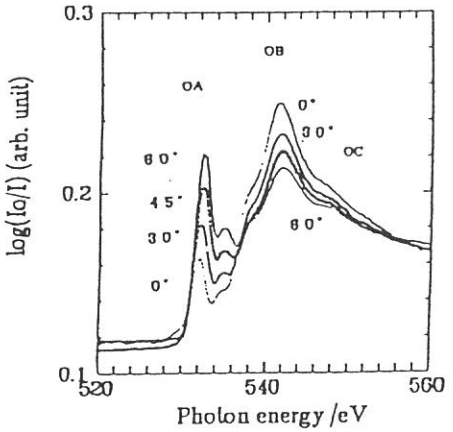

Figure. 4. Total electron yield spectra near oxygen K–edge of a biaxially drawn PEN film 0.78 μ m thick for various incident angles.

[1] I. Ouchi et al., Polymer J., 27 (1995) 127.
[2] J.A. Horsley et al., Chem. Phys. , 83 (1985) 6099.
[3] J. Stohr, "NEXAFS Spectroscopy," in "Springer Series in Surface Science", vol.25, (1992) p 208.
[4] J. Stohr et al., Phys. Rev. B, 36 (1987) 2976.

(BL2B1 & 6A2)

Photoemission Spectra of a Mixed Valent Semiconductor, Yb_3S_4

Shin-ichi KIMURA, Yong Seung KWON[1], Shin-ichiro TANAKA, Masao KAMADA and Takashi SUZUKI[2]

UVSOR Facility, Institute for Molecular Science, Okazaki 444
[1]Department of Physics, Sung Kyun Kwan University, Suwon 440-746, KOREA
[2]Department of Physics, Faculty of Science, Tohoku University, Sendai 980-77

Ytterbium compounds show exotic physical properties like Kondo effect and heavy fermion. Since the 4f hole state in the Yb^{3+}-ion is located near the Fermi level, the 4f hole state mixes to the conduction band. This is the opposite case of Ce compounds. The Yb-ion in the compound has some valence conditions, trivalence, divalence or mixed valence because of the difference of the mixing. So, many studies on Yb compounds, particularly Yb calcogenide and Yb pnictide, are carried out.

Recently, the heavy fermion with low carrier concentration is a problem. Yb_4As_3 is typical one. The material shows heavy fermion and mixed valence characters. [1] Yb_3S_4 also shows the characters. So we measured the photoemission and reflectivity spectra for the purpose of the investigation of the fundamental electronic structure. The reflectivity spectra are separately reported in this issue. [2] Here, the result of the photoemission measurement is reported.

Yb_3S_4 is a semiconductor with the energy gap of 0.4 eV. The crystal structure is Th_3P_4 type. This mean valence of the material is estimated 2.67 by the measurement of magnetic susceptibility. The temperature of the magnetic order is about 1 K. This material has heavy fermion like γ value of specific heat, a few $J/mol \cdot K^2$, in spite of the semiconducting character. [3]

The photoemission spectra were measured at two beam lines, BL2B1 and BL6A2, of UVSOR. The polycrystalline sample of Yb_3S_4 was used. The clean surface was obtained by scrapping by a diamond file *in situ*. The overall energy resolution was about 0.5 eV.

The photoemission spectra in the excitation energies of 82.6 eV and 126.1 eV are shown in Figure 1. The main structure originates from Yb^{2+}-$4f^{13}$, Yb^{3+}-$4f^{12}$ and Yb^{2+}-5p final states. Because of the difference of the excitation energy, the cross section of S-3p valence band is different from each other. So the spectral shape in the binding energy range below 5 eV is different from each other.

The mean valence of Yb-ion is estimated. From the Yb-5p photoemission, the mean valence is equal to the ratio between the intensity of the Yb^{3+}-5p peak and that of the Yb^{2+}-5p peak. From the deconvolution of the structure, which is indicated in Fig. 1, the intensity ratio is Yb^{2+} : Yb^{3+} = 1 : 2.04. This shows that the mean valence of Yb-ion is 2.67. On the other hand, the mean valence can be estimated by the intensity of the 4f peaks. From the difference spectrum between the spectrum in the excitation energy of 126.1 eV and that of 82.6 eV, which is the lowest spectrum in Fig. 1, the intensity ratio of Yb^{2+} : Yb^{3+} is 1 : 2.10. Note that the spectra were normalized at the binding energy of 6 eV. In the case of estimation of the mean valence, the initial electron number must be considered. So the mean valence is derived from the function, (mean valence) = 2 + $I(Yb^{3+})\times14$ / $[(Yb^{2+})\times13 + I(Yb^{3+})\times14]$, where $I(Yb^{3+})$ means the intensity of Yb^{3+}-4f. At the

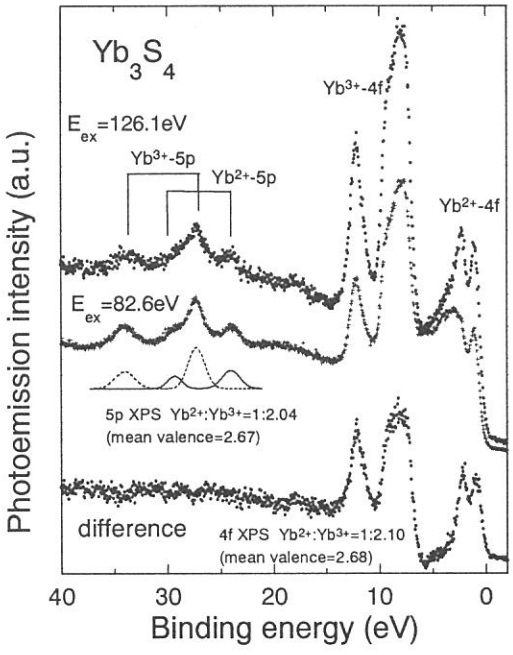

Fig. 1. Photoemission spectra at the excitation energy of 82.6 eV and 126.1 eV and the difference spectrum.

result, the estimated mean valence is 2.68. This value is almost equal to that estimated by Yb-5p photoemission and also estimated by magnetic susceptibility.

From the resonant photoemission spectra in Figure 2, the enhancement of Yb-$4f^{12}$ final state was observed. Generally, the resonant photoemission process of 4d absorption is

$$4d^{10}\,4f^{n} + h\upsilon \rightarrow 4d^{9}\,4f^{n+1} \rightarrow 4d^{10}\,4f^{n-1} + el. \qquad (1)$$

Here n is the number of the occupied state. Since the 4f state is fully occupied in Yb^{2+}-ion, the first process of (1) can not be occurred. So no enhancement appears at the energy of Yb^{2+}-$4f^{13}$ final state. On the other hand, the Yb^{3+}-$4f^{12}$ final state is weakly enhanced because the number of the unoccupied 4f state is a little. The absorption process appears in the total yield spectrum in Fig. 2. The peak at the photon energy of 167.5 eV comes from the S- $2p^{6}\,3d^{0} + h\upsilon \rightarrow 2p^{5}\,3d^{1}$ absorption and that at 183 eV comes from the Yb^{3+}-$4d^{10}\,4f^{13} + h\upsilon \rightarrow 4d^{9}\,4f^{14}$. In the case of the absorption at 167.5 eV, because of the different orbital moment between 2p and 3d, the enhancement of S-$3p^{5}$ final state does not appears. Note that the peak indicated by A is due to the Auger process.

In summary, the photoemission spectra of a mixed valent semiconductor, Yb_3S_4, were measured for the first time. The mean valence of Yb-ion was estimated about 2.67 by the 4f and 5p photoemission.

[1] A. Ochiai, T. Suzuki and T. Kasuya, J. Phys. Soc. Jpn. **59** (1990) 4129.
[2] S. Kimura, Y. S. Kwon and T. Suzuki, UVSOR Activity Report 1995 (1996).
[3] Y. S. Kwon, Y. Haga, C. Ayache, T. Suzuki and T. Kasuya, Physica B **186-188** (1993) 605.

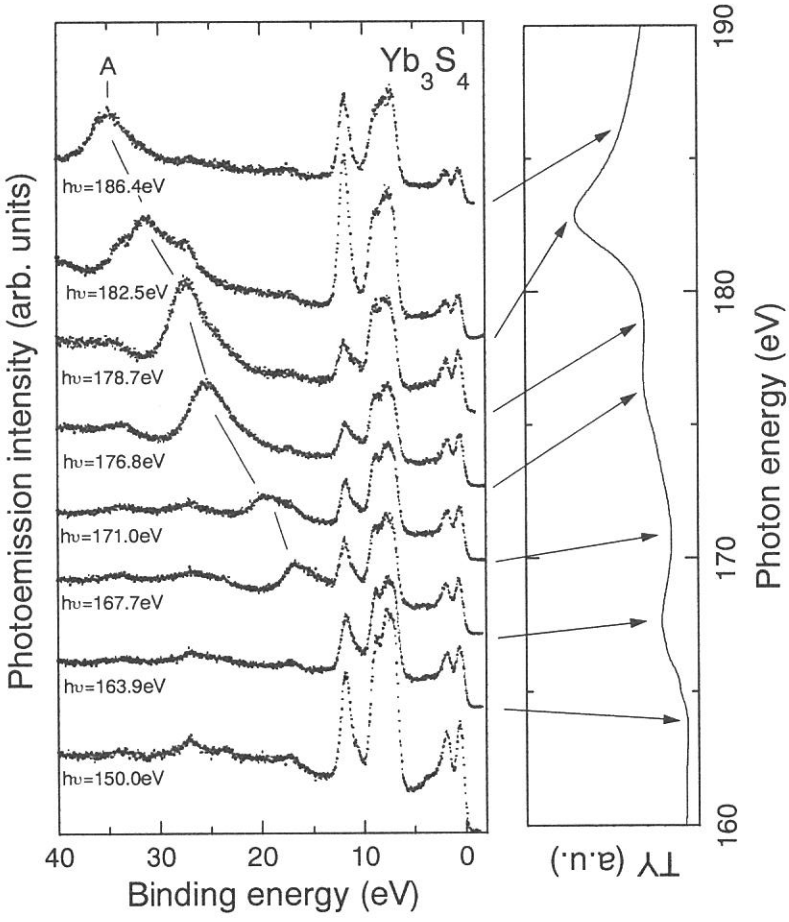

Fig. 2. 4d-4f resonant photoemission spectra of Yb_3S_4. The right spectrum is the total yield.

(BL-2B1)

Si L-absorption spectra of porous silicon

Tokuo MATSUKAWA, Satosi SORIMACHI, Makoto HONDA,
Noboru FUKUOKA and Kouzou ATOBE

Department of Physics, Naruto University of Education, Naruto, 772-01

A electochemically etched surface of crystalline silicon has been kown to emmit efficient visible luminescence, and the one of the possible explanation is quantum confinement effects. We had measured the Si $L_{2,3}$ absorption spectra in porous silicon by total photoelectron yield method. The samples were produced by anodizing bulk silicon crystal in HF and ethanol solution. The samples emmited red orange light under the excitation by He-Cd or Ar LASER illumination.

Figure shows the Si L absorption spectra of porous silicon and crystalline silicon. Any surface treatment had not been carried out in order to keep the microstructure of the porous silicon surface layer. The two kind of the porous silicon with different surface conditions had been prepared. The one is the sample kept in the pure water just after the chemical etching. The procedure is to prevent oxidization on the porous surface. The other porous sample had been exposed in the air for a several months. Thus the surface of the sample might have been oxidized more or less. The both samples were found to emmit the visible luminescence. Although only small spectral changes in the spectra had been observed in the photo-luminescence, intrinsic nature had no been changed. The spectral feature of the L spectrum of the porous silicon is rather closely similar to that of the crystalline silicon dioxide (α -SiO_2).

We had measured also Si K spectra of the porous silicon, and crystalline silicon and α -SiO_2 . The spectral features of the porous silicon were totally different from the spectrum of bulk silicon crystal, or from the α -SiO_2 crystal. A comparison of the L spectrum and the K spectrum is presented in the report on the BL-7A in this issue.

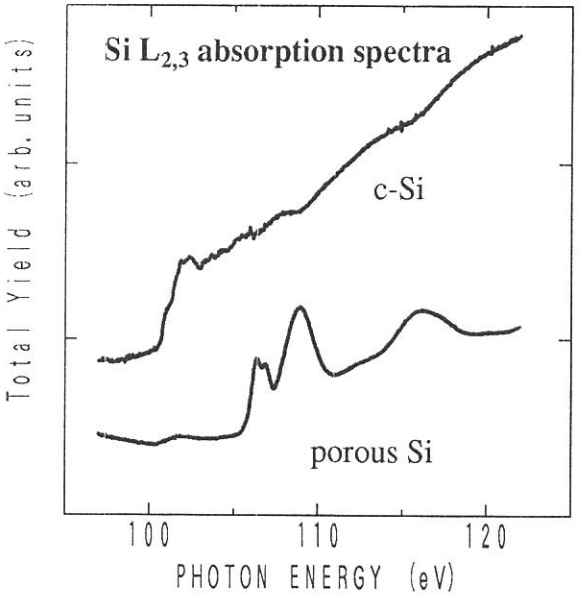

Dr. Hiraya (middle) is smiling beside Mrs. Y. Hagiwara and a waitress at his farewell party with UV members.

Executive committee members of the Joint Symposium of four Synchrotron Radiation Facilities and the Japanese Society for Synchrotron Radiation Research are satisfied with great success (Front: Profs. M. Ando,K. Shobatake (chairman), T. Kinoshita, and Mr. K. Sakai (left to right). Back: Profs. K. Seki, K. Mitsuke, and T. Tahara (middle to left)). Secretaries (K. Nishino, Y. Kobayashi, and Y. Hagiwara (middle to left)) and Prof. M. Kamada join (left) them.

(BL2B1)

Development of Electron–Ion Coincidence Spectroscopy for Study of Surface Dynamics by Using Synchrotron Radiation

Kazuhiko MASE, Mitsuru NAGASONO, Shin–ichiro TANAKA,
Masao KAMADA, and Tsuneo URISU
Institute for Molecular Science, Okazaki 444, Japan

Mechanism of photo–stimulated ion desorption (PSID) induced by core level excitations is an especially attractive topic in synchrotron radiation science as well as surface science, because the details are not understood in spite of numerous investigations so far. A most probable model for PSID is Auger stimulated desorption (ASD) mechanism, which is described approximately as a sequence of three steps: The first step is a core level excitation, the second is an Auger transition, and the final is the decay of the multi–hole excited state and the ion desorption. The best way to investigate the initial core excitation and the intermediate Auger transition are photoelectron spectroscopy (PES) and Auger electron spectroscopy (AES), respectively. Therefore, the coincidence measurement of photoelectrons or Auger electrons and photoions is a most powerful approach for PSID study [1]. In the present article, we describe the details of apparatus for the electron–ion coincidence (EICO) measurement combined with synchrotron radiation (SR).

Figure 1 shows the EICO apparatus, which consists of an electron gun, a coaxial cylindrical mirror analyzer (CMA), a time–of–flight ion mass spectroscope (TOF–MS), a power supply, and an electronic system for measurements. The TOF–MS consists of an ion–extraction grid, a drift tube, a pair of electrodes for ion deflection, a pair of electrodes for ion focusing, and micro channel plates (MCP). A sample surface is excited with SR, and the emitted electrons are analyzed by CMA, while the desorbed ions are accelerated with an extraction electric field towards the TOF–MS. The ion counts are recorded as a function of the TOF difference between the electron and the ion,

by using a multichannel scaler (MCS) taking the energy-analyzed electron signal as the starting trigger. The ions desorbed from the same excited molecule which has emitted the electron give a characteristic peak in the TOF spectrum, while ions irrelevant to the electron raise the background level as a chance coincidence signal. Hence, this technique is called electron-ion coincidence spectroscopy.

The EICO analyzer is attached to an ultra-high vacuum chamber (base pressure: 7×10^{-11} Torr) at the beam line BL2B1 with a grasshopper monochromator in UVSOR. The present apparatus is utilized for AEPICO measurements of condensed H_2O [2], NH_3, and ND_3 [3], and for PEPICO measurements of condensed SiF_4, $Si(CH_3)_4$ [4], and $SiF_3CH_2CH_2Si(CH_3)_3$ [5].

References

[1] M. Nagasono, K. Mase, and T. Urisu, Surf. Sci., in press.

[2] M. Nagasono, K. Mase, S. Tanaka, and T. Urisu, *UVSOR Activity Report BL2B1*, 1995.

[3] M. Nagasono, K. Mase, S. Tanaka, and T. Urisu, *UVSOR Activity Report BL2B1*, 1995.

[4] K. Mase, S. Nagaoka, M. Nagasono, S. Tanaka, and T. Urisu, *UVSOR Activity Report BL2B1*, 1995.

[5] S. Nagaoka, M. Nagasono, K. Mase, S. Tanaka, and T. Urisu, *UVSOR Activity Report BL2B1*, 1995.

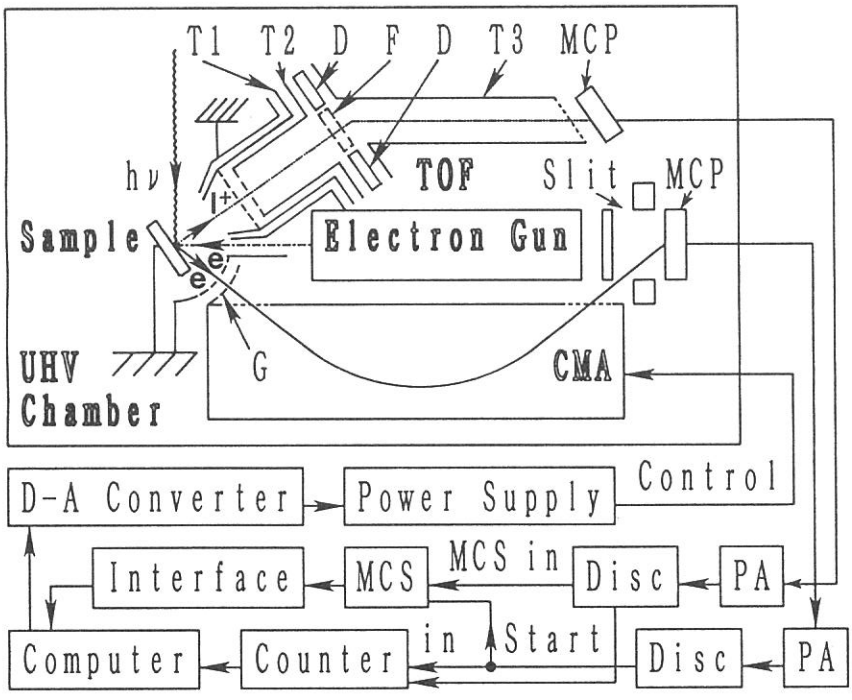

Figure 1. Schematic diagram of the EICO apparatus combined with SR. The abbreviations used are as follows: PA, preamplifier; Disc, discriminator; T1, ion-extraction grid; T2, drift tube; F, focus; D, deflector; and G, retarding grids.

(BL2B1)

Photostimulated Ion Desorption Study of $Si(CH_3)_4$ and SiF_4 Condensed on a Surface by Using Photoelectron–Photoion Coincidence Spectroscopy

Kazuhiko MASE,[a] Shin–ichi NAGAOKA,[b] Mitsuru NAGASONO,[a]
Shin–ichiro TANAKA,[a] and Tsuneo URISU[a]

[a]*Institute for Molecular Science, Okazaki 444, Japan*

[b]*Department of Chemistry, Faculty of Science, Ehime University, Matsuyama 790–77, Japan*

Photostimulated ion desorption (PSID) induced by core level excitations of molecules condensed on a surface is a developing field in surface science as well as molecular physics, because the details of the mechanism and the competing deexcitation processes are scarcely understood. The coincidence measurement of photoelectrons and photoions is a most powerful approach for PSID, because the core level excitations responsible for the ion desorption are directly identified [1, 2]. In the present article, we state a PSID study of $Si(CH_3)_4$ and SiF_4 condensed on a gold surface by using photoelectron–photoion coincidence spectroscopy (PEPICO).

The details of the apparatus used is described elsewhere [1]. The sample surfaces are prepared by exposing a gold foil at 80 K to $Si(CH_3)_4$ of 8 L (1 L = 1×10^{-6} Torr·s) or SiF_4 of 5 L in an ultra–high vacuum chamber. Figure 1(a) and (b) show PEPICO spectra of $Si(CH_3)_4$ obtained with the C 1*s* and the Si 2*p* photoelectron, respectively. H^+ is found to be the only primary species desorbed following the C 1*s* or the Si 2*p* photoionization. These results are in contrast to the case in the gas phase, where CH_3^+, $SiCH_3^+$, $Si(CH_3)_2^+$, $Si(CH_3)_3^+$ are also observed [3]. Figure 2 shows a PEPICO spectrum of SiF_4 obtained with the Si 2*p* photoelectron. F^+ is found to be the only predominant species desorbed following Si 2*p* photoionization. The result is again in contrast to the case in the gas phase, where Si^+, Si^{2+}, SiF^+, SiF^{2+}, SiF_2^+, SiF_2^{2+}, SiF_3^+, SiF_4^+ are also

also observed [4]. These results indicate that the neutralization probability of the polyatomic ions at the surface is much larger than that of monatomic ions.

References

[1] K. Mase, M. Nagasono, S. Tanaka, M. Kamada, and T. Urisu, *UVSOR Activity Report BL2B1*, 1995.

[2] S. Nagaoka, M. Nagasono, K. Mase, S. Tanaka, and T. Urisu, *UVSOR Activity Report BL2B1*, 1995.

[3] P. Morin, G.G.B. de Souza, I. Nenner, and P. Lablanquie, Phys. Rev. Lett. **56,** 131.

[4] E. Shigemasa, T. Hayaishi, K. Okuno, A. Danjo, K. Ueda, Y. Sato, A. Yagishita, J. Electron. Spectrosc. Relat. Phenom, in press.

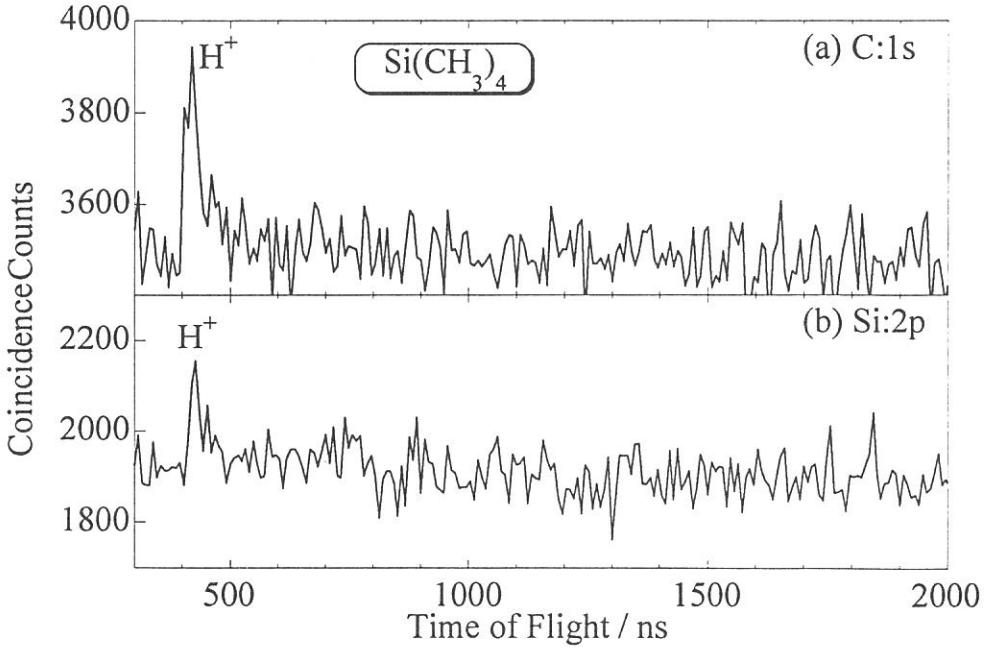

Figure 1. PEPICO spectra of $Si(CH_3)_4$ obtained with (a)C 1*s* photoelectron at hν = 454 eV, and (b)Si 2*p* photoelectron at hν = 270 eV. The accumulation time is 3600 s in both the cases.

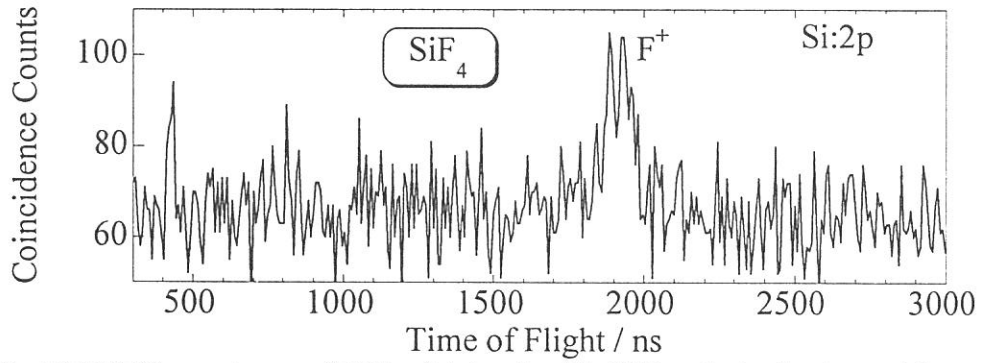

Figure 2. PEPICO spectrum of SiF_4 obtained with Si 2*p* photoelectron at hν = 270 eV. The accumulation time is 3600 s.

(BL2B1)

Photostimulated Ion Desorption Study of H_2O, NH_3, $Si(CH_3)_4$, SiF_4, and $SiF_3CH_2CH_2Si(CH_3)_3$ Condensed on a Surface by Using Time-of-Flight Ion Mass Spectroscopy under Single-Bunch-Mode Operation

Kazuhiko MASE, Mitsuru NAGASONO, Shin-ichiro TANAKA, and Tsuneo URISU

Institute for Molecular Science, Okazaki 444, Japan

Photoelectron-photoion coincidence spectroscopy (PEPICO) and Auger electron-photoion coincidence spectroscopy (AEPICO) presents photoemission- and Auger- final-state-selected ion mass spectra for photostimulated ion desorption (PSID) study [1]. On the other hand, the traditional approach to investigate PSID is time-of-flight (TOF) ion mass spectroscopy under the single-bunch-mode operation of the synchrotron radiation facility, which offers the ion yield integrated over every ion desorption channel. We have measured TOF spectra of H_2O and NH_3 condensed on a gold surface for comparison with the AEPICO results [2, 3]. The TOF instrument of the PEPICO apparatus [1] is used by taking the RF signal synchronized with the single-bunch-mode synchrotron radiation as the starting trigger. Figure 1(a) and (b) show the TOF spectra of H_2O at $h\nu$ = 575 eV and NH_3 at 426 eV, respectively. Similar spectra are obtained for H_2O at 750, 650, 605, 551, and 530 eV, and for NH_3 at 450, 400, 605, 551, and 530 eV. The predominant ion species is H^+ in all of the cases. No clear peak is observed for H_2O^+, OH^+, O^+, NH_3^+, NH_2^+, NH^+, nor N^+. We also measured TOF spectra of $Si(CH_3)_4$, SiF_4, and $SiF_3CH_2CH_2Si(CH_3)_3$ condensed on a gold surface for comparison with the PEPICO results [4, 5]. Figure 2(a), (b), and (c) show the TOF spectra of $Si(CH_3)_4$, SiF_4, and $SiF_3CH_2CH_2Si(CH_3)_3$, respectively. The predominant ion species are H^+, F^+, and H^+ and F^+, respectively. No clear peak is observed for CH_3^+, CH_2^+, CH^+, nor C^+ in the TOF spectrum of $Si(CH_3)_4$. The species with high mass number such as

$Si(CH_3)_4^+$, $Si(CH_3)_3^+$, $Si(CH_3)_2^+$, $SiCH_3^+$, Si^+, SiF_4^+, SiF_3^+, SiF_2^+, and SiF^+, however, is difficult to identify with the present approach, because the low mass resolution and the kinetic energy distribution fades the peak in the TOF spectra.

References

[1] K. Mase, M. Nagasono, S. Tanaka, M. Kamada, and T. Urisu, *UVSOR Activity Report BL2B1*, 1995.

[2] M. Nagasono, K. Mase, S. Tanaka, and T. Urisu, *UVSOR Activity Report BL2B1*, 1995.

[3] M. Nagasono, K. Mase, S. Tanaka, and T. Urisu, *UVSOR Activity Report BL2B1*, 1995.

[4] S. Nagaoka, M. Nagasono, K. Mase, S. Tanaka, and T. Urisu, *UVSOR Activity Report BL2B1*, 1995.

[5] K. Mase, S. Nagaoka, M. Nagasono, S. Tanaka, and T. Urisu, *UVSOR Activity Report BL2B1*, 1995.

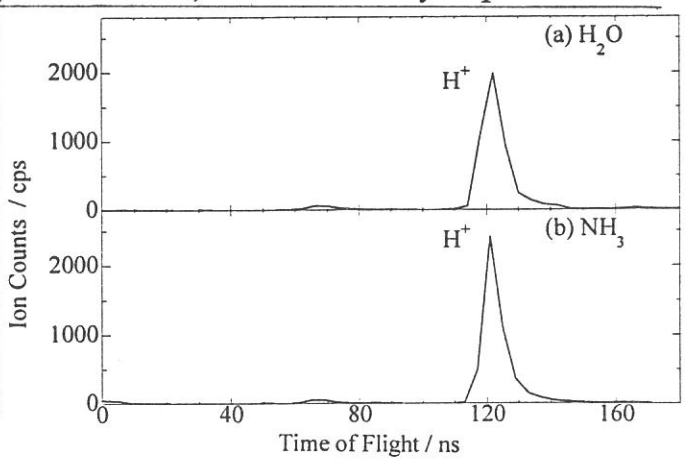

Figure 1. TOF spectra of (a)H_2O at $h\nu$ = 575 eV and (a)NH_3 at 426 eV. The both of voltages at the extraction grid and the drift tube are 1300 eV. The accumulation time is 360 s. The D^+ peak at 67 ns is derived from the contamination of D_2O and ND_3. The true TOF of H^+ is 122 + 177 = 299 ns, where 177 ns is the interval of the single-bunch-mode synchrotron radiation.

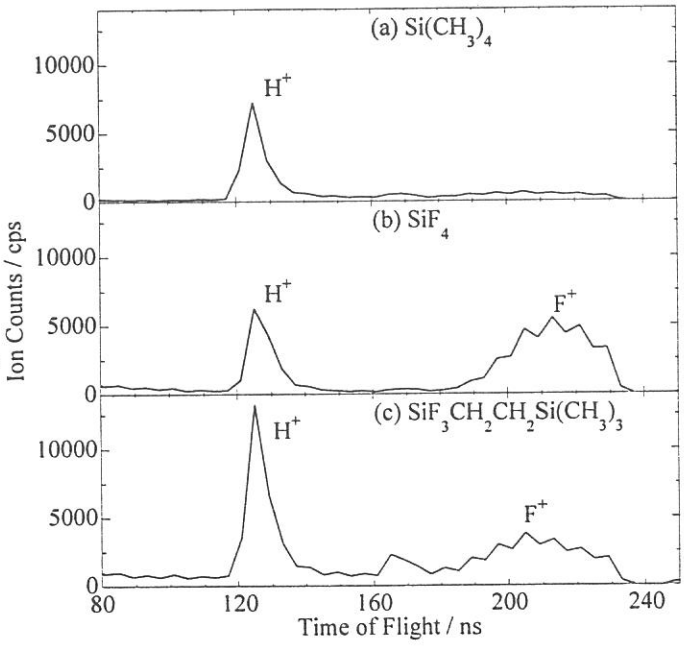

Figure 2. TOF spectra of (a)$Si(CH_3)_4$, (b)SiF_4, and (c)$SiF_3CH_2CH_2Si(CH_3)_3$ at 270 eV. The voltages at the extraction grid and the drift tube are 1500 and 1300 eV, respectively. The accumulation time is 360 s. The H^+ peak in Fig. 2(b) is derived from the contamination of H_2O. The peak at 163 ns in Fig. 2(c) is the artificial signal derived from the ringing of the H^+ signal. The true TOF of H^+ and F^+ are 125 + 177 = 302 ns and 210 + (177 × 7) = 1549 ns, respectively.

(BL2B1)

Auger final state-selected ion desorption study of condensed H_2O by using Auger electron - photoion coincidence spectroscopy

Mitsuru NAGASONO, Kazuhiko MASE, Shin-ichiro TANAKA, and Tsuneo URISU
Institute for Molecular Science, Okazaki 444, Japan

Photon-stimulated ion desorption (PSID) induced by core level excitations is studied for condensed H_2O by using Auger electron - photoion coincidence spectroscopy (AEPICO). The AEPICO spectroscope consists of an electron gun, a cylindrical mirror electron energy analyzer (CMA), a time-of-flight (TOF) ion mass analyzer, and a multi-channel scalar (MCS) [1].

A series of AEPICO spectra for H_2O/Au is measured as a function of the electron kinetic energy at energy steps of 10 eV around the O(KVV) Auger electron energy range (440 eV - 530 eV). Fig. 1 shows an AEPICO yield spectrum for H^+ and an Auger electron spectrum (AES) as a function of the electron kinetic energy around O(KVV). The AEPICO yield spectrum is enhanced at the electron energies corresponding to O(KVV) Auger transitions, which present a clear evidence of Auger stimulated ion desorption mechanism accompanied with the cleavage of a covalent bond [2]. The wide distribution of the AEPICO yield spectrum indicates that several Auger final states are responsible for the H^+ desorptions. The fine structure of the AEPICO yield spectrum, however, is different from that of the AES. Assignment of the AES is estimated with that of H_2O in the gas phase [3]. The Auger peak at an electron kinetic energy of 510 eV (the first Auger peak) is attributed to a overlapping of $KV_{NB}V_{NB}$ Auger transitions and KV_BV_{NB}, where V_B, and V_{NB} represent the bonding valence and the non-bonding valence orbitals, respectively. The Auger peak at an electron kinetic energy of 490 eV (the second Auger peak) is attributed to KV_BV_{NB}. The shoulder Auger peak at an electron kinetic energy of 470 eV (the third Auger peak) is attributed to KV_BV_B. The valley between the first and the second Auger peak, and the valley between the second and the third Auger peak are attributed KV_BV_B.

The $KV_{NB}V_{NB}$ Auger process leads to photoion desorption less efficiently than the KV_BV_{NB} and the KV_BV_B Auger process, because the proportion of the AEPICO yield in the first Auger peak is found to be the smallest among those of the three Auger peaks. The AEPICO yield at the second Auger peak is slightly smaller than those at the two valleys. The secondary electrons produced by energy loss of Auger electrons in subsurface do not contribute to the ion desorption, because the ions are desorbed only

from the topmost layer. The KV_BV_B Auger process, therefore, more efficiently lead to desorption of photoion than the KV_BV_{NB}. Consequently, we conclude that KV_BV_B, KV_BV_{NB}, and $KV_{NB}V_{NB}$ Auger processes contribute to ASID of condensed H_2O in that order.

[1] K. Mase, M. Nagasono, S. Tanaka, M. Kamada, and T. Urisu, *UVSOR Activity Report BL2B1*, 1995
[2] M. Nagasono, K. Mase, and T. Urisu, Surf. Sci. (in press).
[3] H. Siegbahn, L. Asplund, and P. Kelfve, Chem. Phys. Lett. **35,** 330 (1975).

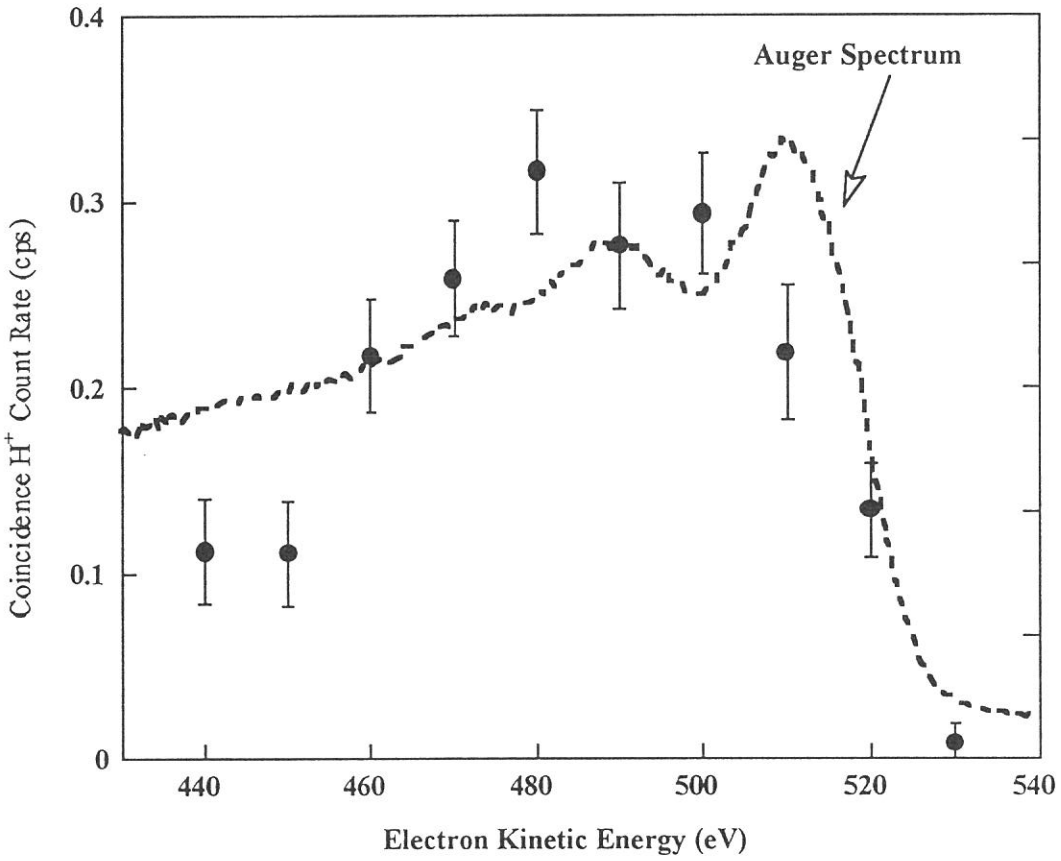

fig. 1. Auger electron - photoion coincidence yield spectrum (closed circles) and Auger electron spectrum (broken line) as a function of the O(KVV) Auger electron kinetic energy.

(BL2B1)

Auger final state-selected ion desorption study of condensed NH_3 and ND_3 by using Auger electron - photoion coincidence spectroscopy

Mitsuru NAGASONO, Kazuhiko MASE, Shin-ichiro TANAKA, and Tsuneo URISU
Institute for Molecular Science, Okazaki 444, Japan

Photon-stimulated ion desorption (PSID) induced by core level excitations is studied for condensed NH_3 and ND_3 (NH_3/Au and ND_3/Au) by using Auger electron - photoion coincidence spectroscopy (AEPICO). The details of the AEPICO spectroscope used is described elsewhere [1].

A series of AEPICO spectra for NH_3/Au and ND_3/Au are measured as a function of the electron kinetic energy around the N(KVV) Auger electron energy range (340 eV - 395 eV). Fig. 1(a) and 1(b) show AEPICO yield spectra for H^+ and D^+, and an Auger electron spectra (AES) of NH_3/Au and ND_3/Au, respectively. The Auger peaks which correspond to Auger final states are broadened with the secondary electrons produced by the energy loss of Auger electrons from the subsurface. The energy lost Auger electrons, however, do not contribute to the ion desorption, because the ions are desorbed only from the topmost layer. The relative intensity of the transition probability and the relative difference of the electron kinetic energy are expected to be almost similar to that of gas phase. The assignment of the Auger final states of NH_3/Au and ND_3/Au, therefore, are estimated with that of the gas NH_3 assuming the electron kinetic energy shift of 14 eV for AES, as shown in fig. 1(c) [2]. $2a_1$ and $1e_1$ orbitals are characterized as bonding (V_B) and $3a_1$ as non-bonding (nitrogen lone-pair) (V_{NB}).

The AEPICO yield spectra are enhanced at the electron kinetic energies corresponding to N(KVV) Auger transitions, which present a clear evidence of Auger stimulated ion desorption mechanism (ASID) accompanied with the cleavage of a N-H or a N-D bond. The fine structure of their AEPICO yield spectra are different from that of their own AES and the gas AES. The AEPICO yield are found to be the highest at the electron kinetic energy of $1e^{-2}$ Auger final state and the local rises are observed at $2a_1^{-2}$ and $3a_1^{-2}$. These results indicate two valence holes produced in the same orbital efficiently lead to the ion desorption. The proportion of AEPICO yield in the relative intensity at the electron kinetic energy of $3a_1^{-2}$ is smaller than that of $1e^{-2}$ and $3a_1^{-2}$. Consequently the KV_BV_B Auger processes efficiently contribute to ASID of NH_3/Au and ND_3/Au than $KV_{NB}V_{NB}$.

Isotope effect arising with ND_3/Au is observed as the low total ion count rate and the fine structure difference of AEPICO yield spectra, but their AES are observed with similar structure. The low total ion count rate is concluded to result from the reneutralization of D^+ before the desorption from the surface, because of the low velocity of D^+ compared with that of H^+. The difference of fine AEPICO yield spectra is not fully understood yet.

[1] K. Mase, M. Nagasono, S. Tanaka, M. Kamada, and T. Urisu, *UVSOR Activity Report BL2B1*, 1995.

[2] J. S. Shaw, JR., J. S. Jen, and T. D. Thomas, J. Electron Spectrosc. Relat. Phenom. **11**, 91, 1977.

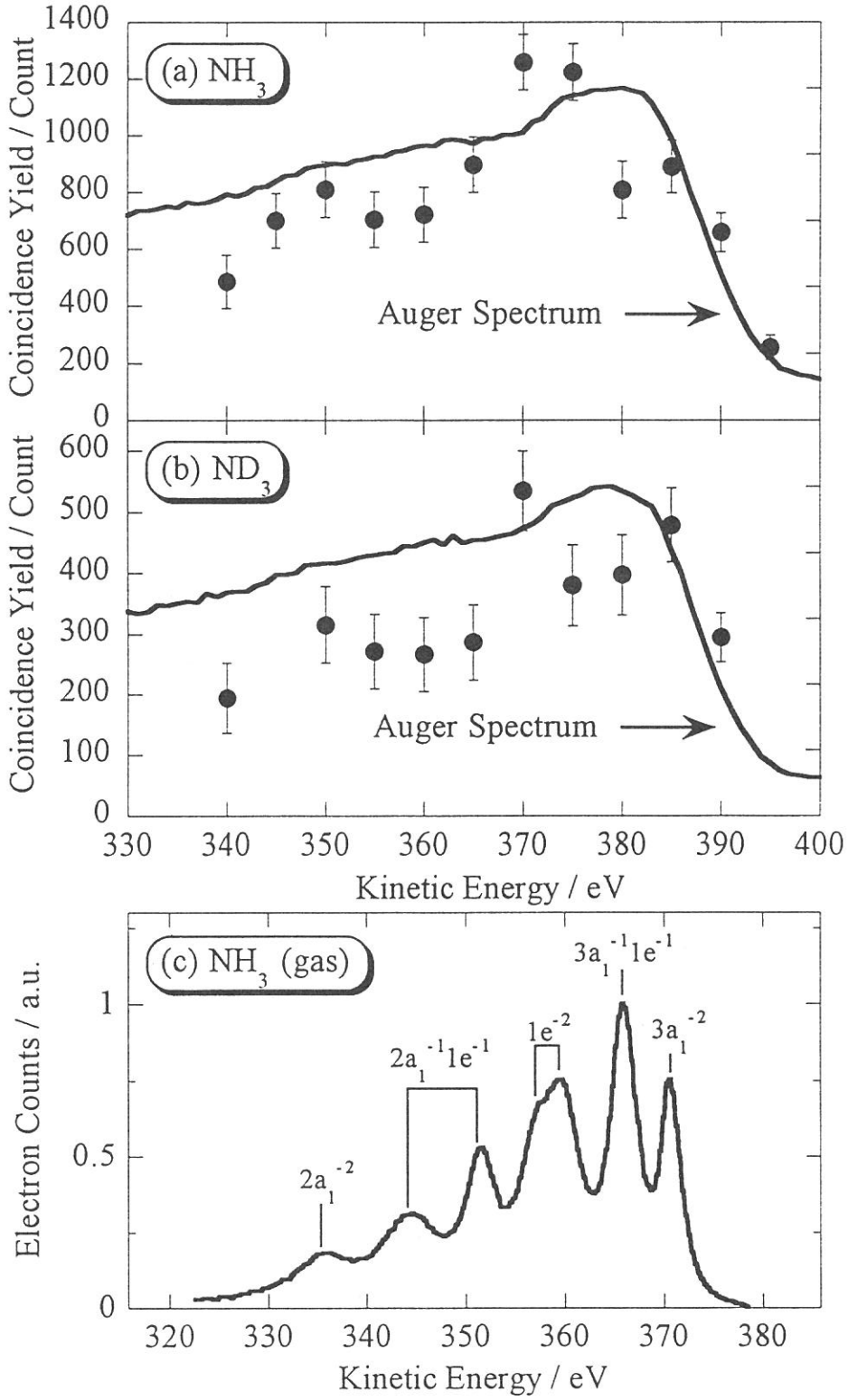

Fig. 1. AEPICO spectra (closed circle) and AES (solid line) of (a) NH_3/Au and (b) ND_3/Au. (c) AES of gaseous $NH_3$from ref. [2].

(BL2B1)

Site-Specific Fragmentation Following Si:2p Core-Level Photoionization of $F_3Si(CH_2)_2Si(CH_3)_3$ Condensed on Au Surface

Shin-ichi NAGAOKA, Kazuhiko MASE,* Mitsuru NAGASONO,* Shin-ichiro TANAKA,* and Tsuneo URISU*

Department of Chemistry, Faculty of Science, Ehime University, Matsuyama 790-77

**Institute for Molecular Science, Okazaki 444*

In recent years, relaxation processes following core ionization in molecules have been a topic of much interest. We have investigated site-specific fragmentation following Si:2p photoionization of (trifluorosilyl)(trimethylsilyl)ethane ($F_3Si(CH_2)_2Si(CH_3)_3$, FSMSE) condensed on Au surface by means of the photoelectron spectroscopy and the photoelectron-photoion coincidence method (PEPICO method).

The experiments were performed using a cylindrical mirror electron-analyzer and a time-of-flight ion detection assembly coupled to a grasshopper monochromator (Mark XV) installed on the BL2B1 beamline of the UVSOR synchrotron radiation facility in Okazaki.[1]

The photoelectron spectrum of FSMSE has two peaks in the region of Si:2p electron emission (Figure 1). Those peaks at 102.2 and 105.9 eV are likely to correspond to 2p-electron emission of the Si atom bonded to three methyl groups (Si[Me]) and that of Si bonded to three F atoms (Si[F]), respectively.

The site-specific fragmentation following the Si:2p core-level photoionization of FSMSE can be seen by means of the PEPICO technique. Figures 2a and b show the PEPICO spectra obtained with emission of Si[Me]:2p and Si[F]:2p electrons, respectively. H^+ and F^+ ions are predominantly desorbed coincidentally with the Si[Me]:2p and Si[F]:2p electrons, respectively.

The site-specific fragmentation pattern of FSMSE condensed on Au surface is quite different from that in the vapor phase.[2]

1. K. Mase et al. UVSOR Activity Report BL2B1 (1995).
2. S. Nagaoka et al. UVSOR Activity Report BL3A2 (1995).

Fig. 1 (left-hand side) Photoelectron spectrum of FSMSE taken at 270 eV of photon energy. The spectrum in the region of Si:2p electron emission in which the horizontal scale is enlarged is shown in the upper right-hand corner.

Fig. 2 (right-hand side) PEPICO spectra of FSMSE taken at 270 eV of photon energy. (a) Si[Me]:2p electron emission. Data collection time is 276 min. (b) Si[F]:2p electron emission. Data collection time is 210 min.

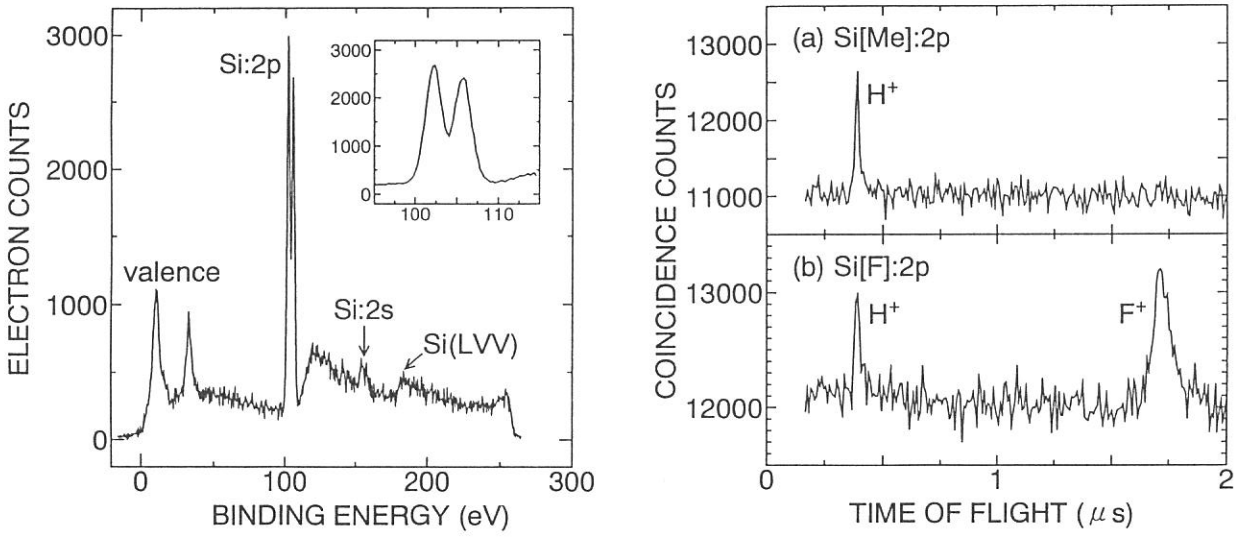

(BL2B1)

Photoemission study of benzene chemisorbed on Si(100)(2 × 1)

Yukihiro TAGUCHI, Yasuaki OHTA, Tetsuya KATSUMI, and Osamu AITA

College of Engineering, University of Osaka Prefecture, Gakuen-cho 1, Sakai 593

Considerable interest exists in the interaction of benzene with a solid surface, and the adsorption on various surfaces, especially on transition-metals, has been studied extensively. We studied benzene adsorption on the (100) and (111) surfaces of silicon by vibrational and desorption methods.[1] A crystal-face specificity was found for benzene adsorption on silicon surfaces, and we proposed that chemisorbed benzene is σ-bonded to the (100)(2 × 1) surface while π-bonded to (111)(7 × 7). However electronic states of benzene and surface Si atoms involved in the adsorption were not discussed explicitly in the study. In this work we employ photoemission (PE) and C K-edge near-edge x-ray absorption fine structure (NEXAFS) spectroscopy to study the chemisorbed state of benzene on the Si(100)(2 × 1) surface.

The sample used was a Si(100) wafer. The clean surface, showing a sharp (2 × 1) low-energy electron diffraction pattern, was prepared by several cycles of Ar^+-ion bombardment and annealing. Benzene was introduced into the chamber through a variable leak valve. The spectrometer used for PE and NEXAFS measurements was a cylindrical mirror analyzer, which is set at 90° to x-ray beam from a grass-hopper monochromator. All measurements were made at room temperature (RT) except those for physisorbed benzene made at 100 K.

Figure 1 shows a valence-band PE spectra of (a) a clean Si(100)(2 × 1) surface and (b) the surface exposed to benzene at saturation coverage at RT. As seen in Fig. 1(b), adsorbate induced features are observed in the binding-energy range higher than 8 eV, along with low-lying surface Si peaks which are modified only a little. In the previous study we found that benzene chemisorbs molecularly on Si(100) at RT. The correlation between gas-phase levels[2] and the peaks observed for chemisorbed benzene is made in the bar diagram. The gas-phase levels are shifted so as to align arbitrarily the high-lying σ_{CH}- and C 2s-derived levels, bands D and E in Fig. 1(b). It is considered with this diagram that the $1e_{1g}$ and $1a_{2u}$ π orbitals are strongly stabilized by 1.9 and 1.4 eV, respectively. These stabilization may be ascribed partly to the large overlap between benzene π orbitals and the dangling-bond orbitals of the Si(100) surface. The total energy calculation suggests that benzene molecule sits on a dimer of surface Si atoms of Si(100) and that two CC bonds interact mainly with each one of Si atoms.[3] This implies that double π bonds are formed upon benzene adsorption and that the above approach with free molecules levels is not well suited for the interpretation of the adsorbate levels. In fact we obtained, in the previous study, qualitatively different vibrational spectra for chemisorbed benzene on Si(100), from benzene π-bonded to transition-metal surfaces. Thus the more careful analysis for the PE spectra of benzene on Si(100) should be required.

Figure 2 shows the C K-edge NEXAFS spectra of the benzene-exposed Si(100) surface. The detector retarding voltage was set at 262 eV. There is a strong π^* resonance at 285 eV for grazing x-ray incidence (20°) and very weak resonance at normal incidence. Clearly, benzene lies nearly parallel to the the surface plane. This is consistent with the theoretical calculation referred above, which predicts 5° of the ring tilt angle with respect to the surface plane.

References

[1] Y. Taguchi *et al.*, J. Chem. Phys. **95**, 6870 (1991).

[2] D. W. Turner *et al.*, Molecular Photoelectron Spectroscopy (Wiley, London, 1970).

[3] B. I. J. Creig, Surf. Sci. **280**, L279 (1993).

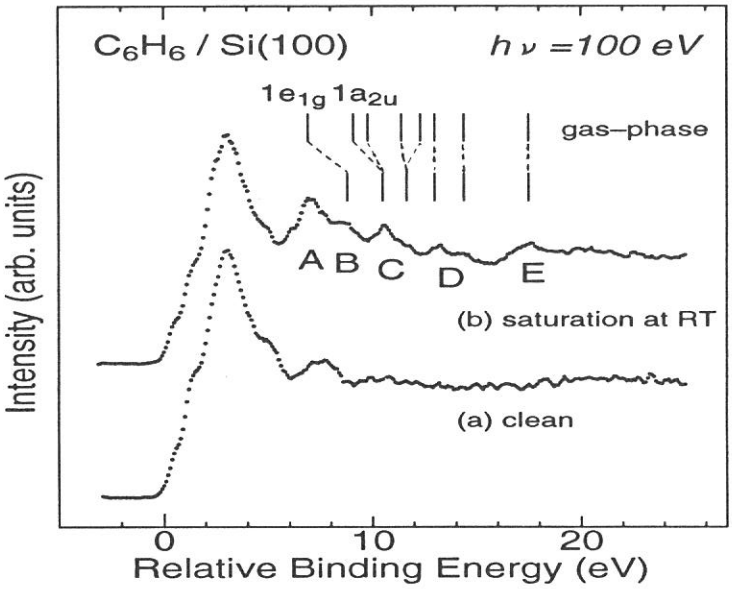

FIG. 1. (a) Valence band spectrum of a clean Si(100) surface and (b) the spectrum indicating a saturation coverage following the exposure of the clean surface to 5×10^{-6} Torr s C_6H_6 at RT. An excitation photon energy $h\nu = 100$ eV. Binding energy is given as VBM=0. The correlation between the gas-phase orbitals is shown in a bar diagram.

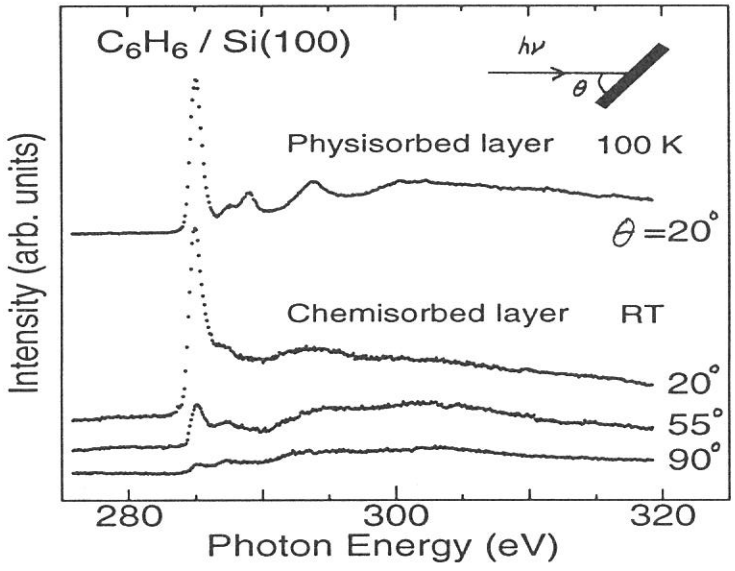

FIG. 2. C K-edge NEXAFS spectra of physisorbed and chemisorbed C_6H_6 on Si(100). Measurements were made at 100 K for physisorbed layer and RT for chemisorbed layer. X-ray incidence angles θ are indicated in the figure.

(BL2B1)

Coadsorption of Cs and Cl on Si(100) studied by XPS

Yuich Takamine, Keita Asao, Misaki Kohama, and Akira Namiki,
Toyohashi University of Technology, Tempaku, Toyohashi441,

Shinichiro Tanaka, and Masao Kamada
Institute for Molecular Science, Myodaiji, Okazaki 444.

Introduction

Halogen molecules may be very reactive towards solid surfaces. It is well known that on the clean Si(100) surface Cl_2 dissociation occurs at the dangling bonds of the top most Si dimers. In this case a covalent natrure of the Si-Cl bond may merge importantly as well as the ionic character. On alkali metal surfaces, on the other hand, as a matter of fact, halogen molecular dissociation results in formation of typically ionic bonds. For the coadsorption of Cl and Cs atoms on the Si(100) surface, we will have a problem which is favourable for Cl atoms to stick, the Si dangling bonds or the alkali adatoms. In this study, we measure the XPS spectra of a Cl and Cs coadsorption system on the Si(100) surface to consider the Cl bonding structure.

Experimental

A clean Si(100) surface was obtained by a standard procedure with Ar^+ ion sputtering and thermal annealing prior to Cs or Cl deposition. Cs deposition was done with a Cs dispencer (SAES Getters) and Cl deposition with a AgCl electrochemical-cell by providing a constatnt electrical current under the pressure less than $4 \times 10^{-10} Torr$. XPS spectra of Cl $2p$, and Si $2p$ and Cs $4d$ were measured respectively with $h\nu$=235 and 130eV lights from the UVSOR of IMS.

Results and Discussion

Figure 1 shows the changes of Si $2p$ spectra at the various stages of Cl depositions on the 0.08ML Cs/Si(100) surfaces. At the zero Cl deposition the Si $2p$ spectrum is already changed a bit by the 0.08ML Cs adatoms from that of the clean Si(100). The Cl_2 exposure for 95s results in a broader spectrum, perhaps accompanying a chemical shift due to Si-Cl bonding. The chemically shifted peak appears more clearly at the stage of 155s Cl_2 exposure. The Si $2p$ spectra are deconvoluted into the bulk component, B, the up, U, and down, D, of the Si dimer, and the Cl-bonded Si as shown in Fig.1. The component U decreases at the early stages of Cl_2 deposition, while the component D begins to decrease after the extinction of the component D, which seems to imply that for the low Cl coverage regime the Cl bonding occurs preferentially at the up atoms. This might be due to the richly populated vital electrons at the up atoms rather than the down atoms.

It is known that the Cs adatoms with low coverage less than 0.2ML are ionized on the clean Si(100) surface (by the work of Souda et al.). Figure 2 shows the changes of the corresponding Cs $4d_{5/2,3/2}$ spectra. No essential difference can be recognized in the Cs $4d$

spectra between the 0 and 95s exposures, which suggests that the Cl atom does not make a bond with the Cs adatom but with the Si dangling bond at least for low Cl coverage region. However, the spectrum is observed to show a quite big change at 155s exposure; the valley between the two peaks due to $5/2 - 3/2$ splitting is now burried by a second component which is further increased in spectral intensity at 275s exposure. Figure 2 includes the spectral decomposition of the Cs $4d$ spectra obtained. The net chemical shift of the second component denoted as Cs' with respect to the original one denoted as Cs is about -1.0eV.

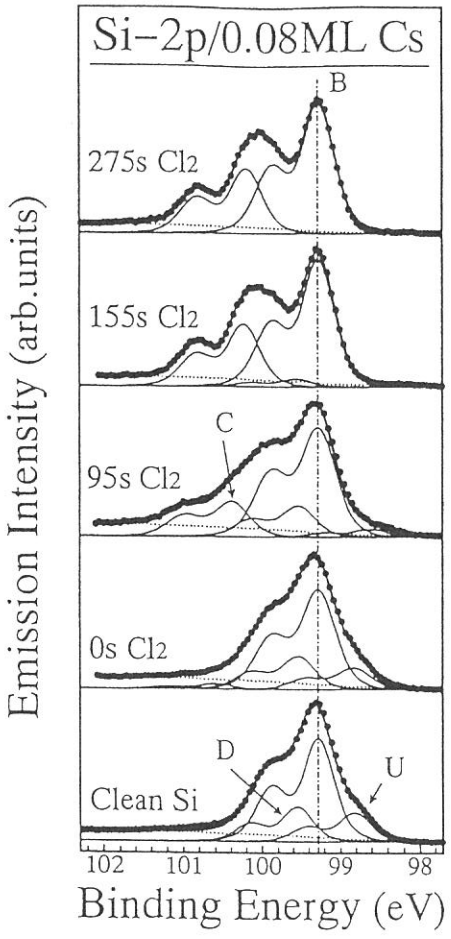

Fig.1 Si $2p$ spectra obtained for various Cl_2 deposition on 0.08MLCs/Si(100) at 300K. The spectral decomposition shows B: bulk Si, U and D: up and down Si atom of the Si dimer, respectively, and C: Cl-bonded Si.

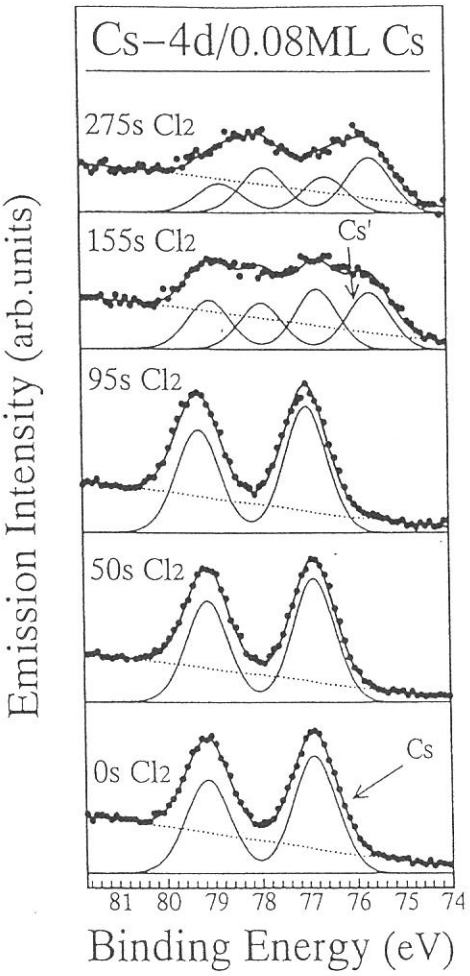

Fig.2 Cs $4d$ spectra corresponding to the Si $2p$ spectra in Fig.1. Neither the chemical shift nor the change in spectral width is seen in the spectra before 95sec exposures.

This large chemical shift does not necessarily mean $Cl^- - Cs^+$ bonding because such highly ionic bond usually results in an energy shift to higher binding energy region. The quite same uptake behaviour of the Si $2p$ component C attributed to the Si-Cl species in Fig.1 may also confirm this statement of no formation of the $Cs^+ - Cl^-$ bonds. For high Cl coverage the surface electron density around Fermi level may be decreased quite much due to the Si-Cl bonds. Therefore, the less screening effect may lead to a larger Madelung energy for the final core hole state. Thus, we consider that the apparent low energy shift of the Cs $4d$ spectra is caused by an influence of the external relaxataion effect to the energy level of the final core hole state of the Cs ion.

(BL2B1)

Adsorption of potassium on the NaCl(100) Surface

S. Tanaka, N. Takahashi, M. Kamada.
UVSOR Facility, Institute for Molecular Science, Okazaki 444, Japan

Alkali halide is typical ionic crystal, and has been extensively studied experimentally and theoretically for long years. However, its surface properties are not well known, because it is an insulator, and cannot be investigated using usual techniques in surface analysis of conducting material. We produced the NaCl(100) surface on the well-ordered Si(100)(2x1) in UHV, and investigated the adsorption of K on the NaCl(100) surface by using surface XAS (X-ray Absorption Spectroscopy).

The experiments were performed at BL2B1 which housed a 'grasshopper' monochoromator (Baker) and a double-pass CMA (phi). NaCl film was produced by thermal evaporation on the Si(100) surface kept at 105K, and subsequent annealing at 560K. The thickness of the film was estimated to be 30 ML (mono-layer), and charge-up effect was not observed in all measurements. The NaCl film exhibited a poor (1x1) LEED pattern which indicated that the NaCl(100) surface with some defects was produced. The commercial dispenser was used for the evaporation of potassium. The sample was kept at 105 K during evaporation of K and measurements. The $L_{2,3}$ absorption edge structure of the K atoms adsorbed on NaCl(100) surface was studied with partial-photoelectron-yield spectra by monitoring K-LMM Auger electron emission with the CMA. The total-photoelectron-yield spectra were also measured by monitoring photocurrent from the sample with a picoammeter. The resolution of the monochromator was less than 0.5 eV in these experiments. The resolution of the CMA for the partial-photoelectron-yield spectrum was set to be more than 10 eV which was large enough to eliminate the influence from directly excited photoelectrons.

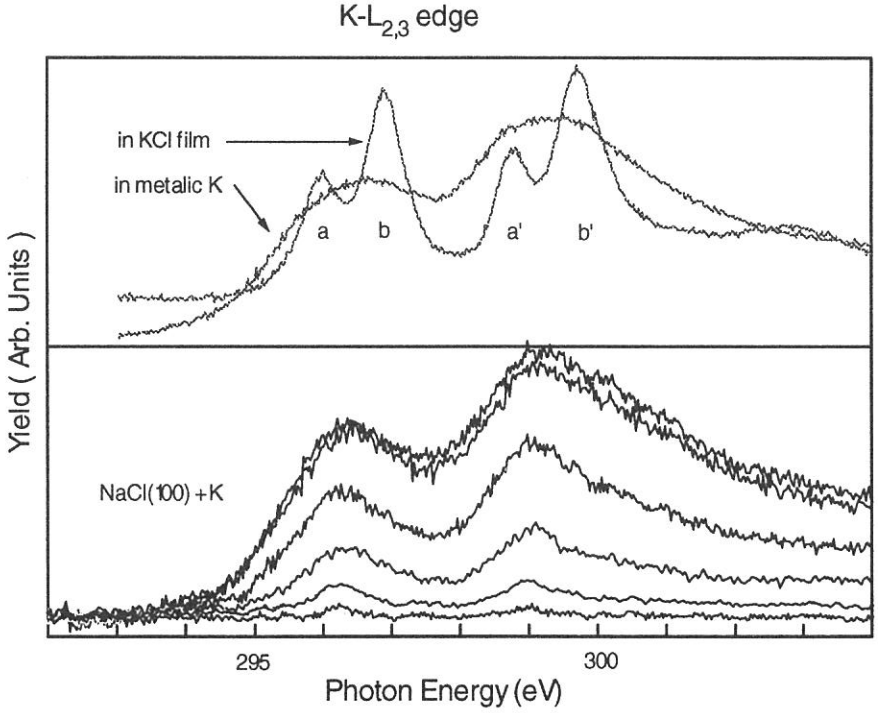

Fig.1. Total photoelectron yield spectra at $L_{2,3}$ edge of K in KCl films and metallic K (upper level), and partial photoelectron yield spectra of K atoms adsorbed on NaCl(100) surface for various coverage.

Figures 1 shows partial yield spectra for K atoms adsorbed on NaCl(100) surface as a function of K coverage (lower level), and total photoelectron yield spectra for metallic K film and KCl film (upper level). The coverage of K was controlled by the time of the evaporation, and the top curve corresponds about 1 ML. The XAS spectra provide information about the local unoccupied density states. Due to the dipole selection rule, the allowed transitions are from K-2p to final states with K-4s and K-3d. For K ion in the KCl film, peaks a and b are excitation from the K-$2p_{3/2}$ state, peaks a' and b' are from the K-$2p_{1/2}$ state. Yanagihara et.al.[1] ascribed peak a and a' to the excitation to the K-4s unoccupied state, and peaks b and b' to the K-3d unoccupied state. For K in the metallic film, there are two broad peaks excited from K-$2p_{3/2}$ state K-$2p_{1/2}$ states. The 4s and 3d states of K are overlapped here. XAS spectra of K atoms adsorbed on the NaCl(100) surface is similar to the spectrum of the metallic K film for all coverage. Thus, it is considered that K atoms adsorbed on the NaCl(100) is not ionic but metallic. Adsorption of alkali metal on the metal and semiconductor surfaces have been studied extensively, and it is generally agreed that the charge transfer between the substrate and the alkali metal is insignificant. This seems to be valid for the case of the adsorption of K on the NaCl(100) surface. Peaks are relatively sharp for lower coverage, but get broader as the coverage is increased, which was also observed in the case of K on Ag(100) surface[2]. It suggests the transition from isolated K atoms to the formation of K-K bonds, where the broadening of the excitations are induced between 4s and 3d orbitals of adjacent K atoms and the formation of 4s and 3d bands.

Figure 2 shows the XAS spectra of K multilayer film on NaCl(100) surface, and that after annealing at about 500K. It is high enough for the desorption of multilayer of K. After heating, the spectrum is very similar to the that of KCl film. It clearly indicates that the adsorbed K is changed to ionic. We also observed the change in the XAS spectrum at Cl-L_{23} edge after heating. It indicates that the potential due to positive ions surrounding Cl ions are considerably changed, and consistent with that K is changed from metallic to ionic on the surface.

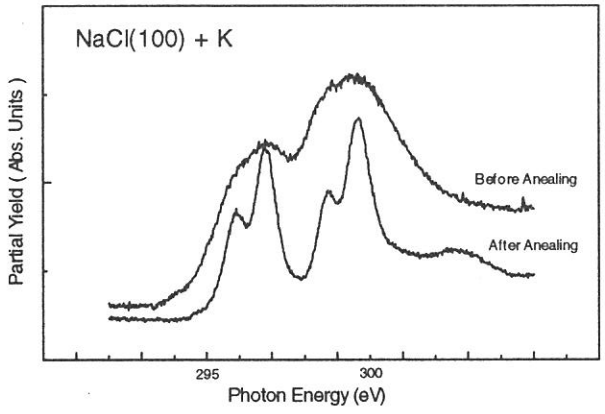

Fig.2. Partial photoelectron spectra at K-$L_{2,3}$ edge of the K film on NaCl(100) surface before and after annealing at about 500 K.

In conclusion, we have investigated the adsorption of K on the NaCl(100) surface, and found that the K atoms on the surface is metallic at 105 K, and it converted to be ionic after heating.

References 1: M. Yanagihara, H. Maezawa, T. Sasaki and Y. Iguchi, J. Phys. Soc. Jpn. 54, 3628(1985).
2: S. Modesti, C.T. Chen, Y. Ma, G. Meigs, P. Rudolf and F. Sette, Phys. Rev. B 42, 5381(1990).

(BL2B2)

Tentative Design of 18m Spherical Grating Monochromator at UVSOR

Hiroaki YOSHIDA and Koichiro MITSUKE

Department of Vacuum UV Photoscience, Institute for Molecular Science, Myodaiji, Okazaki 444

An 18m spherical grating monochromator (SGM) with high resolution and high photon flux has been designed at the bending-magnet beamline 2B2 of the UVSOR for the study of ionization satellites and multiply excited neutral states of molecules. A schematic layout of the monochromator is shown in Fig. 1. The optical system consists of two prefocussing mirrors, a spherical grating monochromator with a movable exit slit, and a refocussing mirror. The monochromator is designed to cover the energy range of 20–200 eV with three gratings: G1 (2400 lines/mm, R=18m) at 80–200 eV , G2 (1200 lines/mm, R=18m) at 40–100 eV, and G3 (2400 lines/mm, R=9.3m) at 20–50 eV. A wavelength scanning mechanism is very simple because movement of the gratings is confined only to mechanical rotation. The directions of incident and exit photon beams are fixed. A small including angle of 140° is adopted for G3 and two plane mirrors M2 and M3 coated with Al are located between G3 and the exit slit as optical filters, which might significantly reduce the high-order lights.

An SGM with a large radius of curvature is well known to have a resolving power of about 10000. However, it is difficult to achieve such a high resolving power because of a relatively large size of an electron beam (0.27 mm) and a moderate emittance (1.15×10^{-8} πmrad) of the UVSOR. We, therefore, plan to set a resolving power of 5000 in a standard operation. This performance requires the following conditions: a movable exit slit can be made to set at the focal distance of the dispersed light; the widths of entrance and exit slits are adjustable to decrease the aberration; and coma aberration at the exit slit can be reduced by shutting off a diverged light using an aperture. Fig. 2 shows image patterns at the exit slit obtained by ray tracing with photon wavelengths of (a) 60 and 60±0.012 Å for G1, (b) 180 and 180±0.036 Å for G2, and (c) 600 and 600±0.12 Å for G3. The exit slit is placed at the focal distances for the respective gratings. The widths of the exit slit corresponding to an expected resolving power of 5000 are also indicated with pairs of horizontal lines. In every case, the central wavelength is well resolved from two neighboring wavelengths. Hence, we conclude that this monochromator provides a resolving power of 5000 as far as other factors, such as a shape error of a grating, are ignored. The photon flux with this resolving power is evaluated to be about 5×10^{10} photons/s/100mA.

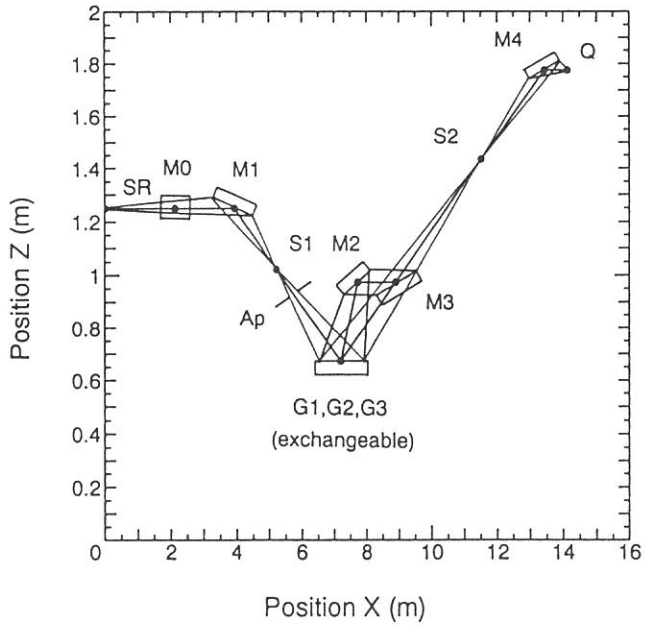

Fig. 1. Schematic layout of the monochromator. Horizontal and vertical axes denote the distance from the synchrotron radiation source and the height from the floor, respectively. Two optical paths with including angles of 160° for G1 and G2 and 140° for G3 are indicated. SR, synchrotron radiation source; M0, cylindrical mirror; M1, spherical mirror; S1, entrance slit; Ap, aperture; G1–G3, spherical gratings; M2 and M3, plane mirrors; S2, exit slit; M4, toroidal mirror; Q, sample position.

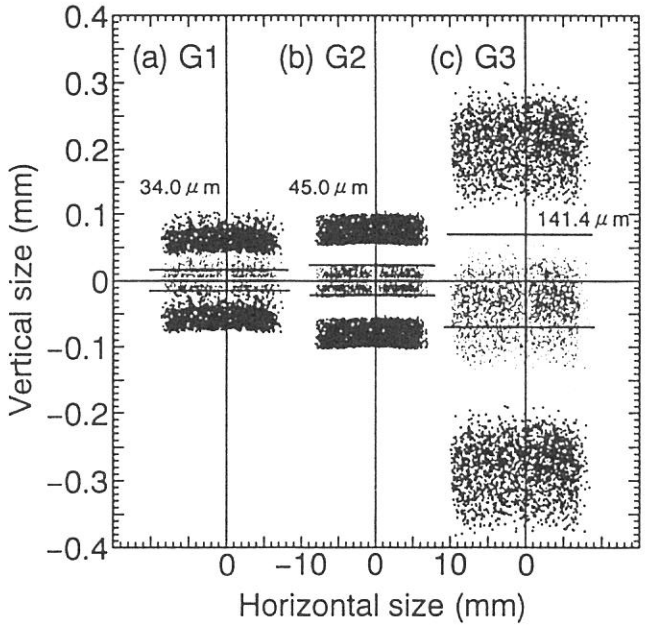

Fig. 2. Image patterns at the exit slit obtained by ray tracing with photon wavelengths of (a) 60 and 60±0.012 Å for G1, (b) 180 and 180±0.036 Å for G2, and (c) 600 and 600±0.12 Å for G3. Pairs of horizontal lines indicate the widths of the exit slit corresponding to a resolving power of 5000.

(BL3A1)

Recombination Luminescence in Lead Halide Crystals

Mamoru KITAURA and Hideyuki NAKAGAWA

Department of Electrical and Electronics Engineering, Fukui University, Fukui 910

The characteristics of the emission bands (UV, B, BG, R) in the $PbCl_2$ crystal were reported previously [1]. They are classified into two types; the one comprising the UV and the B emission originates from the Pb^{2+} cationic STE (self-trapped exciton), and the other (the BG emission) from the [$(Pb_2)^{3+}$ STEL (self-trapped electron) + hole] STE. The latter is just antimorphic one of the [V_k + e^-] STE's in alkali halides. It is somewhat doubtful, however, whether the BG emission arises from radiative annihilation of the [$(Pb_2)^{3+}$ STEL + hole] STE. More detailed informations on the recombination process giving rise to the BG emission are required in order to clarify the recombination processes. Investigation have been carried out on the decay profiles of the BG emission both in $PbCl_2$ and in $PbBr_2$.

The measurements were performed at the BL3A1 undulator beam line. Excitation was made with the VUV light around 36 eV from the undulator through an aluminum filter to remove the visible stray light. The photon energy of the excitation light corresponds to the absorption region far above the band gap energies. It is well known in $PbCl_2$ that the $(Pb_2)^{3+}$ STEL centers are created with some hole trapping centers by the photo-excitation in the energy region above the band gap [2]. In order to make clear the phosphorescent component of the BG emission, decay profiles of the BG emission were measured in the time region of 0.1~100 ms by using a mechanical chopper installed in front of the sample chamber. The PbX_2 (X = Cl, Br) crystals were cut into an appropriate size and mounted on a Cu holder of a contineously flowing liquid He flow type cryostat to cool down to 8 or 13 K.

Figure 1 shows emission spectra of (a) $PbCl_2$ and (b)$PbBr_2$ at 8 K. The BG emission bands are observed in both crystals as shown by the shaded bands in the spectra. While the peak positions of the BG bands are at 2.62 eV in both crystals, the width is somewhat narrower in $PbBr_2$ than in $PbCl_2$. It was comfirmed that the BG emission is also found in the photo-stimulated luminescence spectra, the afterglow spectra, of $PbCl_2$. It is the most likely that the recombunation of the $(Pb_2)^{3+}$ STEL center with the hole produces the BG emission in $PbCl_2$. The BG emission in $PbBr_2$ shows the analogous behavior to that of $PbCl_2$. Although the STEL center has not been found in $PbBr_2$ so far, the BG emission in $PbBr_2$ may also come from the same process as in $PbCl_2$.

Figure 2 shows decay profiles of the BG emission at 13 K in (a) $PbCl_2$ and (b) $PbBr_2$. Note that both the abscissa and the ordinate of the figures are of logarithmic scales. The decay profiles of the BG emission are well approximated by a power function of time t as drawn with the broken lines in the figures. The BG emission in $PbCl_2$ consists of a phosphorescent component having t^{-1} dependence. Such situation is quite similar to the case of tunneling recombination luminescence between a V_k and a Ag^0 center in Ag^+ doped alkali halide crystals [3]. This suggests that the phosphorescent component of the BG emission in $PbCl_2$ comes from the tunneling recombination between the $(Pb_2)^{3+}$ STEL center and the trapped hole. The origin of the BG emission in $PbBr_2$ is probably due to the same mechanism. In the μs range below 0.1ms, the decay curves deviated from the t^{-1} dependence.

On the lead halides, there are many open problems, *e.g.*, how the STEL center and the hole trapping center are created by a photo-excitation. This problem is directly related to photolysis of the lead halides.

[REFERENCES]

[1] M.Kitaura *et al.*, UVSOR Activity Report 1994 p32.
[2] S.V.Nistor, E.Goovaerts and D.Schomaker, Phys. Rev. B48 (1993) 9575.
[3] C.J.Delbecq, Y.Toyozawa and P.H.Yuster, Phys. Rev. B9 (1974) 4497.

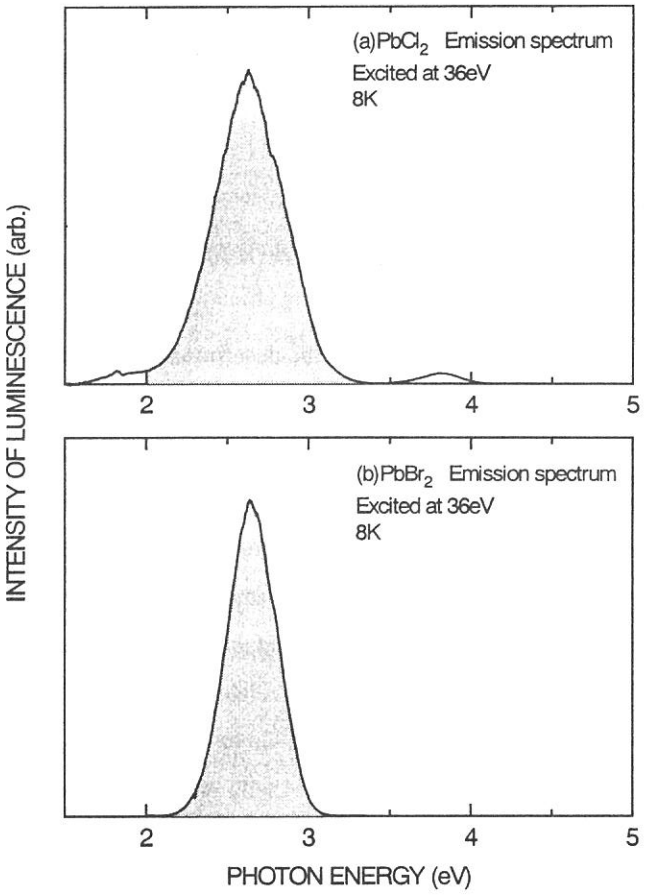

Figure 1. Emission spectra in (a) $PbCl_2$ and (b) $PbBr_2$ observed at 8K. The BG emission band is dominant in each spectrum and is shown by a shaded band. While the peak positions of the BG bands are at 2.62 eV, the width is somewhat smaller in $PbBr_2$ than in $PbCl_2$.

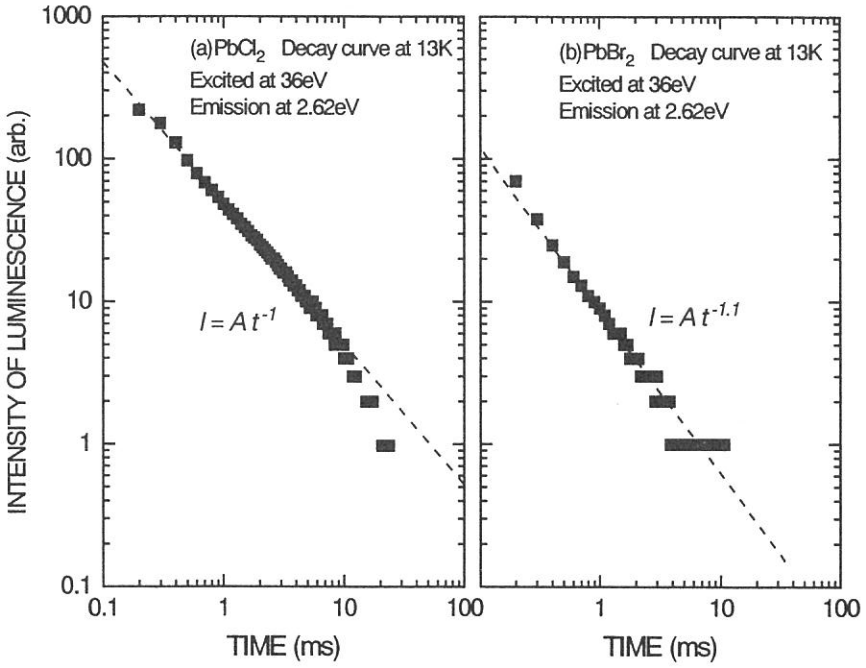

Figure 2. Decay profiles of the BG emission at 13 K in (a) $PbCl_2$ and (b) $PbBr_2$. Solid squres: the experimental values. Broken lines: the caluculated curves given by $I(t)=A\cdot t^n$, where A is a constant.

(BL3A1)

Photon-Stimulated Desorption of Ground-State K Atoms from K-Halides by using Laser-Induced Fluorescence

Sayumi HIROSE and Masao KAMADA

Institute for Molecular Science, Myodaiji, Okazaki 444

Bombardment of solids by energetic electrons and photons induces the desorption of ions and neutral atoms from the surface. Although there have been reported many desorption studies in alkali halides, the dynamics have not been investigated in detail yet. Recently, we have reported that the time response of excited-state alkali desorption consists of the fast component in the ns range and the slow component between 178 ns and 3 ms.[1,2] On the other hand, the time response of ground-state alkali desorption from alkali halides was reported to be in the scale of ms to μs by Kanzaki and Mori,[3] Loubriel *et al.*,[4] and Green *et al.*[5] about ten years ago. Kanzaki and Mori[3] observed the decay time and the temperature dependence of neutrals from alkali halides, and proposed that the desorption process of ground-state alkali atoms is related to the diffusion of V_K centers and the surface reaction of F centers and alkali ions. Loubriel *et al.*[4] and Green *et al.*[5] studied the time dependence of ground-state Li atoms from LiF, and explained the persistence of the Li emission in terms of the slow diffusion of bulk F centers. The purpose of the present works is to know whether the fast time response of ground-state alkali desorption exists or not.

The experiments were carried out with synchrotron radiation (SR) pulses under a single bunch operation at a undulator beam line 3A1. Intense quasimonochromatic undulator radiation of 36 eV was used as an excitation source. The interval of successive pulses was 178 ns and the time width of incident photon pulse including the detector system was about 480 ps. The desorption of ground-state alkali atoms was observed by means of laser-induced fluorescence (LIF). Figure 1 is a diagram of the apparatus used for the experiment. In the LIF experiment, a laser diode (LD) was used, the peak power and the pulse width of which were about 250 mW and about 29 ps, respectively. Ground-state (4s) K atoms desorbed from the surface were excited to the excited state (4p) with 7665 Å light from LD. The laser beam was well aligned to be parallel to the sample surface. The fluorescence was collected with a quartz lens and focused on the entrance slit of a Jobin-Yvon monochromator (HR-320). The fluorescence spectra were obtained by an image-intensified CCD detector. Synchronism of SR and LD was confirmed by observing time profiles of SR and LD with a time-correlated single photon counting method. Single

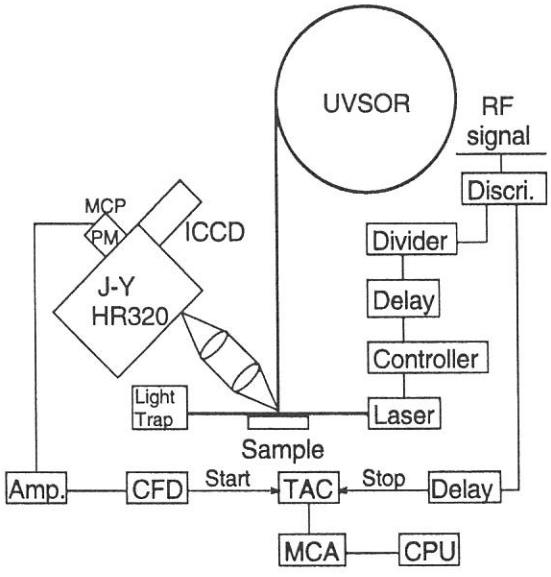

Fig. 1 A diagram of the apparatus used for a laser induced fluorescence method.

crystals of KCl and KBr were cleaved in air and heated up about 500 K. The base pressure in the sample chamber was about 5 x 10^{-7} Pa.

Figure 2 shows the time response of ground-state K desorption from KBr, which was excited with undulator radiation of 36 eV. This time response was obtained by changing the time interval between LD and SR. The origin of the delay time means that SR and LD are just synchronized. As seen in Fig. 2, the LIF intensity rises rapidly and then decays slowly. This indicates that the response time of ground-state alkali desorption has a fast component in the ns range. Moreover, the time response of ground-state alkali desorption has a slow component observed as background more than 178 ns. The slow desorption of ground-state alkali atoms may be explained with the existing model,[3,4] which is related to the diffusion of F or V_K centers and the surface reaction of F centers and alkali ions. However, the fast desorption of ground-state alkali atoms can not be interpreted with the above mechanism and requires a new desorption model. We suggest that the lattice instability due to the electronic excitation in the surface layers may play an important role on the fast desorption of ground-state alkali atoms.

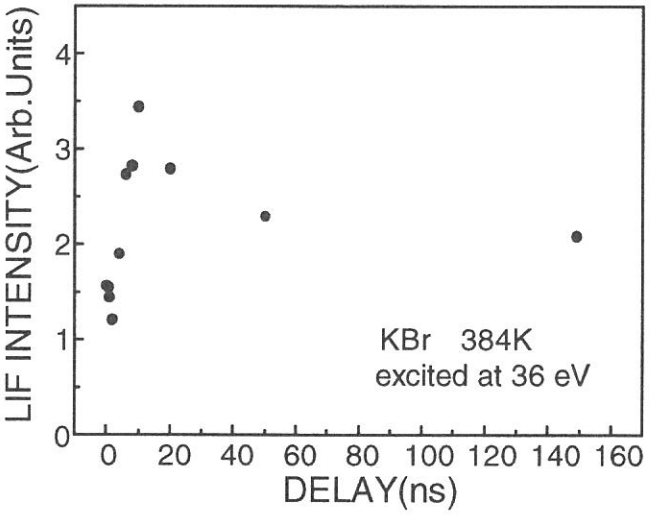

Fig. 2 The time response of ground-state K desorption from KBr excited with a undulator radiation of 36 eV.

References

1) S. Hirose and M. Kamada, J. Phys. Soc. Jpn. 63, 1053 (1994).

2) S. Hirose and M. Kamada, J. Phys. Soc. Jpn. 64, 4434 (1995).

3) H. Kanzaki and T. Mori, Phys. Rev. B 29, 3573 (1984).

4) G. M. Loubriel, T. A. Green, P. M. Richards, N. H. Tolk, R. H. Albridge, R. F. Haglund, K. J. Snowden, L. T. Hudson, D. W. Cherry, R. K. Cole, M. H. Mendenhall, D. M. Newns, and P. M. Savundaraj, Phys. Rev. Lett. 57, 1781 (1986).

5)T. A. Green, G. M. Loubriel, P. M. Richards, N. H. Tolk and R. F. Haglund, Jr., Phys. Rev. B 35, 781 (1987).

(BL-3A1)

Scanning Tunneling Microscope Observation of the Adsorption and Undulator Light-induced Effect of DEZn on MoS_2 (0001)

K.Maeda,O.Hosokawa,A.Ganjoo and A.Yoshida
Toyohashi University of Technology, Toyohashi 441

Studies for understanding the adsorption and the dissociation of metalorganic molecules on semiconductor surfaces give an important clue of the surface processes in the growth of compound semiconductor films by metalorganic chemical vapor deposition. Diethylzinc (DEZn) has been used as the Zn source gas for the deposition of Zn based II-VI compound semiconductor films , such as ZnO, ZnS and ZnSe by photo-excited CVD techniques. Scanning Tunneling Microscope (STM) is a direct method working in real space on an atomic scale to obtain information of the electronic states on the surface and the surface topography.

In the present work, we have studied the adsorption and Undulator Radiation (UR) light -induced effect of DEZn on MoS_2 with an in-situ UHV-STM. UR light was used as the light source due to its high energy and quasi monochromatic behavior.

The experimental set up consists of three chambers, and the block diagram is shown in Figure 1. MoS_2 (0001) was used as the substrate and was cleaved in air and introduced into the preparation chamber. The sample was transferred into the reaction chamber having a base pressure below 2×10^{-8} Torr and was exposed to several dozes of DEZn. After the exposure, the sample was transferred to the UHV-STM chamber and the surface states were observed. The sample was transferred back to the reaction chamber and was irradiated up to 50-500 mA•min of the UR light. After irradiation, the sample was again analyzed using UHV-STM to determine the photochemical change induced by the UR light.

The STM image of the initial MoS_2 (0001) surface on 100Å scale without any exposure to DEZn or UR light, obtained with a sample bias of -0.15V and a tunneling current of 1nA, is shown in figure 2 (a). The hexagonal lattice of the sulfur atoms of the top layer is clearly seen. Figure 2 (b) shows the STM topography of the surface exposed with 10000L of DEZn on 200Å scale. Atomic structure of the MoS_2 substrate and adsorbates on the surface are clearly seen. The circular adsorbates piling up on the surface are found to be DEZn adhering with weak van der Waals interaction. From figure 2(b), DEZn is found to adsorb coherently. The coverage of the substrate surface with the adsorbates was little because of the stability of MoS_2 surface. In fact, only a few percent of Zn signal could be detected by X-ray Photoelectron Spectroscopy (XPS), which was performed on the sample exposed to 10000L.

After the sample was exposed to 10000L , the STM images of the substrate surface on 200Å scale irradiated with 300 and 500 mA•min of UR light are shown in figure 2 (c) and 2 (d) , respectively. As can be seen from figure 2 (c) , the dark circular spots with an average diameter of about 50Å are observed, and some bright regions are clearly seen inside the dark spots at the irradiation of 300mA•min. Small bright spots with a diameter of 10Å seems to be the part of adsorbates shown in figure 2 (b),and have a horseshoe-like shape with a missing part of bright circle. Figure 2 (d) shows the image of the surface at the irradiation of 500mA•min ,

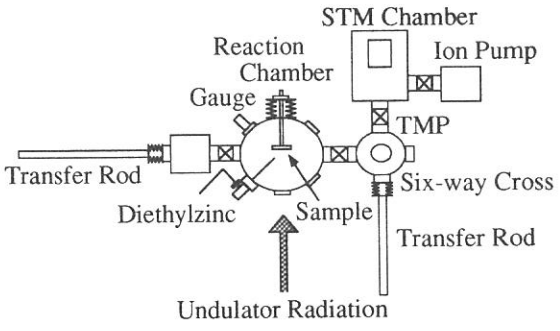

Fig.1 Block diagram of the experimental set up

and the number of the same pattern can be seen to increase over the irradiated area. At the same time, the dark area surrounding the bright spots becomes larger. Thus, in figure 2(d), the horseshoe-like patterns increase with the decomposition of the DEZn molecules, and the increase of the bright regions and the spread of the dark spots seem to arise due to the UR light.

From these images, it is considered that the DEZn molecules adsorbed coherently on MoS_2 are dispersed and decomposed by UR light and Zn atoms adsorb inside or near the bright pattern. When the Zn atoms adsorb on MoS_2, the electron transfer from Zn atoms to the substrate surface seems to be induced because of the low electronegativity of Zn. By this transfer, the area of adsorption and the area around the adsorption becomes positively and negatively charged, respectively. The pattern seems to result from the localization of positive and negative charge. Thus, the adsorption of the metal Zn atom seems to give effect on the occupied electronic states of the MoS_2 surface.

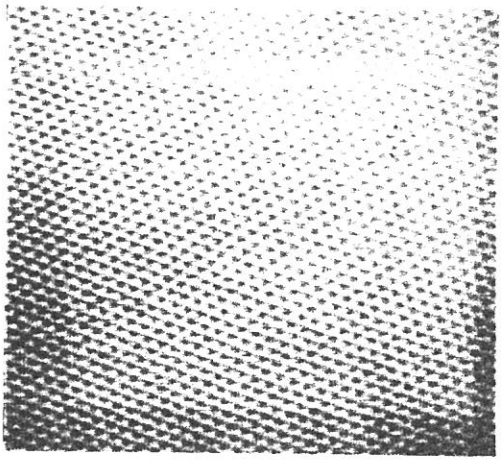

(a) MoS_2 clean surface

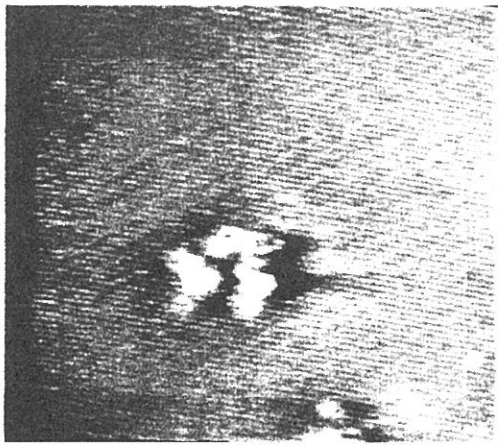

(b) MoS_2 surface exposed to 10000L DEZn

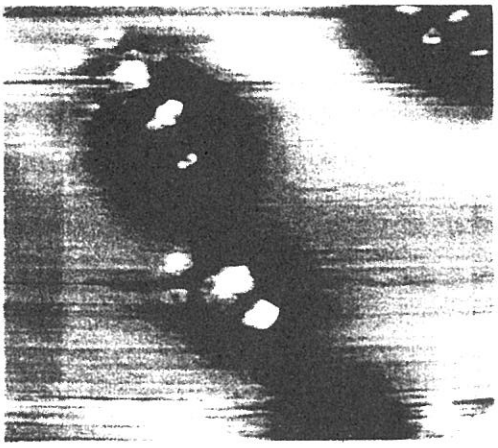

(c) MoS_2 surface irradiated for 300mA・min after 10000L DEZn exposure

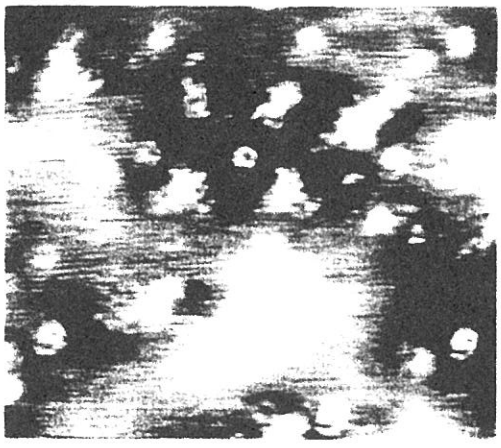

(d) MoS_2 surface irradiated for 500mA・min after 10000L DEZn exposure

Fig.2 STM images taken at the several conditions

(BL-3A1)

STM and XPS Analyses of Zn deposited surface using Undulator Radiation (UR)-excited CVD on MoS_2 and Si

K.Maeda,O.Hosokawa,A.Ganjoo and A.Yoshida
Toyohashi University of Technology, Toyohashi 441

Recently, an interest in the photochemistory of metal-bearing organic molecules has increased, as these compounds are suitable materials for metal photodeposition using UV region light. Zn deposition is useful for several applications such as doping it to ZnO and Zn-containing binary semiconductor compound growth. We have already prepared ZnO thin films by photo-excited CVD using organic molecules and pure oxygen at room temperature.

Diethylzinc (DEZn) has been used as the source gas for Zn-containing II - VI compound semiconductor films grown by MOCVD , and it was chosen as the precursor compound for zinc film photodeposition in the present work. Undulator Radiation (UR) light was used as the light source due to its high energy and we have studied the initial stage of Zn deposited surface using photo-excited CVD by in-situ Scanning Tunneling Microscope (STM) and X-ray photo-electron Spectroscopy (XPS).

MoS_2 was used as the substrate , and it was cleaved in air and was introduced into the preparation chamber. On the other hand, Si substrate was introduced into the preparation chamber after HF treatment. After that, it was cleaned using Ar ion sputter for 30 min. The sample was transferred into the reaction chamber , having a base pressure below 2×10^{-8} Torr. Zn thin films were deposited at the DEZn pressure of 1×10^{-5} Torr and varying the growth time from 500 to 15000 mA • min. After deposition , the changes at different deposition times of Zn on the substrate surface were analyzed with UHV-STM . XPS measurement was also done to determine compositional and chemical states. All experiments were performed at room temperature.

Figure 1 (a) shows the STM image of the MoS_2 clean surface on 500 Å scale at the sample bias of -0.15V and tunneling current of 1nA . No adsorbates were found, and a flat surface was observed.

The STM image of the MoS_2 surface with deposition for 500mA • min and 5000mA • min are shown in figure1 (b) and (c), respectively. These STM images were taken on the same condition as that of the clean surface. From Figure 1 (b), small but a lot of protuberance, with an average diameter of 25Å, can be seen over the entire irradiated area.

After further irradiation, more Zn is deposited and the size of the protuberances

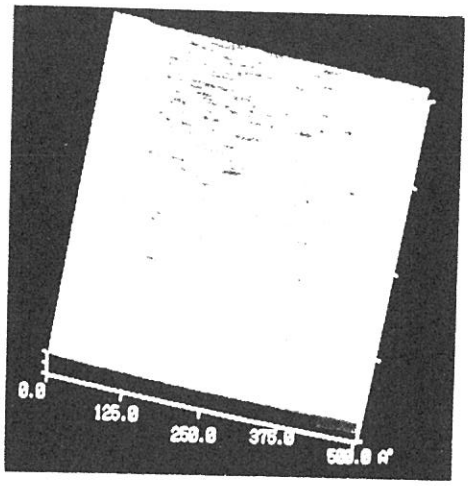

Fig.1 (a) STM image of the MoS_2 clean surface

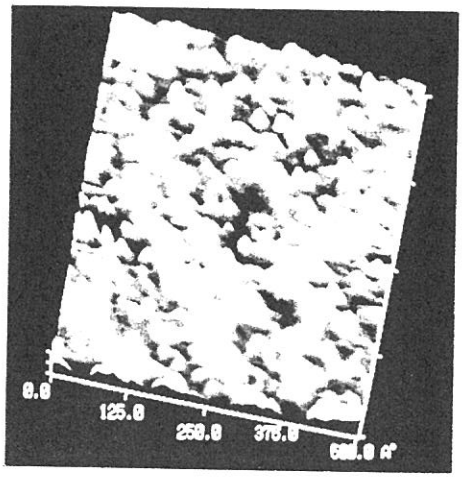

Fig.1 (b) STM image of the MoS_2 surface with depositon for 500mA • min

get increased. With the increase in size, the protuberances close to each other get combined resulting in further increase in size can be seen from figure 1 (c).

Figure 2 (a) shows the Zn $2p_{3/2}$ XPS spectra taken for 10000L adsorbed DEZn (a) at room temperature . This peak arises mainly from the molecular DEZn , because DEZn seems to get adsorbed physically by van der Waals interaction on MoS_2 due to the stability of the layered material surface. Zn $2p_{3/2}$ peaks of the surface deposited with 1000 mA•min and 5000mA•min are shown in figure 2 (b) and (c) , respectively. Deposition by UR light results in the chemical shift of Zn $2p_{3/2}$ peak to the lower energy side. The intensity of the peak gets larger as the growth time increases. Thus, it is considered that the DEZn dissociates by UR light absorption and Zn films are deposited.

Figures 3 and 4 show the change in the ratio of each signals observed in the XPS measurements as a function of the deposition time on MoS_2 and Si , respectively. The deposited films on MoS_2 and Si show the same behavior, and the signals from the substrate decreases as the deposition time increases, while Zn and C signals increase. It is considered that the carbon contamination results from the decomposition of DEZn (the breaking of Zn-C and ethyl radicals) by high photon energy of UR light.

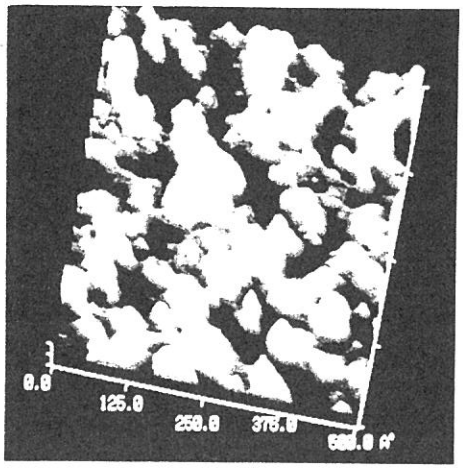

Fig.1 (c) STM image of the MoS_2 surface with deposition for 5000mA•min

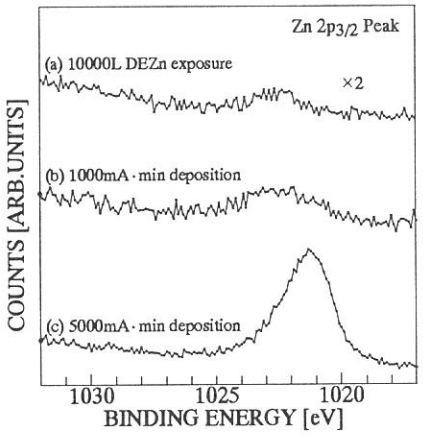

Fig. 2 Zn $2p_{3/2}$ XPS spectra of DEZn exposure and Zn deposition surface

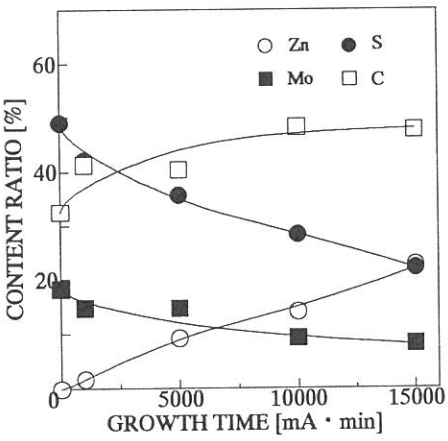

Fig.3 Content ratio of the films deposited on MoS_2

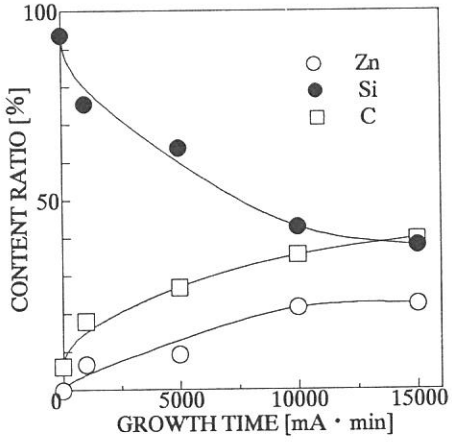

Fig.4 Content ratio of the films deposited on Si

(BL 3A1)

Effect of Undulator Radiation irradiation on the thin films of a-Si:H

Ashtosh Ganjoo, K. Maeda, O. Hosokawa and A. Yoshida
Department of Electronics Engineering,
Toyohashi University of Technology,
Toyohashi - 441.

Hydrogenated amorphous Silicon (a-Si:H) is one of the promising materials for solar cell applications and thin film transistors (TFTs) due to its lower fabrication cost. The incorporation of hydrogen in the films during deposition is considered to play an important role in deciding various properties of a-Si:H. Thus, a lot of attention is required to study the behavior of hydrogen in order to have a deep understanding of various properties of a-Si:H. Keeping this in mind, we have studied the effect of Undulator Radiation (UR) on the thin films of a-Si:H. We have exposed a-Si:H thin films to various doses of UR light and estimated the changes in hydrogen content and the optical band gap of the films.

Thin films of a-Si:H were prepared by windowless photo CVD technique onto Si and Corning 7059 glass substrates [1]. The films were prepared with Si_2H_6 (di-silane) as the source gas and hydrogen (H_2) as the discharge gas. The substrate temperature was 250℃ and the pressure 1.3 Torr during the deposition. The growth temperature of 250℃ was chosen because of the fact that high quality amorphous films can be obtained at this temperature [1]. The hydrogen content in the films was estimated from the FTIR studies. The optical band gap of the films was estimated from the UV-VIS-NIR spectra. The films grown on glass and Si substrates were exposed to various doses of UR radiation at the beam line 3A1 of UVSOR facility at IMS, Okazaki. The films were exposed to 3, 25, 30, 65 A.min. of UR radiation at room temperature in a vacuum chamber. The chamber was maintained at a pressure of ~10^{-8} Torr during irradiation. After each exposure, the FTIR and UV data were again taken to observe the changes in hydrogen content and the optical band gap induced by the UR irradiation.

Figure 1 shows the variation of hydrogen content in the films as a function of UR irradiation dosage. From the figure, it can be seen that for low dosages of UR light, a slight decrease from the initial hydrogen content is observed. However, with increasing the UR dosage, the hydrogen content in the films is observed to change considerably. Figure 2 shows the variation of optical band gap (E_g^{opt}) on the UR dosage. For higher UR dosages the band gap is found to decrease considerably showing a similar behavior as the change of hydrogen content in the films. This can be attributed to the fact that the high energy photons of UR break the Si-H bonds in the a-Si:H films and hydrogen becomes free. After breaking the Si-H bonds, H moves out or hops between the nearest dangling bond sites. After further irradiation, this newly filled dangling bond also breaks and thus H moves away. This may be the reason for having a slow decrease of

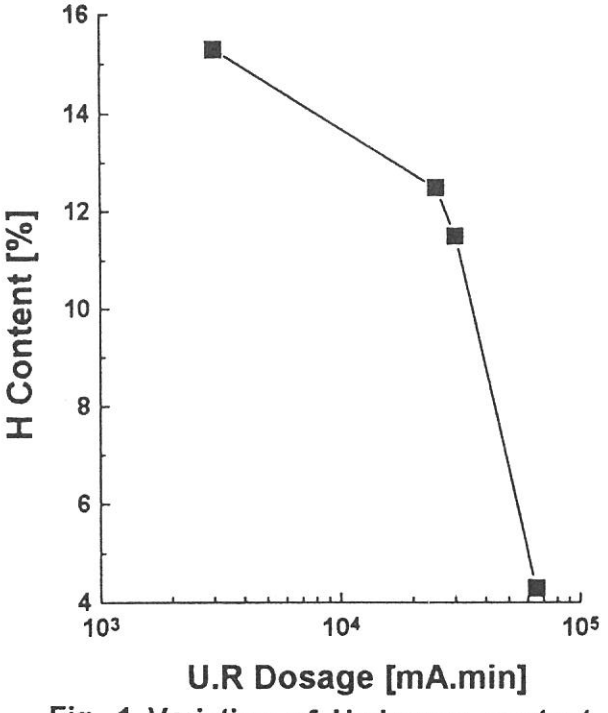

Fig. 1 Variation of Hydrogen content with UR dosage in a-Si:H films

H content at low irradiation dosages as only the H at and near the surface is removed. As the UR dosage is increased, the depth of the bond breaking increases and more hydrogen breaks free to move. Also, as a result of the hydrogen becoming free, Si atoms gets restructured. Diffusion of hydrogen is thought to proceed via restoration of Si-Si bonds and hydrogenation of other bonds till the hydrogen reaches the film surface and gets evolved

The decrease of the band gap is consistent with the decrease of hydrogen content in the films. The valence band spectra for a-Si:H is found to show states identified as hydrogen 1s/silicon 3p-3s bonding orbitals which are sensitive to the bonding configuration of hydrogen [2]. Due to the breaking of the Si-H bonds in a-Si:H films by UR radiation, hydrogen comes out of the films, and as a result, a decrease in the hydrogen 1s/silicon 3p-3s bonding orbitals occurs. This causes a redistribution of states at the band edges resulting in the recession of the valence and conduction band edges. This recession of valence and conduction band edges leads to a decrease in the optical band gap of the films.

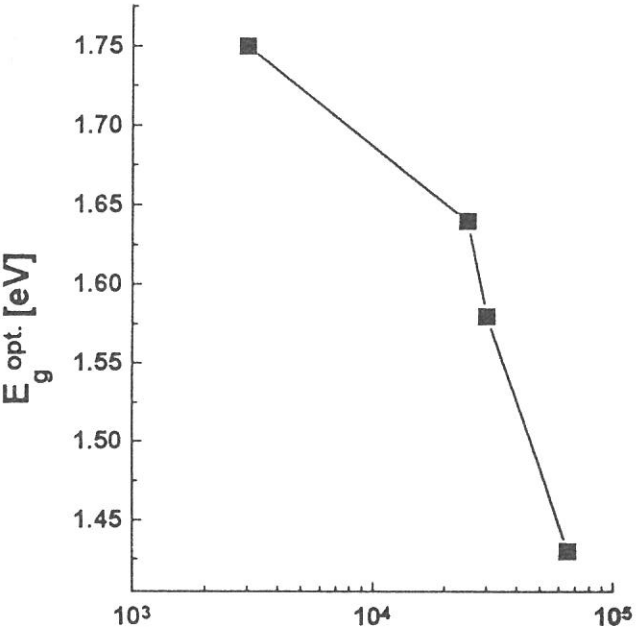

Fig. 2 Variation of optical band gap with UR dosage in a-Si:H films

[1]. A. Yoshida, K. Inoue, H. Ohashi and Y. Saito, Appl. Phys. Lett., **57**, (1990), 484.
[2]. B. von Rodern, L. Ley, M. Cardona and F. W. Smith, Phil. Mag. B, **40**, (1979), 433.

(BL3A1)

Synchrotron Radiation Excited Etching of Diamond

Haruhiko Ohashi , Eiji Ishiguro[2)], Tomohiko Sasano[3)], Takahiro Oguri [4)] and Kosuke Shobatake [1) 4)]

[1)] Institute for Molecular Science, Myodaiji, Okazaki 444, Japan

[2)] College of Education, University of the Ryukyus, Nishihara, Okinawa , 903-01, Japan

[3)] Department of Applied Physics, Osaka City University, Sumiyoshi-ku, Osaka 558, Japan

[4)] School of Engineering, Nagoya University, Chikusa-ku, Nagoya 464-01, Japan,

Since diamond is the hardest material and a good heat conductor, it is expected to become one of the best functional materials. For example it has been used for machining bits since early times. Recently it has been found that diamond thin films can be grown by chemical vapor deposition (CVD) at low gaseous pressures[1-3] and thus a possibility of controlling band gaps in diamond films formed has been realized and the prospect of using diamond as a semiconductor material has increased[4]. Further since diamond is a good thermal conductor, the prospect of using it as an optical material for the third generation high intensity synchrotron radiation (SR) sources is also increasing. One drawback of using diamond however is its high resistance to chemical reactions under mild conditions and thus it is difficult to fabricate its surface to use it as electronics devices and micromachines. Photo-excited etching is a useful technique for microfabrication of materials with high chemical resistance, because its chemical reactivity is so low there exist few practical mask materials which exhibit lower reactivity than diamond.

We report that chemically inert diamond surface can be successfully etched by irradiating synchrotron light in an etchant gas atmosphere even at low temperature (- 140℃). It is demonstrated that only the excited area by SR can be etched.

Irradiation experiments have been carried out using a sample holder schematically shown in Figure 1. The focused SR was shone upon a diamond surface in an etchant gas atmosphere. The undispersed SR was focused on a sample in a reaction chamber using a Pt-coated toroidal mirror. The spot size of SR on the sample was about 2 mm×4 mm. A Ni mesh of 60 lines / inches and 90 % transmittance which is used as a mask was placed 5 mm above the sample surface to see how the pattern is transcribed to the diamond surface. The synchrotron light is irradiated perpendicularly to the surface. Three types of commercially available crystalline diamond were used as specimen; they are industrial diamond made at high pressures, polished thin films grown by chemical vapor deposition (CVD), and natural diamond. Highly oriented graphite sheet purchased from Union Carbide Corp. was also used as a specimen to compare its reactivity with those of diamond samples.

The cross-sectional profile of the etched surface is shown in Figure 2. The pressure of O_2 etchant gas was kept at 0.1 Torr and the substrate temperature of the specimen was - 140℃. It is noted that the roughness of the masked area did not change even after SR excited etching. The shadow area due to 40 μ m wide Ni wires is not etched but the irradiated area is etched, though a mask was placed 5 mm away from the surface of the specimen. The depth of the etched area for the light dose of 50 A•min was measured as 0.8 μ m and the etch rate is estimated to be 16Å/min/100mA from which the quantum yield defined as the number of carbon atoms removed per total number of irradiated photons was estimated to be about 0.2%. It is noted that under the same experimental conditions graphite was hardly or not at all etched.

When the oxygen gas pressure was reduced from 0.1 to 0.01 Torr, the etch rate was decreased to about 1/4, which indicates that the supply of oxygen gas is important for the etching reaction. Vacuum ultraviolet light photodissociates O_2 molecules forming reactive radicals such as O atoms and/or O^+ ions. If thermal reactions by reactive radicals or ions are dominant in etching reactions, a clear distinction in the etch rates between the irradiated and unirradiated areas, as are seen in Fig.2, would *not* have been observed for the following reasons: the unirradiated area would have been also etched by the radicals formed in the irradiated space, since the mean-free-path at an etchant gas pressure of 0.1 Torr is estimated to be about 500 μ m, which is much longer than the width of the mesh wires. Therefore the observed depth profiles suggest that the photo-excitation of the surface

atoms is essential in promoting the etching reaction of the diamond surfaces.

The present success in SR-excited etching of all the three diamond samples used indicates that the reaction proceeds not only for the surfaces of thin films composed of microcrystallites, but also for the surfaces of single crystalline samples, although the former tends to be etched more readily than the latter.

The SR etched surface of CVD diamond becomes darker and sooty. In the case of crystalline diamond grown by high-pressure synthesis, however, no soot or very little soot, if any, was observed on the surface. It is noted that etch pits are observed in some areas for crystalline diamond probably because some types of defects within a crystal are pronounced by etching the surface. This may be due to strong surface orientation dependence of the etch rate. On the other hand in the case of natural diamond soot was not at all observed, though the number of specimens etched is few. The details of these results will be reported in a forthcoming publication.

By varying the temperature of the diamond surface we find that SR-excited etching reaction proceeds even when the surface temperature is lowered, that is the etch rate hardly varies as the surface temperature is lowered from 20 to - 140℃. If the thermal reaction of O radicals with the surface atoms of diamond is dominant, the etch rate would increase as the surface temperature is raised and thus the thermal reaction will definitely cease at -140℃, since O radicals don't etch the diamond surface. Therefore it would be reasonable to conclude that surface excitation by SR promotes the etching reaction and this step determines the etching reaction rate.

It would be worthy to note that graphite was hardly etched under the same experimental condition as diamond is etched. The insulator materials seem to react more readily than conductive materials when SR is shone on the surface in an etchant gas atmosphere. This trend is similar to that observed in SR-excited etching of Si and SiO_2. The lifetimes of the excited surface sites of the insulators such as SiO_2 and diamond are believed to be longer than those of the conductors such as doped Si or graphite. However which surface species are excited, how excitation by SR promotes the etching reaction, if direct excitation of surface adsorbed species is important, and if photoelectron stimulated surface excitation plays some role in the diamond etching are still unanswered questions. Photostimulated desorption (PSD) of adsorbed species can also occur, in which case however it seems to be natural to consider that inner core photoexcitation of surface carbon atoms is essential, because a surface carbon atom is strongly bound to the C atoms on the subsurface layer of the diamond lattice. In order to clarify the mechanism of the present etching reaction further experiments to obtain the wavelength dependence are planned.

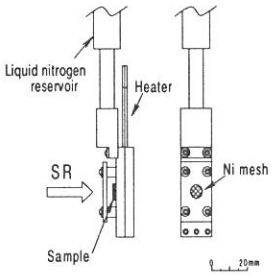

Figure 1 The schematics of the sample holder

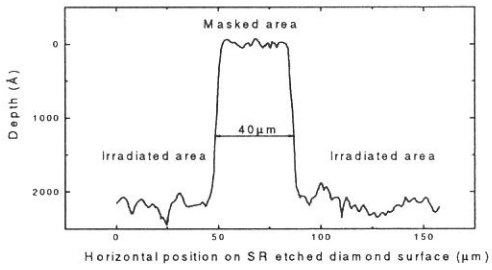

Figure 2 Cross-sectional profile of the etched CVD diamond surface

1 J. C. Angus, H. A. Will and W. S. Stanko, J. Appl. Phys. 39, 2915(1968).
2 D. J. Poferl, N. C. Gardner and J. C. Angus, J. Appl. Phys. 44, 1418(1973).
3 S. Matsumoto, Y. Sato, M. Kamo and N. Setaka, Jpn. J. Appl. Phys. 21, L183(1982).
4 H. Shiomi, Y. Nishibayashi and N. Fujimori, Jpn. J. Appl. Phys. 8, L2153 (1989).

(BL3A1)

Effect of Undulator Irradiation on Pure and Ge-Doped Silica Glasses

Hiroyuki NISHIKAWA

Department of Electrical Engineering, Tokyo Metropolitan University, Tokyo 192-03

Optically-induced phenomena in glass, such as photosensitivity [1] and second harmonic generation [2] in Ge-doped silica fibers, have received much attention because of its possible technological applications, such as fiber gratings and wavelength conversion devices. From the view point of materials research, it is important to understand the mechanism involved in these optically-induced phenomena and to prepare materials desirable for the processing using photons, for example, those having high photosensitivity to processing light and stability in various environments. In this study, the effects of undulator irradiation on pure and Ge-doped silica glasses were investigated by means of photoluminescence (PL) and electron-spin-resonance (ESR) studies.

Samples used in the present experiments were high-purity silica ([OH]<1 ppm) and [OH]: 420 ppm) and Ge-doped silica prepared by the plasma CVD and the soot remelting methods, respectively. Undulator light irradiation was performed at BL3A1 line of the UVSOR facility. Samples were exposed to an intense quasi-monochromatic radiation (~36 eV photons) from the undulator (operating undulator gap: 60 mm) through a pin hole with a diameter of 1 mm and an Al filter. During irradiation, samples were under vacuum of ~10^{-8} Torr. The value of the photon flux is typically 10^{14}-10^{15} s^{-1} mm^{-2}. The PL observed under the undulator irradiation was detected by a photomultiplier (PM, Hamamatsu R955) through either a monochromator (Jobin Yvon HR-320) or optical filters (Toshiba Glass, KL and UV series). Taking into account the decay of the undulator radiation during the PL measurements, the PM output current was normalized by the beam current of the storage ring. The ESR measurements were carried out at room temperature using a spectrometer operating at X-band frequency.

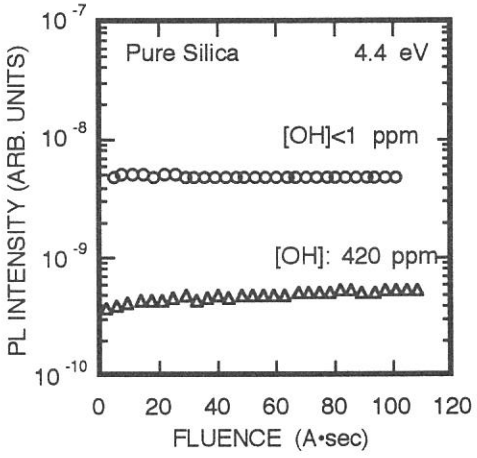

FIG. 1 Changes in the PL intensity at 4.4 eV obtained at room temperature for two types of pure silica samples. The curves are arbitrarily shifted along y-axis for viewing purposes.

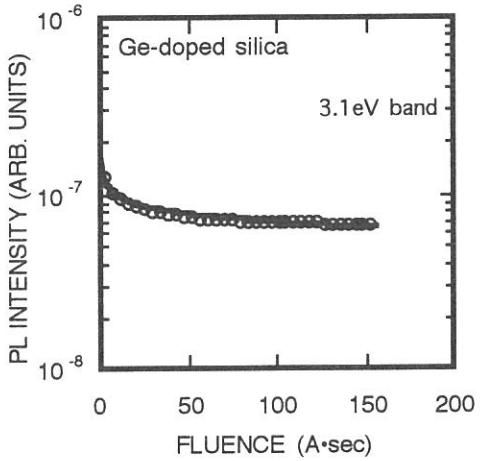

FIG. 2 The changes in the PL intensity at 3.1 eV obtained at room temperature for the Ge-doped silica during undulator irradiation at 36 eV.

Figure 1 show the PL intensity at 4.4 eV observed under exposure to 36 eV photons from the undulator for two types of pure silica samples. Here, the unit of the fluence is represented by the beam current in ampere multiplied by the exposure time in second, "A·sec", which is assumed to be proportional to the incident photon flux to the sample. While the intensity of 4.4 eV band observed for low-OH sample ([OH]<1 ppm) exhibits almost no change, that for the high-OH sample ([OH]: 420 ppm) gradually increases with a single rate constant, which is indicated by the straight line. The curve for the high-OH sample can be fitted to simple exponential

function $I_{PL}(F) = I_{PL}(0) \exp(\alpha F)$, where F is the fluence in unit of A·sec, and the constants $I_{PL}(0)=4.2 \times 10^{-10}$ and $\alpha = 2.4 \times 10^{-3}$ $(A \cdot sec)^{-1}$. Figure 2 shows the PL intensity at 3.1 eV measured for the Ge-doped silica during exposure to 36 eV photons from the undulator. Contrary to the results of pure silica, the 3.1 eV band decays during exposure to undulator radiation. The decay curve cannot be fitted to a single exponential function, and rather be described by a so-called stretched exponential function, $I_{PL}(F) = I_{PL}(0) \exp(-\alpha F^{\beta})$, where $I_{PL}(0) = 3.2 \times 10^{-6}$, $\alpha = 3.2$ $(A \cdot sec)^{-\beta}$, and $\beta = 0.042$. Shown in Fig. 3 are the results of ESR measurements after the exposure of Ge-doped silica to 36 eV photons up to a fluence of 150 A·sec. The ESR signal characterized by g=values of 2.0019 and 1.9957 can be ascribed to the Ge E' centers [3]. Since the undulator radiation is linearly polarized, the sample was rotated to see difference between two cases: $\boldsymbol{E} \parallel \boldsymbol{H}$ and $\boldsymbol{E} \perp \boldsymbol{H}$, where $\boldsymbol{E}$ is the electric vector of incident light and $\boldsymbol{H}$ is the applied magnetic field during ESR measurements. As shown in the Fig. 3, no distinctive difference can be found between the two cases.

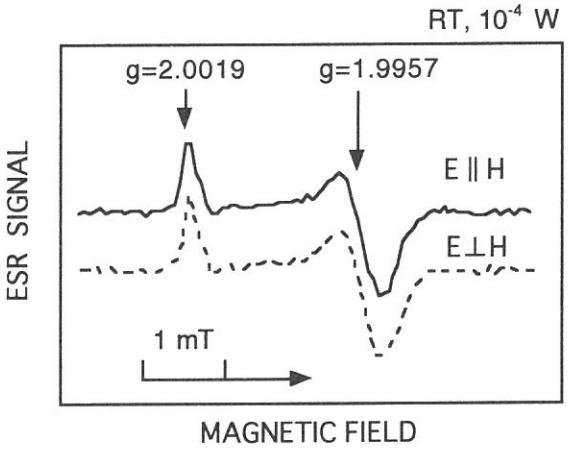

FIG. 3. The X-band ESR spectra obtained at room temperature for the Ge-doped silica exposed to undulator radiation.

On the basis of the electronic structures of SiO_2 reported in the literature [4], excitation of an electron in O_{2s} core states to the conduction bands is expected. The penetration depth is given by $\alpha^{-1}=(4\pi k/\lambda)^{-1}$, where α, k, and λ are absorption coefficient, extinction coefficient, and wavelength, respectively. From the value of k $\sim$ 0.107 at 36 eV [5], most photon energies are absorbed at the surface layer with a thickness of $\sim$25 nm. From the results of ESR, the areal density is 6.1×10^{16} cm^{-2}. Therefore, the concentration of defects in the surface layer is estimated to be about 2.4×10^{20} cm^{-3}. In the case of pure silica, the high-OH sample, which is known to be photosensitive [6], shows an increase of the 4.4 eV PL during irradiation, while the low-OH sample exhibits no change. Since the 4.4 eV band is associated with oxygen vacancy [7], this can be explained in terms of the formation of the oxygen vacancies involving the dissociation of Si-H bonds [6]. Contrary to the case of the pure silica samples, the decay of the 3.1 eV PL was observed for the Ge-doped silica during undulator irradiation. The curve can be fitted to a stretched exponential function. This suggests that the photochemical reaction involved in the bleaching of the 3.1 eV PL is not determined by the single rate constant, but by multiple rate constants which might vary from site to site in the glass [8].

The fact that no difference was observed in the ESR spectrum between the cases of $\boldsymbol{E} \parallel \boldsymbol{H}$ and $\boldsymbol{E} \perp \boldsymbol{H}$, gives some information on the generation mechanism of paramagnetic centers. The present result suggests that the formation mechanism involves trapping of electron or hole resulting from cross band gap excitation by 36 eV photons, since the trapping process should not depend on the polarization of the excitation light [9].

References

[1] K.O. Hill, Y. Fujii, D.C. Johnson, and B.S. Kawasaki, Appl. Phys. Lett. **32**, 647 (1978).
[2] U.L. Osterberg and W. Margulis, Opt. Lett. **11**, 516 (1986).
[3] Y. Watanabe, H. Kawazoe, K. Shibuya, and K. Muta, Jpn. J. Appl. Phys. **25**, 425 (1986).
[6] H. Nishikawa, E. Watanabe, D. Ito, and Y. Ohki, J. Non-Cryst. Solids, **179**, 179 (1994).
[4] D.L. Griscom, J. Non-Cryst. Solids **24**, 155 (1977).
[5] H.R. Philipp, in *Handbook of Optical Constants of Solids*, edited by E.D. Palik (Academic Press, 1985), p. 757.
[7] H. Nishikawa, E. Watanabe, D. Ito, and Y. Ohki, Phys. Rev. Lett. **75**, 2101 (1994).
[8] M. Poirier, S. Thibault, J. Lauson, and F. Ouellette, Opt. Lett. **18**, 870 (1993).
[9] J.H. Stathis, Phys. Rev. Lett. **58**, 1448 (1987).

(BL3A1)

Photodarkening Phenomena in Amorphous Chalcogenide Films

Koji HAYASHI, Atsushi HIRAI*, and Koich SHIMAKAWA*

Center for Cooperative Research, Gifu University, Gifu 501-11
**Department of Electronics and Computer Engineering, Gifu University, Gifu 501-11*

Amorphous chalcogenide semiconductors, such as amorphous As_2S_3, As_2Se_3 etc., show a variety of photoinduced effects. The most prominent photoinduced effects in these materials is so-called photodarkening (PD) arising from the shift of the absorption edge. The absorption shifts in almost parallel way toward lower energies under irradiation of light with the energy corresponding to the optical bandgap. This darkened state is removed by annealing at the glass-transition temperature. The x-ray diffraction and the volume change of the films before and after the irradiation suggest that the photodarkening is attributed to the change of the local structure of amorphous network. Many researchers have reported the reversible photodarkening induced by irradiation of bandgap light[1-3]. To our knowledge, however, there are a few reports on the photoinduced effects of amorphous semiconductors excited by irradiation of higher energy photon. Details of the PD mechanism are still unknown. To obtain a wide knowledge of the photoinduced effects, it is necessary to investigate photoinduced effects on wide energy range. In the previous report, we reported the photoinduced effects in amorphous chalcogenide films (a-AS_2S_3) by the VUV light. That is,

(1)Photodrakening is occurred by the irradiation of the VUV light.
(2)The darkened state is removed by annealing at the glass-transition temperature.
(3)The rate of change in the photodarkening in the VUV light is extraordinarily higher than that in the bandgap light under the same photon number.

In this report, we study the dependence of the irradiated photon energy in the photodarkening around the inner core level of As atom.

Samples (a-As_2S_3) were prepared onto quartz substrates by conventional evaporation technique. After evaporation, samples were annealed at the glass-transition temperature for two hours in a vacuum of 1×10^{-6} Torr. The experiments were performed at a BL3A1 beam line of the UVSOR facility of the Institute for Molecular Science in Okazaki. Samples were irradiated with VUV light that is filtered through an Al film and the energy has been changed in the range between 36 and 46 eV. The photon energy of undulator radiation is selected from 36 to 46 eV moving gap of the periodic permanent magnets. To eliminate visible lights of synchrotron radiation and higher harmonics of undulator radiation, aluminum film was inserted between undulator and samples. The samples were fixed in sample chamber which were evacuated below 10^{-8} Torr. The photon flux of undulator radiation through aluminum film was estimated from the total photoelectric yield of gold mesh. After irradiation, the samples were taken out and the optical absorption was measured with a conventional UV spectrometer.

Figure 1 shows energy shifts (ΔE) in the optical bandgap as a function of the excited energy of the photon. As shown in the figure, the magnitude of PD depends on the photon energy. According to the measurement of the VUV reflection spectra[6], there is a peak around 44 eV corresponding to the 3d core level of As atom. In the figure, the rate of change for around 44eV irradiation is slightly higher than that for other irradiation. However, the penetration depth of VUV light is not considered in the energy shifts. Further experiments should be carried out to confirm the dependence of the excited energy in PD.

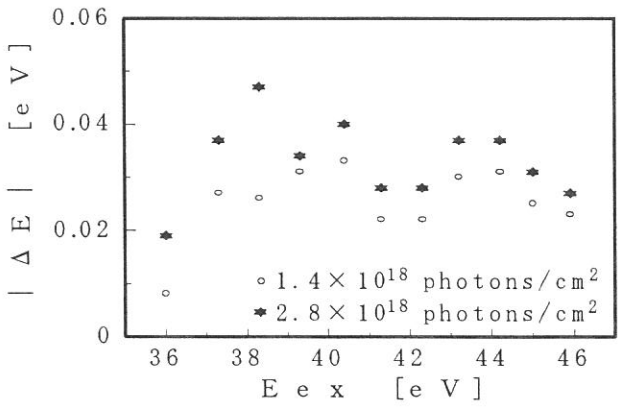

Fig.1 Energy shifts (ΔE) in the optical bandgap as a function of the excited energy of the photon.

REFERENCES

[1] Ke. Tanaka, Rev. Solid State Sci., 4(1990)641.
[2] S.R. Elliott, J. Non-Crst. Solids, 81(1986)71.
[3] A.V. Kolobov et al., J. Non-Cryst. Solids, 45(1981)335.
[4] K. Hayashi et al., UVSOR Activity Report (1993)173.
[5] K. Hayashi et al., UVSOR Activity Report (1994)82.
[6] K. Hayashi et al., UVSOR Activity Report (1994)128.

(BL3A2)

Dissociation ratios of singly charged molecular ions from 30 to 100 eV

Toshio MASUOKA

Department of Applied Physics, Faculty of Engineering
Osaka City University, Sugimoto 3, Sumiyoshi-ku, Osaka 558

At the excitation energies where molecular and dissociative single and double photoionization take place, we have studied the partial cross sections for the two processes and the respective ion branching ratios of singly and doubly charged precursors. That is, the ion branching ratios for the precursor m^+ were determined separately from those for m^{2+}. This enabled us to obtain the dissociation ratios of m^+ and m^{2+}. The dissociation ratios of m^{2+} are usually higher than 0.9 at higher excitation energies because of Coulomb repulsion between two positive charges. Then, what about m^+!

The results are shown in Fig. 1 for carbon monoxide, nitric oxide, carbon dioxide, carbonyl sulfide, and nitrogen dioxide. It is very interesting to note that the results split into two groups, high dissociation ratios[1] for OCS and NO_2 and low dissociation ratios[2] for CO, NO, and CO_2. Why are they so ? This is an open question at present and I would like to welcome any suggestion, comments, or discussion on this subject.

References

1) T. Masuoka and H. Doi, Phys. Rev. A **47**, 278 (1993) and unpublished data.
2) T. Masuoka , Phys. Rev. A **48**, 1955 (1993), *ibid.* **50**, 3886 (1994), and T. Masuoka and E. Nakamura, *ibid.* **48**, 4379 (1993).

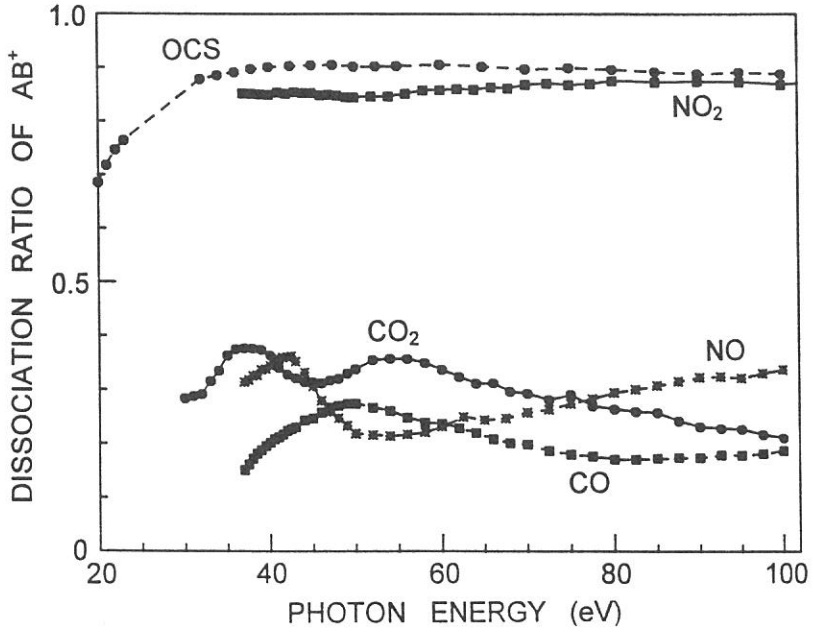

Fig. 1. Dissociation ratios of the singly charged molecular ions at the excitation energies where molecular and dissociative single and double photoionization take place.

(BL3A2)

Dissociative photoionization of SO_2 from 16 to 120 eV

Toshio MASUOKA

Department of Applied Physics, Faculty of Engineering
Osaka City University, Sugimoto 3, Sumiyoshi-ku, Osaka 558

Using synchrotron radiation as a continuum light source, dissociative photoionization of SO_2 has been studied in the photon-energy region of 16-120 eV. The data[1] in the 16-35 eV region were measured in Wisconsin and those above 37 eV at UVSOR, Okazaki. Ion branching ratios were obtained by analyzing time-of-flight (TOF) mass spectra and were converted to the absolute cross sections for the production of SO_2^+, SO^+, $S^+(O_2^+)$, O^+, and SO^{2+} below 70 eV where the total absorption cross sections[2] of SO_2 are available.

TOF mass spectrometers are widely used to measure the ion branching ratios.[3] However, it is not easy to measure ion branching ratios accurately at excitation energies where molecular and dissociative single and double photoionization take place concomitantly. Usually, the photoelectron signal is used as a start pulse for a time-to-amplitude converter (TAC) and the ion signal provides the stop pulse. With this arrangement, the different numbers of ejected electrons in single and double photoionization cause an overestimation of the number of the ions produced in double photoionization because the probability of forming one output pulse in the electron detector is higher for two electrons hitting simultaneously than that for one electron. This problem was overcome above 37 eV by using the rf signal of the storage ring as the start signal of the TAC.[4] Another problem is that when dissociative double photoionization occurs (e.g., $SO_2^{2+} \rightarrow O^+ + SO^+$), the heavier ion ($SO^+$) is not counted if the ion-detection efficiency is high. This is because the lighter O^+ ion stops the TAC. Since the ion-detection efficiency in the present study is of the order of a few percent, the heavier ion is detected with almost the same efficiency as the lighter ion.

The ion branching ratios are shown in Fig. 1 and the partial cross sections for the observed ions in Fig. 2. Since there was slight discontinuity in the ion branching ratios for the respective ions in the vicinity of 36 eV between the data obtained in Wisconsin and those at UVSOR using rf signal, these data were adjusted within a few percent to avoid the discontinuity. Above about 20 eV where the SO_2^+ ion dissociates into $SO^+ + O$, $S^+ + O_2$, $O_2^+ + S$, or $O^+ + SO$, dissociative photoionization becomes dominant as can be seen in Fig. 1. The thresholds for the $O^+ + SO^+$ and $O^+ + S^+$ channels of SO_2^{2+} are at 35.0 ± 0.5 and 37.7 ± 0.5 eV, respectively. The threshold for the $O^+ + SO^+$ channel is reported to be 34.1 ± 0.4 eV by Dujardin *et al.*[5]

References

1) J. A. R. Samson and T. Masuoka (unpublished data).
2) C. Y. R. Wu and D. L. Judge, J. Chem. Phys. **74**, 3804 (1981).
3) Y. M. Chung, E. -M. Lee, T. Masuoka, and J. A. R. Samson, J. Chem. Phys. **99**, 885 (1993).
4) T. Masuoka, Phys. Rev. A **48**, 1955 (1993).
5) G. Dujardin, S. Leach, O. Dutuit, P. -M. Guyon, and M. Richard-Viard, Chem. Phys. **88**, 339 (1984).

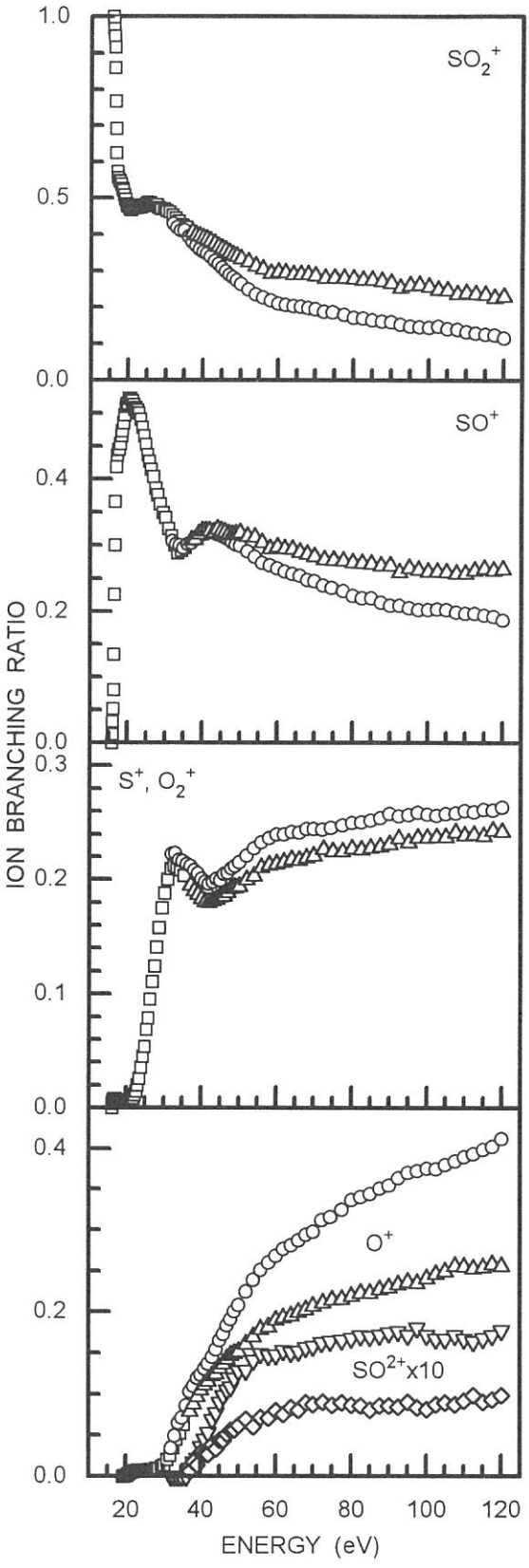

Fig. 1. Ion branching ratios of SO_2. △ and ◇ (rf) and ○ and ▽ (electron), present data; □ from Ref. 1.

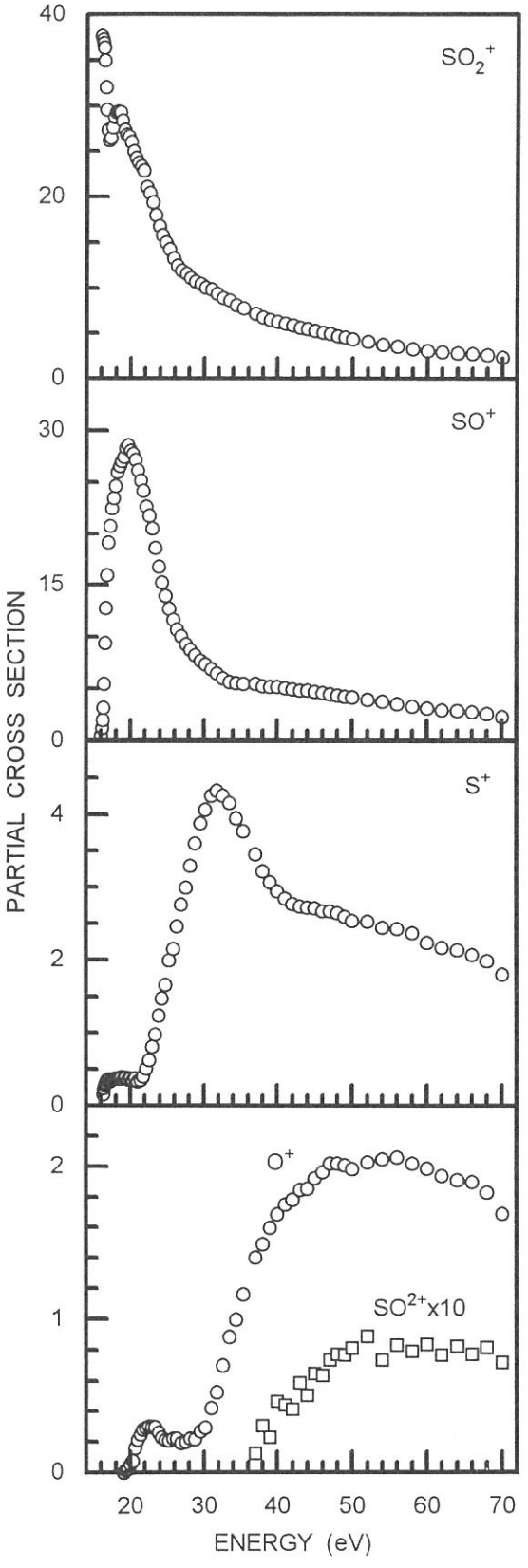

Fig. 2. Partial cross sections for the production of the observed ions.

(BL3A2)

Dissociative single and double photoionization of N_2O

Toshio MASUOKA, Isamu UESHIMA, and Takaaki NAKAMURA

Department of Applied Physics, Faculty of Engineering
Osaka City University, Sugimoto 3, Sumiyoshi-ku, Osaka 558

Photoelectron spectroscopy has been providing important information on double photoionization and so has mass spectrometry. To study dissociative single and double photoionization of N_2O, time-of-flight (TOF) mass and photoion-photoion-coincidence (PIPICO) spectra were measured in the region of 37-120 eV by the use of a constant-deviation grazing incidence monochromator together with synchrotron radiation. The TOF mass and PIPICO spectra were measured at an angle of about 55° with respect to the polarization vector where the second-order Legendre polynomial is close to zero, thus minimizing any effects of anisotropic angular distribution of fragment ions.

The TOF mass spectrometer was operated in two modes for the measurement of TOF mass spectra. In mode A, the photoelectron signal detected by a channel electron multiplier was fed into the start input of a time-to-amplitude converter (TAC). The storage ring was operated in a multi-bunch mode. In this mode of operation of the TOF mass spectrometer, the relative ion yields in single and double photoionization are affected by the different kinetic energies of individual photoelectrons and by the different numbers of photoelectrons in the two processes.

In mode B, the rf frequency of the storage ring was used as the start signal of the TAC. The storage ring was operated in a single-bunch mode, which was essential to obtain meaningful TOF mass spectra. In mode B, it is believed that the observed mass spectra are free from the discrimination effects mentioned above.

The apparent ion branching ratios directly obtained from the mass spectra measured in modes A and B are shown in Fig.1 with those reported by Hitchcock *et al.* using the dipole (e, e+ion) method[1] and by Samson and Masuoka in the 15-35 eV region.[2]

The present results obtained in mode A are in good agreement for NO^+ and N_2^+ with those obtained in mode B, considerably higher for O^+ and N^+, and considerably lower for N_2O^+ than those in mode B. This suggests that a remarkable amount of the O^+ and N^+ ions are produced in dissociative double photoionization which are overestimated in mode A. The N_2O^{2+} peak was not observed at all in the mass spectra, which means that the N_2O^{2+} ions dissociate completely. The data reported by Hitchcock *et al.* are in good agreement (within ±20%) for N_2O^+, NO^+, N_2^+, and O^+ with those obtained in mode B. However, there is a remarkable discrepancy for N^+ between the two sets of data. The reason for this is not clear at present.

References

1) A. P. Hitchcock, C. E. Brion, and M. J. Van Der Wiel, Chem. Phys. **45**, 461 (1980).
2) T. Masuoka and S. Mitani, J. Chem. Phys. **90**, 2651 (1989).

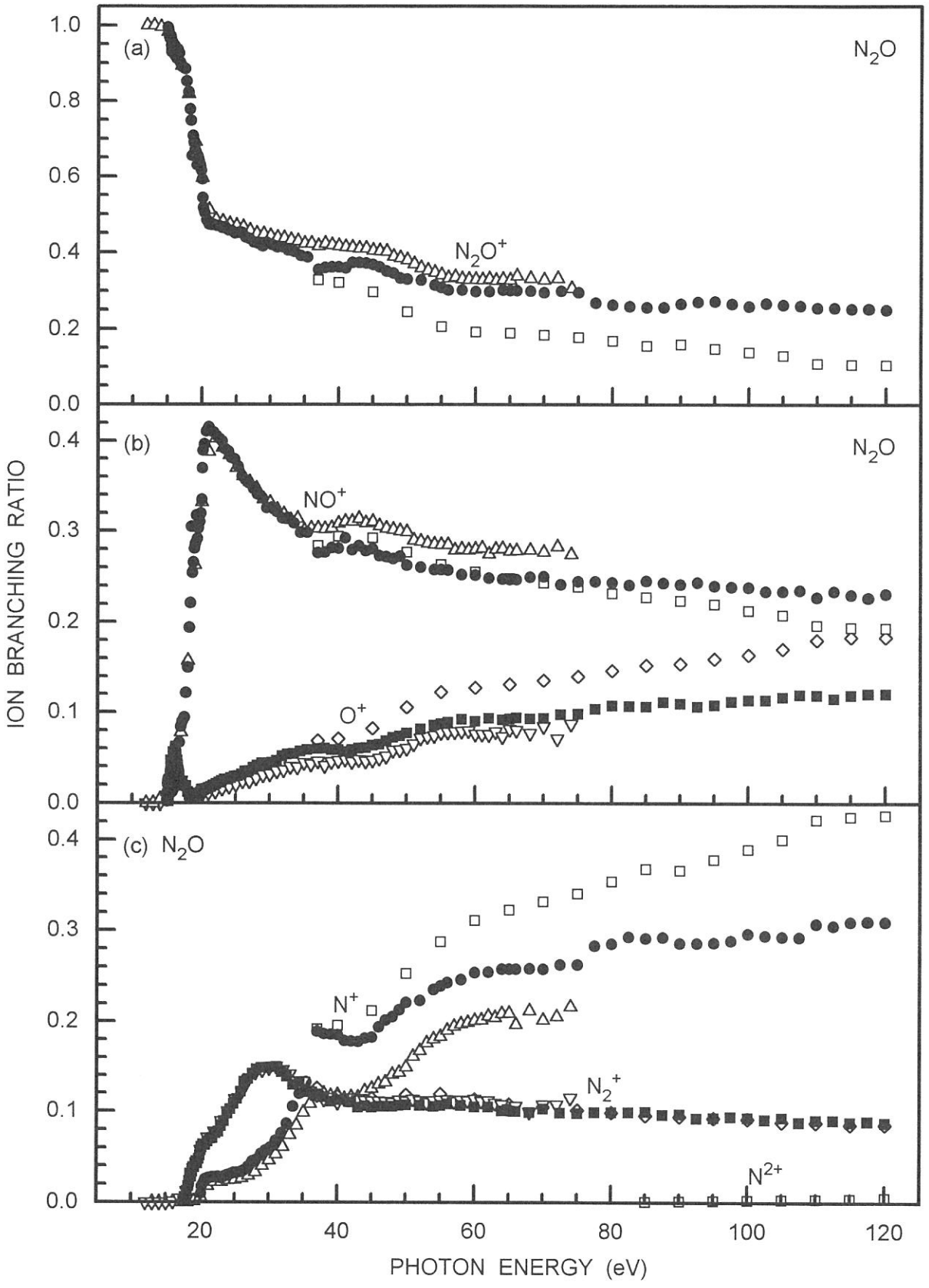

Fig. 1 Apparent ion branching ratios for N_2O directly obtained from the TOF mass spectra as a function of photon energy. □ and ◇ (mode A), ● and ■ above 37 eV (mode B), present data; ● and ■ below 35 eV, from ref. 2; △ and ▽, from ref. 1.

(BL3A2)

Photodissociation of CF_2Br_2 induced by Br(3d) excitation

T. Senga, M. Kawasaki, A. Hiraya[a], and T. Ibuki[b]

Graduate School of Environmental Earth Science, Hokkaido University, Sapporo 060
[a]Department of Material Science, Hiroshima University, Higashi-Hiroshima 724
[b]Institute for Molecular Science, Myodaiji, Okazaki 444

Single- and double-photoionization processes of CF_2Br_2 have been studied in the photon energy region 40-130 eV by use of the time of flight mass spectrometer (TOF-MASS) and photoion-photoion-coincidence (PIPICO) spectroscopy together with synchrotron radiation.

Figure 1 shows the photoelectron yields of CF_2Br_2 around Br(3d) inner shell. The peaks observed at 70.2 and 71.0 eV are assigned as the $\sigma^*\leftarrow 3d_{5/2}$ and $\sigma^*\leftarrow 3d_{3/2}$ transitions, respectively, on the analogy of the photoabsorption spectrum of HBr [1]. The contribution of the resonant $\sigma^*\leftarrow 3d_{5/2}$ band is estimated to be ≈35%. Peaks at 74.9 and 75.9 eV are attributed to the Rydberg transitions of $5p\leftarrow 3d_{5/2}$ and $5p\leftarrow 3d_{3/2}$, respectively, which are on the strong photoabsorption tail of the valence shells.

In the present measurements, singly charged ions detected by TOF-MASS were C^+, F^+, CF^+, F_2^+, CF_2^+, Br^+, CBr^+, $CFBr^+$, CF_2Br^+ and $CF_2Br_2^+$. Small yields of doubly charged photofragment ions of C^{2+} and F^{2+} were also observed. The branching ratios of the singly charged ions observed are shown in figure 2 as a function of the irradiated photon energy. Similar to the previous CF_3Br study [2], the branching ratios of singly charged small photofragment ions, such as C^+, F^+ and F_2^+, increase with the photon energy. It is clear that the F_2^+ formation starts at the Br(3d) excitation and increases with the photon energy.

Figure 3 shows the PIPICO branching ratios depending on the primary photon energy. The relative intensities of the ion pairs (C^+-F^+), (F^+-Br^+), and (C^+-Br^+) increase in the photon energy region higher than the Br(3d) excitation. The discrete structure of the Br(3d) photoabsorption appears clearly in the (C^+-F^+) pair formation which excludes Br atom. The (CF_2^+-Br^+) and (CF^+-Br^+) pairs decrease with increasing photon energy.

In our previous work of CF_3Br [2], the PIPICO branching ratios formed from doubly- and triply-charged molecular ion did not show any noticeable change at the Br(3d) excitation region. However, in the present CF_2Br_2 study, the contribution of Br(3d) inner core excitation is recognizable in the PIPICO spectra. The main difference between the CF_3Br and CF_2Br_2 spectra lies in the photoelectron yields induced by Br(3d) excitations. That is, the $\sigma^*\leftarrow 3d_{5/2}$ transition intensity in CF_3Br is about 15% of the total photoelectron yield, while in CF_2Br_2 it is ≈35%. This observation suggests that the site selective decomposition originated in the Br(3d) excitation becomes observable when the photoabsorption cross section of Br(3d) inner shell is large enough, at least more than 15%.

As far as our knowledge, the $\sigma^*\leftarrow$Br(3d) inner core excitation induces the bond breakage of Br atom in HBr [3], C_2H_5Br and C_2H_3Br [4]. However, it is vague in the present CF_2Br_2 and CF_3Br [2] cases. It may indicate the relaxation processes after the Br(3d) inner shell excitation differ in the fluorinated compounds.

References

[1] D. A. Shaw, D. Svejanovic, G. C. King, and F. H. Read, J. Phys. B **17**, 1173 (1984).
[2] T. Senga et al., UVSOR Activity Report (1994) 104.
[3] P. Morin and I. Nenner, Phys. Rev. Lett., **56**, 1913 (1986).
[4] P. Morin, T. LeBrun, and P. Lablanquie, Bull. Soc. R. Sci. Liege, **58**, 135 (1989).

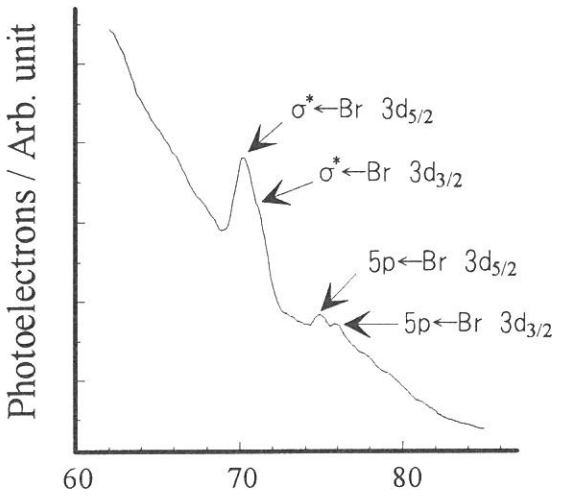

Figure 1 Photoelectron yield spectrum of Br(3d), in CF_2Br_2 .

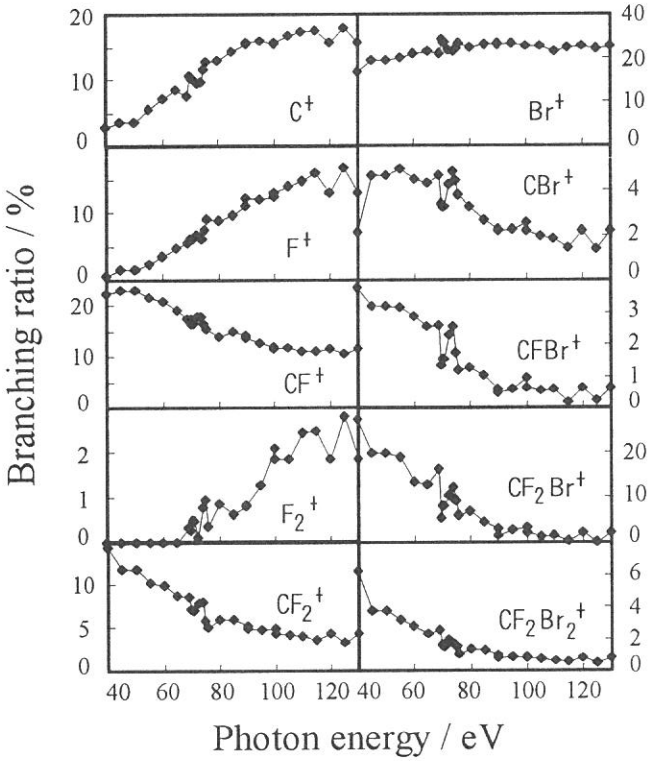

Figure 2 Branching ratios of photofragment and molecular ions as a function of the irradiated photon energy.

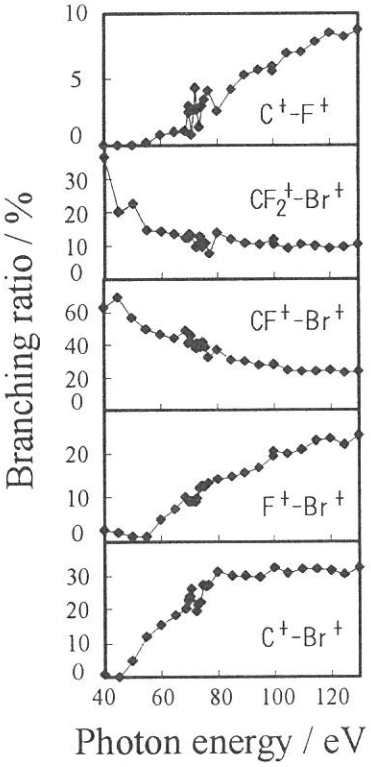

Figure 3 Branching ratios of PiPiCO as a function of the irradiated photon energy.

(BL3A2)

Site-Specific Fragmentation Following Si:2*p* Core-Level Photoexcitation of $F_3Si(CH_2)_2Si(CH_3)_3$ in the Vapor Phase

Shin-ichi NAGAOKA, Tonan FUJIBUCHI, Joji OHSHITA,[a]
Mitsuo ISHIKAWA,[a] and Inosuke KOYANO[b]

Department of Chemistry, Faculty of Science, Ehime University, Matsuyama 790-77

[a] *Department of Applied Chemistry, Faculty of Engineering, Hiroshima University, Higashi-Hiroshima 724*

[b] *Department of Material Science, Faculty of Science, Himeji Institute of Technology, 1479-1 Kanaji, Kamigohri, Hyogo 678-12*

In recent years, relaxation processes following core excitation in molecules have been a topic of much interest. We have investigated site-specific fragmentation following photoexcitation of (trifluorosilyl)(trimethylsilyl)ethane ($F_3Si(CH_2)_2Si(CH_3)_3$, FSMSE) in the range of Si:2*p* excitation by means of the photoelectron-photoion and photoion-photoion coincidence methods (PEPICO and PIPICO methods, respectively).

The experiments were performed using a time-of-flight spectrometer with variable path length, coupled to a constant-deviation grazing incidence monochromator installed on the BL3A2 beam line of the UVSOR synchrotron radiation facility in Okazaki.[1]

The total photoionization efficiency curve of FSMSE has one broad peak and some sharp peaks near the 2*p* core-ionization threshold of the silicon atom (Fig.1). It is close to a superposition of the total photoionization efficiency curves of $Si(CH_3)_4$ and $Si(CH_3)F_3$, which have broad peaks and sharp peaks, respectively.[2,3] Accordingly, the broad peak and the sharp peaks are likely to correspond to the Si:2*p* core-level photoexcitation at the Si atom bonded to three methyl groups (Si[Me]) and at Si bonded to three F atoms (Si[F]), respectively.

The site-specific fragmentation following the Si:2*p* core-level photoexcitaion of FSMSE can be seen by means of the PEPICO technique. Figure 2 shows plots of the ratios of the integrated intensities of $SiCH_3^+$, $Si(CH_3)_2^+$, and $Si(CH_3)_3^+$ to those of SiF^+, SiF_2^+, and SiF_3^+, respectively, in the PEPICO spectrum [$I(Si(CH_3)_n^+)/I(SiF_n^+)$] as a function of photon energy. On going from the Si[Me] peak to the Si[F] peak, $I(Si(CH_n)^+)/I(SiF_n^+)$ decreases rapidly. The fragmentation predominantly occurs around the Si atom where the photoexcitation has taken place.

The total photoionization efficiency curve and the site-specific fragmentation of FSMSE are quite different from those of $F_3SiCH_2Si(CH_3)_3$.[4]

1. E. Ishiguro et al. Rev. Sci. Instr. 60, 2105 (1989). T. Masuoka, and S. Nagaoka, Trends Chem. Phys. 30, 13 (1994).
2. S. Nagaoka et al. J. Phys. Chem. 97, 1488(1993).
3. J. D. Bozek et al. Chem. Phys. 158, 171(1991).
4. S. Nagaoka et al. J. Chem. Phys. 102, 6078 (1995).

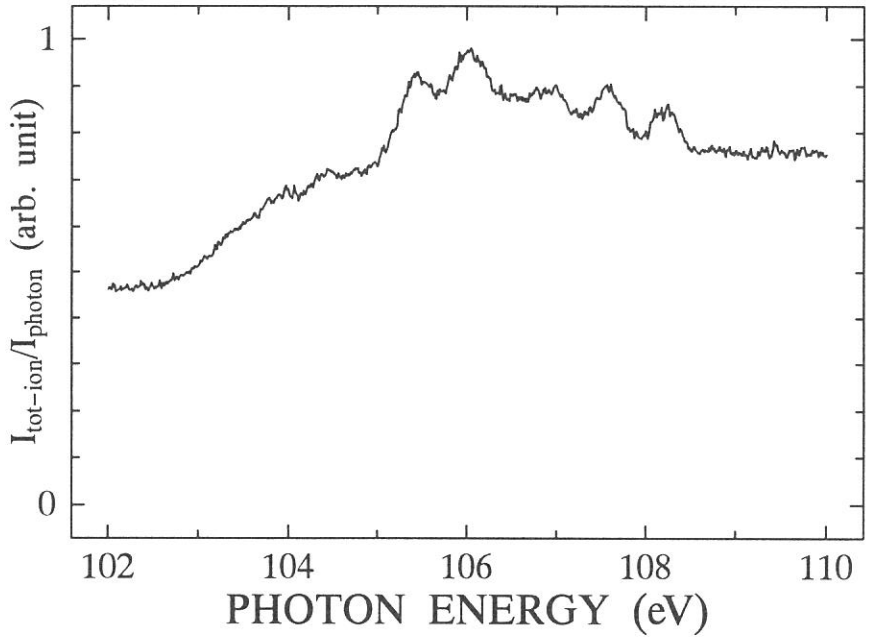

Fig.1 Total photoionization efficiency curve of FSMSE.

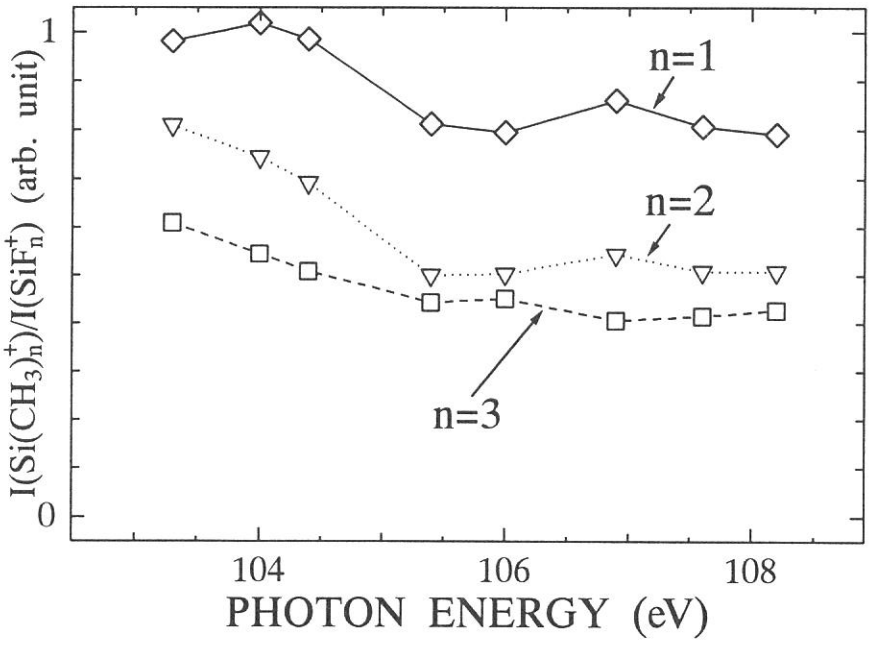

Fig.2 $I(Si(CH_3)_n^+)/I(SiF_n^+)$ in FSMSE as a function of photon energy.

Dissociative Photoionization of Hexacarbonyl Tungsten in the Range 30-120eV.

Yusuke Tamenori, Kazushige Inaoka, and Inosuke Koyano
Department of Material Science, Himeji Institute of Technology, Kamigohri, Japan 678-12

The dissociative photoionization dynamics of metal-carbonyls is of much interest because these compounds have unique bonding properties involving both the weak metal-carbonyl coordination bond and strong covalent C-O bond in a molecule. In order to elucidate dissociation pathways to various fragment ions, we have initiated a series of detailed studies of dissociative photoionization of metal-carbonyl vapors in the range 37-120eV by use of TOF mass spectrometry and photoion-photoion coincidence technique.[1] However, the previous results on pentacarbonyl iron remained somewhat ambiguous because the m/z values of some dications coincided with that of a monocation. In the present work, we extended our measurements to hexacarbonyl tungsten to examine the effect of different metal center and coordination number, and to complement the previous studies .

The details of the apparatus and experimental procedure are given elsewhere,[2] and they will be described only briefly here. Monochromatic radiation is provided by a constant deviation grazing incidence monochrometer installed on the BL3A2 beamline. Produced ions and electrons are extracted from the ionization cell in opposite directions to each other by a weak electric field and ions are then mass analyzed by a double-field type time-of-flight mass spectrometer. The mass spectrometer is used in two different modes of operation: the mass and PIPICO measurement modes. To minimize the effect of anisotropic angular distribution of photoions and photoelectrons, all measurements are carried out at the detection angle of 55°with respect to the polarization vector of the incident photons. The sample gas pressure in the ionization cell is estimated to be $\sim 10^{-6}$ torr from the pressure in the main chamber housing the cell, which is kept at $5\text{-}8\times10^{-7}$ torr.

In the mass spectra, both singly and doubly charged ions of the formulas $W(CO)_n^+$ (n=0-6) and $W(CO)_n^{2+}$ (n=0-6), resulting from simple scission of (a) coordination bond(s) following photoionization, have been identified unambiguously. The branching ratios of various ion of these formulas are shown in Figure 1 as a function of incident photon energy. The occurrence of these types of ions could not be conclusive in previous studies on pentacarbonyl irons because of m/e overlapping. A novel feature is that the whole series (n=0-6) of doubly charged ions $W(CO)_n^{2+}$ are observed and that their abundances becomes larger above about 40eV. Several groups have previously reported, although the abundances are small, the observation of $W(CO)^{2+}$, $W(CO)_2^{2+}$ and $W(CO)_3^{2+}$ in electron impact mass spectra.[3] Our present result adds n=0,4-6 to these previous report. Especially the observation of doubly charged parent ion is interesting, because the occurrence of this ion means that the large excess energy is released as kinetic energy of photoelectrons or/and is kept as internal energy of the parent ion. Moreover, it is particularly interesting that the branching ratio of them increases with increasing photon energy throughout the whole range studied. The second feature is that in both singly and doubly charged ions, five- coordinated species are particularly weak. The low abundance of $W(CO)_5^+$ has been reported previously in the electron impact study.[3] The present work shows that the situations is the same with doubly charged ions.

Figure 2 shows the ion branching ratios of the ions that can originate only through additional breakage of the covalent C-O bond in the ligand. These are ions $WC(CO)_n^+$ (n=0,1) and $WC(CO)_n^{2+}$ (n=0-3). The most abundant among these singly and doubly charged ions are WC^+ and $WC(CO)^{2+}$, respectively. Similar types of ions have been observed in the previous study on pentacarbonyl iron. But the present system differs from the previous one in that the kinds of ions in each type are much more plentiful.The branching ratios of doubly charged ions of this formula, especially that of $WC(CO)^{2+}$ increase rapidly with increasing photon energy in the range from 40eV to 60eV. This energy region corresponds to that of large resonance peak

in the total photoelectron efficiency curve.

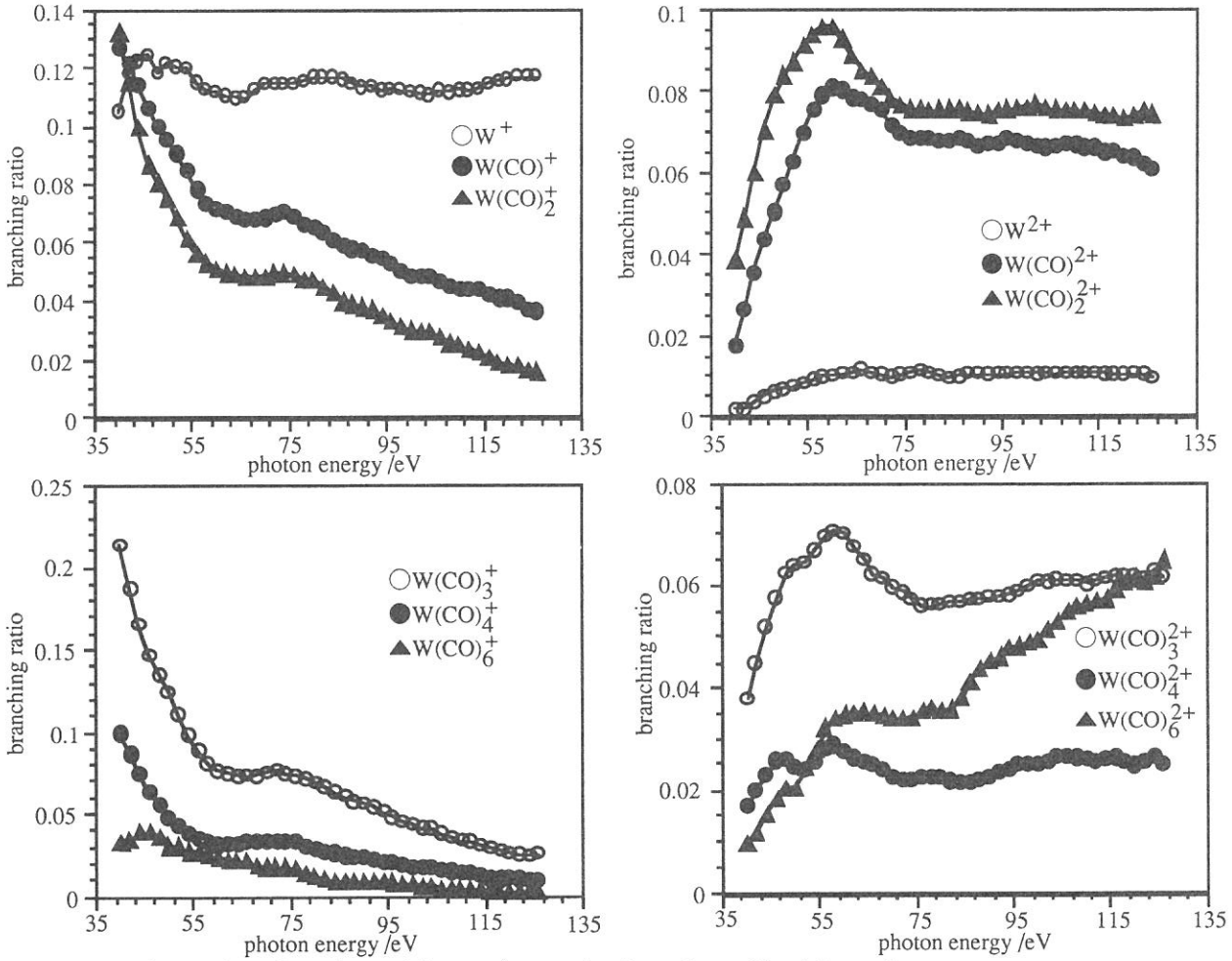

Figure 1Various photoions branching ratios as the function of incident photon energy.

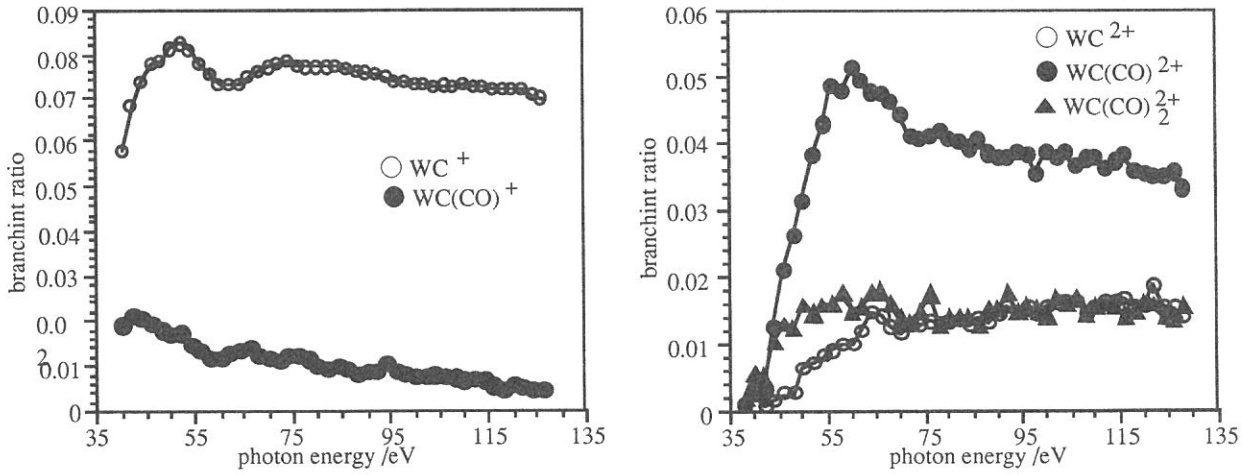

Figure 2 Various PIPICO branching ratios as the function of incident photon energy.

References
1,Y. Tamenori and I. Koyano, UVSOR activity report, 1994, p94.
Y. Tamenori, K. Inaoka and I. Koyano, J. Electron Spectrosc.,(1996) in press.
2,T. Masuoka, T. Horigome and I. Koyano, Rev. Sci. Instrum. 60,2179 (1989)
3,G. Cooper, J. C. Green, M. P. Payne, B. R. Dobson and H. Hillier, J. Am. Che. Soc. 109,3836 (1987)

BL3A2

Dissociative Photoionization of Hexacarbonyl Molibudenum in the Range 37-120eV.

Yusuke Tamenori and Inosuke Koyano
Department of Material Science, Himeji Institute of Technology, Kamigohri, Japan 678-12

We are performing a series of detailed studies of dissociative photoionization of metal carbonyl vapors in the inner-valence region. An impetus comes from their unique bonding properties involving two distinct types of chemical bond in a molecule; one the weak metal-ligand coordination bond and the other strong C-O covalent bond. The details of these properties have been discussed previously.[1] In the present work, we extend our study to hexacarbonyl molibudenum placing emphasis on the incident photon-energy dependence of the dissociation pathways. Details of the apparatus and experimental procedure have also been given elsewhere.[1] Branching ratios of various ions and ion-pairs, determined as a function of incident photon energy, are used to obtain their approximate differential curves, from which electronic states responsible for each dissociation processes are estimated.

Typical ion branching ratio curves and the differential curves of Mo^+ and $Mo(CO)^+$ are shown in the Figure 1. These represent ions of the formula $Mo(CO)_n^+$. All of the branching ratio curves of this type of ions, expect that of the $Mo(CO)_6+$ parent ion, monotonically decrease with the incident photon energy. Especially, the sharp decrease in the differential curve in the range from 40eV to 60eV is noteworthy. This energy region corresponds to that of molibudenum 4p→4d resonance photoabsoption.[2] Moreover, the naked molibudenum ion which is the end product of simple neutral CO elimination, also decreases in the same energy region. Hence, the electronic relaxation and dissociation pathways alternative to it should exist and increase around that energy.

The branching ratios and differential curves of the daughter ions CO^+, O^+ and C^+ are shown in Figure 2. The CO^+ ion shows a drastic increase in the same energy region as that of the significant decrease of $Mo(CO)_n^+$ monocations. Thus, the CO^+ ion production seems to be one of the predominant dissociation pathways that replace the simple neutral CO elimination pathway. Sharp rizes are also seen in the differential curves of C^+ and O^+, but the peaks occur at somewhat higher energies than the energy at which CO^+ increases drastically. A feature seem here is that the peaks and dips in the differential curve of CO^+ just coincide with the dips and peaks, respectively, of the C^+(O^+ as well) differential curve. On the other hand, the relative abundance of C^+ is about three times as large as that of O^+ ions.

The corresponding curves typical of the dications of the formula $Mo(CO)_n^{2+}$ and $MoC(CO)^{2+}$ are shown in Figure 3. All of these ions show a pronounced increase in the branching ratio in the range from 40eV to 60eV. These increases occur in harmony with the decrease of the $Mo(CO)^+$ ion.Summarizing all these observations, the whole wavelength range studied here can be divided into three regions depending on the major processes occurring in each of them.The first is the photon energy region below 40eV. In this energy region, simple neutral CO elimination mainly occurs. The second is the region from 40eV to 60eV, which corresponds to the molibudenum 4p→4d resonance absorption. Here, the doubly charged ions are resonantly increased and, at the same time, CO^+ ion has a maximum of production rate. The third one is the region of the production of daughter ions having no metal atom, *i.e.* above 60eV. From the PIPICO measurement it is shown that the dissociative double photoionization also increases with the incident photon energy in this region.

References

1,Y. Tamenori, K. Inaoka and I. Koyano, J. Electron Spectrosc., (1996) in press.
2,G. Cooper, J. C. Green, M. P. Payne, B. R. Dobson and H. Hillier, J. Am. Chem. Soc. 109,3836 (1987)

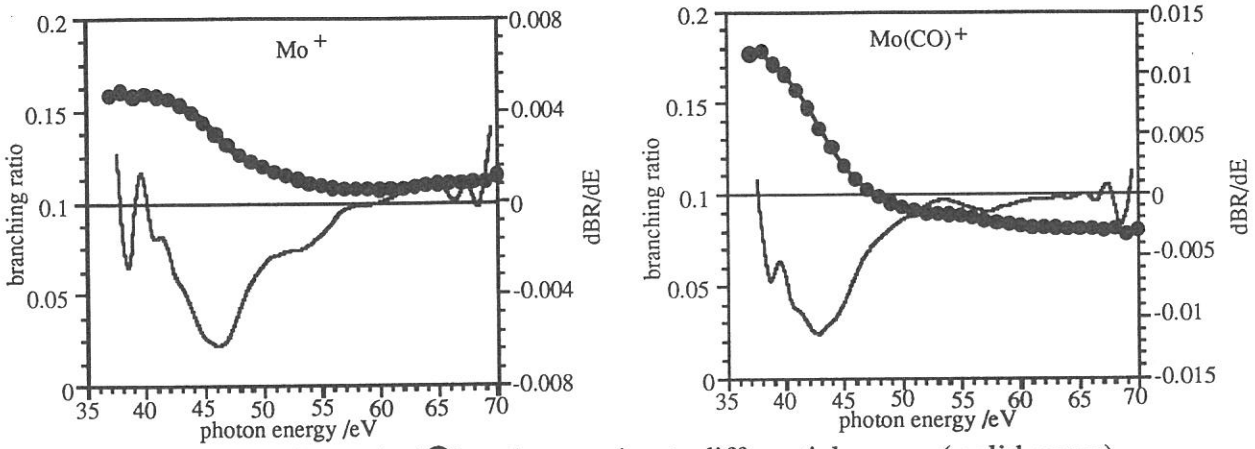

Figure 1 The branching ratio (●) and approximate differential curves (solid curve) of Mo^+ and $Mo(CO)^+$ as a function of incident photon energy.

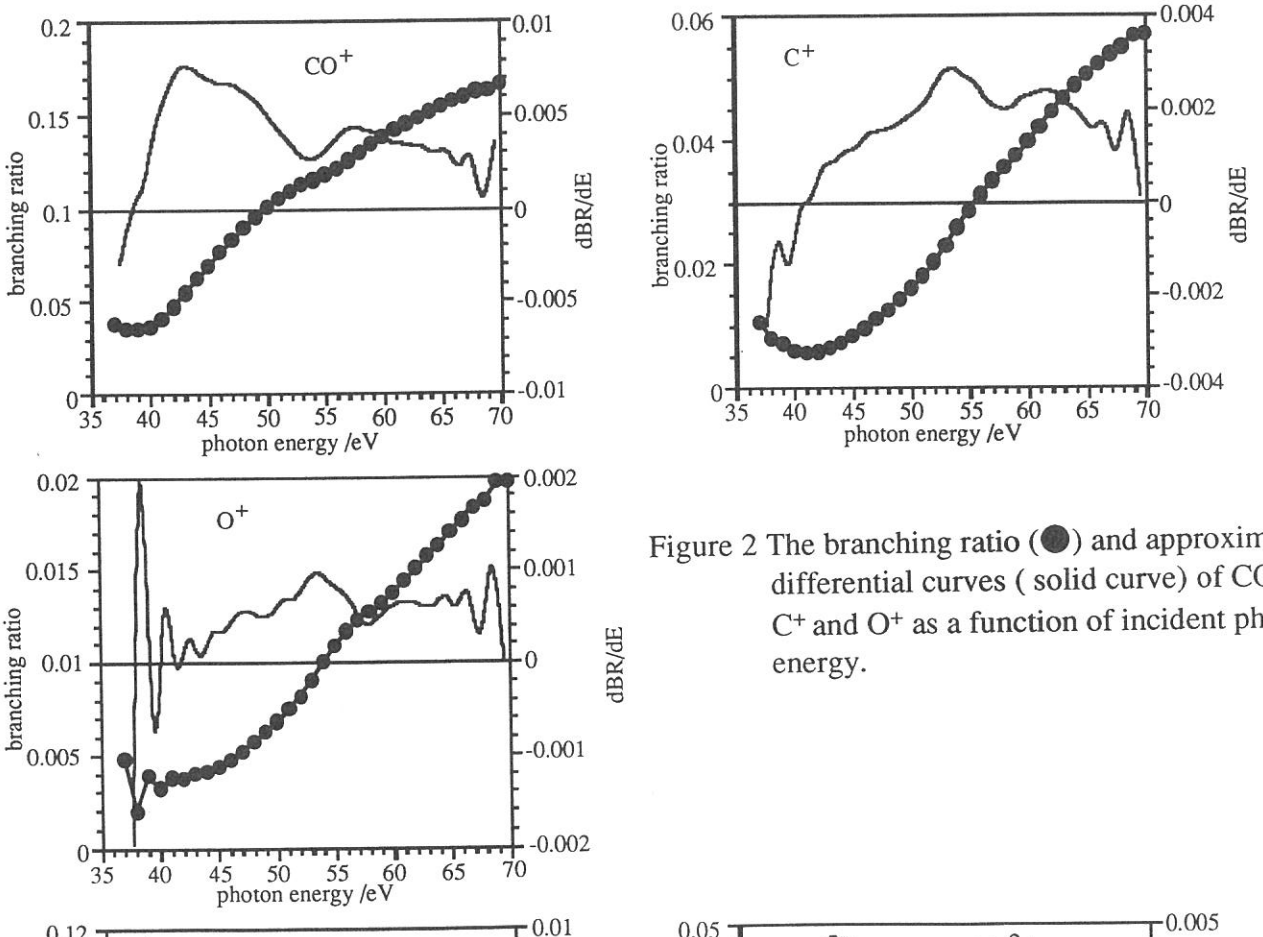

Figure 2 The branching ratio (●) and approximate differential curves (solid curve) of CO^+ , C^+ and O^+ as a function of incident photon energy.

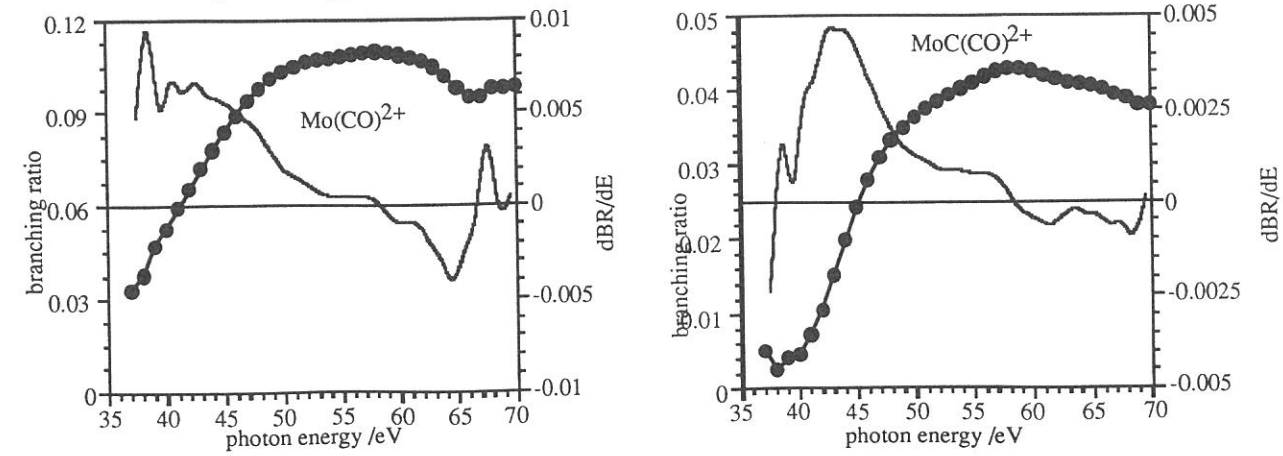

Figure 3 The branching ratio (●) and approximate differential curves (solid curve) of $Mo(CO)^{2+}$ and $MoC(CO)^{2+}$ as a function of incident photon energy.

(BL3A2)

Vacuum UV Spectroscopy Making Use of the Combination of Synchrotron Radiation and Laser — Photoionization of Iodine Atoms Produced by Laser Photodissociation of Methyl Iodide

Masakazu MIZUTANI, Shuji ASAKA, Atsunari HIRAYA* and Koichiro MITSUKE

Institute for Molecular Science, Myodaiji, Okazaki 444
*Faculty of Science, Hiroshima University, Kagamiyama, Higashi-Hiroshima 739

Combining laser with synchrotron radiation for pump-probe or double resonance experiments is one of the most promising spectroscopic methods in the VUV region. Nevertheless, such measurements have been performed by only a few groups: photodissociation of *s*-tetrazine,[1] production of highly excited atoms via two-photon absorption,[2] and detection of atomic iodine produced from I_2.[3] Recently, time-resolved spectroscopy has been achieved by means of a mode-locked laser synchronized with the radiation emitted from the Super ACO storage ring.[4] We are planning to develop new spectroscopy of polyatomic molecules, taking advantage of synchronization of photon pulses between undulator radiation and ultraviolet laser. Our primary goal is to investigate the photodissociation and photoionization dynamics of molecules in a given vibronically excited state.

The schematic diagram of the apparatus is shown in Fig.1. A mode-locked Ti:sapphire laser is made to operate synchronously with the master oscillator (90.115 MHz) for a harmonic RF cavity on the UVSOR ring. Then the second and third harmonics are generated by using an LBO crystal and a BBO crystal, respectively. Into a photoionization chamber, the third harmonics is introduced coaxially with the fundamental of the undulator light from beam line BL3A2. Two LiF windows are located upstream for preventing higher harmonics of the undulator light from entering the ionization region. The molecular beam, which is discharged from a nozzle made of a multi-channel capillary array, intersects at 90° with the two photon beams.

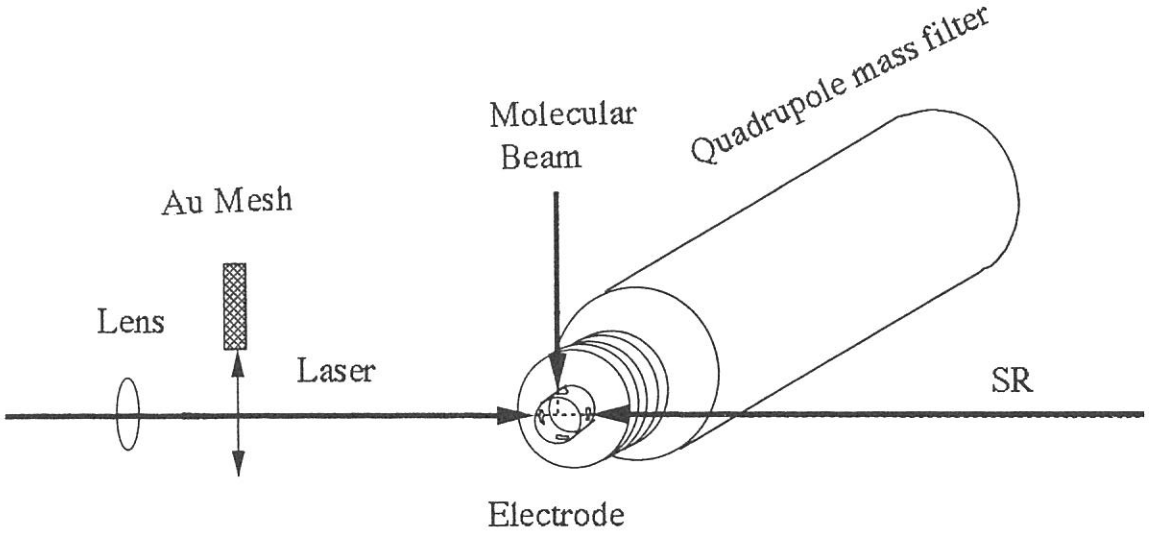

Figure 1: Schematic diagram of the arrangement for pump-probe experiments which make use of the combination of synchrotron radiation and laser.

Photoions are analyzed by a quadrupole mass filter placed perpendicularly with the photon beams and the molecular beam.

The high photon flux of the third harmonics of the laser permits a valence electron to be excited to a Rydberg or antibonding orbital. If temporal overlap of the photon pulses between the laser and undulator light is sufficient, it can be expected that the excited molecule is further dissociated or ionized by an undulator photon. We make the following experiment on photodissociation of CH_3I to ascertain sequential absorption of the two different photons: dissociation of CH_3I into CH_3 and I by irradiation of the third harmonics of the laser at 259nm and subsequent ionization of the I atom with the 9.41 ± 0.5 eV photon of the undulator light. As evidenced in Fig. 2, I^+ ion counts are observed at *m/z* 127, when the laser light is introduced in addition to the undulator light. Since the ground state of atomic iodine has fine structures $I(^2P_{1/2})$ and $I(^2P_{3/2})$ with the ionization potential of 9.51 and 10.45 eV, respectively, the I^+ ions are considered to result from $I(^2P_{1/2})$ produced by laser-induced photodissociation.

1) L. Nahon, P. Morin, M. Lazilliere, and I. Nenner, J. Chem. Phys. **96**, 3628 (1992).

2) M. Meyer, B. Müller, A. Nunnemann, Th. Prescher, E. V. Raven, M. Richer, M. Schmidt, B. Sonntag, and P. Zimmermann, Phys. Rev. Lett. **59**, 2963 (1987); J. M. Bizau, F. Wuilleumier, D. L. Ederer, J. C. Keller, J. L. LeGouët, J. L. Picqué, B. Carré, and P. M. Koch, Phys. Rev. Lett. **55**, 1281 (1985).

3) L. Nahon, L. Duffy, P. Morin, F. Combet-Farnoux, J. Tremblay, and M. Larzilliere, Phys. Rev. A**41**, 4897 (1990); L. Nahon, A. Svensson, and P. Morin, Phys. Rev. A**43**, 2328 (1991).

4) J. Lacoursière, M. Meyer, L. Nahon, P. Morin, and M. Larzillière, Nucl. Instrum. Meth. Phys. Res. A**351**, 545 (1994).

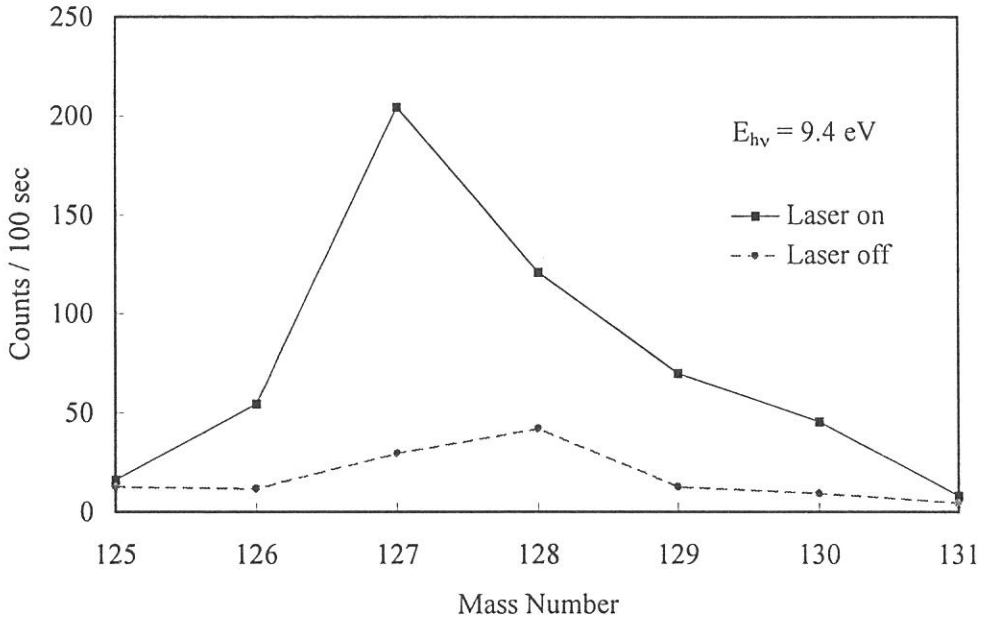

Figure 2: Mass spectrum of I^+ produced by the pump-probe experiment using synchrotron radiation and laser. The 259nm UV laser induces photodissociation of CH_3I and fragment iodine atoms are further ionized by the undulator light at 9.41 ± 0.5 eV. The laser output power is set to about 80mW.

(BL3B)

AUTOIONIZATION OF NO IN AN EXCITED VALENCE STATE AFFECTED BY PERTURBATIONS OF VALENCE–RYDBERG MIXING

Yasumasa HIKOSAKA, Hideo HATTORI,* Takumi HIKIDA, and Koichiro MITSUKE*

Department of Chemistry, Tokyo Institute of Technology, Ohokayama, Meguro 152
*Department of Vacuum UV Photoscience, Institute for Molecular Science, Okazaki 444

A superexcited state of nitric oxide is studied by photoionization and photoelectron spectroscopy using synchrotron radiation.[1] Figure 1 shows a photoionization efficiency curve of NO about 2 – 4 eV above the ionization threshold. The spectrum contains a number of irregularly spaced peaks, grouped into features *F0–F7*. Most of the structures are considered to originate from autoionization of a superexcited state NO*. The complexity of the spectrum is understood as that the vibrational levels of NO* are substantially perturbed by the Rydberg states converging to $NO^+(X\,^1\Sigma^+)$.[2] Figure 2 shows a two–dimensional (2D) photoelectron spectrum at the photon energy $E_{h\nu}$ from 10.7 to 13.4 eV. Patterns running parallel to the photon energy axis correspond to the final vibrational levels v_i=0–15 of $NO^+(X\,^1\Sigma^+)$. Hori–zontal intense patterns super–imposed on direct ionization continua are due to autoionizing resonances at which the vibrational distribution shows several minima. The number of minimum positions increases with the photon energy.

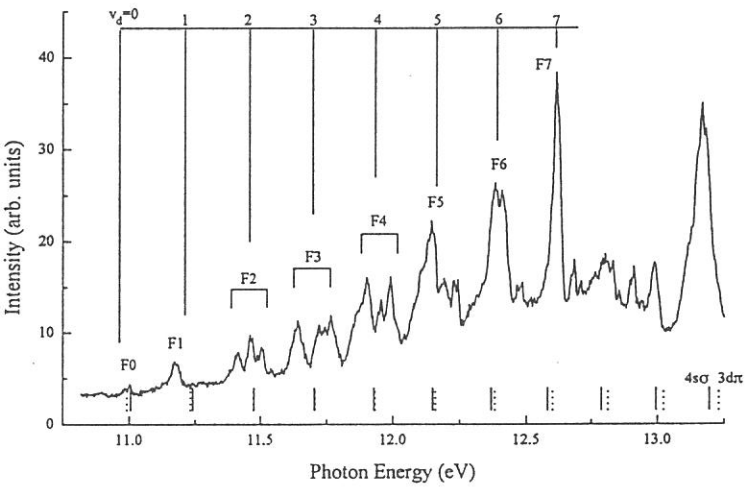

Figure 1. Photoionization efficiency curve of NO with energy resolution of ~5meV. Solid lines represent zero order vibrational levels of the autoionizing state determined by a least–squares fit.

In order to interpret the 2D photoelectron spectrum, we obtain an appropriate potential energy curve for NO*, and then calculate Franck–Condon factors between NO* and NO ($X^2\Pi$) or $NO^+(X^1\Sigma^+)$. We assume that features *F2–F4* in Fig.1 are composed of one vibrational level of NO* and several levels of perturbing Rydberg states. This assumption is supported by the experimental finding that the fine peaks belonging to the respective features give rise to similar vibrational distribution in Fig. 2. Thus, the zero order vibrational levels of NO* are temporarily fixed to the center of features *F2–F4*. The positions are finally determined by the least–squares fit of their levels, together with other zero order levels for features *F0*, *F1*, and *F5–F7*, to transition frequencies given by

$$\nu = \nu_{00} + \omega_e(v_d + 1/2) - \omega_e x_e(v_d + 1/2)^2 - \omega_e/2 + \omega_e x_e/4. \quad (1)$$

The obtained zero order v_d=0–7 levels of NO*, corresponding to features *F0–F7,* respectively, are shown by solid lines in Fig.1. The optimum values of the adjustable parameters are ν_{00}=88410cm^{-1}, ω_e=2060cm^{-1} and x_e=0.0094. A partial cross section for producing $NO^+(v_i)$ through the vibrational level v_d of NO* is calculated using

$$\sigma(v_i) \propto \left|\langle v_g | v_d \rangle\right|^2 \left|\langle v_d | v_i \rangle\right|^2 \Big/ \sum_{v_i'} \left|\langle v_d | v_i' \rangle\right|^2. \quad (2)$$

Here, $|v_g>$, $|v_d>$ and $|v_i>$ denote the vibrational wave functions for the initial ground (v_g=0), the autoionizing, and the final ionic states, respectively. An equilibrium bond length r_e is an adjustable parameter that can be optimized to reproduce the 2D photoelectron spectrum. The simulation at r_e=1.29Å is in the best agreement with the spectrum of Fig. 2. The thick curve in Fig.3 represents the anharmonic potential energy curve of NO* obtained with the above values of ν_{00}, ω_e, x_e, and r_e. In addition, several potential curves of R_X from previous literature[3] are shown by the thin curves. With these potential relations, we can conclude that a binary or trinary combination of the *4sσ*, *3dσ/3dπ*, and *4pσ/4pπ* states causes substantial perturbations to the v_d =2–4 vibrational levels (features *F2–F4*).

1) K.Mitsuke, Y.Hikosaka, T.Hikida, and H.Hattori, J. Electron Spectrosc. Rel. Phenom., in press.

2) A.L.Sobolewski, J. Chem. Phys., 87, 331 (1987).

3) K.P.Huber and G.Herzberg, Constants of Diatomic Molecules, Van Nostrand Reinhold, New York, 1979.

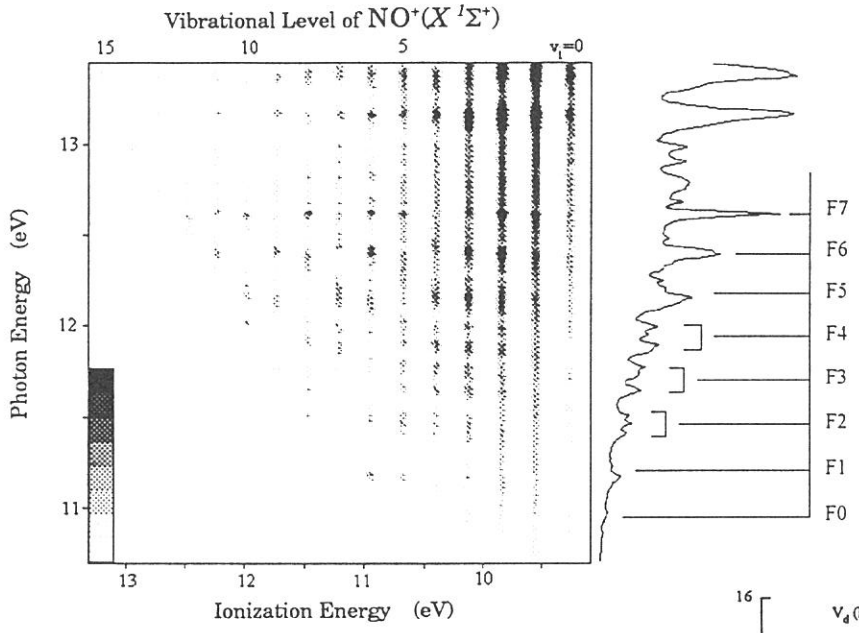

Figure 2. Two-dimensional photoelectron spectrum of NO at the photon energy from 10.7 to 13.4 eV. The electron intensity is shown from light to dark on a linear scale. The curve in the right panel represents summation of electron counts over the whole range of the ionization energy as a function of $E_{h\nu}$.

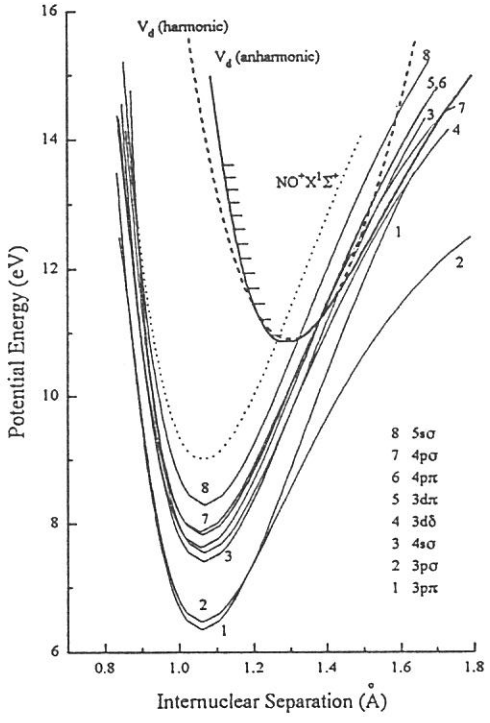

Figure 3. Potential energy curves of the autoionizing state NO* used for the Franck–Condon analysis, and those of the Rydberg states converging to $NO^+(X^1\Sigma^+)$.

(BL3B)

Production of autoionizing nitrogen atoms by photodissociation of NO

Yasumasa HIKOSAKA, Hideo HATTORI*, Takumi HIKIDA, and Koichiro MITSUKE*

Department of Chemistry, Tokyo Institute of Technology, Ohokayama, Meguro 152, Japan
**Department of Vacuum UV Photoscience, Institute for Molecular Science, Okazaki 444 Japan*

Photodissociation of nitric oxide followed by autoionization of an atomic fragment is studied by two-dimensional photoelectron spectroscopy using synchrotron radiation. Figure 1 shows a two-dimensional photoelectron spectrum of nitric oxide at photon energies from 21.2 to 28 eV. The electron counts are plotted on a linear scale as a function of the photon energy ($E_{h\nu}$) and the kinetic energy (E_k) of the ejected electron. The intense structures are truncated. The patterns due to direct photoionization of NO molecules appear as diagonal stripes with a slope of unity on the spectrum, since the ionization energy I_E for a vibronic state of NO^+ is equal to the energy difference $\Delta E \equiv E_{h\nu} - E_k$. For a purpose of clarity, a set of lines with various ΔE values is indicated in Fig. 1.

If an autoionizing transition of atomic fragments takes place between two particular states, one may expect that emission of electrons with a constant kinetic energy results in a pattern running parallel to the $E_{h\nu}$ axis. Actually, five or more vertical stripes at $E_{h\nu}$ = 21.5 - 27 eV are due to autoionization of N** $\rightarrow$ $N^+ + e^-$. Assuming that superexcited N** atoms autoionize at so distant a bond length as to be completely isolated from the counterpart O atoms, one may write the energetical relation as

$$\Delta E \equiv E_{h\nu} - E_k = D^+ + K_{nucl} .$$

Here, D^+ is the dissociation limit for the final product $N^+ + O$ measured from the neutral vibronically ground state NO($X^2\Pi$, $v_g = 0$), and K_{nucl} is the nuclear kinetic energy released during dissociation of NO*.

To obtain a better statistics, electron counts are summed over the ΔE = 22.5 - 26 eV range along the direction of constant kinetic energy. Figure 2 shows an electron energy spectrum thus obtained. Several peak features in this spectrum are assigned to autoionization of the Rydberg states converging to $N^+(^1D^e)$ into the ground state $N^+(^3P^e)$ by comparison with previous data in electron spectroscopic studies.[1,2] Once the electronic state of final N^+ ion is fixed, we can predict that of the counterpart neutral O atom from the lower onset energy ($E_{h\nu}^{\ddagger}$) of the vertical patterns by the use of the equations $K_{nucl} = 0$ and $\Delta E = E_{h\nu} - E_k = D^+$, unless the Franck-Condon region for NO* lies higher than the dissociation limit. Below $E_{h\nu}$ = 30 eV, the $^3P^e$, $^1D^e$, and $^1S^e$ states of an atomic oxygen are energetically accessible, $N^+(^3P^e)$ being produced from NO. The functions $\Delta E = D^+$ corresponding to these three dissociation limits are represented by solid lines in Fig. 1. At a first sight, the $E_{h\nu}^{\ddagger}$ values of the vertical patterns seem to aligned on the $\Delta E = D^+$ line for the $N^+(^3P^e) + O(^1D^e)$ limit. However, some patterns are found to remain below this line. In particular, the pattern with E_k = 0.60 eV (marked as P_1 in Fig. 2) apparently persists throughout the region between the $N^+(^3P^e) + O(^1D^e)$ and $N^+(^3P^e) + O(^3P^e)$ limits. We therefore draw the following conclusion: (1) a neutral atomic pair formed by the dissociation of NO* is N**[converging to $N^+(^1D^e)$]+O($^1D^e$, $^3P^e$), and (2) final products are $N^+(^3P^e) + O(^1D^e, ^3P^e)$.

[1] V. Cermak, J. Electron Spectrosc. Relat. Phenom., **3**, 329 (1974).

[2] S. Boumsellek and V. A. Esaulov, J. Phys. B, **23**, L605 (1990).

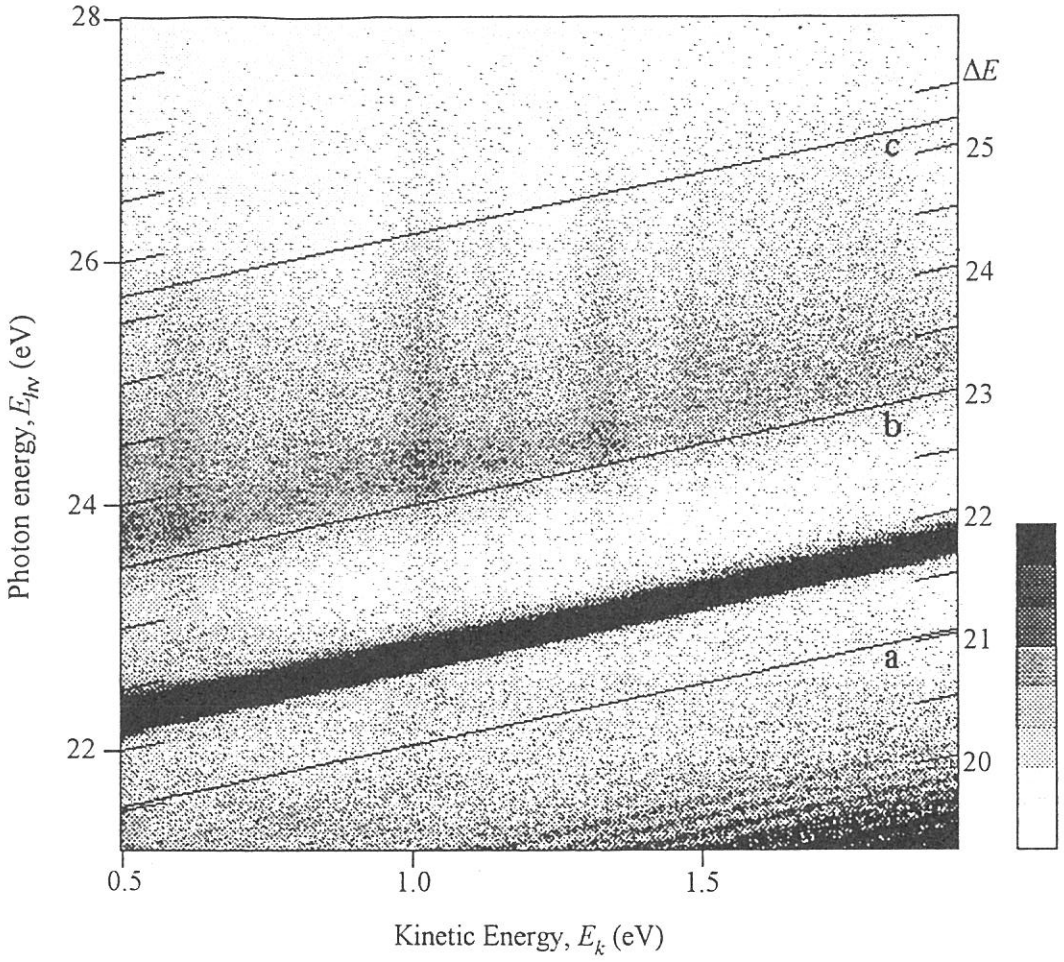

Figure 1. Two-dimensional photoelectron spectrum of NO in the photon energy range 21.2 - 28 eV. The electron counts are shown increasing from light to dark on a linear scale. The solid lines **a**, **b** and **c** represent the dissociation limits of NO for $N^+(^3P^e) + O(^3P^e)$, $N^+(^3P^e) + O(^1D^e)$ and $N^+(^3P^e) + O(^1S^e)$ channels, respectively.

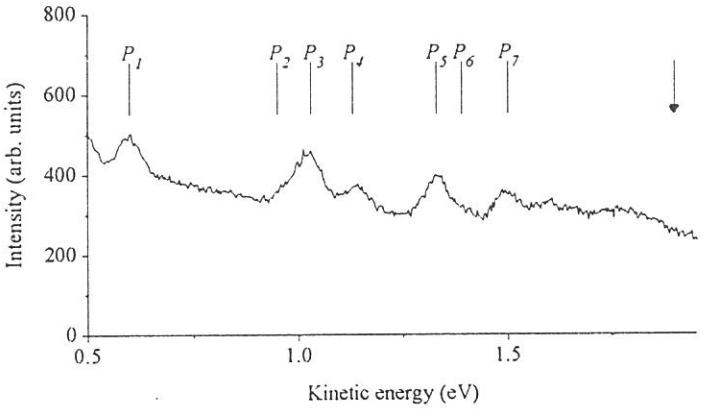

Figure 2. Kinetic energy spectrum of autoionization fragments derived by summing electron counts over the ΔE = 22.5 - 26 eV range along the direction of constant kinetic energy. The arrow represents the converging limit of the Rydberg states for the peaks P_1 - P_7.

(BL3B)

Two-dimensional photoelectron spectroscopy of C_2H_2

Hideo HATTORI, Yasumasa HIKOSAKA*, Takumi HIKIDA*, and Koichiro MITSUKE

Department of Vacuum UV Photoscience, Institute for Molecular Science, Myodaiji, Okazaki 444

** Department of Chemistry, Tokyo Institute of Technology, Ohokayama, Meguro 152*

In the photoionization cross section of C_2H_2, there is a broad enhancement around 13.3 eV, of which the origin(s) have attracted much attention. On the basis of photoelectron spectra of C_2H_2 and C_2D_2 and a CIS (constant-ionic-state) spectrum for the v_1=3 vibrational level, we concluded that this feature is attributed to autoionization of a valence state $(3\sigma_g)^{-1}(3\sigma_u)^1$, which leads to strong excitation of the C-H symmetric stretching mode (ν_1) [1]. Photoelectron spectra between 12.8 and 14.1 eV, however, indicate that the vibrational distribution in $C_2H_2^+(X\,^2\Pi_u)$ differs from one photon energy to another. Therefore, it is necessary to investigate the dependence of the vibrational distribution on the photon energy and to measure CIS spectra for other vibrational levels. This gives us a motivation to perform two-dimensional photoelectron spectroscopy of C_2H_2.

Figure 1 shows a two-dimensional photoelectron spectrum obtained in the photon energy range between 13.0 and 14.5 eV [2]. Structures parallel to the photon energy axis correspond mainly to the vibrational levels of the ν_1 and/or ν_2 (C-C stretching) modes of $C_2H_2^+(X\,^2\Pi_u)$. A plot of the electron intensity for each level as a function of the photon energy gives a CIS spectrum.

The positions of the valence state $(3\sigma_g)^{-1}(3\sigma_u)^1$ and the Rydberg state $(3\sigma_g)^{-1}(3p\pi_u)^1$ are indicated in Fig. 1. The relative intensity at $v_1 \geq 3$ is much smaller in the Rydberg state than in the valence state. This difference in the vibrational distribution may be attributed to the difference in the equilibrium structures between the two excited states.

The CIS spectra for the (v_1,v_2)=(3,0),(3,1),(4,0), and (4,1) vibrational levels of $C_2H_2^+$ $(X\,^2\Pi_u)$ are shown in Fig. 2. Each curve indicates a broad peak structure due to the $(3\sigma_g)^{-1}(3\sigma_u)^1$ state. Furthermore, there are two progressions on the broad peak in each curve, which are previously observed for the (3,0) level [1]. They correspond to vibrational levels of the $(3\sigma_g)^{-1}(3\sigma_u)^1$ state, presumably in the C-C and C-H stretching modes. A closer inspection reveals shifts of the peaks by about 20 meV between the (3,0) and (4,0) curves. Similar shifts are also observed between the (3,1) and (4,1) curves. On the contrary, the positions of the peaks agree well between the CIS spectra with the same v_1, *e.g.*, the (3,0) and (4,0). This result can be explained in terms of the boomerang model, proposed by Herzenberg [3]. Possibly, the autoionization lifetime of the $(3\sigma_g)^{-1}(3\sigma_u)^1$ state is comparable with periods of the ν_1 and ν_2 motion, and vibrational states of the $(3\sigma_g)^{-1}(3\sigma_u)^1$ have no stationary wave function. The peak shifts between the (3,0) and (4,0) curves may be too small to be detected because of the coarse intervals of 1 Å in this measurement of the two-dimensional spectrum.

References

[1] K.Mitsuke and H.Hattori, J. Chem. Phys. **102**, 5288 (1995).

[2] H.Hattori and K.Mitsuke, J. Electron Spectrosc. Relat. Phenom., in press.

[3] A.Herzenberg, J. Phys. B **2**, 548 (1968).

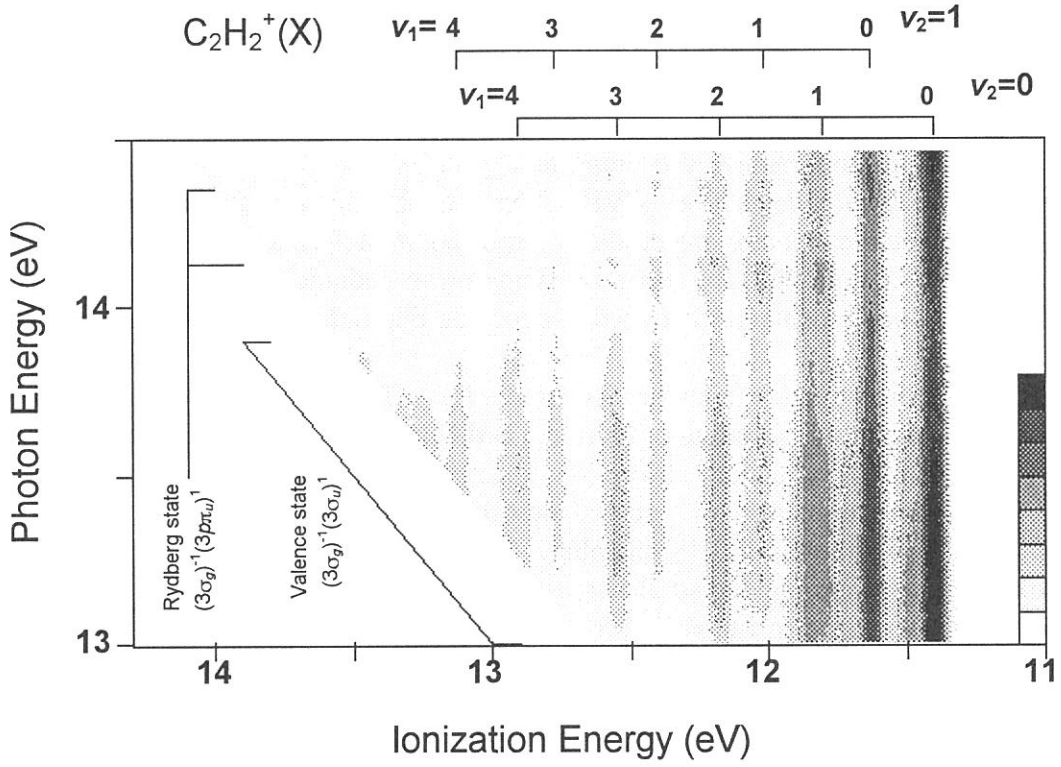

Figure 1. Two-dimensional photoelectron spectrum of C_2H_2. The electron yields are presented by the plots with eight tones from light to dark on a logarithmic scale.

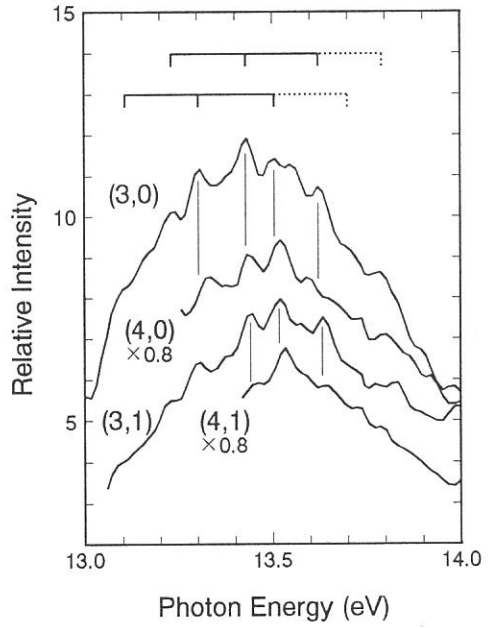

Figure 2. CIS spectra for the (v_1,v_2) = (3,0), (3,1), (4,0), and (4,1) levels. For clarity the intensities for the (4,0) and (4,1) curves are multiplied by 0.8. Marked lines indicate two v_1 progressions in the $(3\sigma_g)^{-1}(3\sigma_u)^1$ state, and dotted lines less unambiguous features.

(BL4A)

Synchrotron radiation irradiation effects on low-temperature condensed layer of dimethyl aluminum hydride on SiO_2 surface

Yoshiaki Imaizumi [a], Yoshiyuki Tsusaka [b], Tsuneo Urisu [b]

[a] *The Graduate University for Advanced Studies and* [b] *Institute for Molecular Science, Myodaiji, Okazaki, 444 Japan*

Organoaluminum compounds are important precursors for aluminum thin film formation by chemical vapor deposition (CVD). The low-temperature condensed layer of these compounds on semiconductor materials is expected to be useful for area-selective deposition of aluminum thin films by laser or synchrotron radiation (SR) beam induced processes. However, our fundamental knowledge about its photochemical properties is very limited.

In this work, the structure and the SR irradiation effects on the low-temperature condensed layer of dimethyl aluminum hydride (DMAH) were investigated by *in situ* measurements of infrared reflection absorption spectroscopy (IRAS), quadrupole mass spectrometer (QMS) measurements for neutral desorbed species, and x-ray photoelectron spectroscopy (XPS), using the same UHV chamber.

The experiments were conducted at beam line 4A of the SR storage ring (UVSOR, beam energy 0.75 GeV) at the Institute for Molecular Science. The ring current was about 10 mA for single-bunch and about 100 mA for multi-bunch. The beam covered the wavelength range longer than 1 nm with its peak at about 10 nm. In the case of the single-bunch, the beam was used without attenuation, but in the multi-bunch, it was attenuated by using a stainless steel mesh. The calculated photon flux on the 1×1 cm^2 sample surface was 1.1×10^{15} photons/s (36 mW) for the single-bunch and $2 \pm 1 \times 10^{15}$ photons/s (65 mW) for the attenuated multi-bunch. The substrates can be cooled to about 110 K by a steady liquid nitrogen flow. The substrate temperature was controlled by electrical current heating and could be read via a chromel-alumel thermocouple attached to the rear of the sample. The error of the temperature reproducibility was less than 2 K. The 60 nm thick amorphous Si (a-Si) / Al / Si (100) structure buried metal layer [1] substrate for IRAS and TPD, and the Si (100) substrate for XPS were used without removing the surface native oxide, so the chemical nature of the substrate surface should be that of SiO_2.

Figure 1 shows how the C/Al ratio changes depending on single-bunch SR irradiation and on plain heating. It is reported that MgK_α irradiation decomposes DMAH [2]. So the change of C/Al by MgK_α irradiation is also shown in Fig. 1. The decrease of C/Al ratio by the plain heating suggests the desorption of C possibly in the form of CH_4 from the DMAH chemisorbed layer, which is shown in the TPD data to exist on the SiO_2 surface. It is shown that SR irradiation decreases the C/Al ratio, but MgK_α irradiation does not. In the case of single-bunch, it has been assured by IRAS and XPS that the rapid desorption of physisorbed layer is not induced even by the continuous irradiation. That is, the surface temperature of photo-thermal effect should be less than 175 K in the single-bunch irradiation. Therefore, it is considered that the observed decrease of C/Al ratio by single-bunch SR irradiation in Fig.1 is mainly due to the photo-decomposition by SR. With the Al2p and C1s XPS signals, the chemical shift (about - 0.6 eV) of binding energy and the spectrum broadening of the FWHM

(2.7→3.7 eV) were observed, respectively. These results qualitatively agree with the results of the 193 nm excimer laser irradiation on DMAH condensed layer [3]. Qualitative evaluations of the chemical shifts are going to be made in the next step.

SR irradiation on the DMAH low temperature condensed layer induces both photo-thermal and photo-decomposition reactions. The DMAH condensed layer changes its adsorbing states from the as-deposited mixture of dimer and trimer to the trimer dominant form by the photo-thermal effect. The C/Al ratio of the condensed layer is substantially decreased by the photo-decomposition induced by SR irradiation, but it is not decreased by the decomposition by MgK_α irradiation on XPS. This difference may be due to the difference of the excitation photon. energy. This point is going to be studied in the succeeding experiments.

REFERENCES

1. Y. Imaizumi, Y. Zhang, Y. Tsusaka, S. Sato and T. Urisu., *J. Molecular Structure*, **352/353** (1995) 447.
2. M. Okawa, H. Tsuruta, and M. Hanabusa, *Appl. Surf. Sci.*, **79/80** (1994) 444.
3. M. Ohashi, S. Shogen, M. Kawasaki and M. Hanabusa, *J. Appl. Phys.* **73** (1993) 3549.

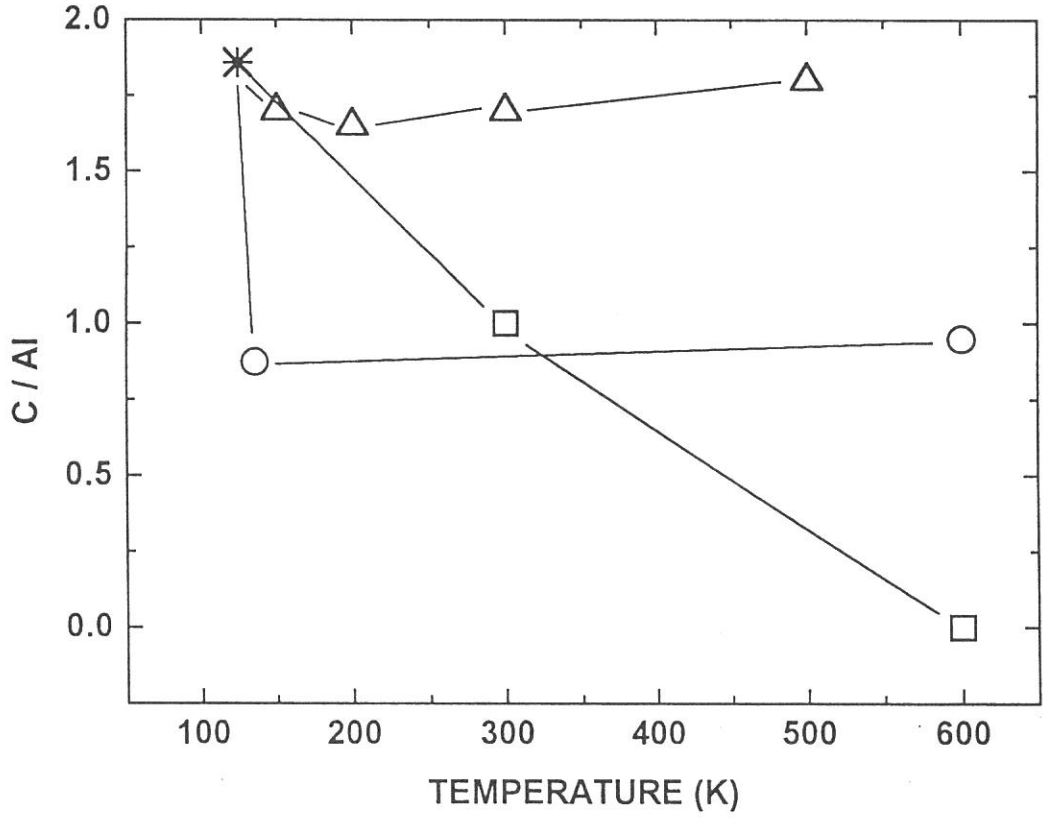

Fig. 1 Change of C/Al ratio by SR irradiation MgK_α irradiation and substrate plain heating. (＊) as-deposited sample, (○) samples heated after 500 mAmin SR irradiation, (△) samples heated after MgK_α irradiations(2～3 hours), and (□) samples with plain heating.

(BL4A)

Photodissociation of Dimethylaluminu Hydride Adsorbed on SiO_2

Mitsugu Hanabusa, Toshinari Nitta, Masahiko Kikuchi, Hironaga Uchida,
Yoshiaki Imaizumi* and Tsuneo Urisu*

Department of Electrical and Electronic Engineering, Toyohashi University of Technology, Tenpaku, Toyohashi 441

** Institute for Molecular Science, Myoudaiiji, Okazaki 444*

Adsorption of dimeythlaluminum hydride (DMAH) on solid surfaces and subsequent dissociation of adsorbates are important as the steps to be followed for the deposition of Al thin films, which are used widely for the interconnection in large scale integrated circuits.[1] For practical purposes a low-temperature processing is highly desirable, and the UV light often assists the dissociation. Among various UV sources, we preferred to use a deuterium lamp, which emits the UV light in two broad bands centered at 160 nm and 240 nm. More recently, we began testing excimer lamps, such as a xenon dielectric barrier discharge lamp.

Recently new light sources that generate high energy photons became available. Needless to say, synchrotron radiation represents the new generation of the light sources. However, it is not easy to get an access to this big machine. Therefore, we were delighted when we discovered that the X-ray source used for X-ray photoelectron spectroscopy (XPS) induced the dissociation of chemisorbed species of DMAH on SiO_2. Namely, when we were carrying out a diagnostic work on the reaction processes involved in the initial stage of the Al film deposition, it became clear that the Al Kα line (1486.6 eV) modified the XPS signals observed for the adsorbates. The C signals showed a tendency to decrease in intensity with time, and at the same time Al2p signal peaks changed their position (namely, binding energy).[2] Since the Al signal strength remained unchanged during this investigation, we concluded that the temporal change corresponded to the dissociation of the chemisorbed species, rather than photodesorption induced by the Al Kα line. The results obtained at three different substrate temperatures are shown in Fig. 1(a).

This inspired us to carry a new experiment using the UVSOR BL4A line. The X-ray source of the XPS apparatus installed on this lime was equipped with Mg, and using

the Mg Kα line (1253.6 eV) we observed a similar shift of the Al2p binding energy with time also. Then, we irradiated the UVSOR white light and obtained the data shown in Fig. 1(b). Unfortunately, many unlucky events kept happening during the experiment, and we did not have time to check the validity of the data. Therefore, the result shown in Fig. 1(b) should be regarded as preliminary.

At first we hoped to select two possible explanations for the X-ray induced dissociation of the chemisorbed species, namely, dissociation by secondary electrons generated by the high-energy photons or direct photodissociation. The energy distribution of the secondary electrons generated by the Al Kα line exhibited a peak near 20 eV, just fitted for electron-induced dissociation. We hoped to take a similar data using UVSOR, which should clarify the dissociation mechanism furthermore, but it could not be done on the BL4A line, because the radiation did not hit the substrate placed for the XPS measurement. Therefore, the task to clarify the mechanism is also left as homework presently.

References

1) M. Okawa, H. Tsuruta and M. Hanabusa, Appl. Surf. Sci. 79/80, 444(1994).

2) T. Nitta and M. Hanabusa, Abstracts of the 55th Fall Meeting of the Jpn. Soc. Appl. Phys., Nagoya, September, 1994, p.743.

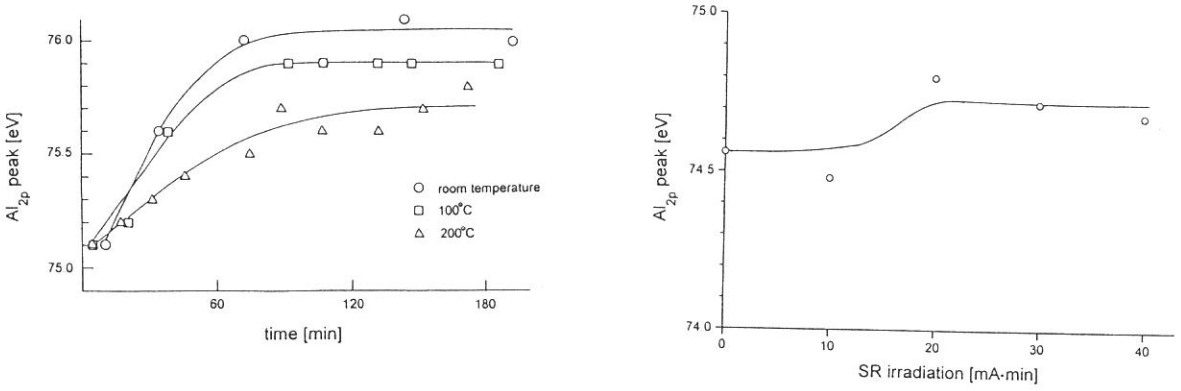

(a) (b)

Fig. 1 The temporal behavior of the Al2p XPS peaks observed from chemisorbed species of DMAH on SiO_2: (a) induced by Al Kα line and (b) by UVSOR.

Synchrotron Radiation Irradiation Effects for SiH_n on Si(100) Surface in the Synchrotron Radiation Stimulated Si Gas Source Molecular Beam Epitaxy

A.Yoshigoe[a], M.Nagasono[b], K.Mase[b], and T.Urisu[b]

[a]The Graduated University for Advanced Studies, Myodaiji, Okazaki 444

[b]Institute for Molecular Science, Myodaiji Okazaki 444

Synchrotron radiation stimulated silicon gas source molecular beam epitaxy using Si_2H_6 (SR-GSMBE) can deposit the silicon single crystal at substrate temperatures below 400℃ where it is impossible by thermal GSMBE. However, it is reported that the crystallinity of the deposited film by SR-GSMBE significantly degraded below 230℃. Silicon hydrides (SiH_n) on the surface or in the deposited films have been thought to make the crystallinity of deposited films worse. However, nothing is known about the characteristics of adsorbed species and their responses to the SR irradiation, which may be the most important information for improving the crystallinity in the low temperature region. In this study, we have investigated the SR irradiation effects for SiH_n on the Si(100) surface by means of infrared reflection absorption spectroscopy using a $CoSi_2$ buried metal layer substrate (BML-IRAS).

Figure 1 shows the SR irradiation effects on the surface SiH_n deposited on the Si(100) BML substrate during SR-GSMBE at 140℃ and 1.0×10^{-3}Torr. For the SiH_n stretching vibrational region, the curve resolution analysis is examined assuming the presence of three peaks with Lorenzian forms for SiH_3, SiH_2 ,and SiH. Figure 2 shows the dependence of the SiH_n vibrational peak intensity on the SR irradiation dose. The intensity of SiH_3 and SiH_2 peaks decrease gradually with an increasing SR irradiation dose for both stretching and bending vibrational regions. On the other hand, the intensity of SiH gets stronger with an increasing SR dose up to about 6000mA·min, then saturates, that is, becomes almost independent of the SR irradiation. Thus, it is simply concluded that SiH_3 and SiH_2 are decomposed to SiH by SR irradiation and the decomposition rate of SiH is extremly slow.

The data of Fig. 2 are explained by the model assuming that the dominant surface reactions are

$$SiH_2(ads) + h\nu \rightarrow SiH\ (ads) + d.s. \quad \cdots\cdots(1)$$

$$SiH_3(ads) + h\nu \rightarrow SiH\ (ads) + d.s. \quad \cdots\cdots(2)$$

$$SiH_3(ads) + h\nu \rightarrow SiH_2(ads) + d.s. \quad \cdots\cdots(3)$$

Here (ads) means the adsorbates on the surface, and d.s. means the desorbed species in the gas phase. From the rate equations expressing these reactions, the reaction cross sections have been calculated to be $\sigma_2 = 5.7\times10^{-20}\ cm^2$ and $\sigma_3+\sigma_3' = 1.7\times10^{-19}\ cm^2$. Here, $\sigma_2, \sigma_3, \sigma_3'$ are the reaction cross sections for the equations (1), (2) and (3). The curve for SiH in Fig. 2 indicates that the decomposition cross section (σ_1) for SiH is much smaller than these values. It must be noted that these reaction cross section values are estimated without considering the excitation photon energy dependence. It has been reported that the localized multihole states excited by core level excitations are important dissociation channels in Si(100): H.[1,2] In the above calculations, the reaction cross sections are evaluated for the non-monochromatized photons, among which the photon flux contributing to the excitation of Si $L_{2,3}$ core levels is roughly 10 %. Therefore, if it is assumed that the present decomposition reactions are mainly

induced by the Si $L_{2,3}$ core level excitations followed by Auger processes, the reaction cross sections based on this assumption which are denoted here as σ_{nc} corresponding to σ_n, are roughly estimated to be $\sigma_{2c} = 5.7\times10^{-19}cm^2$ and $\sigma_{3c} + \sigma_{3c'} = 1.7\times10^{-18}cm^2$. The absorption cross section of Si $L_{2,3}$ core level in the SiH_4 molecule has been reported to be $4.0\times10^{-18}cm^2$.[3] Although we have not yet analyzed the details of the interaction between SiH_n valence multiholes and the substrate electrons, it is considered that the interaction determines the lifetime of the SiH_n valence multihole state and $\sigma_1 < \sigma_2 < \sigma_3$ is predicted from the surface structure, where SiH_3, SiH_2 and SiH combine with substrate Si atoms through one, two and three covalent bonds.

1) D.E.Ramaker,J.Vac.Sci.&Technol.A1(1983)1137.

2) H.H.Madden,D.R.Jennison,M.M.Traum,G.Margaritondo and N.G.Stoffel,Phys.Rev.B26(1982)896.

3) E.Ishiguro,K.Soda,A.Mikuni,Y.Suzuki,S.Iwata and T.Susaki,ISSP ACT.Rep.(1982)66.

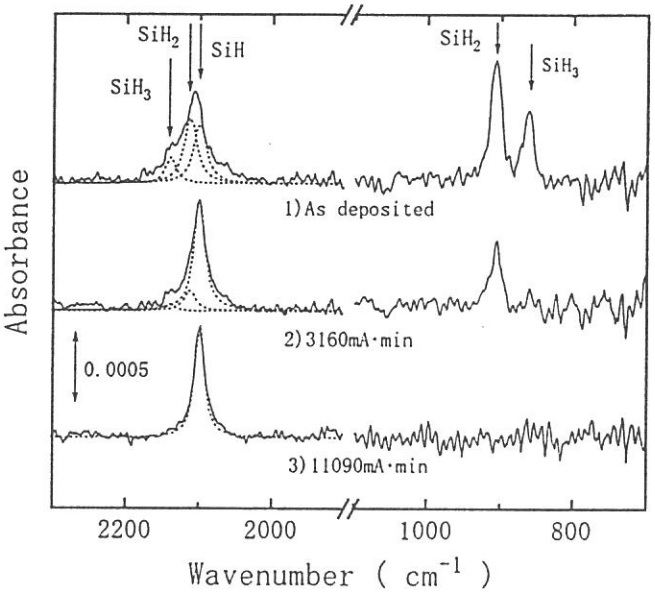

Figure 1. SR irradiation effects on the surface SiH_n. 1) IRAS spectrum was measured just after the SR-GSMBE at 140℃ and 1.0×10^{-3}Torr Si_2H_6 gas pressure. Then the spectrum changed to 2) by SR irradiation of 3160mA·min without Si_2H_6 gas, then to 3) by SR irradiation of more 7930mA·min.Results of the curve resolution analysis are shown by broken lines in the stretching vibrational regions.

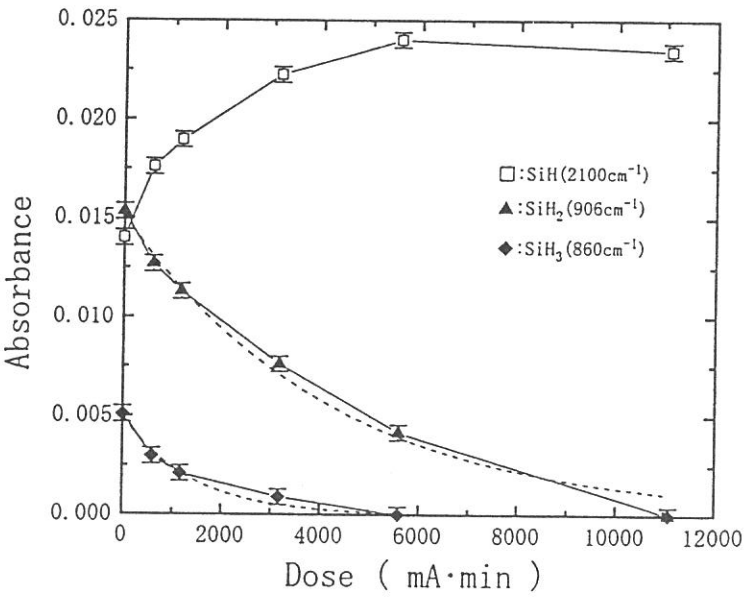

Figure 2. Change in the vibrational peak intensity as a function of irradiation dose for SiH, SiH_2, and SiH_3. The results of the curve fitting are given by broken lines for SiH_2 and SiH_3.

In situ observation of silicon hydrides on Si(100) surfaces during synchrotron-radiation-stimulated Si_2H_6 gas source molecular beam epitaxy

A.Yoshigoe[a], K.Mase[b], Y.Tsusaka[b], and T. Urisu[b], Y.Kobayashi[c] and T.Ogino[c]

[a]The Graduate University forAdvanced Studies, Myodaiji, Okazaki 444

[b]Institute for Molecular Science, Myodaiji, Okazaki 444

[c]NTT Basic Research Laboratories, Atsugi-shi, Kanagawa 243-01

Synchrotron radiation stimulated gas source molecular beam epitaxy (SR-GSMBE) is an interesting low-temperature epitaxial growth technique. Many studies have been carried out, however, the reaction mechanisms have not been made clear yet[1,2]. Silicon hydrides (SiH_n) on the substrate surface during epitaxial growth are thought to be the key species controlling the deposition rate and the crystallinity in GSMBE using SiH_4 or Si_2H_6 gases, especially at low temperatures (≦700℃)[3,4]. However, SiH_n has not yet been detected in situ during SR-GSMBE.

In this work, we have observed the vibrational spectra of SiH_n on the Si(100) surfaces during SR-GSMBE using Si_2H_6 gas, and the effects of the substrate temperature (≦400℃) and the SR irradiation have been investigated by means of infrared reflection absorption spectroscopy using a $CoSi_2$ buried metal layer substrates (BML-IRAS).

Fig. 1 shows the IRAS spectra measured just after the deposition for several deposition temperatures (≦400℃). The observed vibrational bands are assigned to the stretching vibrations of surface SiH_3(2140cm^{-1}), SiH_2(2113cm^{-1}), SiH(2100cm^{-1},2092cm^{-1}) and to the bending scissors vibration of SiH_2(908cm^{-1}) and the degenerate deformation vibration of SiH_3(860cm^{-1})[5-7]. The stretching vibration of the bulk network SiH(2000cm^{-1}) [8]was not observed even after deposition dose of 3000-4000mA·min. From the temperature dependence of the IRAS spectrum shown in Fig.1, it is concluded that SiH is a dominant species at high temperatures (400 and 370℃), and with temperature decrease from 275 to 50℃, the number of SiH decrease, and on the other hand, SiH_2 and SiH_3 appear and increase.

Fig. 2 shows the effects of SR irradiation on the surface SiH_n deposited by SR-GSMBE at 140℃. Curve A is the IR spectrum just after the deposition at 140℃ under 1.0×10^{-3}Torr of Si_2H_6 gas and at a deposition dose of 3115mA·min. Curve B is the IR spectrum after SR irradiation of 11090mA·min without Si_2H_6 gas on the curve A sample. Curve B-A is the difference spectrum between B and A. The curve resolution analysis at the SiH_n stretching vibrationalregion was examined assuming the three peaks with Lorenzian forms for SiH_3, SiH_2 and SiH stretching vibrations. It has been found that the surface SiH_3 and SiH_2 are decomposed to SiH by SR irradiation. It has been found that the decomposition rate of SiH is extremely slow. The different decomposition rates of SiH, SiH_2, and SiH_3 may be due to the different lifetime of the electronic excited state (valence holes)[9].

References

1) J.Takahashi, Y.Utsumi, H.Akazawa, I.Kawashima, and T.Urisu. Appl.Phys.Lett. 58, 2276(1991).

2) Y.Utsumi, J.Takahashi, H.Aakazawa, and T.Urisu. Jpn.J.Appl.Phys. 30,3195(1991).

3) T.Urisu, T.Akutsu, and K.Kuchitsu. Appl.Phys.Lett. 62,2821(1993).

4) T.Urisu, J.Takahashi, Y.Utsumi, T.Akutsu, and K.Kuchitsu. J.Electrochem.Soc. 141,1562 (1994).

5) Y.J.Chabal, G.S.Higashi, K.Raghavachari, and V.A.Burrows. J.Vac.Sci.Technol. A7, 2107(1989).

6) Y.J.Chabal. Surf. Sci. 168, 594(1986).

7) G.Lucovsky, R.J.Nemanich, and J.C.Knights. Phys.Rev. B16, 3556(1979).

8) Y.Toyoshima, K.Arai, A.Matsuda, and K.Tanaka. Appl.Phys.Lett. 57,1028(1990).

9) D.R.Jennison and D.Emin. Phys.Rev.Lett. 51,1390(1993).

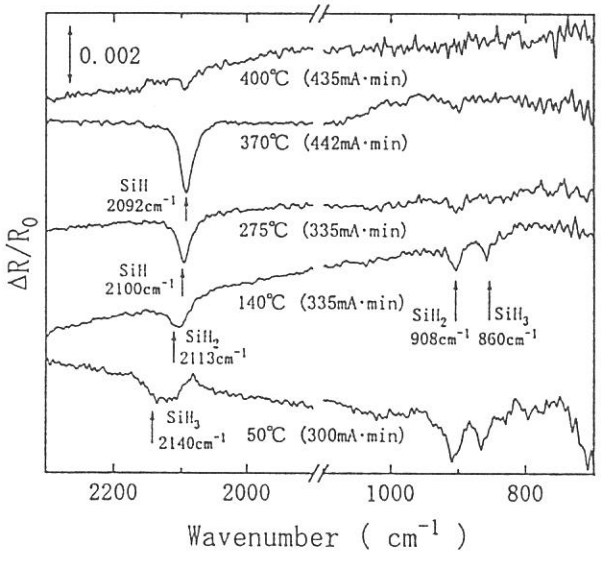

Figure 1. IRAS spectra of films deposited on the Si(100) BML substrate at various substrate temperatures by SR-GSMBE at 1.0×10^{-3}Torr Si_2H_6 gas pressure. Values in parentheses are the SR dose.

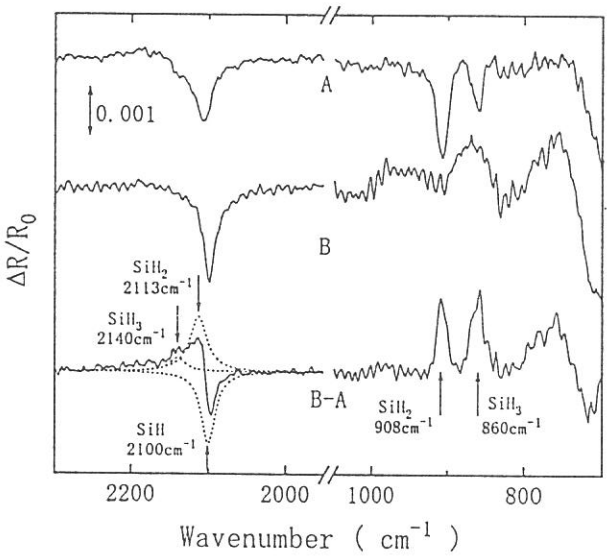

Figure 2. Changes of the IRAS spectra due to SR irradiation at 140 ℃. (A)the spectrum just after the deposition at 140℃ under 1.0×10^{-3}Torr of Si_2H_6 gas and by a deposition dose of 3115mA · min. (B)after SR irradiation of 11090mA·min without Si_2H_6 on the sample A. (B-A) the difference spectrum between B and A. Results of the curve resolution analysis assuming three peaks with Lorentzian form for SiH_3, SiH_2 and SiH stretching vibrations are shown by broken lines. The peakes indicated by arrows are assigned as (b) SiH,2100cm^{-1};(c) SiH_2,2113cm^{-1};(d) SiH_3,2140cm^{-1};(e) SiH_2,908cm^{-1}; and (f) SiH_3,860cm^{-1}.

In Situ Detection of Surface SiH_n in Synchrotron-Radiation-Induced Chemical Vapor Deposition of *a*-Si on an SiO_2

Akitaka Yoshigoe [a], Mitsuru Nagasono [b], Kazuhiko Mase [b], Tsuneo Urisu [b], Setsuko Seki[c] and Yoshitsugu Nakagawa[d]

[a]The Graduate University for Advanced Studies, Myodaiji, Okazaki 444

[b]Institute for Molecular Science, Myodaiji, Okazaki 444

[c]Faculty of Engineering, Takushoku University, Hachioji-shi, Tokyo 193

[d]Toray Research Center, Inc., Otsu, Shiga 520

Silicon hydrides (SiH_n) on the substrate surface or in the depositied films in synchrotron radiation induced chemical vapor deposition (SR-CVD) using Si_2H_6 gas are important species to analyze the reaction mechanisms, since the growth rate and the crystallinity of the deposited films are influenced by SiH_n.[1] However, *in situ* observation of SiH_n has not yet been attained.

Infrared reflection absorption spectroscopy using a buried metal layer substrate (BML-IRAS) which has a metal layer buried under a thin semiconductor or insular film (buffer layer) that is much thinner than the wavelength of IR is suitable for monitoring adsorbates on the semiconductor or insulator surfaces[2,3].

In this work, the sensitivity and the linearity of the BML-IRAS method have been evaluated by using Langmuir-Blodgett (LB) films of barium stearate deposited on BML substrate with SiO_2(15nm)/Al(200nm)/Si(100) structure, then the BML-IRAS technique has been used to monitor the surface SiH_n *in situ* in SR-CVD using Si_2H_6.

Fig. 1 shows the comparisons of the IRAS spectra of LB films deposited on the BML substrate and Si(100) substrate for various infrared beam incident angles. The LB film thickness was five monolayers. The improved performance of BML substrates can be clearly seen: the peaks in the BML spectra all increase gradually with increasing incident angle, and have sufficient sensitivity for one-monolayer film thickness. On the other hand, in the case of the Si substrate, the signal distortion is significant and depends on the wavelength and the incident angle.

Fig. 2 shows the IRAS spectra of *a*-Si observed *in situ* after deposition at 423K with several different doses (=storage ring current×irradiation time). The deposition rate was about 0.03nm/100mA・min, so the present BML-IRAS technique has sufficient sensitivity to detect submonolayer adsorbates of SiH_n. The 950 cm^{-1} peak is assigned to Si-O-Si stretching vibration in the O-doped *a*-Si[4]. The 860 and 908cm^{-1} peaks are assigned to SiH_3 symmetric deformation and SiH_2 bending scissor vibrations, respectively. The peak at 2109cm^{-1} was constructed by SiH_3 symmetric stretching (2140cm^{-1}), SiH_2 symmetric stretching (2113cm^{-1}), and SiH stretching vibrations. From these results, SiH_2 and SiH_3 have been found to be the main adsorbates at 423K in SR-CVD.

References

1) T.Urisu, J.Takahashi, Y.Utsumi, T.Akutsu, and K.Kuchitsu. J.Electrochem.Soc. 141, 1562(1994).

2) M.McGonigal, V.M.Bermudez, and J.E.Butler, J.Electron Spectrosc. Relat. Phenom. 54/55, 1033(1990).

3) W.Ehrley, R.Butz, and S.Mantl, Surf.Sci, 248, 193(1991).

4) P.G.Pai, S.S.Chao, Y.Takagi, and G.Lucovsky. J.Vac.Sci.Technol. A4, 689(1989).

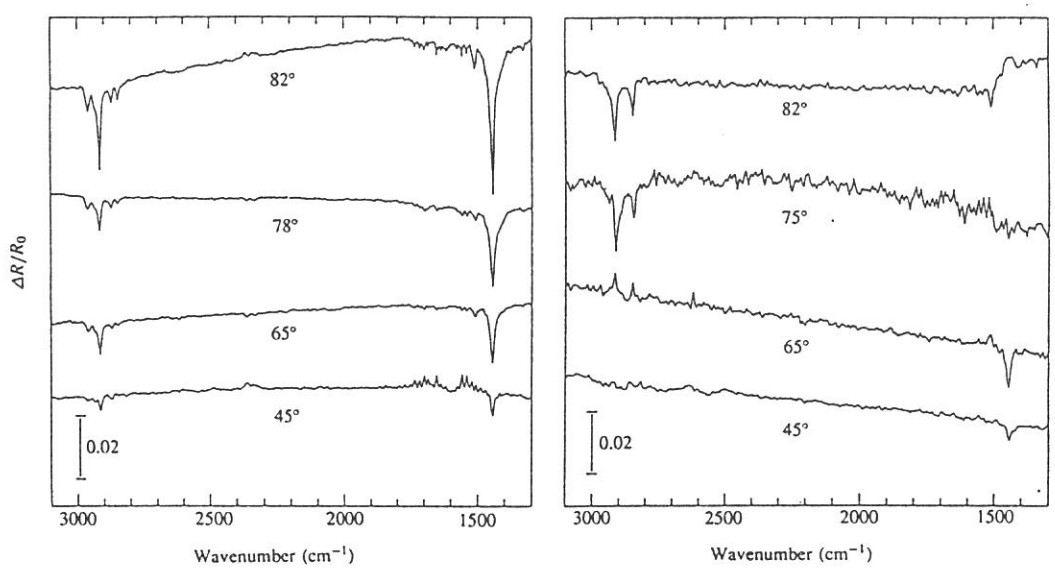

Figure 1. Observed IRAS spectra of five monolayers of barium stearate Langmuir-Blodgett film deposited on the SiO_2 BML substrate (left) and on the Si(100) substrate (right) for various infrared beam incident angles.

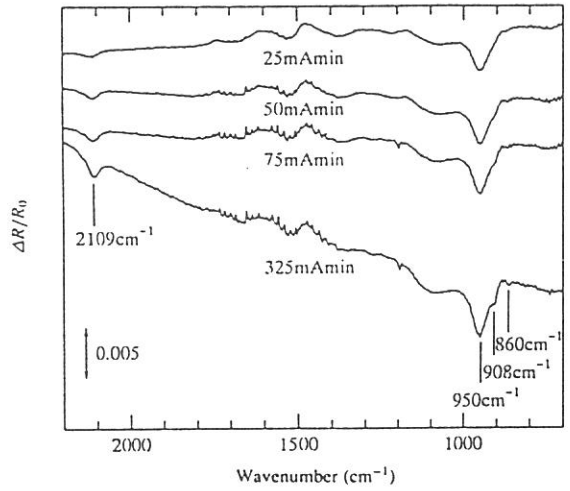

Figure 2. The IRAS spectra of the in situ observation with the *a*-Si deposited by SR-CVD on the SiO_2 BML substrate. The dose (storage ring current×irradation time) dependence is shown. The substrate temperature was 423K. The Si_2H_6 gas pressure was 1.0×10^{-3}Torr.

(BL5A)

Construction of SGM-TRAIN at BL5A

M. Kamada, K. Sakai, M. Hasumoto, N. Mizutani, T. Horigome, S. Kimura, S. Hirose,
and K. Fukui[a]
UVSOR, Institute for Molecular Science, Myodaiji, Okazaki 444
[a]College of Engineering, Fukui Univ., Fukui 910

A new monochromator called SGM-TRAIN (Spherical Grating Monochromator with Tranlational and Rotational Assemblies Including Normal-incident-mount) has been designed for the use of circularly polarized lights (1). The SGM-TRAIN is an improved version of the constant deviation and constant length monochromator (CDCL-SGM) designed by Ishiguro et al. (2). The SGM-TRAIN and its pre-mirror system have already been constructed and now the test of the performance is in progress. In the followings, a part of the results in testing the SGM-TRAIN is given, although the SGM-TRAIN is tentatively aligned along a beam line with 152 ° in horizontal direction and will move to a new beam line, where circularly polarized lights from a new helical undulator are available (3).

Figure 1 shows the drawing of SGM-TRAIN, which has a constant length of 3500mm between entrance and exit slits. The length can be changed by 40 mm. A grating-and-mirror chamber translates with rotating a grating in order to get a good focus by following the Rowland condition approximately. This requires the stable and precise motion of the chamber. The vertical displacement of the monochromator stage during the 1400 mm travel of the chamber was checked to be within 30 μm by using a laser-measurement system (HP 5528A). This displacement corresponds to 0.05 eV at 100 eV. However, the reproducibility of the displacement is so high (less than 2 μm) that the effect may be canceled by our new driving system, which can translate the chamber and rotate gratings independently.

Figure 2 shows photoelectron yield spectra from an Au-mesh with slits of 0.1 mm. The Au-mesh was located about 300 mm after an exit slit, since a post-mirror chamber was not ready in the present test. The output spectra cover the wide energy range from 6 to 150 eV with three gratings. The present photon fluxes obtained with G1M21 and G2M22 combinations are $4x10^{10}$ and $6x10^{11}$ /s around 120 eV, respectively. It should be noted that this output is not our final performance of the SGM-TRAIN. Expected maximum energy is 250 eV and calculated photon flux in the combination of G1M21 is about $5x10^{11}$/s for a resolving power of 1000. The difference between our calculation and the present results may be partly due to the experimental conditions for testing such as the horizontal reflection angle of 152 ° and no post-mirror, and also due to the real efficiency of mirrors and gratings. Moreover, the result shown in Fig.2 is the first output we obtained this January. We will continue the fine adjustment of optical elements to get final performance of the SGM-TRAIN.

References
(1) M. Kamada, K. Sakai, S. Tanaka, S. Ohara, S. Kimura, A. Hiraya, M. Hasumoto, K. Nakagawa, K. Ichikawa, K. Soda, K. Fukui, Y. Fujii, and E. Ishiguro, Rev. Sci. Instrum. 66, 1537 (1995).
(2) E. Ishiguro, M. Suzui, J. Yamazaki, E. Nakamura, K. Sakai, O. Matsudo, N. Mizutani, F. Fukui, and M. Watanabe, Rev. Sci. Instrum. 60, 2105 (1989).
(3) S. Kimura, M. Kamada, H. Hama, X. M. Marechal. T. Tanaka, and H. Kitamura, to be published in Proc. of VUV 11.

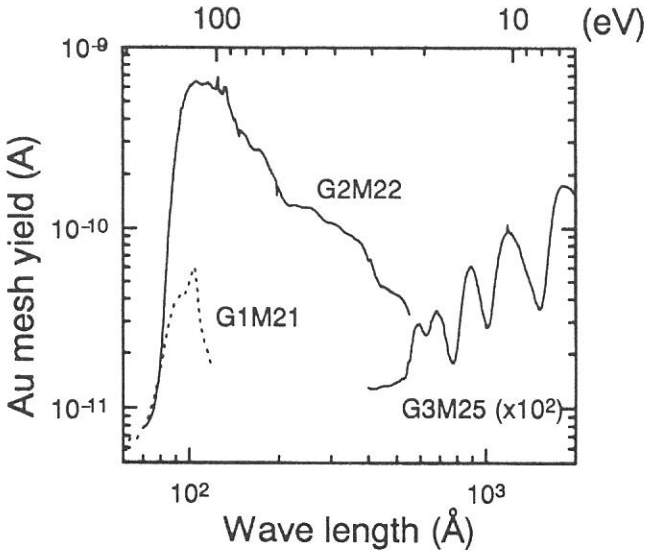

Fig. 2 Yield spectra from an Au-mesh with slits of 0.1 mm

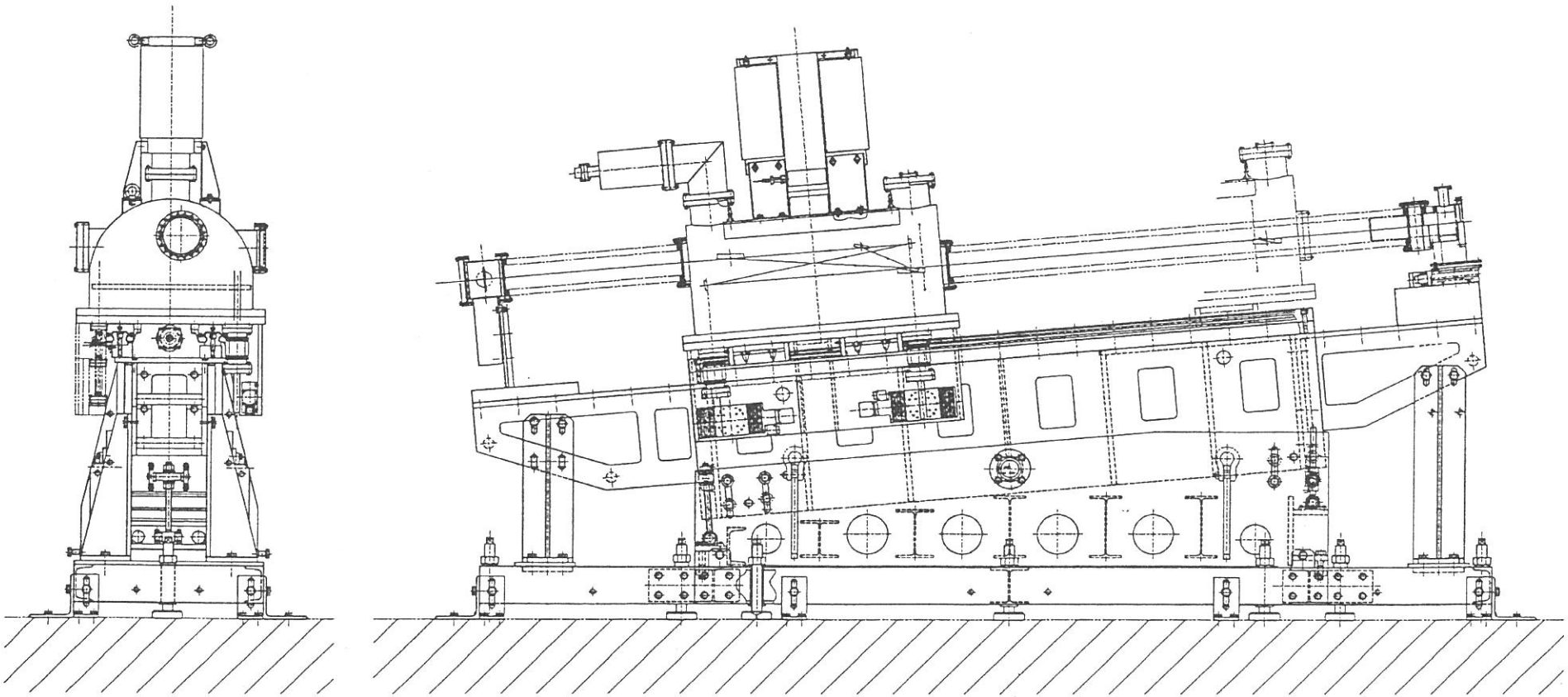

Fig. 1 Drawing of SGM-TRAIN

(BL5A)

Construction of a Spin- and Angle-Resolved Photoelectron Spectrometer

Naoshi TAKAHASHI[1,2], Masatake ICHIKAWA[3], Koichi NAKANISHI[4,*], Yasuo FUJII[4], Shigeo OHARA[5], Shin-ichiro TANAKA[1] and Masao KAMADA[1]

[1]*Institute for Molecular Science, Myodaiji, Okazaki 444*
[2]*The Graduate University for Advanced Studies*
[3]*College of Engineering, Fukui University, Fukui 910*
[4]*Osaka City University, Osaka 558*
[5]*Nagoya Institute of Technology, Nagoya 466*

Spin- and angle-resolved photoelectron spectroscopy is considerably new method for investigation of bulk and surface electronic structure of magnetic and non-magnetic materials. Now a new beam line BL5A is under construction. This beam line consists of three parts, Helical Undulator,(1) SGM-TRAIN(2) and Spin- and Angle-resolved photoelectron spectrometer. In this paper we will describe the new electron spectrometer.

Recent years, many interesting studies of magnetic materials have been made by using spin-resolved photoelectron spectroscopy.(3) The most popular spin analyzer in these studies is the Mott type detector, and the Mott detector has been also established in the field of high energy physics. However, this kind of detector which based on high energy Mott scattering needs a very high voltage (about 100 kV) for acceleration of electrons, and thus the whole spectrometer including a power supply and a space from it for protection is quite large (1-10 m^3). This is a serious problem in a limited experimental area, and several kinds of smaller spin detector have been proposed and constructed, e.g. SPLEED and low energy electron diffraction detector. We have chosen the latter one, and constructed it in order to install to BL5A, because this type of detector is very small (about 10^{-3} m^3), and does not need higher voltage than several hundred volts.

Figure 1 shows a schematic view of the spin detector using low energy electron diffraction. Electrons emitted from the sample go through a lens system 1 into a hemispherical electron energy analyzer (VSW HA-54). The energy resolution(E/ΔE) is 100. Electrons out of the analyzer go through a lens system 2 into a 90-degrees deflector. We can get angle-resolved photoelectron spectra by using a channeltron behind the 90-degrees deflector. The 90-degrees deflector plays an important role to observe spin polarization along the surface normal, because spin direction of an electron along the surface normal is impossible to be observed. The deflector changes the beam direction by 90 degrees without changing the spin direction, so that we are able to know spin information for both of parallel and perpendicular

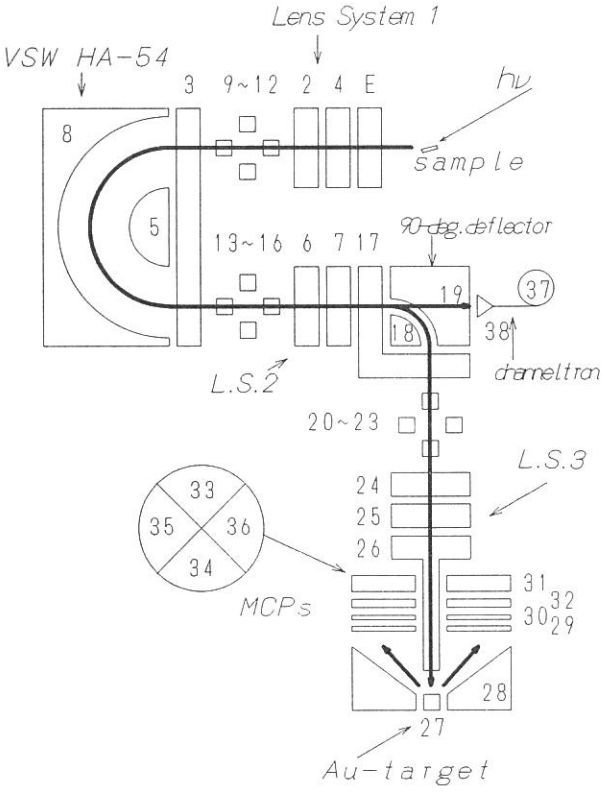

Fig.1 Schematic view of a spin- and angle-resolved photoelectron spectrometer

*present address : Business Communications Headquarters, NTT

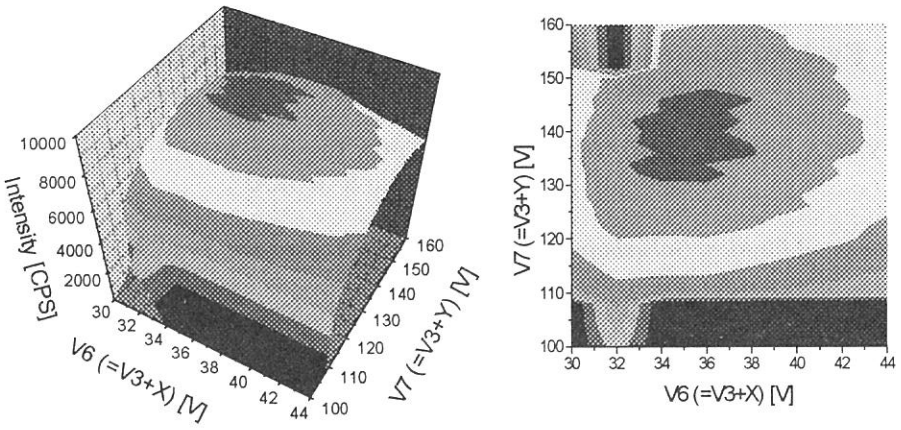

Fig.2 3-D fitting and its projection map of lens system 2 with two parameters

directions to the surface normal. Deflected electrons go through lens system 3 and reach to an Au-target prepared by evaporation in another place. The electrons diffracted by the Au-target are detected by MCP (cut to 4 pieces). The intensity of the diffracted electrons involves the information of spin-polarization due to spin-orbit interaction between diffracted electrons and Au atoms. We have optimized lens parameters first by using electron gun which supplies electrons more than 150 eV. The parameters have finely been adjusted by using emitted electrons from GaAs(100) surface excited with the He-I line. Figure 2 shows, for example, how to optimize parameters of the lens system 2 by using the channeltron. We optimized parameters by maximizing the intensity, and all parameters were fixed like this way. For fixing parameters of the lens system 3 and the 90-degrees deflector, we used another channeltron instead of Au-target. Typical photoemission spectrum from clean surface of GaAs(100) obtained by using He-I ($h\upsilon$ = 21.22 eV) with all MCPs is shown in Fig.3. The clean surface was prepared after several cycles of Ne-ion sputtering and annealing. It is noted that Ne-ion is milder than Ar-ion and suitable for a soft substrate like GaAs. After cleaning, no C or O was observed on the surface by AES, and a sharp LEED [c(2x8)] pattern was observed.

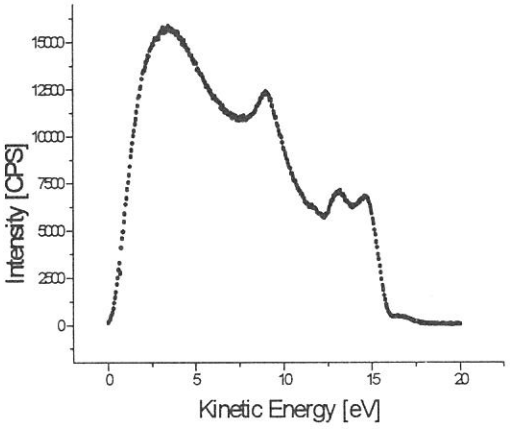

Fig.3 Typical photoelectron spectrum of GaAs(100)

In this February, we are going to carry out next test with uses circularly polarized lights from a Ti-sapphire laser. Negative electron affinity (NEA) surface of GaAs(100) is ready to measure the spin polarization. We will reach the final step in a series of these tests this summer by using circularly polarized SR lights from the new helical undulator.

References

(1) S. Kimura *et al.*: to be published in proc. of VUV 11
(2) M. Kamada *et al.*: *Monochromator for circularly polarized synchrotron radiation in the energy rang of 5-250 eV*, Rev. Sci. Instrum. 66, 2(1995)
(3) See, for example, E. Kisker: *3d-metallic magnetism and spin-resolved photoemission*, in *Metallic Magnetism, Topics in Current Physics*, edited by H. Capellmann (Springer-Verlag, Berlin, 1987), p. 513
(4) J. Kirchner: *Polarized Electrons at Surface*, (Springer-Verlag, Berlin, 1985)
(5) J. Unguris, D. T. Pierce and R. J. Celotta: Rev. Sci. Instrum., 57, 1314(1986)

(BL5B)

Exciton induced desorption of Ne metastable atoms from the surface of pure Ne solid.

Takato HIRAYAMA, Munehide ABO, Takafumi KUNINOBU, Toshihiro KOIKE, Ichiro ARAKAWA, Koichiro MITSUKE[a] and Makoto SAKURAI[b]

Department of Physics, Gakushuin University, Mejiro, Toshimaku, Tokyo 171, JAPAN
[a]Institute for Molecular Science, Myodaiji, Okazaki 444, JAPAN
[b]Department of Physics, Kobe University, 1-1 Rokkodai, Nada, Kobe 657, JAPAN

The process of the Desorption Induced by Electronic Transitions (DIET) in rare gas solids (RGS) has been extensively studied in these 10 years [1]. RGS is a model system to investigate the dynamic processes of DIET because of its simplicity and similarity of the electronic structure to the isolated atom.

The processes of neutral atom desorption by the excitonic excitation from pure RGS can be explained using two mechanisms, excimer dissociation (ED) and cavity ejection (CE) [2]. The desorption via ED process is due to a dissociation of a molecular-type self-trapped exciton (m-STE) similar to the dissociation of an excited dimer (excimer) in the gas phase. As to the CE mechanism, negative electron affinity of the matrix is known to be essential to have a repulsive interaction between the excited atom and the surrounding ground state atoms. This corresponds well to the experimental facts, i.e., the desorption species via CE process can be observed for Ne and Ar solids, whose electron affinities are negative, but not for Kr and Xe solids because of their positive electron affinities in the bulk due to the large polarizabilities. Further evidence has been obtained by using adsorbed and mixed rare-gas systems. Weibel et al. [3] measured Ne metastable desorption from thin layer of Ne on bulk Ar, Kr and Xe. They concluded that the CE mechanisms still worked in such adsorbed systems. Runne et al. [4] revealed the systematic correlation between the electron affinity and the existence of the desorption atoms via CE process for pure and doped rare-gas solids.

The experiments have been carried out at the beam line BL-5B at UVSOR in Institute for Molecular Science, Okazaki. Details of the setup and the experimental procedure have been already published elsewhere [5, 6]. Briefly, a liquid He cryostat is installed in an UHV chamber (base pressure < 10^{-8}Pa). A Pt(111) crystal is attached to the cryostat, and the temperature is kept at about 6K or less. The thickness of the rare gas solid is about 800 layers or more. Monochromatized synchrotron radiation is pulsed using a mechanical chopper, whose width and the interval of the light are 15μsec and 2.5msec, respectively. The photon beam is incident at 30 deg from the normal direction of the sample surface.

The desorbed metastable atoms (Ne*, $2p^5 3s\ ^3P_{0,2}$) are detected by a MCP with 40mm diameter (Galileo Electro-Optics Co.). Charged particles are rejected by applying suitable potentials on the input surface of the MCP and the retarding grids in front of the MCP. The detector is fixed at the distance of 358mm from the sample in the normal direction of the sample. The distance is about 5 times longer than our previous experimental setup, which results in the improvement of the resolution in the time-of-flight (TOF) spectra.

The dependence of Ne* (CE) yield from pure Ne solid on the excitation photon energy is shown in fig.1. The position of each peak corresponds to the excitation energy of the surface (S1, S') and the bulk (B1, B2, B3) excitons. The time-of-flight and kinetic energy spectra measured at the incident photon energies of 17.1eV (S1), 17.6eV (B1), 19.0eV (S') and 20.3eV (B2) are shown in fig.2 and 3, respectively. Detailed analysis of these spectra have already been given [6]. Present TOF spectrometer with the flight length longer than the previous one, which results in better time resolution, enabled us to obtain information on the desorption spectra in more detail. The strongest peak at time zero in fig.2 is due to scattered and emitted light. The higher kinetic energy peak ($t_f \approx 100$ μsec,

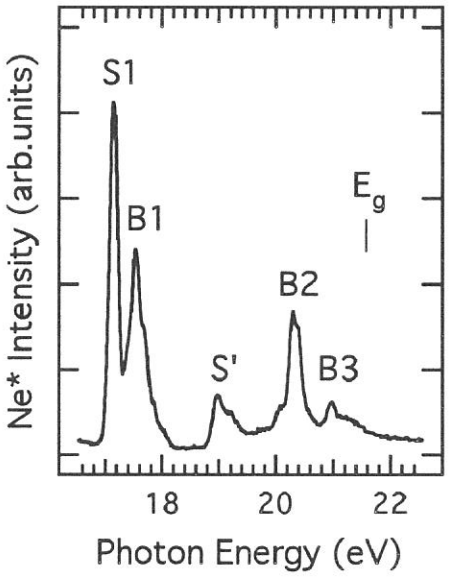

Figure 1. Dependence of Ne*(CE) yield from pure Ne solid on the excitation photon energy. The assignments for each peak and the position of the band gap energy (E_g) are shown.

(BL5B)

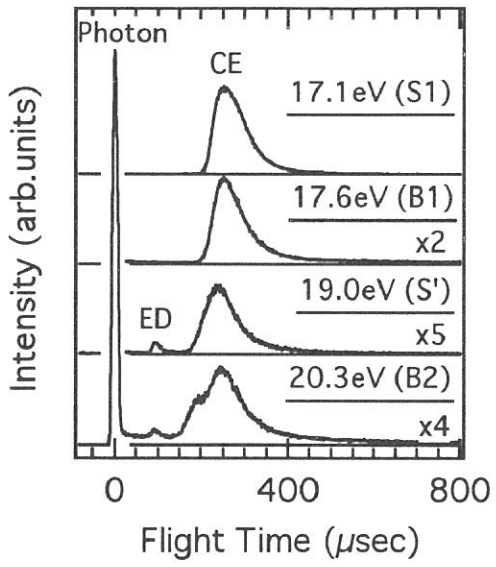

Figure 2. Typical time-of-flight (TOF) spectra of desorbed metastable Ne atoms from pure Ne solid at excitation photon energies corresponding to the surface (S1, S') and bulk (B1, B2) excitons.

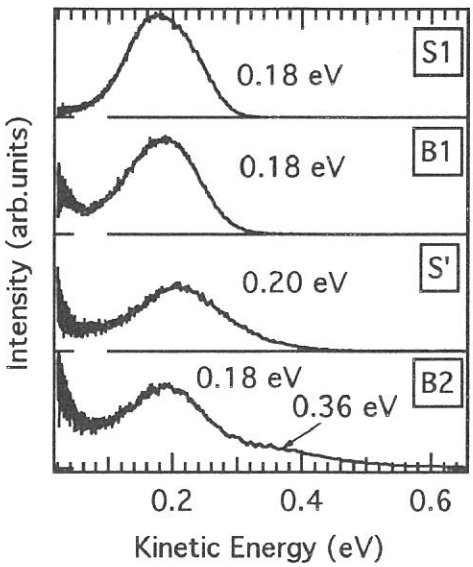

Figure 3. Kinetic energy spectra of desorbed metastable Ne atoms from pure Ne solid at excitation photon energies corresponding to the surface (S1, S') and bulk (B1, B2) excitons. The energy region of ED peak is not covered.

E_k = 1.4 ± 0.1 eV) is due to the excimer dissociation (ED) process (not shown in fig.3). The present kinetic energy is in good agreement with our previous ESD results[7] using a channel electron multiplier with small acceptance angle, while it is significantly larger than our previous PSD results (E_k=1.15eV) using a MCP with large acceptance angle (61 deg.) and short flight length [6]. This discrepancy can be attributed to large uncertainty of flight time in the previous PSD experiments for ED peak because of its very broad angular distribution.

The kinetic energies of CE peaks ($t_f \sim 250$ μsec) for S1, B1, and B2 excitation are found to be the same within the experimental uncertainty (E_k = 0.18±0.02 eV), while that for S' excitation, E_k = 0.20±0.02 eV. This fact may suggest that the desorbed Ne*(CE) at S1, B1, and B2 excitation are, at least when leaving from the surface, all in the same electronic states, probably in $2p^5 3s$ ($^3P_{0,2}$). The initial electronic state of B2 exciton ($2p^5 4s$) is known to relax very rapidly ($\sim 10^{-13}$ sec) to the 1st order excitonic state [8], which is consistent with the discussion above. Additional shoulder appeared in the higher energy side in B2 spectrum ($t_f \sim 180$ μsec), whose kinetic energy is 0.36±0.04eV, can be the contribution of Ne* in $2p^5 4s$ state at the desorption. The Ne*(CE) at S' excitation is in $2p^5 3p$ state at the desorption, and decay to $2p^5 3s$ state in vacuum [9].

REFERENCES

1 for recent review, see M. Runne and G. Zimmerer, Nucl. Instrum. Meth. Phys. Res., B101 (1995) 156, and references therein.
2 T. Kloiber and G. Zimmerer, Radiat. Eff. Def. Solids, 109 (1989) 219.
3 D. E. Weibel, A. Hoshino, T. Hirayama, M. Sakurai and I. Arakawa, in *Desorption Induced by Electronic Transitions - V*, ed. A.R.Burns, E.B.Stechel and D.R.Jenninson, Springer-Verlag, 1992, p. 333.
4 M. Runne, J. Becker, W. Laasch, D. Varding and G. Zimmerer, Nucl. Instrum. Meth. Phys. Res., B82 (1993) 301.
5 M. Sakurai, T. Hirayama and I. Arakawa, Vacuum, 41 (1990) 217.
6 I. Arakawa, D. E. Weibel, T. Nagai, M. Abo, T. Hirayama, M. Kanno, K. Mitsuke and M. Sakurai, Nucl. Instrum. Meth. Phys. Res., B101 (1995) 195.
7 D. E. Weibel, T.Hirayama and I. Arakawa, Surf. Sci., 283 (1993) 204.
8 N. Schwentner and E. E. Koch, Phys. Rev., B14 (1976) 4687.
9 T. Kloiber and G. Zimmerer, Phys. Scr., 41 (1990) 962.

CALIBRATION OF THE PROTO-TYPE XUV INSTRUMENTS ONBOARD PLANET-B

Masato NAKAMURA, Masafumi HIRAHARA, Yoshiyuki TAKIZAWA, Ichiro YOSHIKAWA, Atsushi YAMAZAKI, and Hirotomo NODA

Earth and Planetary Science, Graduate School of Science, University of Tokyo

Purpose of the calibration

The plasma observation around the Earth has been mainly done by the so called *in situ* measurement where the probes are sent into the regions of interest. Such observation cannot separate the temporal variation and the spatial change of the phenomena and our knowledge about the space plasma has been limited so far. We have been developing a new instruments for the plasma measurement, i.e. the plasma imager using the extreme-ultra violet light which cover the whole plasma environment within a short time interval compared to the temporal variation time constant. The main candidate wavelength are the resonant scattering from the Helium ions (30.4nm HeII) and from the Oxygen ions (OII 83.4nm). The imager in the extreme-ultra violet region has been difficult to build because the light of such high energy penetrate into the materials and is not reflected at the mirror surface effectively. Now we can design and construct it with the developments of the multi-coated layer mirror and the thin metal foils.

Our first trial of the plasmaspheric imagery was done by the Helium Emission Monitor onboard S-5209-19 sounding rocket launched from Kagoshima Space Center in January 1995. It was calibrated using the SOR light at the Institute for Molecular Science and the mission was quite successful. We measured the Helium emission from the plasmasphere and decided the temperature and the density of it. Also we did confirm the existence of the meta-stable Oxygen ions in the F-region of the ionosphere.

Our next target is the Helium emission from the Mars' ionosphere. We will build the extreme ultra-violet scanner (XUV) and put it onboard the PLANET-B space probe which will be launched in 1998 to Mars. During 1995 fiscal year, we have been calibrating the proto-type of this instrument and the calibration was done at UVSOR BL-5B. In this abstract, we report the results of the calibration. The characteristics of the thin metal filters and the MCP were measured. Also the electronics to process the signal onboard PLANET-B was checked using the SOR light.

We are also planning to develop this kind of plasma imager. It is quite possible that such instruments will be onboard the Swedish satellite (AKKA) in 1999, and Lunar Orbitor in 2002. Oxygen ion monitor is also under design and is planned to be onboard the SS-520-1 sounding rocket in 1998. The calibration this time will be a data base in designing those instruments, too.

Calibration

We used nude-type photo-multiplier for the detector in the measurement. At first we measured the characteristics of the spectroscope on the BL-5B. We decided the optimum pair of the mirrors and the gratings on the BL-5B for EUV which are the grating #3 and the mirror #5 for 30.4nm (HeII) and 58.4nm (HeI). The figure shown below gives the profile of the SOR light obtained by the photo-multiplier in the chamber.

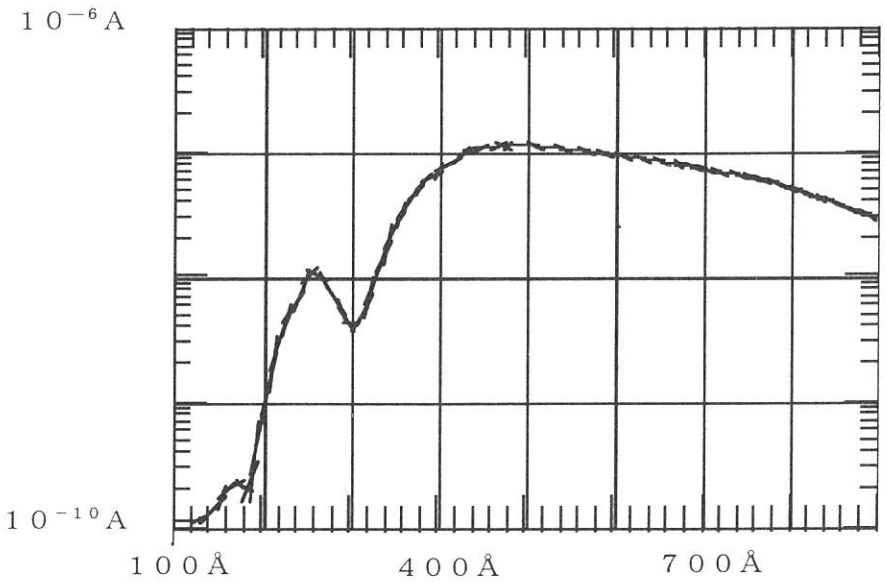

However the 83.4nm line (OII) could not detected by the photo-multiplier. This measurement should be done again using the micro channel plate (MCP).

Next, we measured the transmittance of thin metal foils. They are

1) Al/Mg filter
2) Al/Sn filter

The Al/Mg filter was found to be good to select the 25-90nm EUV light among the contamination from longer and shorter wavelength. The Al/Sn filter was found to be good to select the 45-90nm EUV light. We also tried an Al/In filter, however with the poor detection efficiency of the photo-multiplier at 80-100nm wavelength, we could not confirm the transmittance of it.

Finally we connected all the electronics of the XUV and introduced the SOR light into the MCP directly. The test was quite successful. The signals through the pre-amplifier were properly processed by the digital circuit onboard PLANET-B and confirmed by the ground support equipment (GSE).

Our next target in 1996

In the 1995 UVSOR season, we could not confirm the reflectivity of the mirror used for the XUV. This is due to the delivery delay of mirror by the constructor. We are planning to confirm it in the 1996 UVSOR season using MCP & position sensitive anode which will be available in coming April.

(BL5B)

Characterization of 284ÅMulti-Layer XUV Mirrors for XUV Telescope Aboard Sounding Rocket

Saku TSUNETA, Taro SAKAO*, Ryouhei KANO,
Tsuyoshi YOSHIDA, Shin'ichi NAGATA, Masahiko MIZUTANI

Institute of Astronomy, University of Tokyo, Mitaka, Tokyo 181
**National Astronomical Observatory, Mitaka, Tokyo 181*

The Fe XV line at 284.15Åis an important diagnostic line in astronomy, because it is one of the strong lines, and is emitted by the high plasma temperature of ~2 MK, which can not be observed with other lines between 40–300Å. This line is particularly important for the observations of the solar corona, because its temperature is around 1–5MK. On the other hand, this line is located close to the intense HeII line at 304Åin solar observations. The HeII lines are emitted from plasmas with temperature about 0.1 MK. The requirements of the solar observations for 284Åmirror are, therefore, (1) high wavelength resolution to isolate the FeXV line from the HeII line (The goal is $\lambda/\Delta\lambda \sim 35$.), and (2) High reflectivity ($> 20\%$).

We have characterized the multi-layer plain mirrors tuned for the 284Åline for the purpose of developing the XUV telescope aboard the ISAS sounding rocket. From the numerical simulation, we have chosen aluminum and SiC(silicon carbide) as the combination of the materials to satisfy both the requirements. In this pair, SiC serves as X-ray reflecting layers, and Al as spacers. Two mirrors were fabricated at Nikon cooperation. The ratios of the thickness of the SiC layers with the total thickness of the pair (SiC+Al) (Γ parameter) are chosen to be 0.2 and 0.4 from the numerical simulation. The wavelength resolution is higher for smaller Γ, *ie.* the higher penetration depth of XUV photons. The combination of the materials for XUV multi-layer has not yet been reported in the literature.

The reflectivity of the two mirrors was measured as a function of wavelength at UVSOR BL5B beamline. We employ the silicon photodiode detector with very thin dead layer (silicon dioxide) made by International Radiation Detectors (IRD). The detector has high and known quantum efficiency, wide dynamic range, and is stable against intense XUV irradiation. The overall performance of the mirrors was quite satisfactory. Figures 1 and 2 shows the reflectivity near the peak wavelength.

Table 1 summarizes the preliminary result from the measurements. The wavelength resolution is close to that obtained from the numerical simulation. The peak reflectivity is about 1/3 of the prediction. We will examine whether this lower reflectivity is due to the interdiffusion of the two layers or due to the apparent decrease by the scattered and higher order XUV photons. We plan to measure the long term stability of the peak reflectivity, the wavelength resolution, and the out-of-band rejection over wide wavelengths (50–400Å) in the future measurements. The out-of-band rejection is important to characterize the scientific performance of the mirror. The paper to report the measurements is in preparation (Nagata et al. 1996).

SiC/Al multi-layer mirror at 284Å(Preliminary)

Γ	Peak Reflectivity	$\lambda/\Delta\lambda$
0.2	~12 %	~26
0.4	~14 %	~17

Note: Incidence angle is 89 degree (near normal) in these measurements.

We would like to thank the X-ray optics group of the Nikon cooperation for the simulation and fabrication of the XUV mirros, and Prof. Yamashita and his group of the Nagoya University for the initial preparation of the experiment.

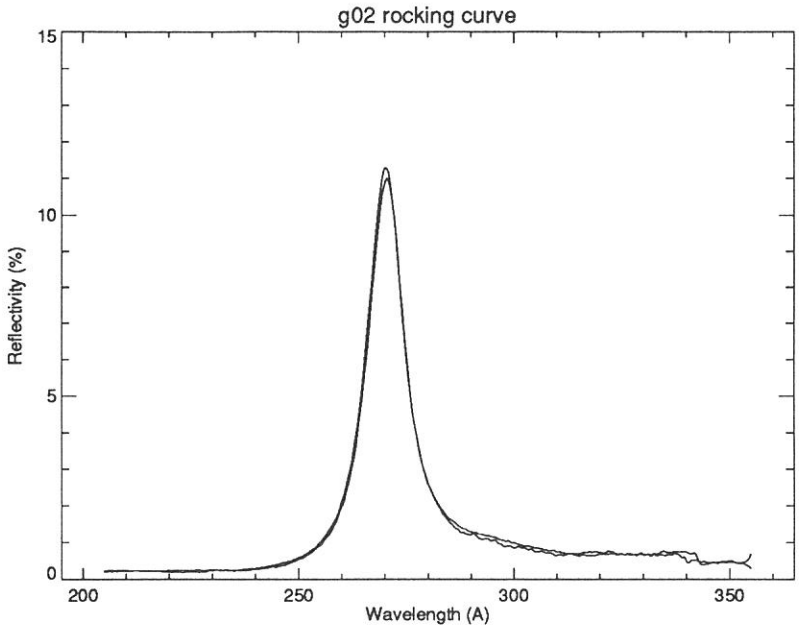

Figure 1: SiC/Al XUV multilayer mirror reflectivity as a function of wavelength (Γ =0.2 mirror). The incidence angle is 70 degree (near normal).

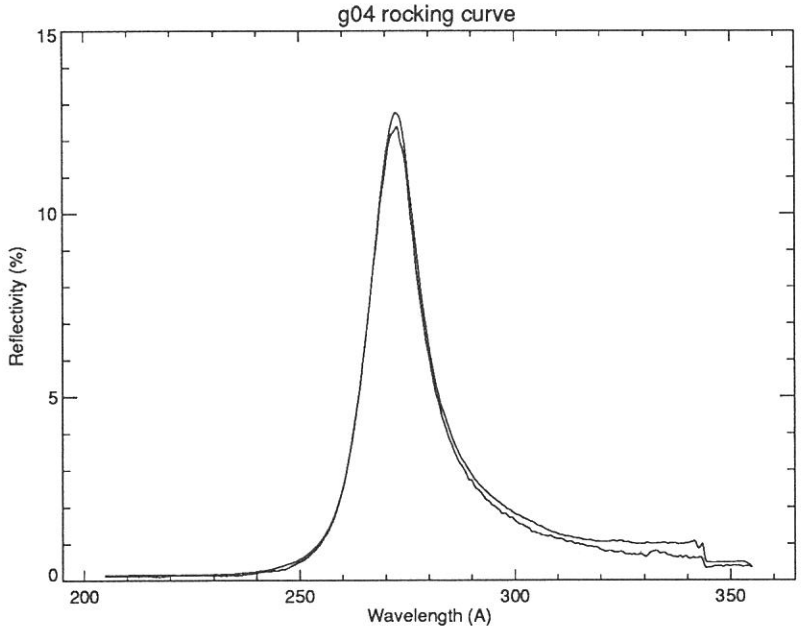

Figure 2: SiC/Al XUV multilayer mirror reflectivity as a function of wavelength (Γ =0.4 mirror). The incidence angle is 70 degree (near normal).

(BL5B)

Fabrication of soft X-ray multilayer mirrors by atomic layer epitaxy

Yoshinobu AOYAGI, Sohachi IWAI, Masashi ISHII and Hirofumi KAWADA

The Institute of Physical and Chemical Research (RIKEN)
2-1 Hirosawa, Wako, Saitama 351-01, Japan

Recently, applications of X-ray technology have been expanding into wide a range of fields. In particular, the wavelength range of 2-4 nm is well known as a "water window", which is important for biological applications with X-ray microscopy. Multilayer mirrors[1-4] are widely used in the soft X-ray region, because X-ray reflective indices of almost all materials are close to unity. In the short wavelength region such as the water window, the period of the multilayer becomes of atomic order, so that precise layer thickness controllability is necessary during fabrication. A sputtering method, in which two materials are alternatively sputtered and each layer thickness is controlled by deposition time, is a familiar way to make multilayer mirrors at present. However, the thickness controllability of this method is not sufficient for fabrication of short wavelength multilayers.

Atomic layer epitaxy (ALE)[5-7] is considered to a powerful method for fabrication of quantum devices using superlattice structures. In ALE, source gases are alternatively introduced into the growth chamber, and according to a "self-limiting mechanism", the epitaxial growth is automatically stopped at strictly 1 monolayer (ML) in one alternative gas supply. By repetition of this gas supply sequence, precise thickness control, ideal abrupt interface, and high uniformity are expected. These advantages are also favorable for X-ray mirrors. In this report, ALE is adopted as a fabrication process of X-ray multilayer mirrors for the first time, and the reflectivity is evaluated by using monochromatized synchrotron radiation at the Ultraviolet Synchrotron Radiation Facility (UVSOR).

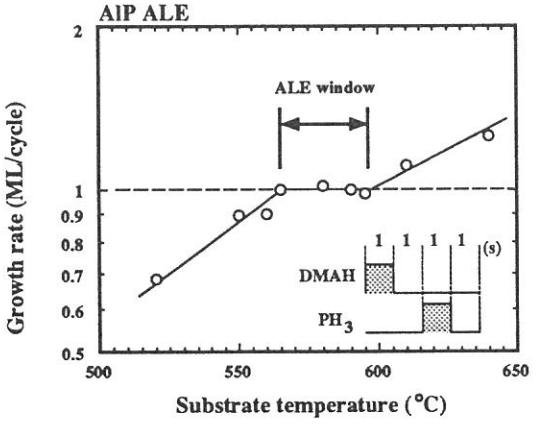

Fig. 1 Growth rate of AlP as a function of growth temperature.

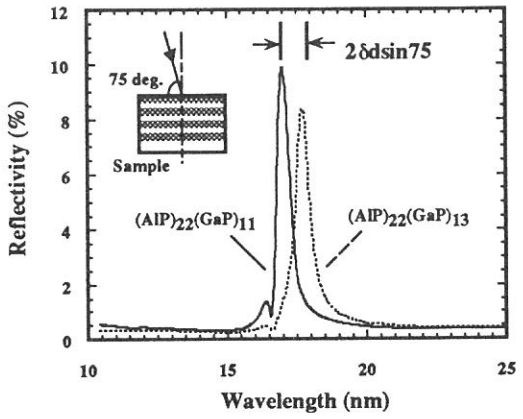

Fig. 2 Reflectivity of $(AlP)_{22}(GaP)_{11}$ and $(AlP)_{22}(GaP)_{13}$ at 75 deg. of incidence angle.

As a material combination for the multilayer, AlP/GaP is used. ALE of these materials were performed in a metalorganic vapor phase deposition (MOCVD) system.[8] The metalorganic gas sources of group-III element were dimethylaluminum hydride (DMAH) for AlP and trimethylgallium (TMG) for GaP. Phosphine (PH_3) was used as the group-V gas source. Figure 1 shows the growth rate of AlP as a function of growth temperature. The growth rate is constant at 1ML/cycle between 565 and 595 ℃; the self-limiting mechanism is involved in AlP ALE. In the case of GaP ALE, 1ML/cycle of growth rate independent of source gas feeding rate, is also confirmed at 590 ℃. Note that this temperature is included in the range of AlP ALE condition, and AlP/GaP multilayer can be deposited by only changing the gas source with atomic order accuracy.

Figure 2 shows the reflectivity of two multilayer mirrors, $(AlP)_{22}(GaP)_{11}$ and $(AlP)_{22}(GaP)_{13}$ at 75 degree of incidence angle. According to Al L absorption edge, reflection of ~10 % is observed, indicating that the X-ray mirror is fabricated by ALE for the first time. The difference of the reflection wavelength between these two samples, is expressed as $2\delta d\sin 75$, where δd is difference of the periods. δd is only 2 ML of GaP in this case; nevertheless the wavelength difference is clearly seen in this figure. This fact indicates that the reflection wavelength can be easily controlled by ALE cycle with high accuracy. This advantage is also useful to fabricate the non-periodic multilayer like super mirror, as well as short wavelength mirror.

In summary, atomic layer epitaxy (ALE) is used for fabrication of X-ray multilayer mirrors for the first time. By virtue of the atomic order thickness controllability in ALE, the reflection wavelength can be controlled with high precision; it is demonstrated that ALE would be a powerful technique for fabricating X-ray optics.

References

1 T. W. Barbee, J. Mrowka, Stanley and M. C. Hettrick, Appl. Opt. 24, 883 (1985).

2 C. Montcalm, B. T. Sullivan, M. Ranger, J. M. Slaughter, A. Kearney, C. M. Falco and M. Chaker, Opt. Lett. 19, 1004 (1994).

3 C. Sella, K. Youn and R. Krishnan, Appl. Surf. Sci. 33/34, 1208 (1988).

4 J. F. Seely, G. Gutman, J. Wood, G. S. Herman, M. P. Kowalski, J. C. Rife and W. R. Hunter, Appl. Opt. 32, 3541 (1993).

5 T. Suntola, Thin Solid Films 216, 84 (1992).

6 J. Nishizawa, J. Electrochem. Soc. 132, 1197 (1985).

7 Y. Aoyagi, J. Vac. Sci. Technol. B5, 1460 (1987).

8 H. Isshiki, Y. Aoyagi, T. Sugano, S. Iwai and T. Meguro, Appl. Phys. Lett. 63, 1528 (1993).

(BL5B, 6A1 & 7B)

Reflectivity Spectra of a Mixed Valent Semiconductor, Yb_3S_4

Shin-ichi KIMURA, Yong Seung KWON[1] and Takashi SUZUKI[2]

UVSOR Facility, Institute for Molecular Science, Okazaki 444
[1] Department of Physics, Sung Kyun Kwan University, Suwon 440-746, KOREA
[2] Department of Physics, Faculty of Science, Tohoku University, Sendai 980-77

Mixed valence state in rare-earth compounds shows various interesting physical properties. Yb_3S_4 is one of such materials in which the mean valence is 2.67. The material is also a semiconductor with the energy gap of 0.4 eV. In spite of the semiconductor character, the γ value of the specific heat is very large, the value is a few J/mole·K^2. So Yb_3S_4 was reported a heavy fermion material with no carrier. [1] However, heavy fermion with no carrier is a problem in itself, what is the origin of the large γ value in spite of no carrier. We measured the reflectivity spectra of Yb_3S_4 in a wide energy range of 5 meV - 50 eV and also measured the photoemission spectra for the investigation of the electronic structure. The photoemission spectra are separately reported in this issue. [2] Here the electronic structure expected by the reflectivity spectrum is reported.

The measurement was done using a polycrystalline sample. The size of the sample surface was 1.0 × 1.5 mm^2. The reflectivity spectra of Yb_3S_4 were measured in the energy range of 5 meV - 50 eV using three beam lines, BL6A1, 7B and 5B of UVSOR and using a conventional spectrometer system [3]. Though the measurement was done at the temperatures of 10 and 299 K, the main character of the reflectivity spectrum does not change. This means that the electronic structure does not change as the temperature changes. This is consistent with the magnetic susceptibility data. [1]

The obtained reflectivity spectrum at 299 K is shown in Figure 1. Large structure of the reflectivity spectrum at the photon energy of 30 meV originates from optical phonons. Since the optical phonons appear and Drude like reflectivity does not appear, Yb_3S_4 is confirmed to be an insulator.

After the Kramers-Kronig transformation, the electronic structure is estimated. Figure 2 shows that the comparison between the optical conductivity and photoemission spectra [2] of Yb_3S_4. In the figure, the zero binding energy (Fermi level) of the photoemission spectrum is

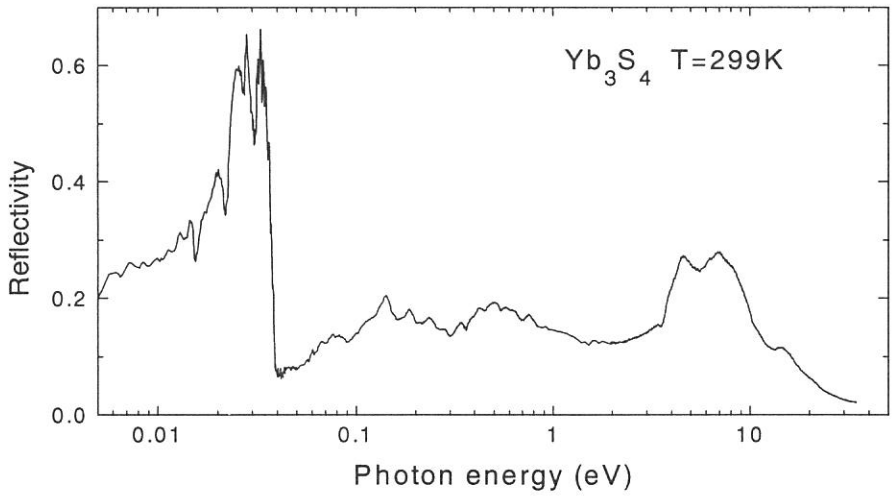

Fig. 1. Reflectivity spectrum of Yb_3S_4 in the photon energy range of 5 meV - 50 eV at 299 K.

shifted by 6.5 eV from the optical conductivity spectrum. The peaks at 7.5, 15 and 19 eV in the optical conductivity spectrum is seen to correspond to those in the photoemission spectrum. These absorptions are considered to be commonly due to the transition to the Yb-5d band. Therefore the main band of the Yb-5d is seen to be located at 6.5 eV above the Fermi level.

On the other hand, the steep rise structure in the optical conductivity spectrum is seen at the photon energy of 4 eV. So the lowest limit of the Yb-5d band is seen to be 4 eV above the Fermi level.

The energy gap was reported to be 0.4 eV by the transport measurement. [1] From the optical conductivity spectrum, a small absorption is seen below 4 eV. Certainly, an energy gap is appears at 0.4 eV in the optical conductivity spectrum but the absorption intensity is very small. The transport measurement is thought to observe the energy gap. However, main absorption band appears above 4 eV. The absorption band seems to be due to the charge transfer excitation from S-3p to Yb-5d because the absorption intensity is very large. So the Yb-5d band is not located at 4 eV below the Fermi level.

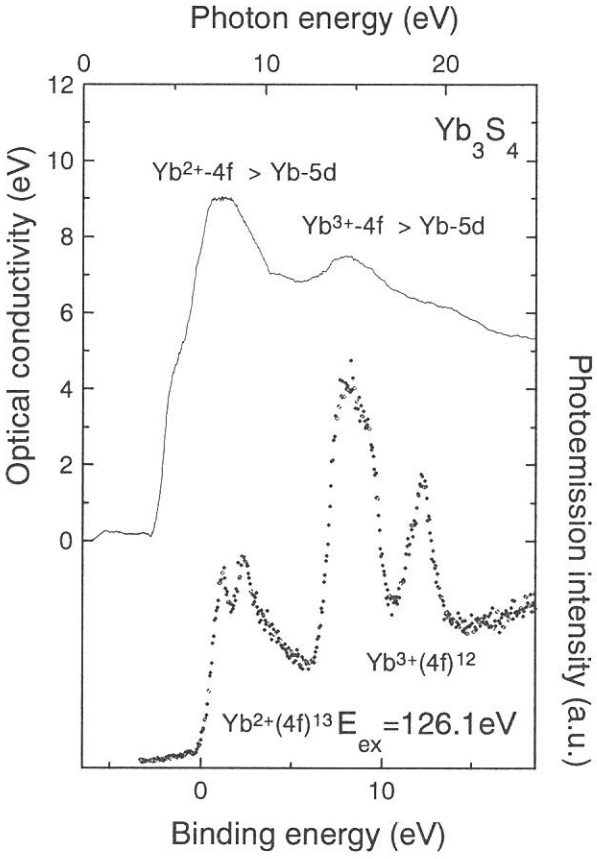

Fig. 2. Optical conductivity and photoemission spectra of Yb_3S_4. The Fermi level of the photoemission spectrum is shifted by 7.5 eV for comparison with the optical conductivity spectrum.

The origin of the weak absorption is thought to be due to the transition from the S-3p to the Yb^{3+}-4f unoccupied state. It is certain that the Yb^{3+}-4f unoccupied state is located in the main gap between the S-3p and the Yb-5d states, because the Coulomb repulsion energy, U_{ff}, between 4f electron and 4f hole is known to be 8-9 eV. So theYb^{3+}-4f unoccupied state is located at 1-2 eV above the Fermi level. Weak absorption between the S-3p and the Yb-4f states is thought to appear in the case that the Yb-5d character mixes to the Yb-4f state. In this case, the conduction band includes the Yb-4f character. This is thought to be the origin of the heavy γ value.

References

[1] Y. S. Kwon, Y. Haga, C. Ayache, T. Suzuki and T. Kasuya, Physica B **186-188** (1993) 605.

[2] S. Kimura, Y. S. Kwon, S. Tanaka, M. Kamada and T. Suzuki, UVSOR Activity Report 1995 (1996).

[3] S. Kimura, T. Nanba, S. Kunii and T. Kasuya, Phys. Rev. B 50 (1994) 1406.

(BL6A1)

Improvement of Far-Infrared Beamline BL6A1

Makoto SAKURAI, Hidekazu OKAMURA, Katsumi WATANABE, Nozomu HIRAOKA, Takao NANBA, Shin-ichi KIMURA[a] and Masao KAMADA[a]

Department of Physics, Kobe University, Kobe 657, JAPAN
[a]Institute for Molecular Science, Myodaiji, Okazaki 444, JAPAN

Far-infrared beamline BL6A1 initially constructed in 1986 has proved the advantage of SR for FIR regions and has been utilized for various transmission and reflection measurements. However, optical experiments such as the determination of optical constant require wide energy range from FIR to VUV regions. For another example, the energies of surface vibrations measured by infrared reflection absorption spectroscopy reside in FIR - IR regions. Then, it is useful to extend the covering energy range to higher energy regions for many applications.

We have reconstructed the beamline BL6A1 to meet following requirements;
(1) enlarge the energy range to 5-10000 cm^{-1},
(2) make it possible to perform specific experiments, e.g. surface vibrational spectroscopy or time resolved spectroscopy, which emphasizes the characteristics of synchrotron radiation such as low emittance, polarized and pulsed nature.

In order to fulfill the former requirement we installed another spectrometer (BRUKER IFS 66V) which covers energy range of 50 - 10000 cm^{-1}.
The spectrometer is a FT-IR spectrometer which is in principle Michelson interferometer operated in vacuum. The beam-splitter is exchangeable among quartz , KBr and mylar films with different thickness (6 and 12 μm), and its adjustment is optimized by computer control.
Figure 1 shows a schematic diagram of revised version of BL6A1. The specification of the revised beamline is summarized as follows.

(1) The beamline has two spectrometers, i.e. a far-infrared spectrometer (a Martin-Puplett interferometer) which covers energy range of 5 - 300 cm^{-1} and the infrared spectrometer.

(2) The optical transport system is divided for each spectrometer; the SR beam is switched at the first switching mirror to either spectrometer and introduced to the same sample chamber by the second switching mirror. It is also possible to extract the beam right way toward another experimental system (not shown in Fig.1).

(3) The vacuum of the system is classified to low vacuum regions (both spectrometers and both focusing mirror chambers) and high to ultrahigh vacuum regions (collecting pre-mirrors, two switching mirrors and the sample chamber), and they are separated with two diamond windows and a mylar film.

(4) Either of two detectors is selectable with the third switching mirror system according to the energy range in use.

The diamond windows are 20mm in diameter and 0.2 mm thick, almost transparent for visible light, and are made slightly wedged shape (0.2 deg) to avoid an oscillatory interference pattern in the spectrum. The transmittance of them were measured for the energy range of 30 - 4000 cm^{-1} and is within 0.6 - 0.8 over the measured range.

Figure 2 shows output spectra of SR over the energy regions of both spectrometers. Curves signed with WG(wire grid) correspond to the spectra of FIR spectrometer. Intensities of the spectra taken with different detector are not comparable. This figure shows that the upper limit of the effective energy range is extended from 300 to 10000 cm^{-1}.

The advantage of low emittance of SR beam was demonstrated as below. Parallel beam from the second switching mirror was focused at sample position. The SR beam was masked with various size of aperture at the sample position. Spectral intensities did not change until the smallest aperture size of 0.5ϕ, whereas the spectra for the globar source in the IFS 66V changed with the aperture size.

Polarization distribution of the SR beam was also measured. Measured polarizability is about 0.6 for the almost all energy ranges, which is consistent with the calculated value derived from integration of original polarizability distribution over the acceptance angle.

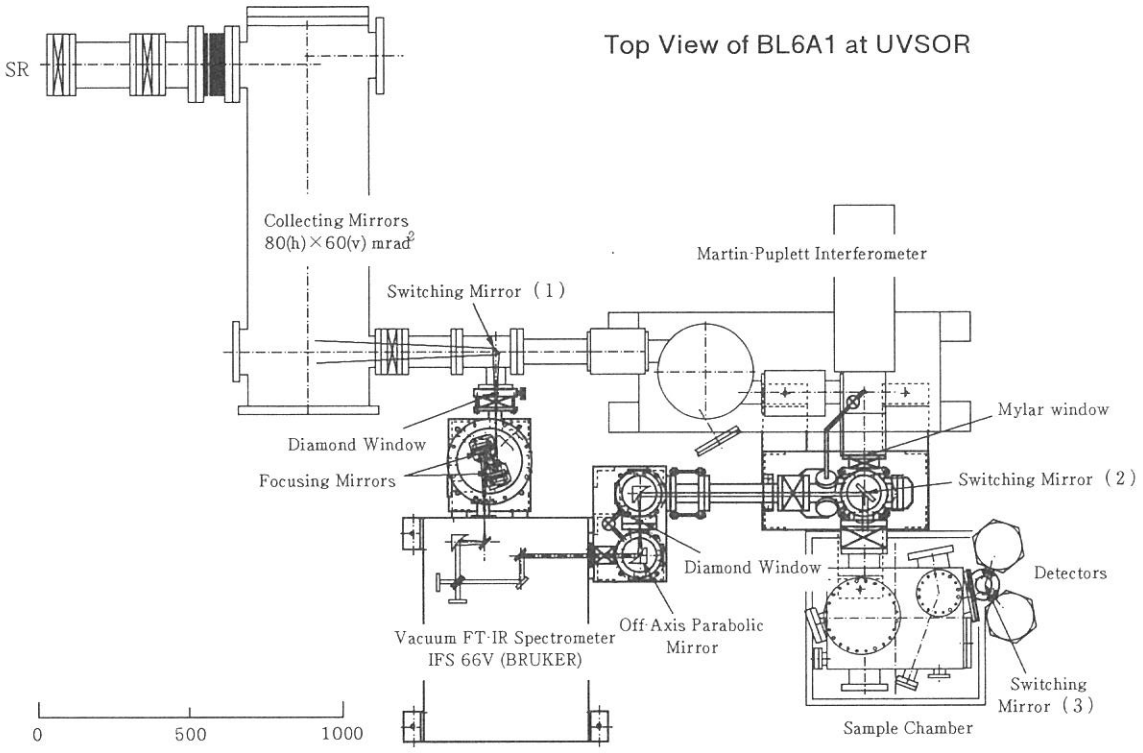

Figure 1. Top view of new version of BL6A1. Components drawn with thick lines are added parts for the present reconstruction.

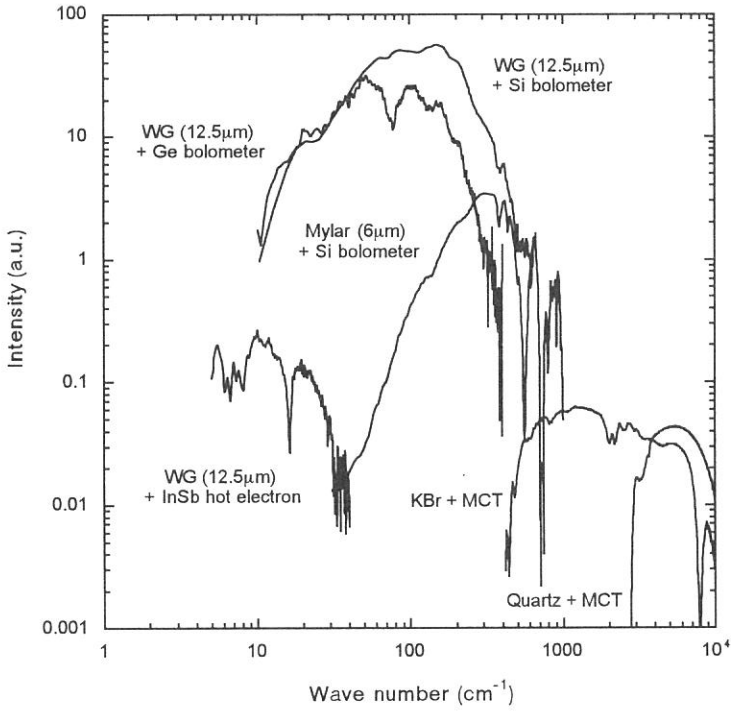

Figure 2. Output Spectra of BL6A1.

(BL6A1)

Change in the Phonon Spectrum of CdS Microcrystals Due to Phase Transition

Takao Nanba, Makoto Muneyasu and Nozomu Hiraoka

Department of Physics, Faculty of Science,

Kobe University, Kobe 657

In general, microcrystals whose size become smaller than a wavelength of an incident light show different optical properties from those in a bulk state because of its boundary condition at a surface to an elecromagnetic wave. For example, a transverse optic (TO) phonon mode in a bulk state changes to a so-called surface phonon mode in a microcrystal. On the other hand, a structural stability of microcrystal under high pressure related with a phase transition is one of the most attractive subjects. In the previous report in 1994 [1], we observed the pressure dependence of the TO phonon spectrum of the CdS microcrystals and presented the clear experimental evidence to show the size-dependence of the critical pressure (P_c) of the microcrystals at which the phase transition occurs. The smaller microcrystals gave the higher P_c than that in the bulk state. Successively, we made similar experiments in order to know more clear size-dependence of the P_c of CdS microcrystal.

Sample preparation and transmision measurements under pressure

CdS microcrystals which have different mean sizes in diameter were produced by a gas-evaporation technique in helium gaseous pressure. The shape and the mean diameter of the microcrystals was determined by the TEM method. Small microcrystal with a mean size in diameter down to 150 A was produced. The transmission measurements under high pressure up to 15 GPa at a room temperature were done using a diamond anvil cell combined with the spectroscopic system at the BL6A1. The peak position of the absorption by the surface phonon of the CdS microcrystal was found to give suddenly a

large red shift in energy at the pressure where the phase transition occured.

Results

Values obtained for P_c for each CdS microcrystal are plotted in Fig.1 as the function of the mean particle size. Electrical resistance data reported by Osugi *et al* [2] which shows the precursor phenomena of the gradual increase in the P_c of CdS microcrystals in a few micron meter range are also plotted together by open circles. Our data showed that (1) a clear increase in P_c by almost 1 GPa and (2) the saturation of the increase in the P_c up to around 4 GPa even for a very small microcrystals.

References

[1] T.Nanba *et al*: UVSOR Activity Report (in 1994), p.138.

[2] J.Osugi *et al*: Rev.Phys.Chem.Jpn.**36(2)** 59 (1966).

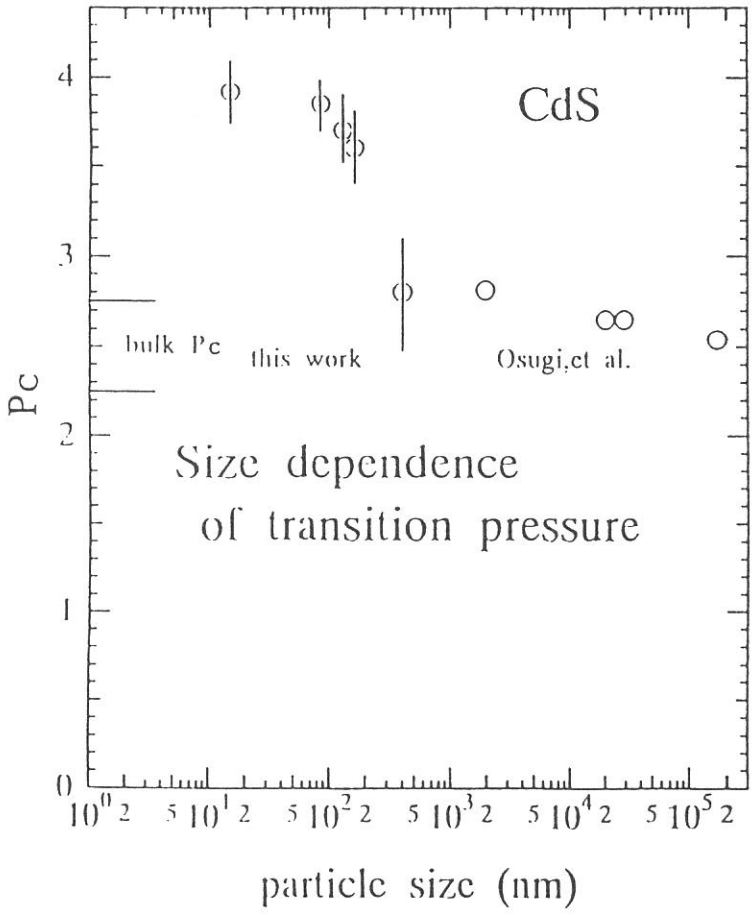

Fig.1

Measured values of the critical pressure (P_c) of CdS microcrystals as the function of the mean diameter together with data reported by Osugi *et al* [2] by open circles. The P_c in the bulk state was also shown by solid lines.

(BL6A1) Generation of High Pressure up to 20 GPa in The Far-infrared Spectroscopy

Takao Nanba, Makoto Muneyasu and Nozomu Hiraoka

Department of Physics, Faculty of Science,

Kobe University, Kobe 657

In general, spectroscopy under very high pressure in the GPa range can be achieved by using a diamond anvil cell (DAC) technique. The utilization of a DAC in the far-infrared spectroscopy ,however, has been quite rare and then obtained pressure in many experiments has stayed less than 1 GPa. The reason was mainly the lack of brilliant broad-band light source in the far-infrared region. Hitherto by the experiments at UVSOR, we proved that UVSOR is a very brilliant light source in the far-infrared and millimeter wave regions. We developed a lever-arm type of a DAC and started the experiment under high pressure of GPa range by using it combined with a spectroscopic system at the BL6A1 of UVSOR. Recently we could perform high pressure experiment up to 20 GPa which is a highest pressure in the far-infrared region. Typical example of high pressure measurement at UVSOR is shown in Fig.1.

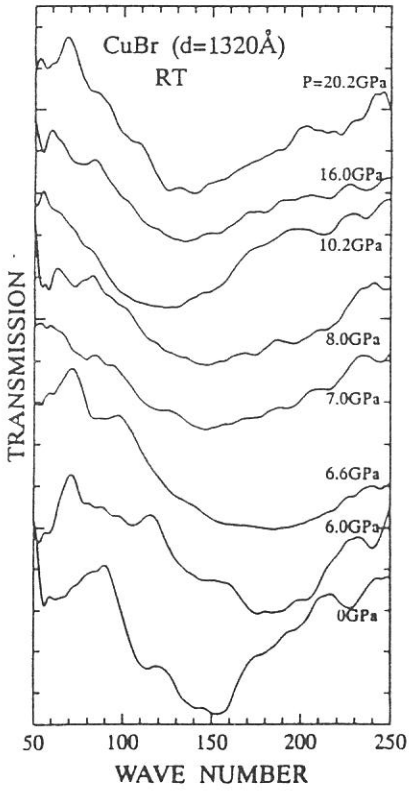

Fig.1

The development of the transmission spectra of CuBr microcrystals whose mean diameter was 1320 A with the pressure. Spectrum was measured under pressure up to 20.2 GPa. The large dip at arround 150 cm^{-1} in the curve at P=0 is due to the absorption by the surface phonon of the microcrystal.

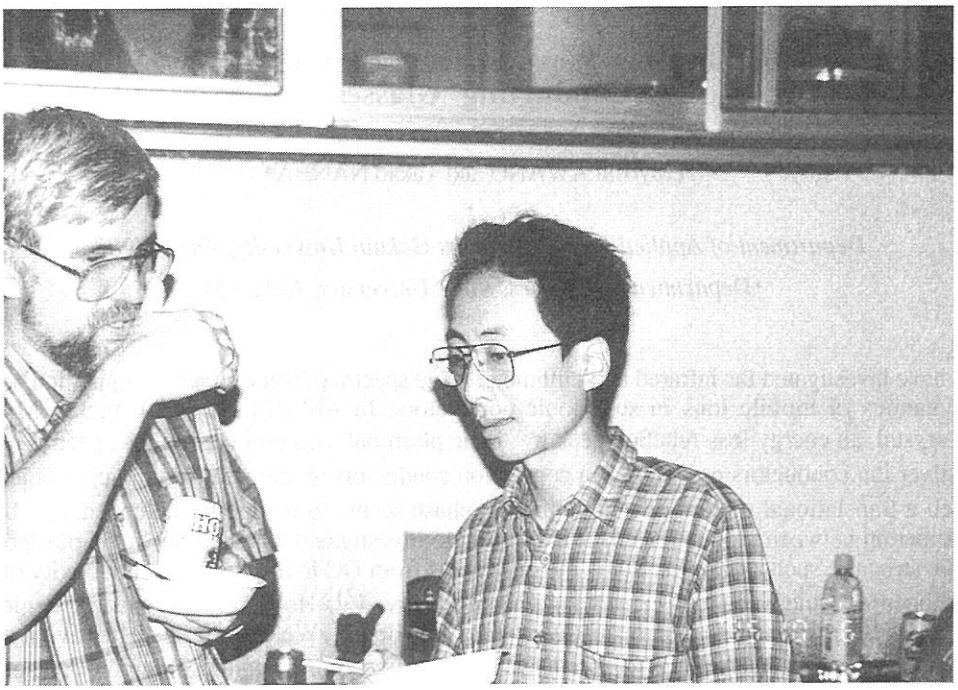

Prof. A. Lushchik (inviting associate professor from Estonia) is explaining his recent study on multiplication under synchrotron radiation. Dr. K. Mase is interesting in his talk.

Prof. N. Kosugi has explained the future plan of UVSOR at the second UVSOR Workshop last October.

(BL6A1)

Far-infrared and Millimeter Wave Spectroscopy of Silver or Cuprous ion Conducting Glasses

Teruyoshi AWANO and Takao NANBA*

Department of Applied Physics, Tohoku Gakuin University, Tagajo 985

**Department of Physics, Kobe University, Kobe 657*

We have investigated far-infrared and millimeter wave spectra of some silver or copper ion conductors to study the dynamics of mobile ions in superionic conductors. In AM_4X_5 (A=alkali metal; M=Ag or Cu; X=halogen) crystal, an energy loss function peak by "ionic plasmon" was observed in the spectral region below 10 cm^{-1} in silver ion conductors or 30 cm^{-1} in copper ion conductors at temperatures of superionic conducting phase[1]. Such a translational motion of mobile ions in phase seems to be due to the correlation by Coulomb repulsive interaction between mobile ions. It is interesting to investigated whether the "ionic plasmon" exists in a non-periodic structure such as glasses. Some measurements from DC to microwave conductivity of superionic glasses have been executed and two power laws were observed[2]. However, the spectral region between microwave and FIR region have not been investigated in detail. We measured reflectivity spectra and transmission spectra of $(AgI)_x(AgPO_3)_{1-x}$ (x=0, 0.25, 0.5) glasses in FIR and MW region[3]. There were two broad peaks around 90 cm^{-1} and 15 cm^{-1} commonly in the reflectivity spectra of the $(AgI)_x(AgPO_3)_{1-x}$ glasses at 298 K. The low energy tail below 9 cm^{-1} slightly increased in the superionic conducting glasses (x=0.5) in energy loss function spectra. This suggests that longitudinal oscillation of the carrier ion exist. However, this structure of the "ionic plasmon" was not so clear as in AM_4X_5 crystals. This seems to be due to the non-periodic structure of the glass. This structure by the longitudinal motion of conduction ion decreased slightly at 77K. This change was not so drastically as that in AM_4X_5 crystal. This seems to be due to the random and coarse network of the AgI_4 tetrahedron.

In this study, we measured reflectivity spectra (and transmission spectra if it was possible) of $(CuI)_{0.25}(CuPO_3)_{0.75}$ glass and $((CH_3)_4NI)_{0.1}((C_2H_5)_4NI)_{0.1}(AgI)_{0.8}$ glass in spectral region from 3 to 250 cm^{-1}. We expected a shift of the plasma frequency by the substitution of conduction ion from Ag^+ to Cu^+. In the case of $((CH_3)_4NI)_{0.1}((C_2H_5)_4NI)_{0.1}(AgI)_{0.8}$, the network structure of glass does not exist but each molecule of AgI, $(CH_3)_4NI$ and $(C_2H_5)_4NI$ disperses randomly. It is expected that the ionic plasmon is more strongly scattered in this glass than in $(AgI)_x(AgPO_3)_{1-x}$.

The mixture of CuI, Cu_2O and P_2O_5 was kept at 900 K for 30 minutes and quenched rapidly to obtain $(CuI)_{0.25}(CuPO_3)_{0.75}$ glass. Stoichiometric amounts of AgI and $(CH_3)_4NI$ and $(C_2H_5)_4NI$ were kept at 500 K for 30 minutes and quenched rapidly to obtain $((CH_3)_4NI)_{0.1}((C_2H_5)_4NI)_{0.1}(AgI)_{0.8}$ glass.

Fig. 1 shows reflectivity spectra of $(CuI)_{0.25}(CuPO_3)_{0.75}$ glass. Drude like structure is observed in millimeter wave region. This decreased at low temperature. However, the change was not so drastic as that at the phase transition of superionic crystals. Fig. 2 shows conductivity spectra of $(CuI)_{0.25}(CuPO_3)_{0.75}$ glass, which were obtained by K-K analysis of the reflectivity spectra. Main peaks were observed at 140 cm^{-1}, which is due to breathing mode of a cuprous ion in a cage of tetrahedron of iodine ions. A band by attempt mode, which is observed in silver ion conductors in submillimeter region, was not clear. Fig. 3 shows energy loss function, which is the imaginary part of the reciprocal of dielectric constant. An absorption peak was observed around 8 cm^{-1}. This suggests that longitudinal oscillation of the carrier ion exists. This seems to be due to the "ionic plasmon". The parameters of the Drude curve fitting are shown in the figure.

Figs. 4 and 5 show absorption and reflectivity spectra of $((CH_3)_4NI)_{0.1}((C_2H_5)_4NI)_{0.1}(AgI)_{0.8}$ glass. Absorption spectra were measured from 3 to 20 cm^{-1} and connected with those obtained from reflectivity spectra. An absorption band was observed around 7 cm^{-1}. The origin of this band is unknown. In this glass, the Drude like structure is not clear even at the room temperature. Fig. 6 shows conductivity spectra. Main peaks were observed around 100 cm^{-1} and 220 cm^{-1}. The attempt mode as observed in $(AgI)_x(AgPO_3)_{1-x}$ was not seen in this glass. Fig. 7 shows energy loss function spectra. The "ionic plasmon" was not observed in this glass.

The "ionic plasmon" was observed clearly only in $(CuI)_{0.25}(CuPO_3)_{0.75}$ among the glasses of $(AgI)_x(AgPO_3)_{1-x}$, $(CuI)_{0.25}(CuPO_3)_{0.75}$ and $((CH_3)_4NI)_{0.1}((C_2H_5)_4NI)_{0.1}(AgI)_{0.8}$. It is interesting that the translational motion of conduction ions is different even in the same glass structure of $(AgI)_x(AgPO_3)_{1-x}$ and $(CuI)_{0.25}(CuPO_3)_{0.75}$. This seems to be due to electronic carriers in cuprous halide glass.

Fig. 1. Reflectivity Spectra of $(CuI)_{0.25}(CuPO_3)_{0.75}$ glass.

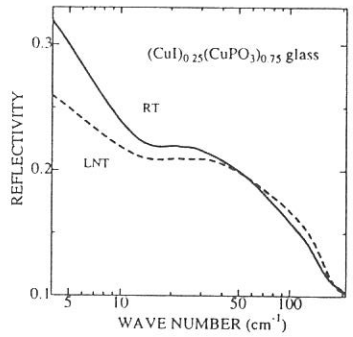

Fig. 2. Conductivity spectra of $(CuI)_{0.25}(CuPO_3)_{0.75}$ glass.

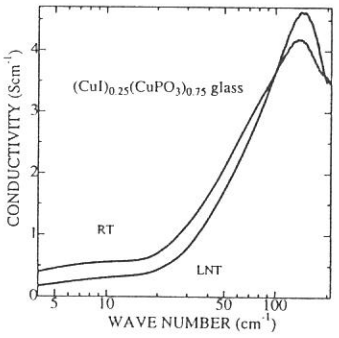

Fig. 3. Energy loss function of $(CuI)_{0.25}(CuPO_3)_{0.75}$ glass.

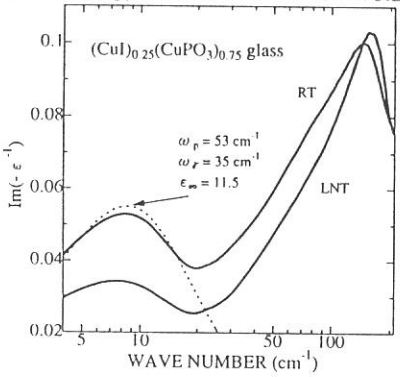

Fig. 4. Absorption spectra of $((CH_3)_4NI)_{0.1}((C_2H_5)_4NI)_{0.1}(AgI)_{0.8}$ glass.

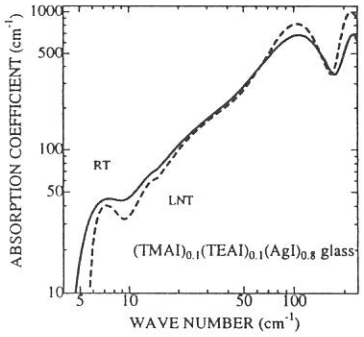

Fig. 5. Reflectivity spectra of $((CH_3)_4NI)_{0.1}((C_2H_5)_4NI)_{0.1}(AgI)_{0.8}$ glass.

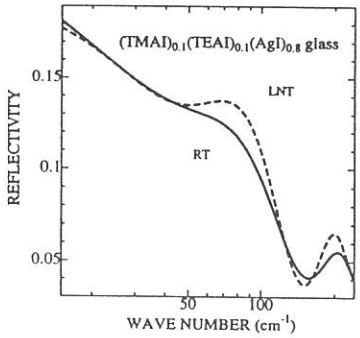

Fig. 6. Conductivity Spectra of $((CH_3)_4NI)_{0.1}((C_2H_5)_4NI)_{0.1}(AgI)_{0.8}$ glass.

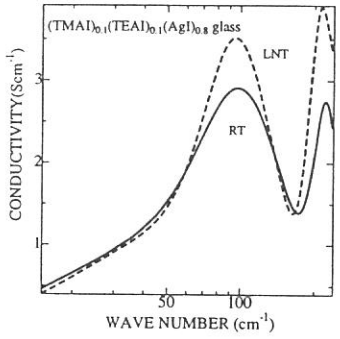

Fig. 7. Energy loss function spectra of $((CH_3)_4NI)_{0.1}((C_2H_5)_4NI)_{0.1}(AgI)_{0.8}$ glass.

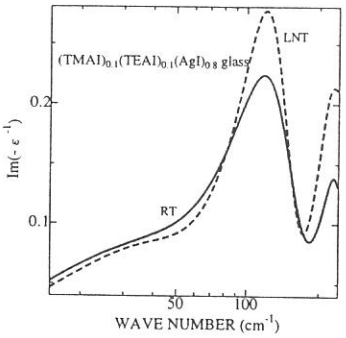

References

1) T. Awano, T. Nanba and M. Ikezawa, Solid State Ionics, 53-56 (1992) 1269.
2) C. Cramer et al., 10th International Conference on Solid State Ionics (Singapore, 1995) 3-3AO66.
3) T. Awano and T. Nanba, UVSOR activity report 1994, 146.

(BL6A1)

Optical Observation of the Interaction between Low Frequency Plasma and Magnetic Field in $La_{2-x}Sr_xCuO_4$ ($x \approx 0.1$) II

Shin-ichi KIMURA, Mikihiko IKEZAWA[1], Hironao KOJIMA[2], Isao TANAKA[2], Takashi WATANABE[2] and Masashi TACHIKI[3]

UVSOR Facility, Institute for Molecular Science, Okazaki 444
[1] Research Institute for Scientific Measurements, Tohoku University, Sendai 980-77
[2] Faculty of Engineering, Yamanashi University, Kofu 400
[3] Institute for Materials Research, Tohoku University, Sendai 980-77

The conduction along c-axis in a high Tc-cuprate superconductor is known to show a semiconductor like one above the temperature of Tc and show superconducting one below the Tc. The character is different from that along the c-plane. In the superconducting state, since the carrier number is small, the plasma edge is located in the sub-millimeter region (a few ten cm^{-1}). The relaxation time becomes infinite because of the superconducting state. The evidence appears in reflectivity spectra. [1] The plasma is stable because the plasma is located inside the gap of the superconducting, and is not so strongly interrupted by phonon scattering.

Our main purpose is to investigate the interaction between the plasma and magnetic field. Generally, vortices are created in the case that the magnetic field which is higher than a lower critical magnetic field, H_{c1}, is applied to a type II superconductor. Normal conducting state appears in the vortices. In the case that the light, which electric vector is not parallel to the magnetic field, is applied, the vortices are driven by the incident light. The effect is theoretically predicted by Tachiki *et al.* [2]

The dielectric functions which are derived from the theory are follows. In the case of $H // E$, where H is the magnetic field vector and E the electric field vector.

$$\tilde{\varepsilon}(\omega) = \varepsilon_c - \frac{\omega_{ps}^2}{\omega^2}\left(1 + \frac{B_0}{H_{c2}}\frac{\tau_v / \tau_n}{1 - i\omega\tau_v - M\omega^2 / \kappa_p}\right)^{-1} - \frac{\omega_{pn}^2}{\omega(\omega + i\gamma_n)} \quad (1)$$

Here, ω_{ps} and ω_{pn} are plasma frequencies in the superconducting state and the normal state, respectively, B_0 is applied magnetic field. H_{c2} is the upper critical magnetic field, τ_n and τ_v are relaxation times of normal electron and vortex, respectively, M is the inertial mass, κ_p is pinning force and γ_n is the damping constant of the normal conduction.

On the other hand, in the case of $H \perp E$,

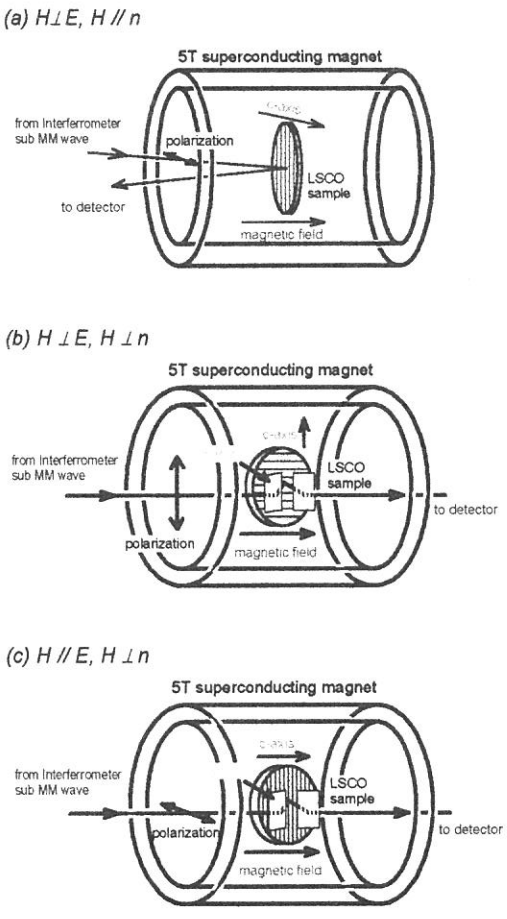

Fig. 1 Configurations of measurements under magnetic field.

$$\tilde{\varepsilon}(\omega) = \varepsilon_0 - \frac{\omega_{ps}^2}{\omega^2}\left(1 - \frac{B_0}{H_{c2}}\right) - \frac{\omega_{ps}^2}{\omega(\omega - i\gamma_s)}\frac{B_0}{H_{c2}} - \frac{\omega_{pn}^2}{\omega(\omega + i\gamma_n)}. \quad (2)$$

Here, γ_s is the damping constant inside the vortex.

The reflectivity spectra under magnetic field were measured at the beam line 6A1. The magnetic field up to 5 T was produced by a superconducting magnet. The configurations of the measurements are shown in Fig. 1. The light was guided to sample and detector by light pipes. The indices of the figure show configurations of (a) H // E and H // n, (b) H // E and $H \perp n$ and (c) $H \perp E$ and $H \perp n$. Here n means the normal vector of the sample and in all cases E // c is fixed.

The obtained reflectivity spectra are shown in Fig. 2. Configurations (a) and (b) are almost equal to each other. The result means that the interaction is independent of the direction of the sample surface. In the configuration (c), the magnetic field dependence is larger than that of (a) and (b). From the functions of (1) and (2), the difference is thought to come from the anisotropy of H_{c2}. By the fitting using the dielectric functions to the obtained reflectivity spectra, H_{c2} = 4.5 T in H // c and $H_{c2} \approx$ 100 T in $H \perp c$. This is known to be qualitatively equal to the result of magnetization measurement. [3]

[1] K. Tamasaku, Y. Nakamura and S. Uchida, Phys. Rev. Lett. 69 (1992) 1455.

[2] M. Tachiki, T. Koyama and S. Takahashi, Phys. Rev. B 50 (1994) 7065.

[3] Y. Koide, T. Nakanomyo and T. Fukase, Jpn. J. Appl. Phys. 27 (1988) L841.

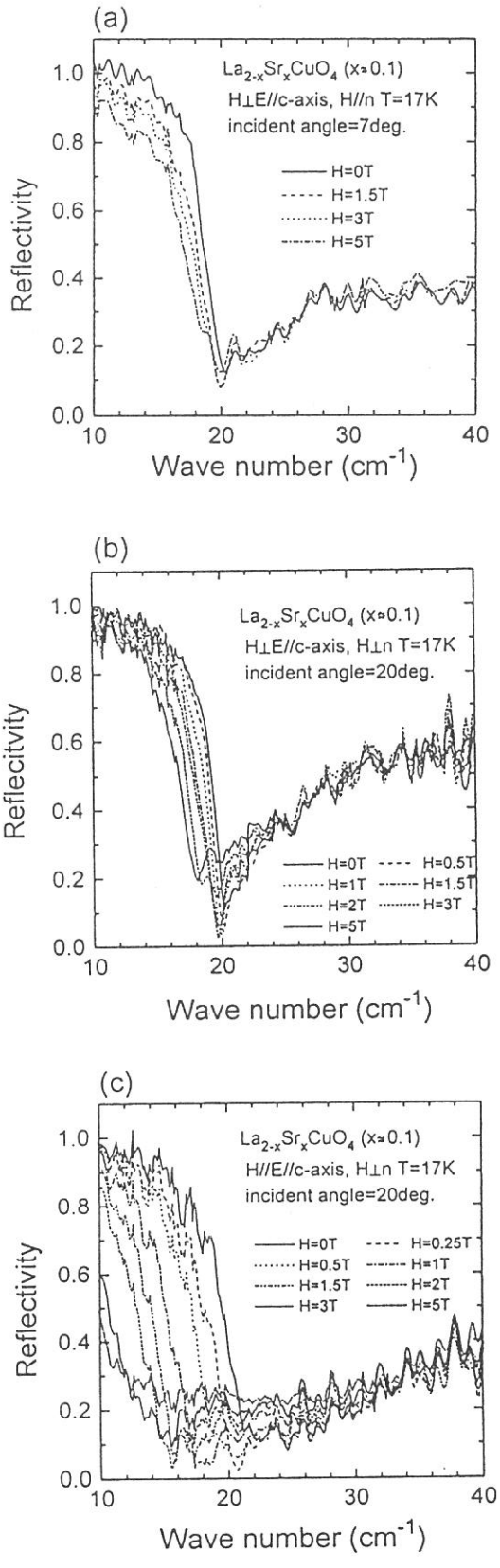

Fig. 2 Reflectivity spectra under magnetic field of $La_{2-x}Sr_xCuO_4$ (x ≈ 0.1). the indices (a), (b) and (c) correspond to those in Fig. 1.

(BL 6A2)

Sulfur Passivation of LPE Grown InGaP and AlGaAs

J. M. Seo, Y. K. Kim*, H. G. Lee*, Y. -S. Chung*, S. H. Kim*,
S. -I. Tanaka** and M. Kamada**

Jeonbuk National University, Jeonju 561-756, Korea
* KAIST, Daejon 305-701, Korea
**Institute for Molecular Science, Myodaiji, Okazaki 444, Japan

Sulfur passivation of III-V compound semiconductors has attracted much attentions for more than 10 years, hoping that it would solve the problems of high density surface states and Fermi level pinning near the midgap of compound semiconductor surface. As to S-treatment III-V ternary materials, however, very limited investigations concerning passivation effects and etching characteristics have been reported.

In this study investigated were nominally undoped n-type $In_{0.5}Ga_{0.5}P$ and n-type $Al_{0.6}Ga_{0.4}As$ layers grown on n^+-GaAs substrate by liquid phase epitaxy(LPE). Prior to introducing them into the ultra-high vacuum chamber, the S-treatment was carried out by dipping the degreased samples in the S-enriched $(NH_4)_2S_x$ solution at 50℃ for 30 min, which is the similar process of Iyer and Lile.[1]

Figure 1 shows both Ga and In reacted with S in the S-treatment due to their broad and increased peak intensities at higher binding energies than their bulk peaks. Through annealing near 200C, the relative intensity of Ga to In increased, which implies that the redistribution of S from In-S to Ga-S. Since the photoionization cross section of In 4d for 54eV (Fig. 1(a)) is about two times larger than that for 70eV (Fig. 1(b)) and the photoionization cross section of Ga 3d is about the same[2], the broad and increased peak intensity of Ga in Fig. 1(b) is due to S-redistribution due to annealing. After Ag deposition, the core levels did not move and In reacted with Ag as shown by the asymmetric shoulder at the lower binding energy of In 4d. After sputtering, core levels moved to lower binding energy by 0.6eV and Ga 3d peak became smaller and sharper. Therefore, it can be understood as follows; S-treatment initially produced In-S and Ga-S, the post-annealing induced the S-redistribution resulting in mainly Ga-S, the post deposited Ag produced Ag-In and Ga-S surface, and the final sputtering removed S and the band bended by 0.6 eV due to the produced gap-states.

On the other hand, for $Al_{0.6}Ga_{0.4}As$, S-treatment could not remove Al oxide initially as shown in Figure 2. Post-annealing near 200C induced the redistribution of S from As-S to Ga-S. Final sputtering removed S and the band bended by 0.2eV. Therefore it can be concluded that S-treatment can not remove Al oxide but the remaining Ga and As can be passivated in the similar fashion as GaAs.[3]

References

[1] R. Iyer and D. L. Lile, Appl. Phys. Lett. **59**, 437 (1991).
[2] J. J. Yeh and I. Lindau, Atomic Data and Nucl. Data Tables **32**, 51 and 69 (1985).
[3] T. Ohno and K. Shiraishi, Phys. Rev. B**42**, 11194 (1990).

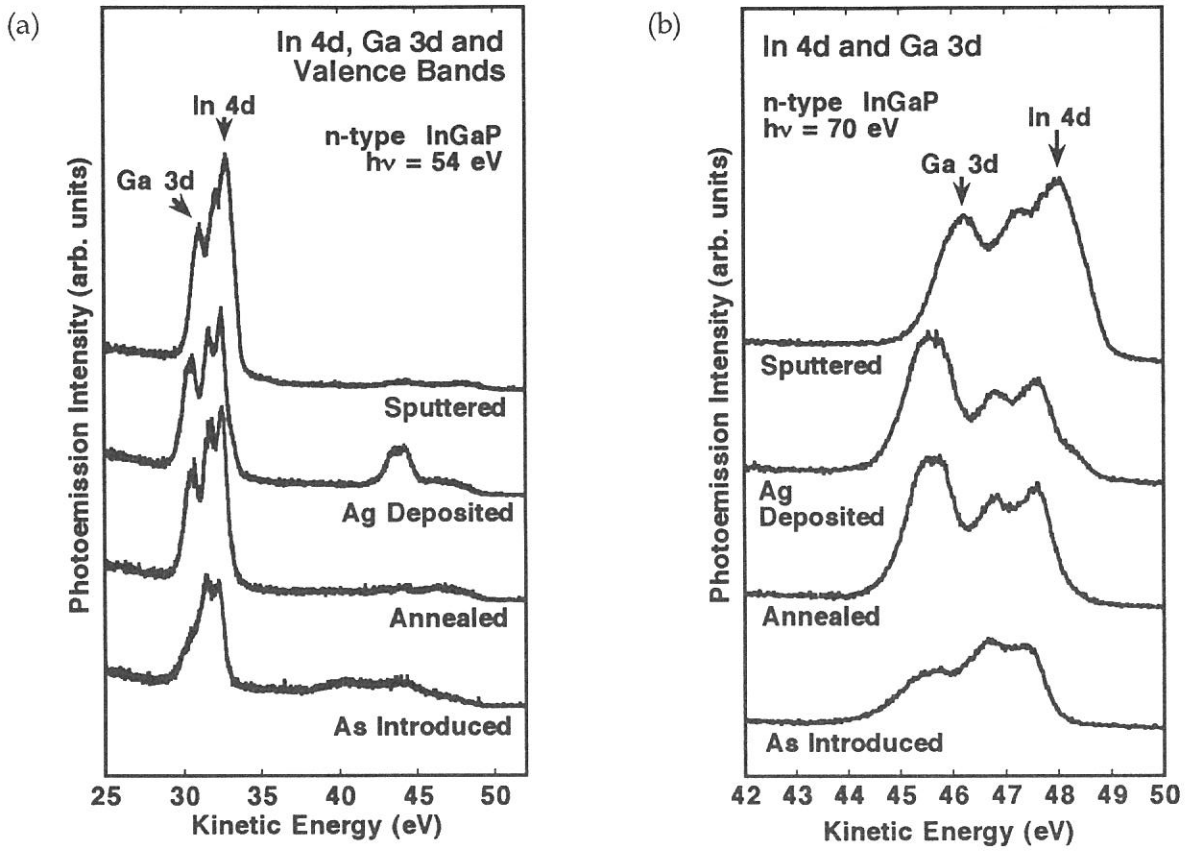

Figure 1. Photoemission spectra of S-treated $In_{0.5}Ga_{0.5}P$ for (a) 54 eV and (b) 70 eV photon energy.

Figure 2. (below) Core-level photoemission spectra of S-treated $Al_{0.6}Ga_{0.4}As$.

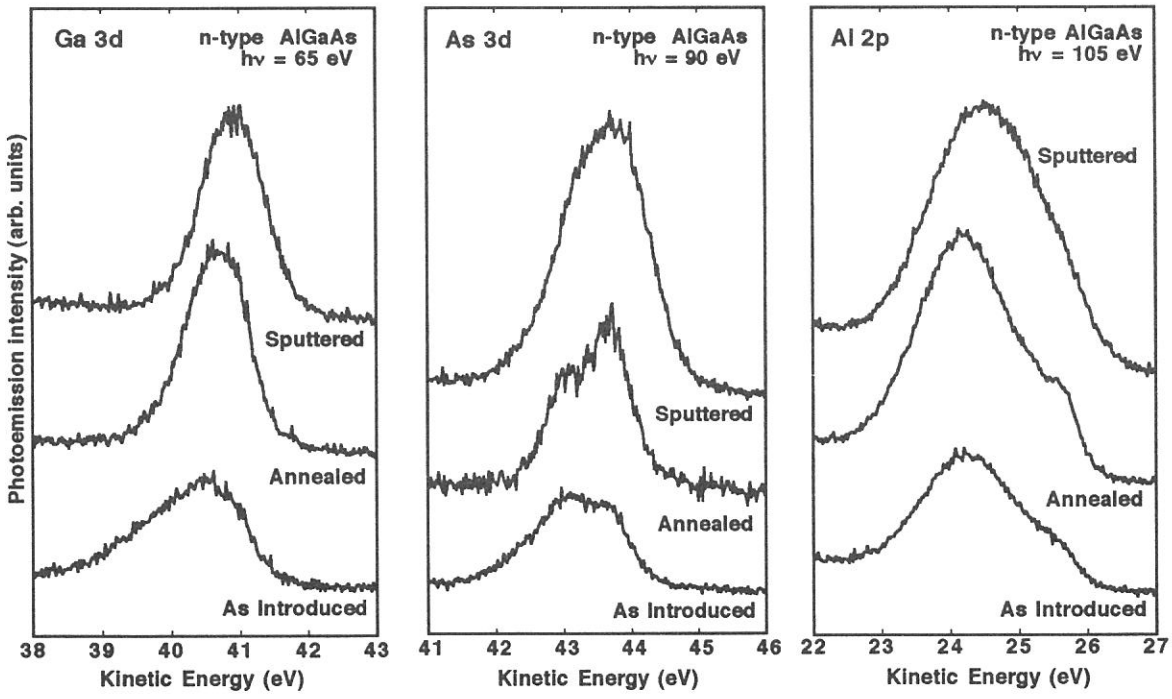

The Properties of $PbWO_4$ Crystal Using Synchrotron Radiation

Jie Deng, Zhengfu Han, Guobing Zhang, Chaoshu Shi
National Synchrotron Radiation Lab., USTC, 230026 Anhui, China
M. Kamada
UVSOR Facility IMS, Japan

I. Introduction

The properties of $PbWO_4$ have been studied since the late 1940s [1,2]. Recently the fast luminescence of nano-second order of $PbWO_4$ was discovered, and $PbWO_4$ became the first candidate material of Large Hadro collidator (LHC) of CREN [3]. It has some special characters such as high density (8.9 g/cm^3), short radiation length (0.98cm, the known shortest), high radiation hardness (>10^6 rad), fast luminescence decay (~2 ns) and lower cost compared with other new scintillator (e.g. CeF_3) [4]. The main shortage of $PbWO_4$ is the low luminescence efficiency (4.4% as much as that of BGO scintillator). Many research works have been done on $PbWO_4$, most of which on its application. However few have been done on its luminescence mechanism. For getting further knowledge of $PbWO_4$, we have measured its emission, excitation spectra and decay constant at different temperature using synchrotron radiation.

II. Experimental

The $PbWO_4$ single crystal is of the sheelite type and is grown by the Bridgman method. No.1 sample was come from Russia and No.2 sample from Shanghai Ceramic Institute of China. The emission and excitation spectra and lifetime were measured on UVSOR BL6A2 beamline in Japan.

III. Results and discussion

The emission spectral was measured by using zero order light with Al filter i.e. λ_{ex}<130nm, as shown in Fig.1. The emission spectral is a broad band complexing in the whole visible range (370-700 nm), its FWHM is 125 nm and the peak position is at 510 nm. The emission spectral is asymmetry, so it must be superposed by several bands (one blue band, two green bands and one red band [5]). This result coincide with the decay time measurement.

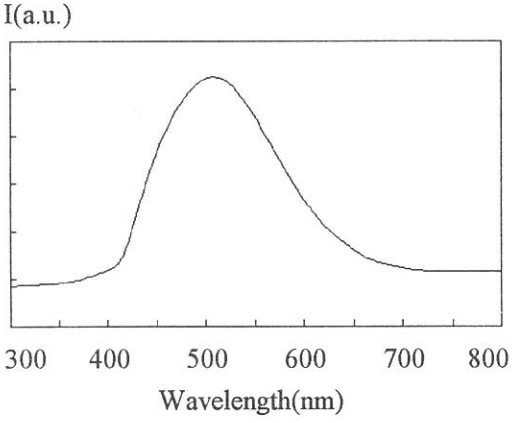

Fig.1 The emission spectral of $PbWO_4$ crystal excited by λ_{ex}<130nm.

According to the emission spectral, we measured excitation spectra of 430, 520, 570 and 630 nm bands from $PbWO_4$ crystals. The strongest excitation range is in 5-8 eV. In the range of 8-22.5 eV there are three bands peaked at about 11.0, 16.5 and 21.0 eV (Fig.2). The first two bands are stable ,but the last one was varied with different emission bands or different temperatures. At lower temperature (~131K) it changed into narrow band and disappeared for the 630 nm band. On the other words, the excitation band at 21.0 eV was very sensitive to emission band and sample temperature, it may be originated from the excitation of impurity level in the second or the third band gap. The excitation range of 5-8 eV can be assigned to transition from valence band to high excitation states of conduct band. The excitation band peaked at 16.5 eV is probably originated

from $5d_{5/2}$ (18.1 eV) of Pb state excitation.The weak excitation band at about 34.5 eV (Fig.3) may be related to the excitation of core electrons (W-$5P_{3/2}$ 36.8eV, W-$4f_{5/2}$ 33.4eV and W-$4f_{7/2}$ 31.4eV).

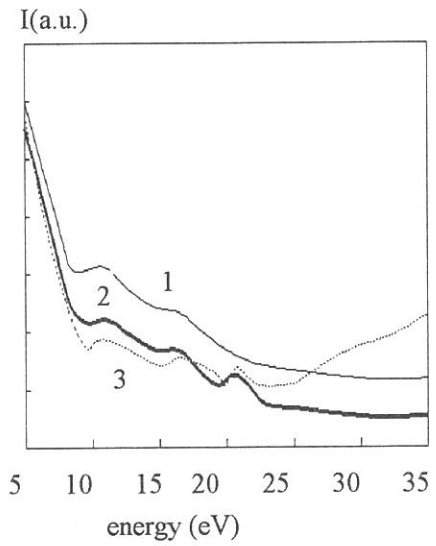

Fig.2 The excitation spectra 1-630nm at RT
2-520nm at RT, 3-520nm at 131K

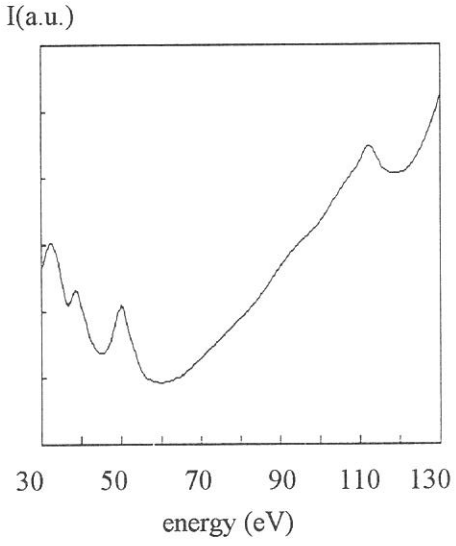

Fig.3 The excitation spectral of 520nm emission at RT.

We measured the luminescent decay of $PbWO_4$ by time-related single photon counting, and the results are listed in the table. At the room temperature, decay time of $PbWO_4$ crystal was increased with rising emission wavelength, so fast components of 0.62, 1.33, 2.33 ns were for 400, 430 and 500 nm emission respectively. For each emission band, decay time was shortened by increasing temperature. For example, at 430nm emission the decay times of 6.25 and 95.3ns was at 131K, 3.57 and 51.8ns at 152K, 1.33 and 4.52ns at room temperature respectively. For 500 nm emission band only slow component of decay time 145.6 ns was detected at 131K. At 172K, the fast and middle components(5.04 and 94.7 ns) were measured. At low temperature decay time of every emission band was extended. Meanwhile there is a rise time of luminescence (1.5-2.0ns) before luminescence decay. The rise time was increased with increasing emission wavelength. It indicates that luminescence centers are acceptor centers of energy.

The experimental results coincide with No.1 and No.2 sample.

Table. the decay time of $PbWO_4$ at different emission wavelength excited by λ_{ex}<130nm

λ_{em} (nm)	400			430			500			550		
decay time (ns)	τ_1	τ_2	τ_3	τ_1	τ_2	τ_3	τ_1	τ_2	τ_3	τ_1	τ_2	τ_3
300K	0.62	3.44		1.33	4.52	205.2	2.32	20.5	101.8		12.0	60.6
172K							5.0	94.8				
152K				3.57	19.2	84.4						
131K		51.3	92.3	6.25	95.3			145.6		5.24		108.8

[1] F.A. Kroger, Some Aspects of the Luminescence in Solids (Elsevier, Amsterdam, 1948).

[2] R. Grasser et al., presented at the Int. Conf. ICL'93, Storrs, USA, August 1993.

[3] V.G. Baryshevsky et al., Nucl. Instr. Meth. A322, 231 (1992).

[4] O.V. Buyanov et al., Nucl. Instr. Meth. A349, 62 (1994).

[5] J.P. Peigneux, Nucl. Instr. Meth. A351, 197 (1994).

(BL6A2)

Angle-Resolved Photoelectron Spectroscopy of Si(111)-$\sqrt{3}\times\sqrt{3}$-(Au, Cu) and Related Si(111) Surfaces with Single Noble Metal Adsorbates

Kazuo SODA, Kazuhiko YAMASAKI, Dai ISHIKAWA, Junji YUHARA, and Kenji MORITA

Department of Crystalline Materials Science, School of Engineering, Nagoya University
Furo-cho, Chikusa, Nagoya 464-01

A system of binary metal adsorbates on the Si(111) surface is more complicated than those of single adsorbates, but has a fascinating possibility of modifying the optical, electrical and thermal properties of a thin film because of the additional interaction between the two different adsorbates. We have so far investigated atomic structures and composition of such binary noble metal adsorbates on the Si(111) surface by means of a combined analyzing technique of low-energy electron diffraction (LEED), Auger-electron spectroscopy (AES), and high-energy ion scattering (HEIS). We have found an ordered phase of Au-Cu binary adsorbates, that is a Si(111)-$\sqrt{3}\times\sqrt{3}$-(Au, Cu) surface, and proposed formation of an ordered two-dimensional alloy of Au_4Cu on the Si(111) surface. [1-4] In order to elucidate its electronic structure, we have performed angle-resolved photoelectron measurement of the binary adsorbate system as well as the related surfaces with a single adsorbate, *i.e.* Si(111)-quasi 5×5-Cu and Si(111)-$\sqrt{3}\times\sqrt{3}$-Au, at BL6A2 of UV-SOR. In this report, we present a preliminary result.

We used a mirror-polished *n*-type Si(111) wafer of 3×15×0.5 mm^3 in size and 3.0 Ωcm in resistivity as a substrate. The Si(111)-quasi 5×5-Cu surface was prepared by deposition of about 1 monolayer (ML) Cu onto the Si(111)-7×7 surface, cleaned by direct-current heating, and subsequent annealing at about 450 °C, and the Si(111)-$\sqrt{3}\times\sqrt{3}$-Au surface by about 0.7 ML Au deposition onto the cleaned Si(111)-7×7 surface followed by annealing at about 500°C. The Si(111)-$\sqrt{3}\times\sqrt{3}$-(Au, Cu) surface was obtained by annealing at about 200°C after deposition of about 0.2 ML Cu onto the Si(111)-5×2-Au surface, which was prepared by Au deposition onto the cleaned Si(111)-7×7 surface and subsequent annealing. The Fermi-level position was determined by photoemission from the metallic Ta sample holder, and the excitation photon energy was calibrated by measuring the difference in the kinetic energy between the Ta *d* photoelectrons excited by the first-order light from the monochromator and those by the second-order light.

Figure 1 shows typical angle-resolved photoelectron spectra of the Si(111)-$\sqrt{3}\times\sqrt{3}$-(Au, Cu) (a), Si(111)-quasi 5×5-Cu (b), and Si(111)-$\sqrt{3}\times\sqrt{3}$-Au (c) surfaces measured with the *p*-polarized 22.2 eV exciting photons incident along the $[1\bar{0}\bar{1}]$ direction at the polar angle of 45°. The polar angle of emitted photoelectrons along the $[10\bar{1}]$ direction is indicated in the figure. As for the Si(111)-quasi 5×5-Cu and Si(111)-$\sqrt{3}\times\sqrt{3}$-Au surfaces, obtained spectra are similar to those reported so far. [5,6] Prominant peaks around 3 and 4 eV below the Fermi level for the Si(111)-quasi 5×5-Cu surface are mainly due to the Cu3*d* states, while the emission bands around -4.5 and -6.5 eV in the spectra of the Si(111)-$\sqrt{3}\times\sqrt{3}$-Au surface are ascribed mainly to the Au5*d* states. Corresponding peaks are observed around -3.5, -4.5, and -6.5 eV in the spectra of the Si(111)-$\sqrt{3}\times\sqrt{3}$-(Au, Cu) surface. Clear surface states are also recognized between -2 eV and the Fermi level in the spectra measured at the polar angles of 50° and 60° for the Si(111)-$\sqrt{3}\times\sqrt{3}$-(Au, Cu) surface. Detailed analysis is now in progress and will be reported elsewhere.

References

[1] M. Sasaki, J. Yuhara, M. Inoue, and K. Morita, Surf. Sci. **283** (1993) 327.
[2] J. Yuhara, M. Inoue, and K. Morita, J. Vac. Sci. Technol. A **11** (1993) 2714.
[3] J. Yuhara, R. Ishigami, and K. Morita, *Control of Semiconductor Interfaces*, ed. I. Ohdomari, M. Oshima, and A. Hiraki, (Elsevier Science B.V., North-Holland, 1994) p.399.
[4] J. Yuhara, R. Ishigami, and K. Morita, Surf. Sci. **326** (1995) 133.
[5] C. J. Karlsson, E. Landemark, L.S.O. Johansson and R. I. G. Uhrberg, Phys. Rev. B **42** (1990) 9546.
[6] D. D. Chambliss and T. N. Rhodin, Phys. Rev. B **42** (1990) 1674.

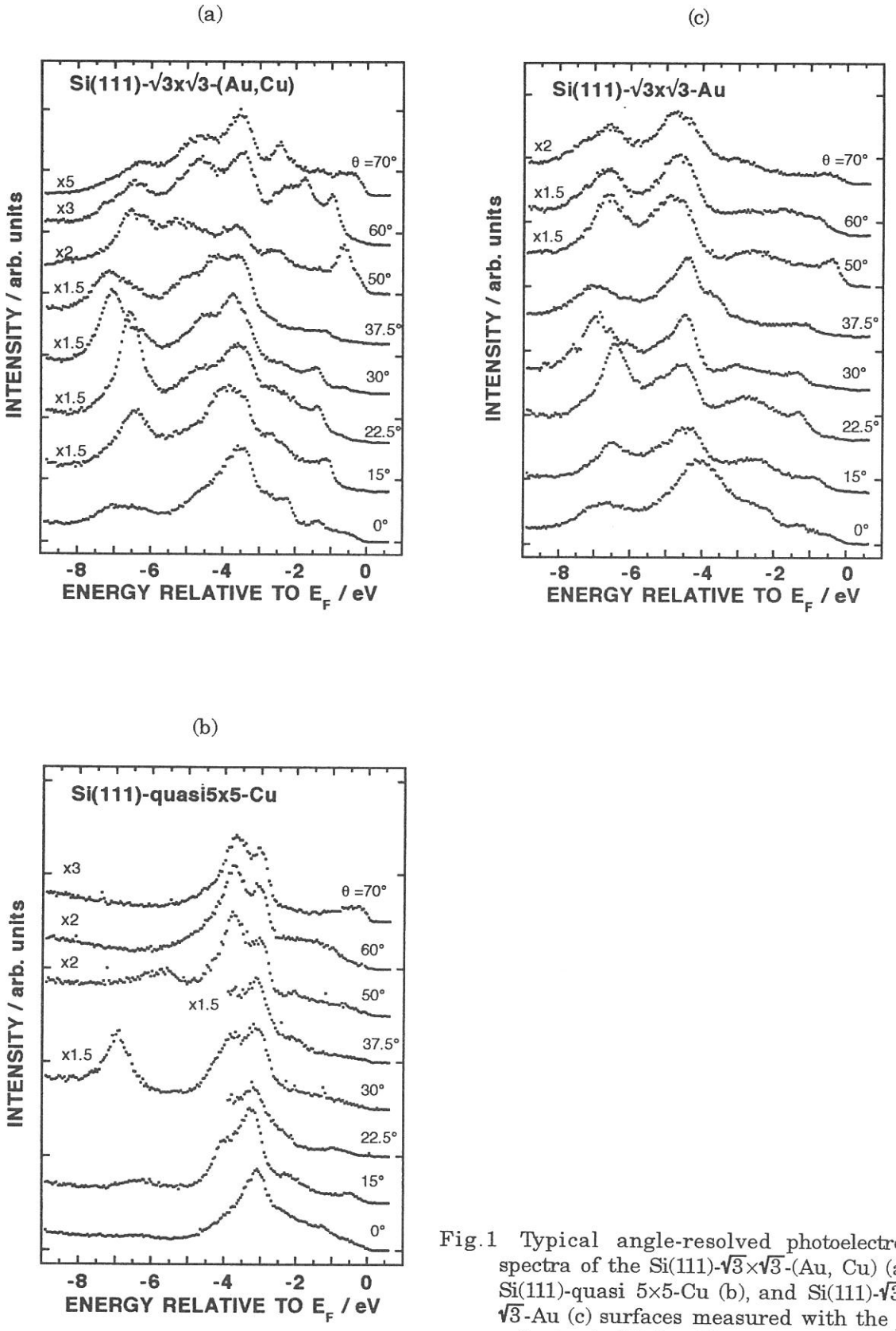

Fig.1 Typical angle-resolved photoelectron spectra of the Si(111)-$\sqrt{3}\times\sqrt{3}$-(Au, Cu) (a), Si(111)-quasi 5×5-Cu (b), and Si(111)-$\sqrt{3}\times\sqrt{3}$-Au (c) surfaces measured with the *p*-polarized 22.2 eV exciting photons incident along the [10$\bar{1}$] direction at the polar angle of 45°. The polar angle of emitted photoelectrons along the [10$\bar{1}$] direction is indicated in the figure.

Clean and Hydrogen Exposed GaAs(111)A and (111)B Surfaces studied by Angle-resolved Photoemission

YQ Cai, S Tanaka, N Takahashi, and M Kamada.
UVSOR, Institute for Molecular Science, Okazaki 444, Japan.
DA Woolf
University of Wales, College of Cardiff, Cardiff CF2 3YB, United Kingdom.

GaAs is an important semiconductor. So far, there have been numerous studies of its surface electronic and geometric properties[1]. However, these studies have been mostly concentrated on the (110) and (100) surfaces for technical reasons, and not so much for the (111)A and (111)B surfaces. The latter two surfaces are of interest because they are known to exhibit very different electronic structures[2], even though the ideal surfaces have the same geometrical arrangement with only the two species interchanged. The real surfaces, however, reconstruct in different ways depending on the surface stoichiometry and the way in which the surfaces are prepared[3].

In order to investigate the fundamental question of how the surface electronic structure and the surface geometry are related to each other, we have carried out comparative studies of clean and atomic hydrogen exposed GaAs(111)A and (111)B surfaces using angle-resolved photoemission on beamline 6A2. The samples were grown by MBE and were protected by a thick amorphous As cap, which was removed later by thermal heating.

The core level spectra and the valence band spectra indicate that upon hydrogen exposure of 1×10^{6}L, both the Ga-terminated (111)A and the As-terminated (111)B surfaces become virtually identical. This conclusion is based on the line shape (Fig.1) and the integrated intensity ratio (Fig.2) of the As3d and Ga3d core levels from the two surfaces, as well as on similar valence band spectra that show a non-dispersive and dominant feature at around 5eV below the valence band maximum (see Figs.3 and 4). The observed LEED pattern of the surfaces shows faint 1×1 spots with

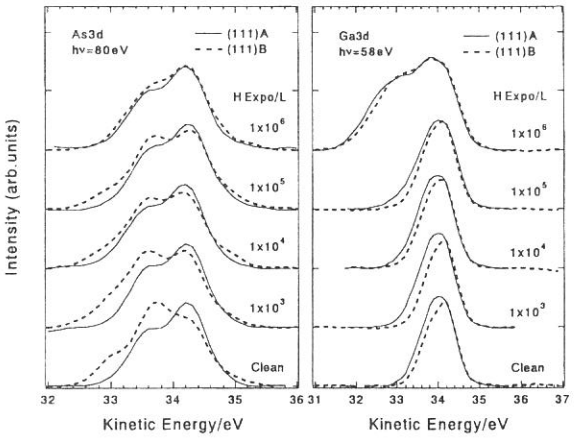

Fig.1 As3d and Ga3d spectra with different hydrogen exposures.

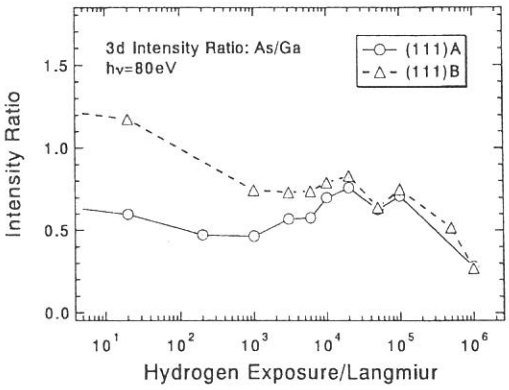

Fig.2 Integrated Intensity ratio of As3d/Ga3d corrected with inner-shell photoionization cross sections.

bright and diffuse background, indicating that the surfaces might be disordered, consistent with the valence band measurements.

Although the final surfaces after 1×10^6L of hydrogen exposure appear to be identical, the surfaces with less hydrogen exposure show distinctively different behavior, as suggested by both the core level (Fig.1) and the valence band spectra (Figs.3 and 4). The valence band measurements show that the adsorbed hydrogen contributes strongly to the valence spectra of the (111)B surface, with sharp and prominent features at around 3 and 5eV below VBM, whereas on the (111)A surface, features due to hydrogen are small and often invisible. Detailed analysis of the core level spectra involving the fitting of the spectra with surface and bulk components is underway and should produce information on how the surface geometry evolves upon hydrogen exposure. The study of the surface valence band structure, particularly of the hydrogen-induced features, within the surface Brillouin zone, should also produce interesting and important data for comparison with theoretical calculations.

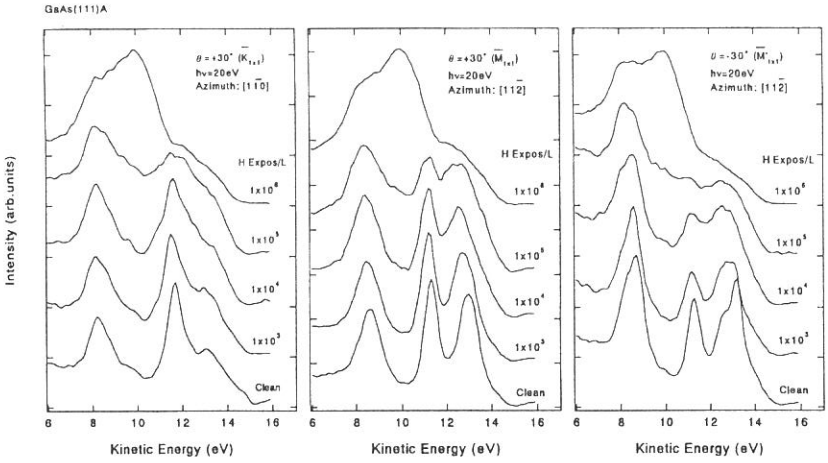

Fig.3 Angle-resolved photoemission spectra taken from the GaAs(111)A surface. Each set of the spectra corresponds roughly to a critical point (indicated in the figure) of the surface Brillouin zone.

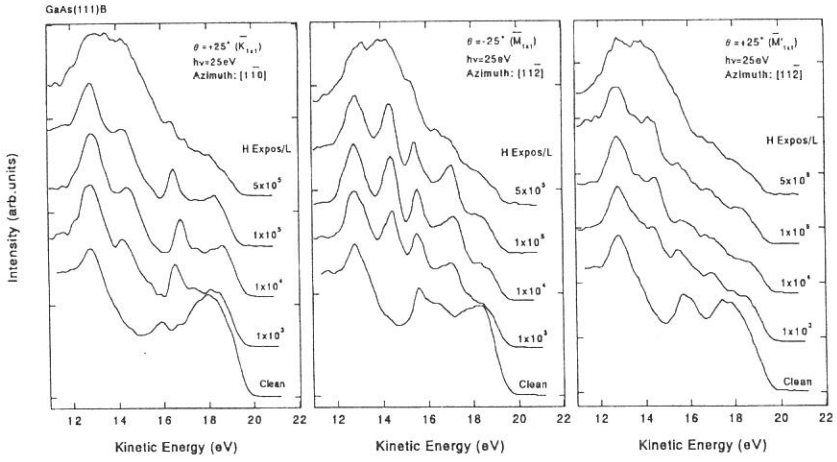

Fig.4 Angle-resolved photoemission spectra taken from the GaAs(111)B surface. Each set of the spectra corresponds roughly to a critical point (indicated in the figures) of the surface Brillouin zone.

[1] R.I.G. Uhrberg and G.V. Hansson, CRC Crit. Rev. Solid State Mater. Sci. **17**, 133 (1991), and references therein.
[2] R.D. Bringans and R.Z. Bachrach, Phys. Rev. Lett. 53 (1984) 1954.
[3] W. Ranke and K. Jacobi, Prog. Surf. Sci. 10 (1981) 1.

(BL6A2)

CIRCULAR DICHROISM OF PHOTOELECTRON SPECTRA FROM GaAs (111)

Masao Kamada, Naoshi Takahashi, Yong Q. Cai, and Masatake Ichikawa[a]

UVSOR, Institute for Molecular Science, Okazaki 444

[a]College of Engineering, Fukui University, Fukui 910

Synchrotron radiation provides circularly polaried lights in VUV region. We can get useful informations of electronic structures of magnetic and non-magnetic materials by using circular polarization of synchrotron radiation. We have designed a new type of helical undulator (1), which provides circularly polarized lights in the energy range of 4-40 eV and elliptically polarized lights up to 250 eV. This undulator is going to be installed in the straight section of a UVSOR storage ring this March. The purpose of this study is to see circular dichroism in photoelectron spectroscopy on non-magnetic materials.

Experiments were carried out at a beam line 6A2 with using a plane-grating monochromator which has no entrance slit. Synchrotron radiation was introduced to a grating through two pre-mirrors which made the light path pararell. Elliptically polarized lights were obtained from an upper or a lower part of synchrotron radiation from a bending magnet by using a diaphragm installed between the first pre-mirror and the second one. The degree of circular polarization was estimated to be about 20-30 % by using optical constants of all mirrors and a grating. A clean GaAs (111)B surface was prepared by thermal heating of an As-capped GaAs in low of 10^{-10} Torr range. A hydrogen-terminated GaAs(111)B surface was also prepared by hydrogen exposure of $1x10^5$ L. A hemi-spherical electrostatic analyser was used to observe photoelectron spectra. The overall resolution of the present experiments was about 0.2 eV around 50 eV, and the angular resolution was about 1.1 degree. Figure 1 shows the schematic geometrical arrangement. The intensity of the incident lights was monitored by a gold mesh located between a post-mirror and samples. All spectra were normalized by using photoelectric yield of this gold mesh.

Figure 2 shows the circular dichroism of photoelectrons of a clean GaAs. The dichroism of the valence band spectra is too small to be observed, while the Ga 3d spectra show a remarkable circular dichroism depending on the azimuthal angles Φ. It is obvious that the dichroism increses with increasing the azimuthal angles. It should be stressed that the circular dichroism of the Ga 3d from the hydrogen-terminated surface has an opposite polarity compared to that from the clean surface. This indicates that the present dichroism is not due to an aligned atom with spherical symmetry, but due to an atom affected by a crystalline field in the surface layer.

While there are many works of circular dichroism on magnetic materials, a few works have been carried out on non-magnetic materials. Schonhense (2) has reviewed their pioneer works on adsorbates on metallic substrate and explained the dichroism of valence band spectra in terms of interference between final-state wavefunctions. Dimon et al. (3) has observed a dichroism of Si 2p photoelectrons by using a 2-dimentional analyser and interpreted it from a view point of photoelectron diffraction effects.

When only the interference between the final-state p wavefunctions affected by a crystalline field is taken into account, the circular dichroism is expressed by

$$CD \propto \sin 2\Phi \cdot \sin\Theta \cdot \sin(\delta_{pz}-\delta_{pxy}), \qquad (1)$$

where $\sin 2\Phi \cdot \sin\Theta$ is a structural factor and $\sin(\delta_{pz}-\delta_{pxy})$ is a phase factor. From this

equation, the difference in polarity of the dichroism between the clean and the hydrogen-terminated surfaces is attributed to the difference in the phase factor.

However, the dichroism of Ga 3d photoelectrons from the hydrogen-terminated surface increased with increasing the azimuthal angles and showed a dip around 40 degree. This dip cannot be explained with the simple interference mentioned above. The photoelectron diffraction effects cannot explain the dip either, since it must have a peak around 47 degree. The interference between p and f symmetries as well as p_z and p_{xy} symmetries in the final-state may cause the dip in the dichroism.

References

(1) S. Kimura, M. Kamada, H. Hama, X. M. Marechal, T. Tanaka, and H. Kitamura, to be published in proc. of VUV 11.

(2) G. Schonhense, Phys. Scr. T31, 255 (1990).

(3) H. Daimon, T. Nakatani, S. Imada, S. Suga, Y. Kagoshima, and T. Miyahara, Jpn. J. Appl. Phys. 32, L1480 (1993).

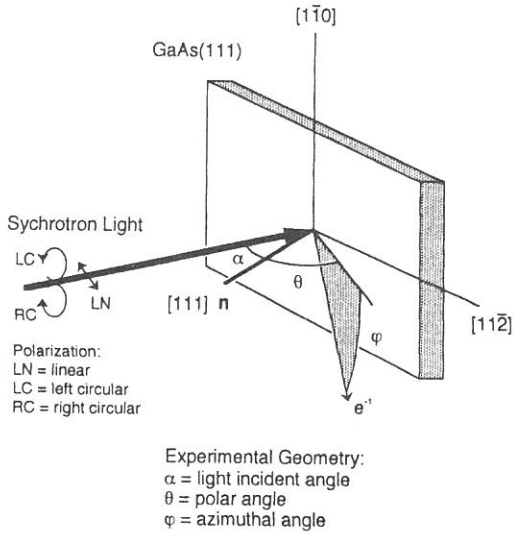

Fig. 1. Schematic geometrical arrangement.

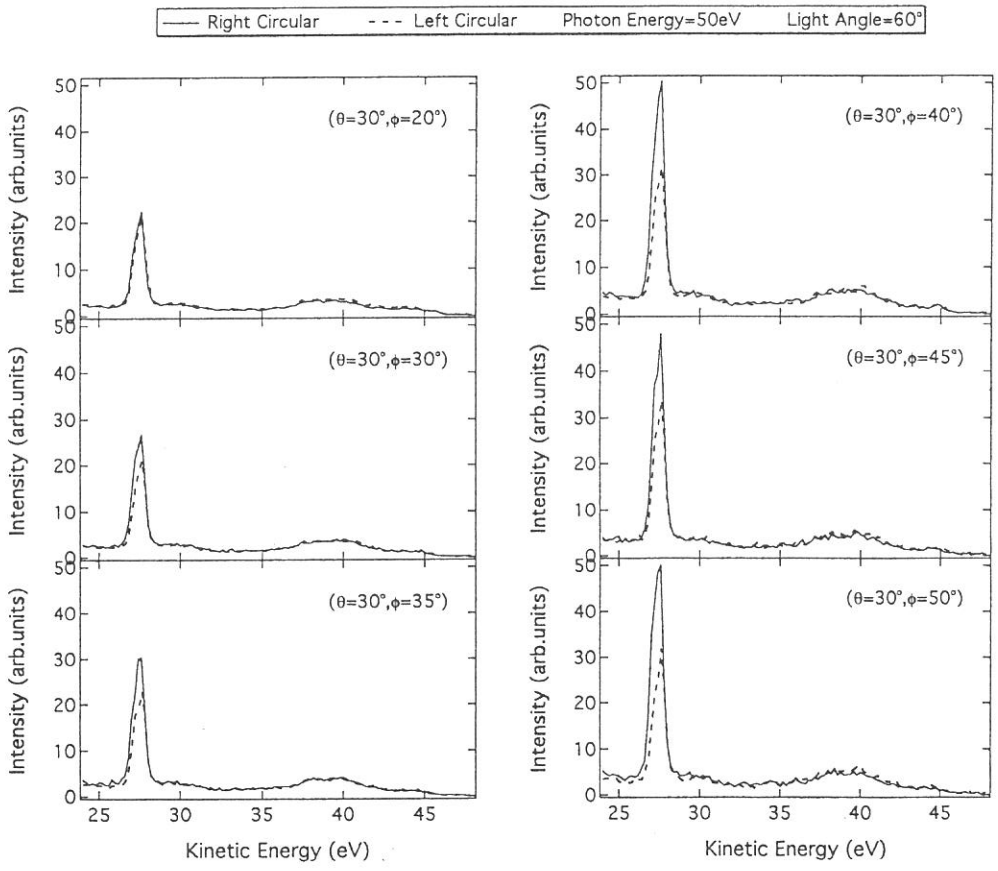

Fig. 2. Circular dichroism of photoelectrons of a clean GaAs(111).

(6A2)

Photoelectron and Luminescence Spectra of BaFCl and BaFBr

M. Kamada, N. Takahashi, S. Hirose, S. Ohara,[a] M. A. Terekhin,[b] S. S. Galaktionov,[c] and S. S. Galaktionov[d]

Institute for Molecular Science, Myodaiji, Okazaki 444, Japan

[a]Nagoya Institute of Technology, Nagoya 466, Japan

[b]Russian Research Center "Kurchatov Institute", Moscow 123182, Russia

[c]Mendeleev University, Moscow 125190, Russia

[d]NPO "Simplex", Moscow 123367, Russia

Barium halides have attracted much interest in recent years, because they show clear resonant effects in the photoelectron spectra, and also because they have a variety of luminescence. For examples, the intensities of the Ba-$5p_{1/2}$ photoelectrons in BaF_2, $BaCl_2$, and BaB_{r2} are resonantly enhanced at the excitation photon energy of Ba-4d electrons. [1,2] Moreover, BaFCl and BaFBr including rare-earth elements show the strong recombination luminescence band. These luminescence have been applied to a fast scintilation and a resistration of x-rays. However, their detailed electronic structures are still not clear, and systematical studies are required. The purpose of the present work is to understand the electronic structures of BaFCl and BaFBr, and to investigate the luminescence properties in the energy regions corresponding to the Ba-4d excitation.

Experiments were carried out at beam line 6A2 of UVSOR facility, Institute for Molecular Science. The monochromatized synchrotron radiation through a plane grating monochromator was used as an light source. Absorption spectra were obtained by measuring total electron yields from samples. Photoelectron spectra were measured with a cylindrical energy analyser. The overall resolution was about 0.4 eV around 100 eV.

Excitation spectra were obtained by using an interference filter, since the luminescence intensity from evaporated films was too weak. Samples were prepared by in-situ evaporation on gold substrates in a preparation chamber, and were transfered into an analysing chamber, the pressure of which was about $2x10^{-8}$ Pa. Thickness of the samples were about 10 and 100 nm for photoelectron and luminescence spectroscopies, respectively.

Figures 1(a) and 1(b) show photoelectron spectra of BaFCl and BaFBr obtained at 110 eV, respectively. Binding energies are given relative to the top of the valence band. The Ba-$5p_{3/2}$, Ba-$5p_{1/2}$, and Ba-5s levels are seen about 11, 13, and 26 eV, respectively. Broad bands denoted by A1 and A2 are attributed to the N4,5-O2,3V and $N_{4,5}$-$O_{2,3}O_{2,3}$ Auger electrons, respectively. It should be noted that the Cl-3p and F-2p states in BaFCl are so close in energy that the valence band consists of mixing of these two states, while the Br-4p and F-2p states in BaFBr are splitted in energy and then the valence band may be separated into two branches originated from each halogen p state.

Luminescence bands are observed around 382 and 245 nm on BaFCl and BaFBr, respectively. Excitation spectra of these luminescence on BaFCl and BaFBr are shown in Figs. 2 and 3, respectively, as well as absorption spectra. Constant-initial-state (CIS) spectra with the initial state at the peak of the valence band originated from Cl-3p and Br-4p states are also shown in the figures, for comparison. There are several peaks and shoulders in the Ba-4d absorption spectra. The small and sharp peaks denoted by a and b are due to the multiplet states (^3P and ^3D) of the $4d^9 4f^1$ configuration, while the other intense structures denoted by c-f are attributed to the ^1P state of the $4d^9 4f^1$ mixing with the other $4d^9 nf^1$ states (n=5, 6, and so on). Crystal field and autoionization into the continuum from the multiplets also affects the spectral structures c through f.

The CIS spectrum of BaFCl decreases monotonously with increasing the photon energy, while that of BaFBr shows a small hump around the photon energy corresponding to the peak d. This result indicates that the direct excitation of valence electrons does not cause the structures in the excitation spectra. On the other hand, the excitation spectra of BaFCl and BaFBr show structures corresponding well to the absorption peaks. Therefore, it is supposed that the optical luminescence is produced by secondary processes induced by the decay of the Ba-4d holes.

By assuming that the luminescence intensity due to the Ba-4d excitation, I_c, superposes the intensity due to

the valence excitation, I_v, and that the energy dependence of I_v is negligible in the energy region of the Ba-4d excitation, the ratio of the quantum efficiencies between the Ba-4d and the valence excitations is given by,

$$\eta_c/\eta_v=(I_c\mu_v)/(I_v\mu_c), \qquad (1)$$

where μ_v and μ_c are the absorption coefficient for valence and core-level excitations, respectively. The ratios η_c/η_v obtained from the observed excitation and absorption spectra are about 0.62 and 2.2 for BaFCl and BaFBr, respectively, at the photon energy corresponding to the excitation energy of ^{3}D. The ratios for ^{1}P are alomost the same as those for ^{3}D. Therefore, it is supposed that the valence holes may localize in the Br-4p state of BaFBr to recombine with electrons better than in the Cl-3p state of BaFCl. This idea is consistent with the valence band spectra mentioned above.

References

1] M. kamada, K. Ichikawa, and O. Aita, Phys. Rev. B47 (1993) 3511.

2] K. Ichikawa, O. Aita, K. Aoki, M. Kamada, and K. Tsutsumi, Phys. Rev. B45 (1992) 3321.

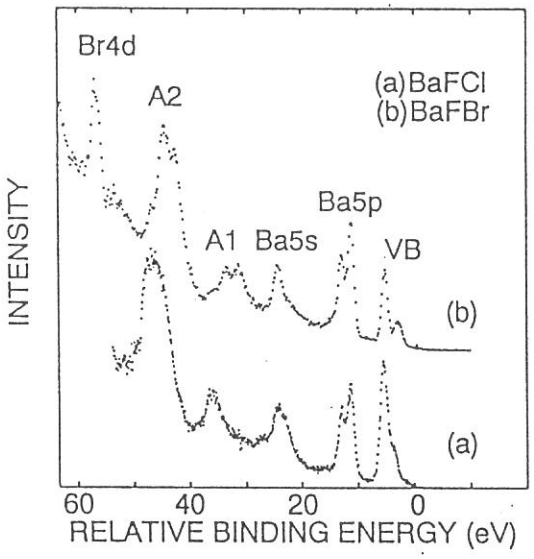

Fig. 1 Photoelectron spectra of BaFCl and BaFBr obtained at 110 eV, respectively.

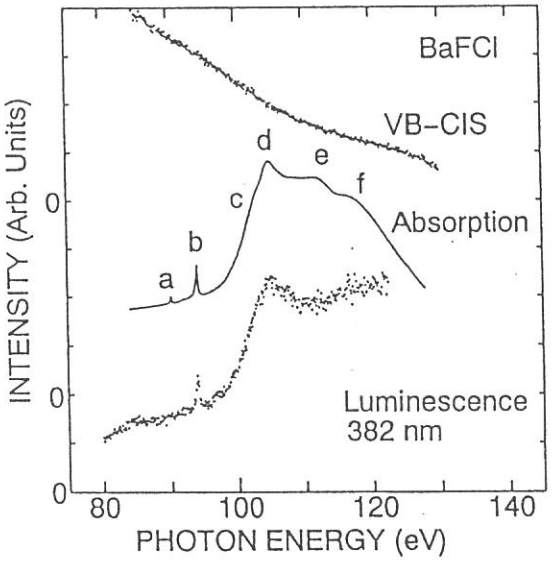

Fig. 2 Excitation spectrum of the 382 nm band, absorption spectrum obtained with a total-electron yield method, and a Cl-3p CIS spectrum.

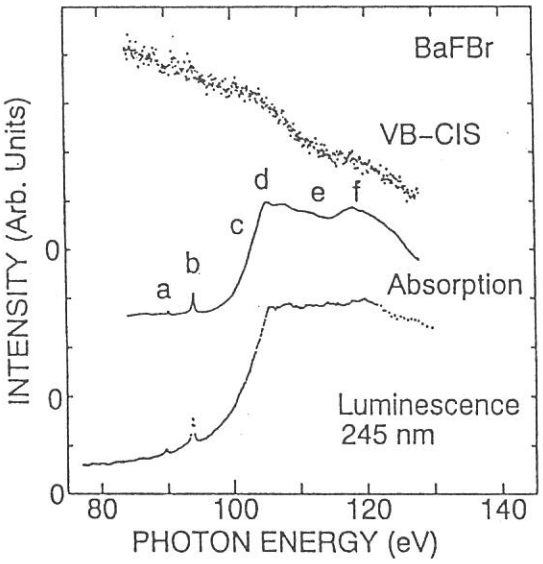

Fig. 3 Excitation spectrum of the 245 nm band, absorption spectrum obtained with a total-electron yield method, and a Br-4p CIS spectrum.

(BL-6A2)

Magnetic Circular Dichroism of Absorption and Photoelectron Spectroscopies at Ni $M_{2,3}$-edges

Shinya Yagi and Toyohiko Kinoshita

UVSOR Facility, Institute for Molecular Science, Myodaiji, Okazaki 444, JAPAN

Introduction

Recently, the investigation of magnetic circular dichroism (MCD) in ferromagnetic materials has attracted a lot of interest. The MCD measurements of ferromagnetic Ni at $M_{2,3}$-edges were performed by Koide *et al.*[1] and Muto *et al.*[2] Since the samples of their MCD measurements were not checked the cleanliness and the order of the surface atoms, their results were not for surface property. In this report, we have measured the MCD for the well-established Ni(110) surface at $M_{2,3}$-edges in order to investigate surface magnetic properties. We have also measured the MCD for the valence-band photoemission spectra to understand the resonant process of the 6-eV satellite[3].

Experiment

A Ni(110) single crystal was mechanically and electrochemically polished, and then mounted in an UHV chamber whose base pressure was 2×10^{-8} Pa. The crystal was cleaned by Ne^+ ion bombardment and annealing at about 1000 K by means of electron bombardment. The cleanliness and order were checked by AES and LEED, respectively. The shape of the sample is picture frame which is described elsewhere[4]. An each side of the Ni(110) sample was oriented along the <111> direction. We equipped one side with a coil (ceramic-coated Cu wire). Saturated magnetization (in-plane) was easily achieved by supplying a pulsed current of $\pm$20 A to the coil. All measurements were carried out at BL-6A2 which equipped with a plane grating monochromator (PGM). In order to obtain circularly polarized light, we have used the upper part light above the beam orbit by using the diaphragm which was set in front of the first mirror. Angle between the incident light and the sample surface was fixed at 10° . Absorption spectra around Ni $M_{2,3}$-edges (50-85 eV) were measured by use of the total photoelectron yield (PY). Photoelectron spectra (normal emission) were recorded using the angle-resolved photoelectron spectrometer.

Results and Discussion

Figure 1 shows the PY spectra of Ni $M_{2,3}$-edges for two opposite magnetization directions. Inset of the figure 1 shows the MCD spectrum which was derived from the PY spectra. In comparison with the MCD spectrum measured by Koide *et al.*[1], whose peak-to-peak signal intensity of the MCD spectrum was about 14 % at 80 % circularly polarized light, it was estimated that the circular polarizability in our measurements was about 20 %. The present MCD intensity of negative contribution in the lower-energy region (pre-threshold energy) is nearly equal to that of positive contribution in the higher-energy region (post-threshold energy). The result was quite different from the results of Koide *et al.*[1] and Muto *et al.*[2]. When we measure an absorption spectra, it has been known that surface sensitivity is enhanced by using total PY and grazing light incidence. Thus it seems that our MCD result reflect the surface electronic structure of Ni. According to sum rule, the shape of the MCD spectrum depends upon the ratio between orbital magnetic moment and spin one. If the orbital magnetic moment is absent, the intensity of the positive region for the MCD signal is equal to the negative one at $M_{2,3}$ region[5]. Our MCD result shows nearly equal ratio between positive and negative contribution. This means that the in-plane component of the 3d orbital magnetic moment in the Ni(110) surface is almost absent whereas the perpendicular one exists.

Figure 2 shows the intensity difference of the photoelectron spectra for two opposite magnetization directions. Noticeable excitation energy dependence can be seen in pre-threshold and post-threshold region. There are peaks of $3d^9$ (first peak) and 6-eV satellite composed of ^3F (3.8 eV below the Fermi level), ^1D (5.0 eV), ^3P (5.4 eV) and ^1G (6.4 eV) in the valence band region. Figure 3 shows the photon

energy dependence of the intensity difference for $3d^9$, ^3F, ^1D, ^3P and ^1G. It can be seen that the behaviors of the intensity difference for each component are similar to that of the MCD of PY spectra shown in figure 1. In comparison with behaviors between the difference spectra at hν=70.5 eV (post-threshold) and at 66 eV (pre-threshold) in figure 2, we notice that the intensity of the 6-eV satellite is maximum around 6 eV for hν=70.5 eV, and is minimum around 5 eV for hν=66 eV. This means that the dominant components of each multiplet in the MCD measurements differ from each other in the excitation photon energy. The selection and sum rules lead those results, but details are not cleared.

Acknowledgments

We would like to thank to Dr. M. Kamada and members of UVSOR facility staff for their experimental support.

References

1) T.Koide *et al.*, Phys. Rev. B **44** (1991) 4697.
2) S.Muto *et al.*, Rev. Sci. Instrum. **63** (1992) 1470.
3) C. Guillot et al., Phys. Rev. Lett. **39** (1977) 1632.
4) T. Kinoshita *et al.*, Phys. Rev. B **47** (1993) 6787.
5) A. Yoshida and T. Jo, J. Phys. Soc. Jpn. **60** (1991) 2098.

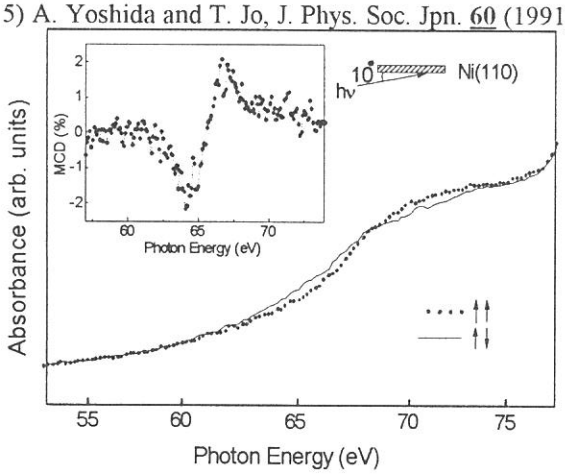

Figure1: Photoelectron yield spectra of Ni $M_{2,3}$-edges for two opposite magnetization directions. MCD spectrum derived from the yield spectra is shown inset.

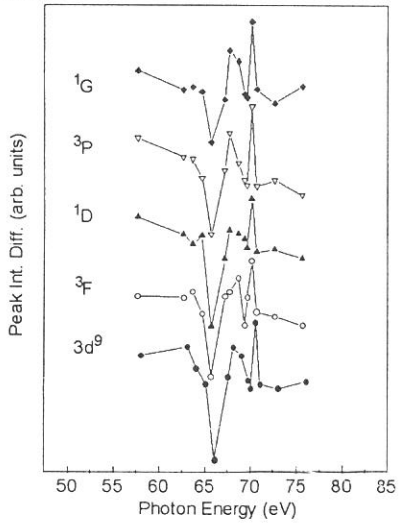

Figure 3: Intensity difference of the 3d photoelectron spectra at $3d^9$, ^3F, ^1D, ^3P and ^1G binding energies.

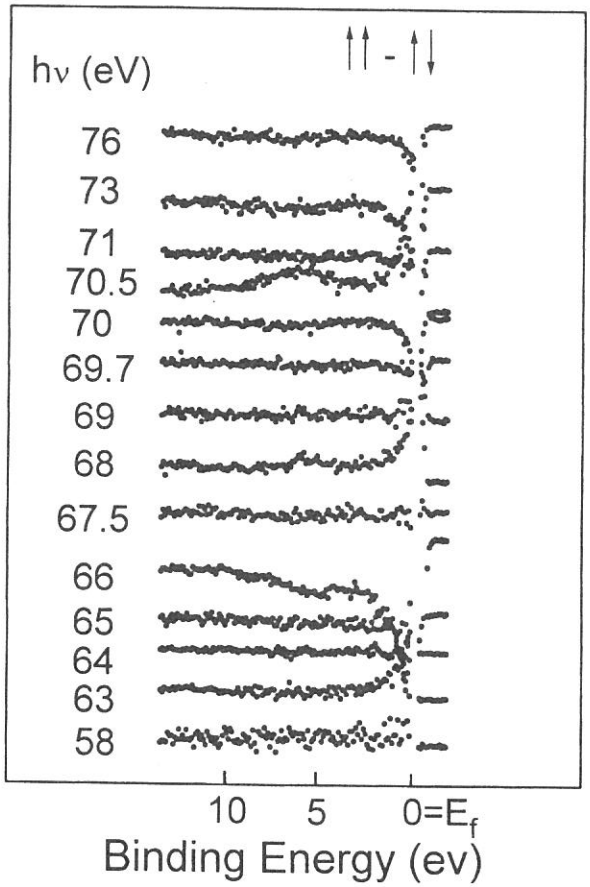

Figure 2: Intensity difference of the 3d photoelectron spectra for two opposite magnetization directions.

(BL7A)

DETECTION OF ORDER-DISORDER IN PYROXENES OF THE JADEITE-DIOPSIDE SERIES VIA X-RAY ABSORPTION SPECTROSCOPY AT THE Ca-Na AND Mg-Al K EDGES, AND ITS INTERPRETATION BY THE MULTIPLE SCATTERING CALCULATION METHOD

Annibale MOTTANA, Takatoshi MURATA*, Ziyi WU** Augusto MARCELLI** and E. PARIS†

Department of Geological Sciences, Third University of Rome, Italy
**Department of Physics, Kyoto University of Education, Kyoto 612, Japan*
***I.N.F.N., Laboratori Nazionali di Frascati, Italy*
†Department of Earth Sciences, University of Camerino, Italy

Soft X-ray absorption spectroscopy studies have been carried out on a number of natural clinopyroxenes of different origin straddling the compositional join between diopside, $CaMg[Si_2O_6]$, and jadeite, $NaAl[Si_2O_6]$, with only minor substitutions of Fe^{2+} for Mg, and of Fe^{3+} for Al. The crystal structure of the two endmembers is disordered (space group *C2/c*)as are those of intermediate members compositionally close to both ends of the series. Other intermediate members close in composition to Di:Jd = 1:1 ratio of "ideal" omphacite, $Ca_{0.5}Na_{0.5}Mg_{0.5}Al_{0.5}$ $[Si_2O_6]$, crystallize in the space group *P2/n* and show variable degrees of ordering. The phase relationships in the diopside-jadeite join are blurred by a miscibility gap occurring between $Di_{40}Jd_{60}$ and $Di_{20}Jd_{80}$.

XAFS spectra have been collected at the BL7A line. Beryl is used as monochromator crystal to scan across the K edges of Na (1070.8 eV) and Mg (1303.0 eV); quartz for the Al (1558.98 eV) edges. The entire set-up is evacuated to 1×10^{-7} Torr during operation. The finely ground mineral sample is spread as a thin film on the first photocathode of the electron multiplier. The total yield output of the photoelectrons is measured. Intensity calibration is made with reference to standard metal foil of Al, as well as to synthetic jadeite (Na, Al) and diopside (Ca, Mg), both disordered at high *P,T* conditions.

Previous Ca K edges of the same and of other equivalent samples, independently measured at ADONE (Frascati, Italy) in the PULS line[1], complete the information required to evaluate order-disorder effects which are known to occur among the pairs Ca-Na and Mg-Al, respectively in the *M2* (C.N. = 8) and *M1* (C.N. = 6) cation sites of the clinopyroxene structure.

Calculation of the spectra is made by the program package developed by C.R. Natoli and his coworkers [2,3], which is based on the multichannel multiple scattering (MMS) formalism. Starting data are the atomic positional parameters and other crystal structure data determined by G. Rossi *et al.* [4] on the same samples, or on closely analogous materials (e.g. synthetic jadeite and diopside). Experimental results of Na, Mg and Al XANES spectra and the calculated spectra are shown in Figs. 1-3.

The XANES K-edge spectra for Na and Ca, the two cations competing for the *M2* site, are distinctly different between *C*- and *P*-clinopyroxenes: the former exhibit a sharp pattern with only one peak at an energy (1077 eV) lower than the edgetop (1082 eV) in the full scattering region (FMS); the latter ones have two peaks (1077 and 1079 eV) before the edgetop (1082 eV). Further, more subtle differences are to be seen in the region of intermediate scattering (IMS) that merges continuously in that of single scattering (SS i.e. EXAFS regime). The Garnet Ridge P1-25 omphacite, the structure of which could be solved in the *C2/c* space group, has a XANES spectrum consistent with that of intermediate omphacites with *P2/n* space group.

The XANES K edge spectra for Mg and Al, the cations competing for the M1 site, are less distinctly different in the FSR than they are in the ISR: the major difference lay in the Al spectra where the intensity ratio of the second peak (1572 eV) to the edge top (1568 eV) changes, and a clear third peak (1576 eV) develops in the ordered *P*-samples that is irrelevant in the disordered *C*-ones. In turn, the two peaks occurring in the ISR of disordered *C*-samples at 1585 and 1589 eV merge into one broad bump at 1589 eV in the ordered *P*-ones.

REFERENCES

1) Davoli I., Paris E., Mottana A. and Marcelli A. (1987), Phys. Chem. Minerals, **14**, 21-25. Rev. Sci. Instrum., **63**, 1309-1312.
2) Natoli C.R. and Benfatto M. (1986) J. Phys. (Paris), **47**, C8, 11-23.
3) Natoli C.R., Benfatto M., Brouder C., Ruiz Lopez M.Z. and Foulis D.L. (1990) Phys. Rev., **B42**, 1944-1968.
Paris E., Wu Z., Mottana A. and Marcelli A. (1995) Eur. Journ. Mineral. in press
4) Rossi G., Smith D.C., Ungaretti L. and Domeneghetti M.C. (1983) Contrib. Mineral. Petrol., **83**, 247-258.

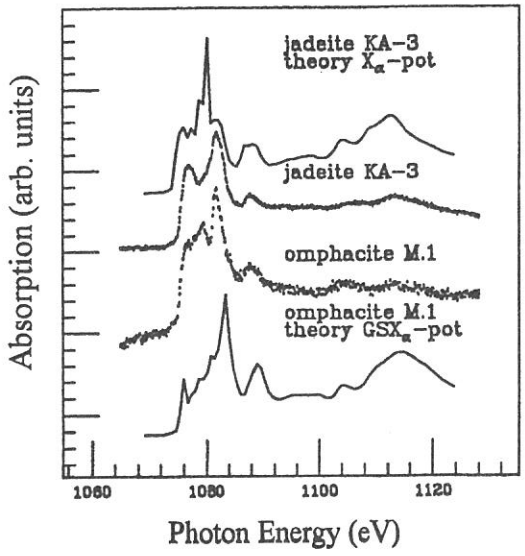

Figure 1. Experimental and calculated XANES spectra at the Na K-edge for a disordered *C2/c* jadeite from Guatemala (KA-3), and an ordered *P2/n* omphacite from Italy (M.1). The calculated spectra were computed using ground-state potentials.

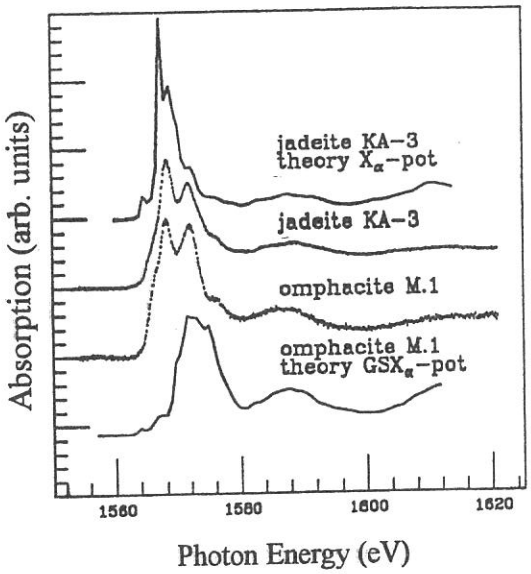

Figure 2. Experimental and calculated XANES spectra at the Al K-edge for the same minerals given in Fig. 1.

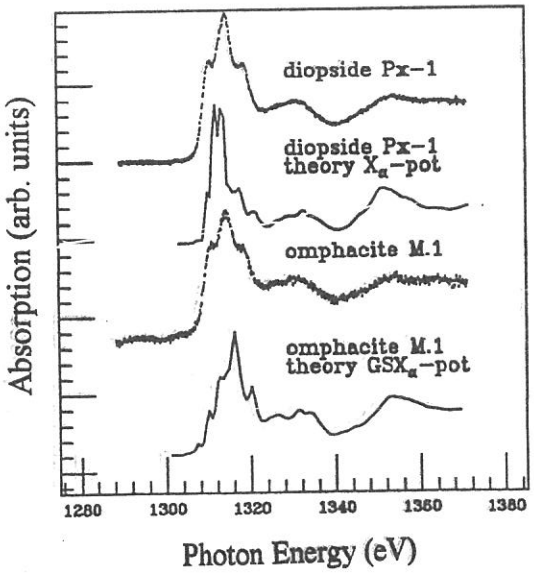

Figure 3. Experimental and calculated XANES spectra at the Mg K-edge for the ordered omphacite (M.1) and for a disordered *C2/c* diopside from Canada (Px-1).

(BL7A)

Al *K*-XANES Spectroscopic Investigation on the Local Structure around Al for $Ti_{1-x}Al_xN$

Masao TAKAHASHI, Hideyuki SUGIYAMA and Fumikazu KANAMARU

The Institute of Scientific and Industrial Research, Osaka University, 8-1 Mihogaoka, Ibaraki, Osaka 567

INTRODUCTION

$Ti_{1-x}Al_xN$ ($0<x<1$), the solid solution between TiN and AlN, is one of those having much attention for their durability against corrosion and/or erosion. TiN is used as a coating material for cutting tools, diffusion barrier layer for electronic devices but is easily oxidized above 600 °C in the air, while $Ti_{1-x}Al_xN$ is not oxidized below 900 °C in the air. As for AlN, which has been expected as substrate for electronic circuits, there is a practical difficulty with the durability against water, whereas the durability against water is improved as Ti is substituted to Al in AlN. Such solid solution, however, has not been prepared by the therm-equilibrium reaction, since the crystallographic and physicochemical properties between TiN and AlN are different each other; TiN takes NaCl-type structure in which both Ti and N atoms are surrounded by six counter atoms , respectively, while the crystal structure of AlN is würtzite-type structure in which Al is coordinated by four N atoms and vice versa. Regarding physicochemical properties, TiN has good electrical conductivity, large hardness, whereas AlN is the insulator and good thermal conductor. Taking high melting point is the only similar property.

In the decade, the thermo-nonequlibrium processing, such as several vacuum deposition techniques, has been progressed in and new compounds have been found one by one. $Ti_{1-x}Al_xN$ has also been prepared by using the reactive sputtering deposition technique. As mentioned above, $Ti_{1-x}Al_xN$ has some improvement for its properties compared with both end members, however, the coordination and the electronic states for Al atom in $Ti_{1-x}Al_xN$ has not been clear. In the present study the Al *K*-edge XAFS for $Ti_{1-x}Al_xN$ has been measured, and the local structure around Al has been discussed by comparing Al *K*-XANES spectra for the solid solution with that for AlN.

EXPERIMENTAL

Preparation. $Ti_{1-x}Al_xN$ films were deposited on polystyrene films, coated on a glass slide, using the rf-magnetron sputtering apparatus under the mixed gas atmosphere, comprising Ar and N_2. Metal composites formed by Al tips on Ti disk or Ti tips on Al disk were used as the target. Metal composition in the films was controlled by means of the ratio of area of both metals on the target surface. Deposited substrate was sunk in THF to separate product film from the glass slide and the film was washed three times by THF to remove polystyrene. The purified films were stored in *n*-hexane to prevent surface oxidation of films.

XAFS measurements. Al *K*-edge XAFS spectra were measured at the BL-7A in UVSOR of Institute for Molecular Science, Okazaki, Japan. The two-crystal monochrometer of a beryl was used and the photon energy was calibrated using Al metal powder. The sample, mixed with active carbon in *n*-hexane, were applied on the first dinode of the electron multiplier. I_0 was monitored by the gold mesh transmitting 80% of photons and the total electron yield was recorded.

RESULTS and DISCUSSION

$Ti_{1-x}Al_xN$ crystallizes in three crystal phases with Al content, x, ie., NaCl-type solid solution with $0< x \leq 0.58$, würtzite-type solid solution with $0.83 \leq x < 0$ and a intermediate phase belonging to the hexagonal system in the vicinity of x =0.7. Variation of lattice constant is found in both solid solutions. In the NaCl-type solid solution, lattice constant, *a*, decreases with x, which is caused by substituting Al for Ti, of which metallic radius is larger than that of Al. In the case of the würtzite-type solid solution, lattice constant, *a*, decreases with x, similar to the variation in the NaCl-type solid solution, while lattice constant, *c*, hardly changes through all the würtzite-type solid solution. Consequently *c*/*a*, which value in AlN is 1.60 and slightly smaller than the ideal value of *c*/*a* for the würtzite-type compound, decreases with a decrease of x, meaning that the solid solution becomes instable with decreasing Al content from a crystallographic point of view. These findings seem to indicate that Al successfully substitutes for Ti in TiN as for the NaCl-type solid solutions and so does Ti for Al in AlN as to the würtzite-type solid solution, while the coordination states around both Ti and Al have not been clear so much. Thus the XAFS spectra at Al *K*-edge for AlN and $Ti_{1-x}Al_xN$ have been measured to clarify the local structure around Al. Furthermore the XAFS spectra at Ti *K*-edge for TiN and $Ti_{1-x}Al_xN$ have been recorded at BL-12C in Photon Factory, KEK, pointing out the followings; Ti atoms occupy the octahedral site in TiN and the NaCl-type solid solution and the tetrahedral site in the würtzite-type solid solution.

Figure 1 shows Al *K*-edge XANES spectra for AlN and $Ti_{1-x}Al_xN$. As for AlN a sharp absorption peak, named peak A, is found at 1562.8 eV and another peak, labelled peak B, is located at 1568.7 eV. The spectral shape for $Ti_{1-x}Al_xN$ (x =0.8) with the würtzite-type structure closely resembles that for AlN, but the position of the peak A only a little shifts to 1563.0 eV. The position of the peak A further changes to 1563.4 eV and becomes broader for $Ti_{1-x}Al_xN$ (x =0.7), which is the intermediate phase. With an increase of Ti content the peak A moves to higher energy side but the peak B does not alter, though the amount of the shift for peak A is quite small and looks like within the error. It appears that the peak A is assigned to the level consisting of mainly Al 3p, judging from both the change in the spectral feature with the variation of x and results of the DV-Xα MO calculation for AlN. Further investigations on both the DV-Xα MO calculation and the EXAFS analysis have been in progress. The XANES spectra for the NaCl-type solid solutions are completely different from that for AlN, indicating that Al no more occupies the tetrahedral site.

Finally the followings could be deduced by both the information from the x-ray diffraction measurements and the survey of the Al *K*-XANES spectra for AlN and $Ti_{1-x}Al_xN$; (1)the local structure around Al in the würtzite-type solid solution resembles to that for AlN, ie., Al occupies the tetrahedral site. (2)As for the intermediate phase $Ti_{1-x}Al_xN$ ($x \approx 0.7$), the coordination and the electronic states for Al somewhat differ from those for AlN, though the phase takes the structure which resembles to the würtzite-type one. (3)Al occupies the octahedral site in the NaCl-type solid solution.

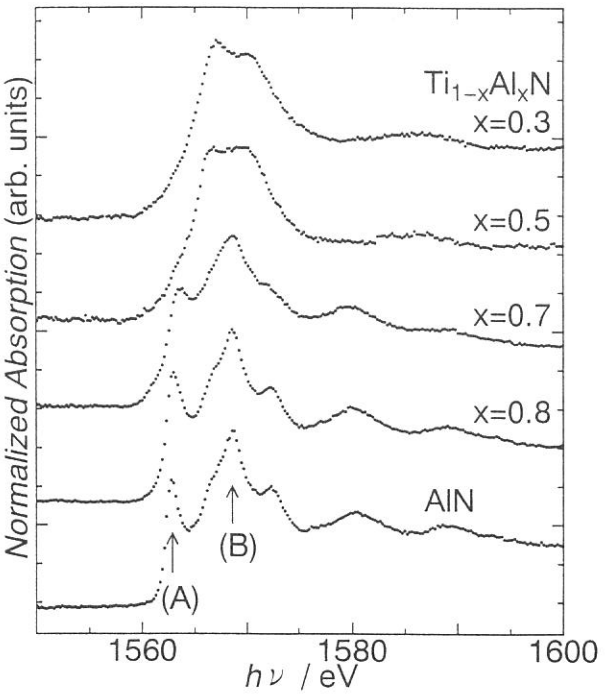

Fig. 1 Al *K*-XANES spectra for AlN and $Ti_{1-x}Al_xN$.

(BL7A)

XAFS analyses of the NiO-MgO System

Tomoko Yoshida, Tsunehiro Tanaka, Hisao Yoshida, Takuzo Funabiki, Satohiro Yoshida

Department of Molecular Engineering, Kyoto University, Kyoto 606-01

NiO/MgO is a catalyst or a catalyst precursor, used for methanation of CO and CO_2,[1,2] and N_2O decomposition, *etc.* It is known that the Ni^{2+} dispersion into MgO support is one of the important factors to control the property of NiO/MgO catalysts. The dispersion has been widely investigated by XRD,[3,4] UV/VIS spectroscopy,[2,3] IR,[5,6] XPS,[7,8] and TPR techniques.[2,9] However, most of the previous studies have been done by focusing on whether nickel ions exist preferentially on the surface or in inside. An atomic level investigation of the Ni^{2+} dispersion in MgO matrix is still required, since the property of a Ni ion in the NiO-MgO system should be different with the fractions of its neighboring Ni and Mg atoms. To examine this, we investigated the surroundings around Mg and Ni atoms in NiO-MgO system by Mg and Ni K-edge X-ray absorption fine structure (XAFS).

NiO-MgO samples ($Ni_xMg_{1-x}O$: x = moles of Ni / (moles of Ni + moles of Mg)) were prepared by impregnation of MgO powder with an aqueous solution of $Ni(NO_3)_2$, and drying at 373 K over night, followed by calcination in a dry air stream for 4 h at 773 K.

Mg K-edge X-ray absorption experiments were carried out on the beam line 7A at UVSOR, Institute for Molecular Science, Okazaki, Japan with a ring energy 750 MeV and stored current 80-200 mA. X-ray absorption spectra were recorded at room temperature, using a beryl two-crystal monochromator. The samples were mixed with active carbon in dry hexane and were put on the first photocathode made of CuBe of the electron multiplier. Data were collected in a total electron yield mode.

Fig.1 shows the comparison of the k-weighted Mg K-edge EXAFS of MgO (a) and the k-weighted Ni K-edge EXAFS of the samples and NiO (b-g). Ni K-edge EXAFS spectra were measured on the BL6B at Photon Factory in National Laboratory for High Energy Physics, Tsukuba. Ni K-edge EXAFS spectrum of the sample of x = 0.02 resembles Mg K-edge EXAFS of MgO, revealing that the surroundings around Ni atoms in this sample is the same as that around Mg atoms in MgO. This result indicates that Ni ions dissolve into MgO matrix substitutionally in the sample of x = 0.02. The occurrence of the Ni-Mg substitution is expected for the samples of $0.02 < x \leq 0.36$ since the features of EXAFS of these samples still resemble the EXAFS of MgO. Although the EXAFS of the sample of x = 0.86 is similar to that of NiO, the EXAFS of the sample of x = 0.48 is still different from that of NiO. For all the samples, the curve-fitting analyses of k^3-weighted Ni K-edge EXAFS were performed, and the following results were revealed.

1) The Ni-Mg substitution occurs regardless of the compositions of the samples, and the samples form NiO-MgO solid solutions. 2) The local structure of the solid solution is

dominated by the stable structure of MgO and NiO in the range of $x < 0.2$ and $x > 0.6$, respectively. In the range of $0.2 < x < 0.6$, the solid solution has an intermediate structure.

Therefore, the change of the EXAFS oscillation shown in Fig. 1 would reflect the changes of the local structure and the composition of the second-neighboring Ni and Mg ions around a Ni atom.

In Fig. 2, Mg K-edge XANES of MgO and samples are shown. For all the XANES spectra, the energy positions of these absorption are the same, indicating that the rock salt structure of MgO is retained up to $x = 0.63$. This result also supports the occurrence of the Ni-Mg substitution in these samples. However, the feature of Mg K-edge XANES of the samples are not strictly the same as that of MgO, as noted by the decrease in the peak intensity at around 1310 eV with the increase in the nickel concentration, x. As for the prominent peak at around 1310 eV, Tanaka *et al.*[10] succeeded in the simulation of this peak in MgO by the molecular orbital calculations using sets of 1s-3p, 1s-4p and 1s-3d transition. On the basis of their work and the results of our EXAFS analyses as mentioned above, we conclude that the feature of XANES spectra would reflect the change of electronic states of central Mg ions which results from the change of the composition of the second neighboring Ni and Mg ions.

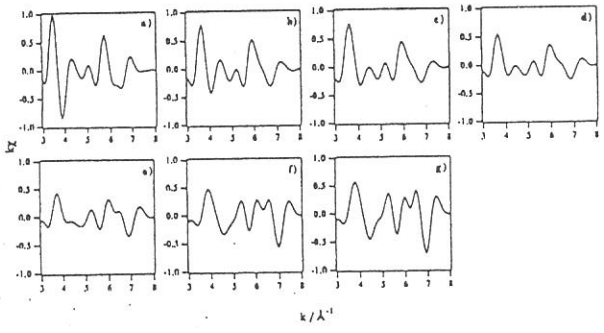

Figure 1 *k*-weighted Mg K-edge EXAFS of (a) MgO and *k*-weighted Ni K-edge EXAFS of $Ni_xMg_{1-x}O$. (b) $x = 0.02$, (c) $x = 0.18$, (d) $x = 0.36$, (e) $x = 0.48$, (f) $x = 0.86$, and (g) NiO.

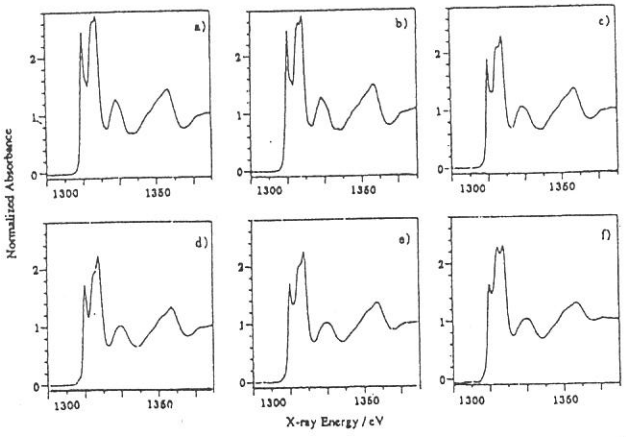

Figure 2 Mg K-edge normalized XANES of MgO and $Ni_xMg_{1-x}O$. (a) MgO, (b) $x = 0.02$, (c) $x = 0.18$, (d) $x = 0.36$, (e) $x = 0.48$, and (f) $x = 0.63$.

1) C. Mirodatos, H. Praliaud, and M. Primet, *J. Catal.*, **107**, 275 (1987).
2) N. Takezawa, H. Terumura, M. Shimokawabe, and H. Kobayashi, *Appl. Catal.*, **23**, 291 (1986).
3) A. P. Hagan, M. G. Lofthouse, F. S. Stone, and M. A.Trevethan,*Preparation of Catalysts II*. B. Delmon, P. Grange, P. A. Jacobs and G. Poncelet, Eds., (Elsevier, Amsterdam, 1979).
4) T. Borowiecki, *Appl. Catal*, **10**, 273 (1984).
5) A. Chiorino, E. Garrone, G. Chiotti, E. Guglielminotti, and A. Zecchina, Proceedings of 7th International Congress on Catalysus part A (Elsevier, Amsterdam, 1980), pp. 136.
6) A. Zecchina, G. Spoto, S. Coluccia, and E. Guglielminotti, *J. Chem. Soc., Faraday Trans. 1*, 1891 (1984).
7) G. C. Bond, and S. P. Sarsam, *Appl. Catal.*, **38**, 365 (1988).
8) F. H. Arena B. A.Cocke, D. L. Parmaliana, A. Giordano, N., *J. Catal.*, 58 (1991).
9) A. Parmaliana, F. Arena, F. Frusteri, and N. Giordano, *J. Chem. Soc., Faraday Trans.*, **86**, 2663 (1990).
10) I. Tanaka, J. Kawai, and H. Adachi, *Solid State Comm.*, **93**, 533 (1995).

(BL-7A)

Ga L-edge XANES Study on Gallium Oxide Catalysts.

Koji NISHI, Mikio TAKAMATSU, Hisao YOSHIDA and Tadashi HATTORI

Department of Applied Chemistry, School of Engineering, Nagoya University, Nagoya 464-01

Introduction

It is known that Ga_2O_3 species promote the dehydrogenation steps during the aromatization of light alkanes on HZSM-5 zeolite catalysts [1]. We found that the specific activity of propane dehydrogenation increases with increasing Ga_2O_3 crystallite size [2]. However, the relationship between the local structure and the catalytic activity of these Ga_2O_3 species has not been clarified. In recent years X-ray absorption spectroscopy has become a powerful tool for the study of the local structures. But Ga L-edge XANES has merely been used for the elucidation of local structure of Ga species. In the present study, we carried out a structural analysis of Ga_2O_3 samples by Ga L-edge XANES spectroscopy.

Experimental

Ga_2O_3 samples were prepared by calcination of gallium hydroxide ($Ga_2O_3 \cdot nH_2O$) and gallium nitrate ($Ga(NO_3)_3 \cdot nH_2O$) at various temperatures (698-1073 K) for several hours (referred to as H(calcin. temp.)-(hours) and N(calcin. temp.)-(hours), respectively). The reference sample of α-Ga_2O_3 was obtained from calcination of $Ga_2O_3 \cdot nH_2O$ at 802 K for 6 h, and a commercially supplied gallium oxide was used as the reference of β-Ga_2O_3. $ZnGa_2O_4$ was supplied from Nippon Tokushu Togyo Co.. The crystal phases of these samples were confirmed by X-ray diffraction (XRD) techniques.

Ga L-edge X-ray absorption spectra measurements were performed at BL-7A of UVSOR facility, Institute for Molecular Science, using a beryl double-crystal monochromator. The sample was mixed with active carbon in dry hexane and was put on the first photocathode made of Cu-Be of the electron multiplier. The absorption spectra were recorded by monitoring total photoelectron yield. From the each absorption spectrum, the background was subtracted. Each XANES spectrum was normalized by the absorbance at 1126 eV.

Results and Discussion

Fig. 1 shows Ga L_3 and L_2-edge XANES spectra of α-, β-Ga_2O_3 and $ZnGa_2O_4$. The spectra of α- and β-Ga_2O_3 are clearly different from each other, especially around at Ga L_3-edge. In the spectrum of α-Ga_2O_3, the relative intensity of the white line is larger than the near edge region, showing that the spectrum of α-Ga_2O_3 is distinguishable from that of β-Ga_2O_3. There are two kinds of coordination for Ga^{3+} ions in β-Ga_2O_3 spinel structure, namely tetrahedral and octahedral, while there are only an octahedral site in α-Ga_2O_3 corundum structure [3]. $ZnGa_2O_4$ has spinel type structure in which Ga^{3+} ion exists in octahedral site. Although the coordination number of Ga^{3+} ion both in α-Ga_2O_3 and $ZnGa_2O_4$ is identical, the feature of XANES spectra are different each other. From these results, it could be concluded that these XANES spectra reflect not only the coordination state but also the crystal structure.

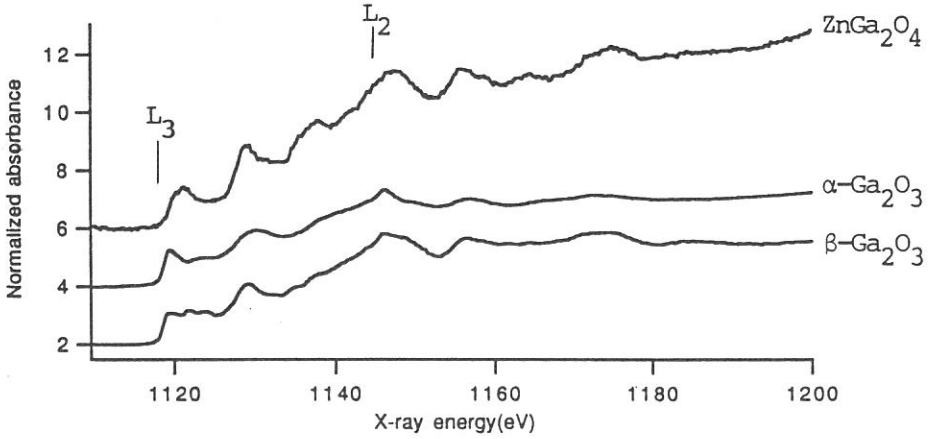

Fig. 1 Ga L_3, L_2-edge XANES of α -, β -Ga_2O_3 and $ZnGa_2O_4$.

Fig. 2 shows Ga L_3-edge XANES spectra of H- and N-samples. The feature of XANES spectra of H-samples varied from that of α -Ga_2O_3 to that of β -Ga_2O_3 with an increase in the calcination temperature. The samples calcined below 923 K exhibited the same XANES spectra as that of α -Ga_2O_3, although these H-samples are XRD amorphous. We found that Ga ion is in α -phase-like octahedral site in the samples obtained from $Ga_2O_3 \cdot nH_2O$, even when it was calcined at such high temperatures. The XANES spectrum of N-sample calcined at 823 K is close to that of α -Ga_2O_3, although the white line shifts further to higher energy side. X-ray diffraction pattern of this sample showed that metastable δ - and ε -Ga_2O_3 phase coexist. These results suggest that the local structure of surface layer differs from the bulk structure in this sample, since XANES spectra measured in this method reflect mainly the surface layer [4]. The samples calcined above 923 K exhibit the same XANES spectra as that of β -Ga_2O_3 in agreement with known XRD data.

The present study has strongly indicated that Ga L-edge XANES spectra provide the useful information about the local structure and about the property of crystal phase of Ga_2O_3 samples even if they are XRD amorphous.

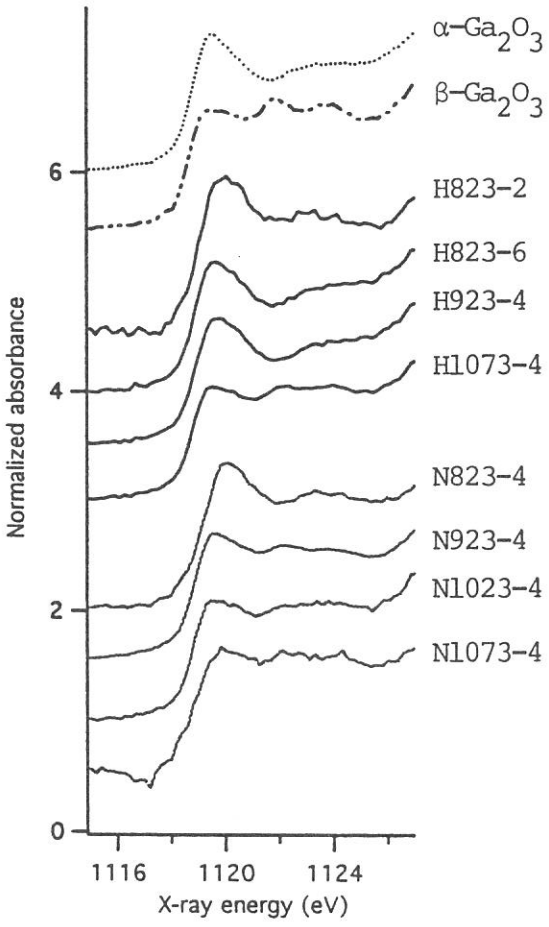

Fig. 2 Ga L_3-edge XANES of Ga_2O_3 prepared from $Ga_2O_3 \cdot nH_2O$ and $Ga(NO_3)_3 \cdot nH_2O$.

[1] M. Guisnet, N.S. Gnep and F. Alario, *Appl. Catal. A*, **89** (1992) 1.

[2] M. Takamatsu, K. Nishi, S. Komai, H. Yoshida, A. Satsuma and T. Hattori, unpublished results.

[3] S. Geller, *J. Chem. Phys.*, **33** (1960) 676.

[4] T. Yoshida, T. Tanaka, H. Yoshida, T. Funabiki, S. Yoshida and T. Murata, *J. Phys. Chem.*, **99** (1995) 10890.

(BL-7A)

Si K-absorption spectra of porous silicon

Tokuo MATSUKAWA, Eishin ICHIMIYA, Satosi SORIMACHI, Makoto HONDA,
Noboru FUKUOKA and Kouzou ATOBE

Department of Physics, Naruto University of Education, Naruto, 772-01

The porous silicon is a new kind of material which is recently discovered to emmit visible light, and has been attracting much attention from the points of view not only of the possibility of the quantum confinement effect, but also of the new feasibility of the new opto-electronics devices. Alternative explanations on the visible luminescence had been proposed too, and the origin is controversial.

It is the purpose of this study to present the Si K-absorption spectra which had been measured by total photo-electron yield method at the soft x-ray beam line BL-7A in the UVSOR. We had also measured the Si-L spectra, which was reported in this issue on the report of the BL-2B1. The porous silicon was made by a standard method of anodizing the bulk silicon crystal in HF solution. The prepared samples had exhibited the photo-luminescence spectra centered at 1.8eV. The measurements had been carried out not only on the porous silicon , but also on crystalline silicon and silicon oxide (α SiO_2).

Figure 1 shows the Si-K absorption spectra which presents a comparison on the three silicon materials . The spectra of crystalline silicon and α SiO_2 are the same as the spectra reported so far. The absorptopn spectra of the porous sillicon is totally differrent from the spectrum of the crystalline sillicon and from the spectrum of the α SiO_2. The main feature of the spectrum of the porous sillicon is that three absorption structures were observed at the edge. The third structure, the absorption peak, might correspond to the prominent absorption peak at the absorptin edge in α SiO_2. The energy position of the peak agrees quite well to each other. Therefore the origin of the absorption peak might be due to Si-O chemical bond. The threshold structure of the porous sillicon could not be attributed to the bulk, crystalline silicon structure, since the weak doublet humps at the absorption edge maximum in the crystalline silicon spectrum could not observed. The second absorption peak in the porous silicon is the characteristic feature of the spectrum. There is no such corresponding structure in the crystalline silicon, nor in the α SiO_2 .

Figure 2 shows a comparison of the Si K-absorption spectrum and Si L-absorption spectrum in the porous silcon. The photon energy of the each spectrum is shifted so that the leading edge of the respective absorption threshold should be aligned in each other. In the figure the energy seperation of the characteristic structures in the both spectra correspond to each other, except that slight deviation of the energy position. The deviation may be adjusted by the estimation

of energy position of the leading edge. The fitting should be better if the absorption threshold energy should be determined not by the leading edge, but by the inflection point of the curve. The structures are attributed to the maximum in the density of states. In the higher energy, the broad maximum in the L -spectrum is not observed in the K-spectra. The maximum may be due to the Si 3d states.

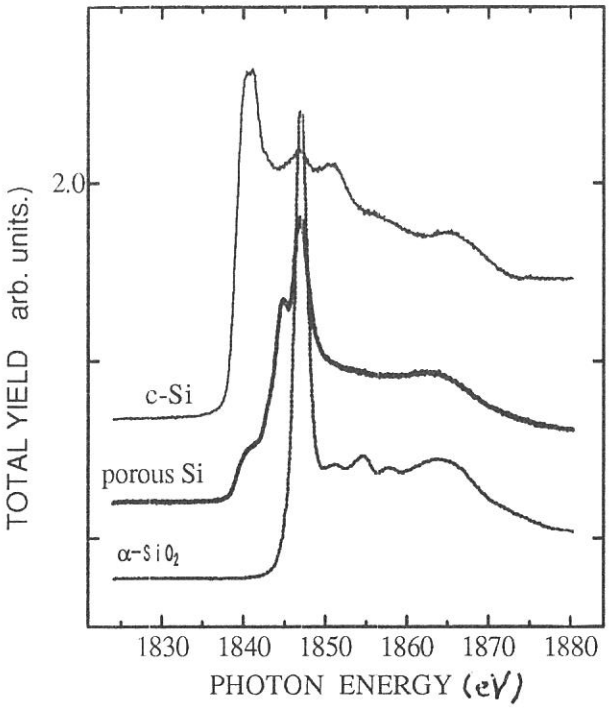

Fig.1
Si-K absorption spectra of crystalline silicon, porous silicon and α -SiO_2.

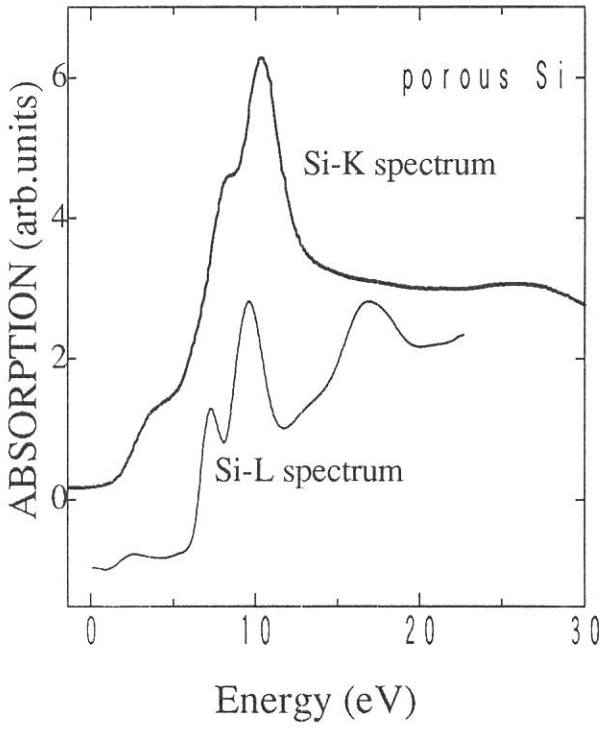

Fig.2
Si-K absorption spectrum and
Si-L absorption spectrum of porous Si.

(BL-7A)

Local Structure in the Surface layer of Mo-Mg Binary Oxide in Oxidized/Reduced States Studied by Mo L_3-edge XANES

Hirofumi ARITANI, Tsunehiro TANAKA, Takuzo FUNABIKI,
Satohiro YOSHIDA, Masataka KUDO* and Sadao HASEGAWA**

Division of Molecular Engineering, Kyoto University, Kyoto 606-01
** Criminal Investigation Laboratory, Metropolitan Police Department, Chiyoda, Tokyo 100*
*** Department of Chemistry, Tokyo Gakugei University, Koganei, Tokyo 184*

Introduction

As described in the previous report,[1-3] a highly molybdenum-containing MoO_3-MgO (Mo/(Mo+Mg)=0.6-0.7) pretreated with hydrogen at 773K exhibits a high activity for propene metathesis. This is a significant finding because MoO_3-MgO was thought to be inactive for the olefin metathesis and the nature of the active species must be reexamined since it is hardly acceptable that the binary oxide with a high Mo ratio has MoO_4 tetrahedra.

We investigated the Mo *K*-edge XANES/EXAFS of MoO_3-MgO in oxidized and reduced state to clarify the structure of Mo-Mg binary oxides and structural change by reduction with hydrogen.[2] We concluded that highly molybdenum-containing MoO_3-MgO samples (Mo ratios are 0.6-0.7) are easily reduced to form highly dispersed MoO_2 phase by H_2 treatment at 773K, and it is suggested that this bulk species relates to active sites for metathesis. In the present work, we studied the Mo L_3-edge XANES of Mo-Mg binary oxide in oxidized and reduced state to clarify the local structure of molybdenum ions in the surface layer and obtain an information of the active species for metathesis.

Experimental

Mo-Mg binary oxide (MoO_3-MgO) samples were prepared as described previously.[1] The measurements of Mo L_3-edge XANES spectra were carried out on a facility of BL-7A station of soft X-ray beamline. Each sample was prepared for measurement by grinding with hexane, and then spread on a beryllium-copper dinode which was attached to a first position of electron multiplier into the beamline chamber. After the chamber had been evacuated ($< 1.0 \times 10^{-7}$ Torr), the spectrum was recorded in a total electron yield mode at room temperature, using a Ge(111) double crystal monochromator. At around Mo L_3-edge (2.52 keV), energy solution of approximately 0.5 eV can be obtained. The spectrum in a total electron yield mode is mainly due to the detection of Mo LMM Auger electron, whose escape depth is about 30 Å. Thus, the spectrum is believed to reflect the structure of the samples in the surface layer.

Results and Discussion

The origin of Mo L_3-edge XANES is the electron transition from a core level, $2p_{3/2}$, to a vacant 4*d* state, and Teo and Lee showed the contribution to L_3-edge absorption spectra from the allowed *p-d* transition is about fifty times that of *p-s* transition.[4] Fig. 1 shows the Mo L_3-edge XANES spectra of reference compounds having Mo^{6+} ion, except for MoO_2 with Mo^{4+} ion. In case of the samples having Mo^{6+} ion, the energy gap between two white lines of XANES spectra is different between MoO_6 octahedra and MoO_4 tetrahedra. The energy gap is calculated by using the second derivative curve of XANES spectrum. The result is shown in Table 1. For the samples of Na_2MoO_4 and $MgMoO_4$, having tetrahedral molybdena, the gap is 2.1 eV. For the samples having octahedral molybdena, the gap is more than 3 eV, and the energy of the gap increase with increasing the distortion of MoO_6 octahedron. These results are consistent with the initial observations reported by Bare *et al.*[5] and Hedman *et al.*[6] On the other hand, the relative peak intensity of two white lines are different between octahedral and tetrahedral molybdena, as discussed in the previous report.[1]

Fig. 2 shows the XANES spectra of MoO_3-MgO samples. For the samples of low Mo ratio less than 0.5, each spectrum resembles each other and almost similar to that of $MgMoO_4$,

indicating that Mo ion is stabilized as a MoO_4 tetrahedron. For more than 0.6 of Mo ratio, the relative intensity of the white line at a low energy side becomes larger with an increase in Mo ratio. This is explained by coexistence of octahedral and tetrahedral molybdena. However, main component is MoO_4 tetrahedra even at 0.7 of Mo ratio, from the result of the energy gap (Table 2).

For the reduced samples, XANES spectra shown in Fig. 3 are little changed in low Mo ratio less than 0.5. However, for the samples of 0.7-0.8 of Mo ratio, other component is overlapped with the two white lines. It is suggested that reduced Mo ion such as Mo^{5+} and/or Mo^{4+} is brought about in the surface layer, because that spectrum is not observed in the sample including Mo^{6+} ion but is nearly observed in MoO_2, for example. In this manner, it is explained that Mo ion is easily reduced by H_2 treatment for higher Mo ratio of MoO_3-MgO.

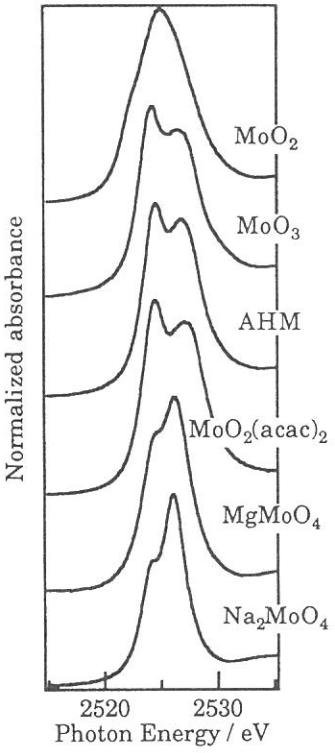

Fig. 1 Mo L_3-edge XANES spectra of reference compounds.

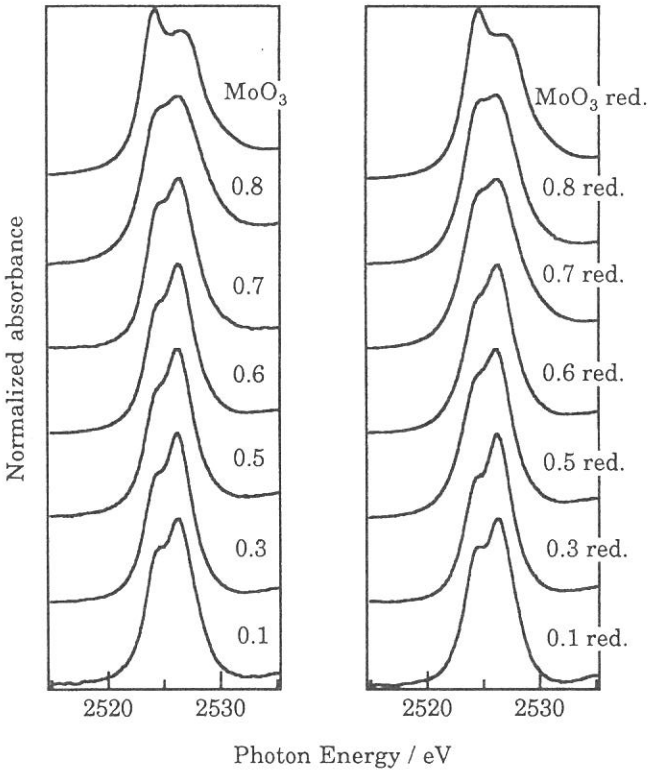

Fig. 2 Mo L_3-edge XANES spectra of MoO_3-MgO in oxidized (left) and reduced (right) state.

Table 1 The energy gap between two white lines of Mo L_3-edge XANES over reference samples.

Sample	Local structure	splitting / eV
Na_2MoO_4	T_d	2.12
$MgMoO_4$	T_d	2.11
AHM	O_h (distorted)	3.32
MoO_3	O_h (distorted)	3.40
$MoO_2(acac)_2$	O_h (distorted)	3.49

Table 2 The energy gap between two white lines over MoO_3-MgO in oxidized (left) and reduced (right) state.

Mo ratio	splitting / eV	Mo ratio	splitting / eV
0.8	2.5	0.8 red.	unclear
0.7	2.1	0.7 red.	unclear
0.6	2.1	0.6 red.	2.2
0.5	2.2	0.5 red.	2.1
0.3	2.2	0.3 red.	2.0
0.1	2.1	0.1 red.	2.1

References

1) H. Aritani, T. Tanaka, T. Funabiki, S. Yoshida, S. Hasegawa, *UVSOR Activity Report*, (1995) 164.
2) H. Aritani, T. Tanaka, T. Funabiki, S. Yoshida, M. Kudo, S. Hasegawa, *J. Phys, Chem.*, in press.
3) S. Hasegawa, T. Tanaka, M. Kudo, H. Mamada, H. Hattori, S. Yoshida, *Catal. Lett.*, **12** (1992) 255.
4) B. K. Teo, P. A. Lee, *J. Am. Chem. Soc.*, **101** (1979) 2815.
5) S. R. Bare, G. E. Mitchell, J. J. Maj, G. E. Vieland, J. L. Gland, *J. Phys. Chem.*, **97** (1993) 6048.
6) B. Hedman, J. E. Penner-Hahn, K. O. Hodgson, In *EXAFS and Near Edge Structure III*, berlin (1984).

(BL-7A)

Mo L_3-edge XANES Study of MoO_3-ZnO

Yasuyuki Nishino and Sadao Hasegawa

Department of Chemistry, Tokyo Gakugei University, Koganei, Tokyo 184

1. Introduction

Supported and unsupported molybdenum oxides catalysts are utilized cracking, oxidation, hydrogenation, isomerization, and metathesis of olefin. We had been reported the formation of active sites for metathesis or hydrogenation of propene on oxidized or reduced MoO_3-MgO catalysts.[1] In the case of higher-contents of MoO_3 catalyst the metathesis activity for propene were recognized. We also had been reported about the local structure around Mo and Mg ions in MoO_3-MgO binary oxides by L_3-edge and Mg K-edge XANES spectroscopy.[2]

In this report, we describe the local structure around Mo ions in MoO_3-ZnO oxides by L_3-edge XANES spectroscopy.

2. Experimental

Oxidized MoO_3 -ZnO catalysts (atomic ratio of Mo/Zn from 0.1 to 0.9) were prepared by the impregnation method. Calculated amounts of $(NH_4)_6Mo_7O_{24}\cdot 4H_2O$ were dissolved in a volume of H_2O corresponding to ZnO to be impregnated at the temperature of 363K. The impregnate was air-dried for 24h at 393K. Reduced MoO_3-ZnO catalysts were prepared by the reduction of oxidized catalysts at 773K in hydrogen. The Mo L-edge adsorption spectra of the catalysts were measured at BL-7A soft X-ray beam line with UVSOR facilities, when used a Ge(1,1,1) two-crystal monochrometer.

3. Results and Discussion

Mo L_3-edge XANES in MoO_3-ZnO is shown in Fig.1. The white lines assigned to the dipole allowed $2p \rightarrow 4d$ transition are observed at 2532 eV and 2534 eV. The splitting of white lines reflects resolution of the ligand field splitting of the final state d-orbital. For the octahedrally coordinated MoO_3, the white lines are attributed to the electron transition of $2p_{3/2} \rightarrow t_{2g}$-$e_g$ of 4d atomic orbital. The first peak (to t_{2g}) is more intense than the second peak (to e_g). In the case of tetrahedrally coordinated $MgMoO_4$, the white lines are due to the transition of $2p_{3/2} \rightarrow t_2$-e of 4d state.[2] Contrary to case of MoO_3, the first peak (to e) is smaller than the second peak (t_2). For low atomic ratio below 0.5, a feature of white lines of MoO_3-ZnO was similar to $MgMoO_4$, indicating that tetrahedral coordinated Mo is stabilized at lower content. At the higher atomic ratio above 0.6, the relative intensity of a white line at lower energy side became larger with an increase in Mo/Zn ratio. This suggests that the octahedrally coordinated Mo is formed at higher atomic ratio and octahedral and tetrahedral co-exist in MoO_3-ZnO.

Fig.2 shows Mo L_3-edge XANES in reduced MoO_3-ZnO. The second peak disappeared at lower atomic ratio when MoO_3-ZnO was reduced. The activities for the metathesis and isomerization of 1-butene are observed on the reduced catalysts of MoO_3-ZnO as shown in Table1. For the isomerization, MoO_3-ZnO acts acidic catalysts in lower atomic ratio. The activities for metathesis are higher at lower atomic ratio which the second peak of white lines disappeared by the reduction. These results are suggested that the molybdena is present as isolated species because the tetrahedrally coordinated Mo is easily reduced by hydrogen.

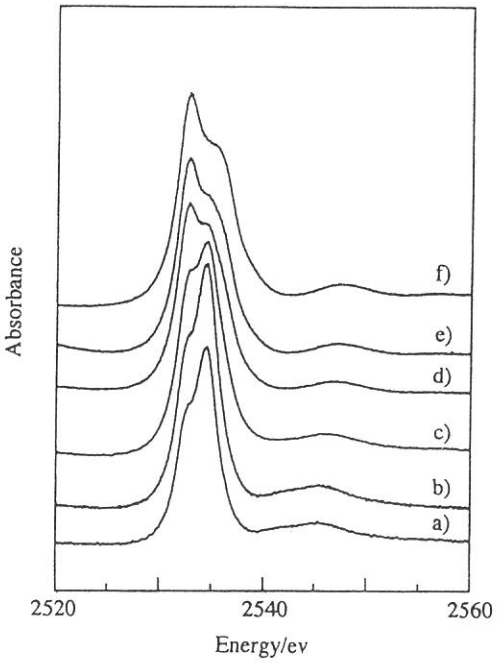

Fig.1 Mo L_3-edge XANES of MoO_3-ZnO
;atomic ratio(Mo/Zn) are a)0.1 b)0.4 c)0.5 d)0.6 e)0.8 respectivly and f)MoO_3.

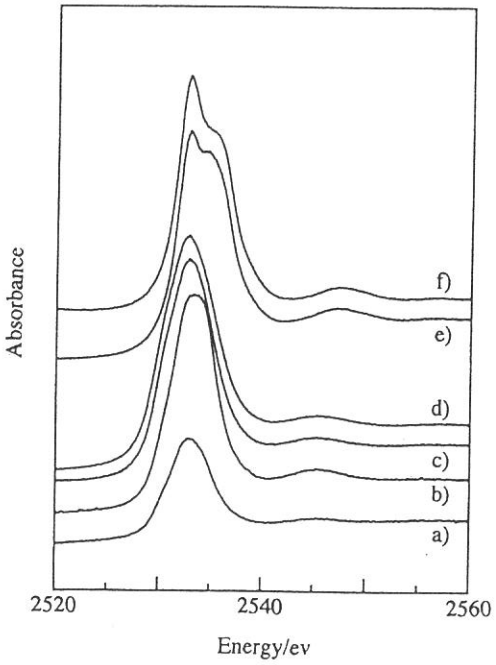

Fig.2 Mo L_3-edge XANES of reduced MoO_3-ZnO
;atomic ratio(Mo/Zn) are a)0.1 b)0.4 c)0.5 d)0.6 e)0.8 respectivly and f)MoO_3.

Table 1 Isomerization or metathesis of 1-butene over reduced MoO_3-ZnO catalysts[1)]

Atomic ratio	conversion/%	selectivity/%						cis/trans ratio
		1-butene	cis-2-butene	trans-2-butene	C3	C6	C5atc	
0.1	91.3	8.6	31.9	59.3	0.1	-	0.1	0.54
0.4	90.7	9.2	30.6	58.9	1.1	0.1	0.1	0.52
0.5	91.4	9.5	30.5	57.6	1.4	0.5	0.4	0.55
0.6	80.6	17.9	29.6	50.1	1.5	0.7	0.2	0.59
0.8	39.4	60.5	22.7	16.6	0.1	-	0.1	1.37

1) Catalysts were reduced at 673K in H_2.
reaction temperature ; 373K
reaction time ; 60min

1)S.Hasegawa, T.Tanaka, M.Kudo, H.Mamada, H.Hattori, S.Yoshida, *Catal. Lett.*, 12(1992)255.
2)H.Aritani, T.Tanaka, T.Funabiki, S.Yoshida and S.Hasegawa, UVSOR ACTIVITY REPORT, 1994-164

Photoluminescence Study on Point Defects in SIMOX Buried SiO_2 Film

Kwang Soo SEOL, Akihito IEKI, Yoshimichi OHKI

Department of Electrical Engineering, Waseda University
3-4-1 Ohkubo, Shinjuku-ku, Tokyo 169, Japan

With the development of high speed and high power devices, the parasitic capacitance and the lateral insulation have become serious problems. To solve these problems, various fabrication methods for an silicon-on-insulator structure were developed. Among these developed methods, formation of an oxide layer in a monocrystalline silicon by implantation of high-energy oxygen ions is thought to be the most competitive for mass production. This is usually referred to as separation by implanted oxygen (SIMOX). However, there have recently been a number of deviating observations on devices with SIMOX buried oxides, which are induced by unusual behavior of the buried oxide such as enhanced electrical conductivity[1], charge buildup, and significantly enhanced sensitivity[2] to defect generation as compared to the conventional thermal oxide. It is suggested that there is a distinct difference between the two oxides in such points as structure, uniformity and the degree of nonstoichiometry. From such a viewpoint, many researches have been done recently on the properties of SIMOX[1,2]. Here, we report PL and its time resolved study upon SIMOX buried oxide film by synchrotron radiation and excimer laser excitation, and discuss the nature of the defects which are responsible for PL.

The SIMOX buried oxides (hereafter abbreviated as SIMOX) were produced by implanting O^+ ions up to a dose of 1.7×10^{18} ions/cm^2 with an energy of 180 keV into a p-type (100) Si substrates maintained at 550 ℃. The substrates were then annealed at 1300 ℃ in Ar+O_2 for 6 h. For PL experiment, the Si overlayer was etched off in a KOH solution [KOH:H_2O = 3:7 (by weight)] stabilized at 23℃ to expose the buried oxide. The PL spectra were measured using a monochromator equipped with a multichannel detector and the ms-order decay profiles were measured with a photomultiplier under excitation by a KrF excimer laser (wavelength: 248 nm (5.0 eV), pulse width: ~20 ns). The PLE spectra and ns-order decay profiles were measured using synchrotron radiation (SR) at BL7B line of UVSOR operated at an electron energy of 750 MeV. While the PLE spectra were measured under multi-bunch operation, the decay profiles were measured by a time-correlated single photon counting technique under single-bunch operation The emitted photons collected with a lens at 30° or 90° to the incident beam and dispersed by a band-pass filter were detected by a photomultiplier for PLE or by a micro-channel-plate photomultiplier for the decay.

Shown in Fig.1 is the PL spectrum of SIMOX obtained under excitation by the KrF excimer laser at room temperature. Two PL bands are observed at 4.3 eV and 2.7 eV. With a decrease in temperature, the intensity of the 4.3 eV PL band increases, while that of the 2.7 eV band decreases. Therefore, by lowering the measuring temperature down to 90 K, the PLE spectrum was able to be obtained only for the 4.3 eV PL. Figure 2 shows the result. Here, the obtained luminescence intensity was divided by the intensity of the excitation photons. The measurement was done at 90 K. A clear PLE band is seen at 7.4 eV. On the steep increase beginning around 5.4 eV which is due to scattered excitation photons through the band-pass filter with a transmittance window at 4.3 eV, a shoulder is seen around 5.0 eV. As will be confirmed below, this shoulder is thought to be a PLE peak of the 4.3 eV band. Figure 3 shows the decay of the 4.3 eV PL excited at 7.4 eV (a) and at 5.0 eV (b) for SIMOX, measured at 32 K. The data were fitted by the least squares method with the time derivative of a stretched exponential function:

$$I(t) \propto (\beta / \tau)(\tau / t)^{1-\beta} \exp[-(t / \tau)^{\beta}]. \quad (1)$$

Here, τ and β are the effective decay constant and a parameter which takes a value of $0 < \beta < 1$, respectively. This is consistent with many reports which revealed that the luminescence decay in many amorphous materials measured below 50 K is described by the above equation[4]. On the other hand, The 2.7 eV PL decays exponentially with the decay constant of 9.7 ms, which was excited by the KrF excimer laser. Among many PL bands observed in high-purity silica, two PL bands at 4.3 eV and 2.7 eV are the best-characterized bands. When they appear simultaneously like a geminate pair in one sample, and if the sample has two absorption bands around 5.0 eV and 7.6 eV, the sample can be considered to be oxygen-deficient[7]. The 4.3 eV PL band in the oxygen-deficient silica glass has a decay constant of 4.2 ns for the 5.0 eV excitation and that of 2.1 ns for the 7.6 eV excitation[7], while the 2.7 eV PL band has a decay constant around 10 ms[8]. These are in good agreement with the results shown in Figs.1-3, except for some subtle differences like the existence of PLE band at 7.4 eV rather than at 7.6 eV. A slight shift in the peak energy of PLE band often occurs, since electronic excitation is influenced by the surrounding atmosphere of the point defect. We found that ion-implanted thermal SiO_2 films also have the corresponding PLE band at 7.4 eV[6]. Therefore, all the

obtained results indicate that the present SIMOX oxide is oxygen-deficient in nature. This is to say, the PL pair at 4.3 eV and 2.7 eV and the absorption (PLE) pair at 5.0 eV and 7.4 eV are due to the same point defects as in the case of bulk silica glass, and not due to the quantum effect of small silicon islands, which may exist in SIMOX oxide.

References

[1] G.A. Brown and A.G. Revesz, IEEE. Trans. Elec. Dev. NS-40, 1700 (1993)
[2] A. Stesmans, R. Devine, A.G. Revesz, and H. Hughes, IEEE. Trans. Nucl. Sci. NS-37, 2008 (1990)
[3] For example, D.L. Griscom, Rev. Solid State Sci. 4, 565 (1990)
[4] K. Murayama and T. Ninomiya, Jpn. J. Appl. Phys. 21, L512 (1982)
[5] K. Ishii, Y. Ohki, and H. Nishikawa, J. Appl. Phys. 76, 5418 (1994)
[6] H. Nishikawa, E. Watanabe, D. Ito, M. Takiyama, A. Ieki, and Y. Ohki, J. Appl. Phys. (to be published)
[7] For example, H. Nishikawa, E. Watanabe, D. Ito, and Y. Ohki, Phys. Rev. Lett. 72, 2101 (1994)
[8] R. Thomon, Y. Shimogaichi, H. Mizuno, Y. Ohki, K. Nagasawa, and Y. Hama, Phys. Rev. Lett. 62, 1388 (1989).

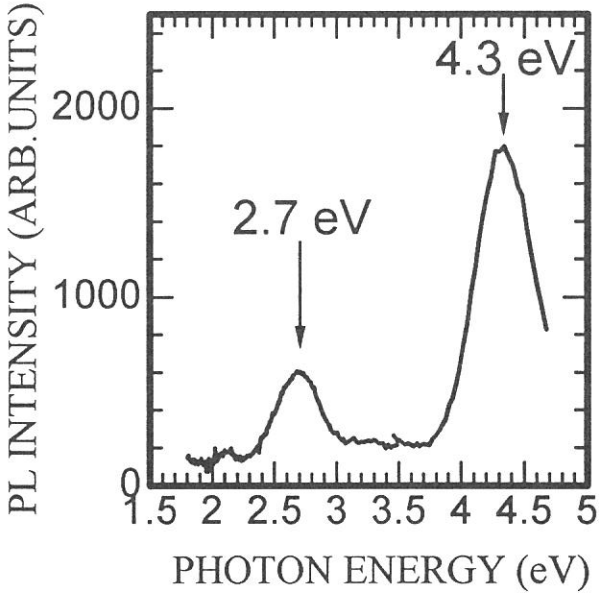

Fig. 1 Photoluminescence spectrum at room temperature from SIMOX oxide when excited by a KrF excimer laser.

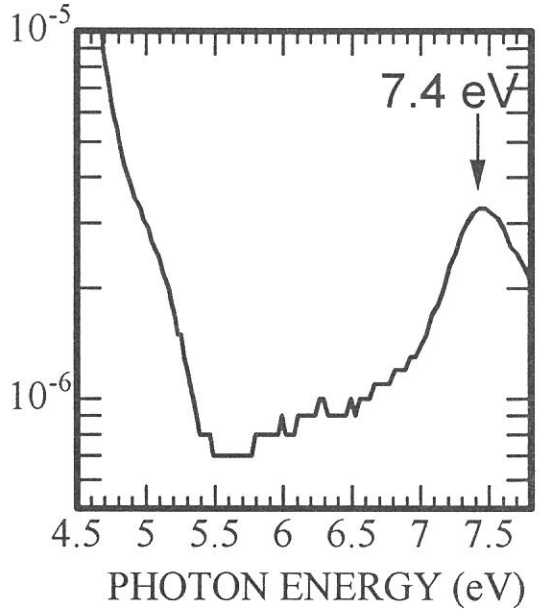

Fig. 2 Photoluminescence excitation spectrum obtained at 90 K for 4.3 eV PL band in SIMOX oxide.

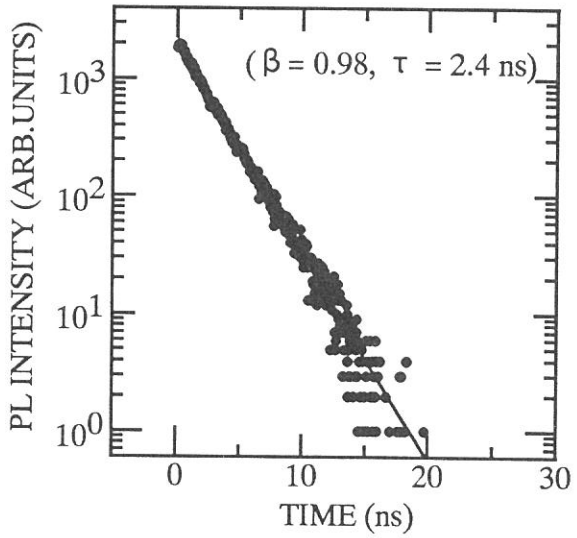

(a) Excited by 7.4 eV photons

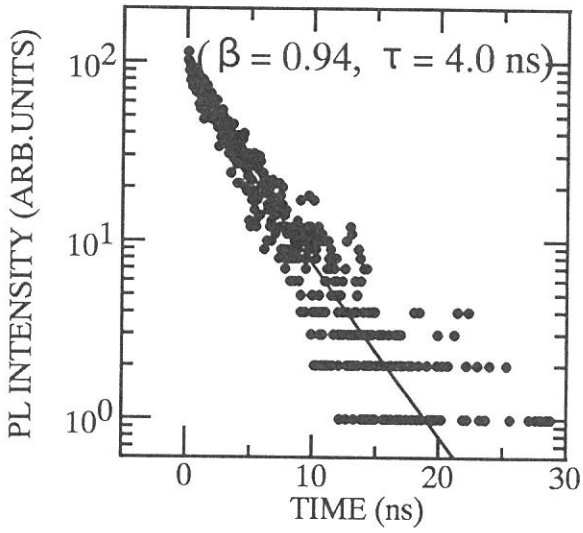

(b) Excited by 5.0 eV photons

Fig. 3 Decay profiles of the 4.3 eV PL band excited at 7.4 eV (a) and at 5.0 eV (b), for SIMOX oxide. Solid curves are drawn by assuming the stretched exponential function, Eq. (1).

(BL7B2)

Reflection spectra of TiO_2 and $CaTiO_3$ single crystals

K.Ueda, R.Waseda, M.Mizuguchi, H.Mizoguchi and H.Kawazoe
Research Laboratory of Engineering Materials, Tokyo Institute of Technology
4259 Nagatsuta, Midori-ku, Yokohama 226, Japan

N.Ueda and H.Hosono
Institute for Molecular Science
Myodaiji, Okazaki 444, Japan

Understanding of the electronic structure is essential in design of the electronic materials. There are some techniques for estimation of the electronic structure such as photoemission spectroscopy and reflection spectroscopy. Reflection spectra are not sensitive to the sample surface in comparison with photoemission spectra. Dielectric functions can be calculated from reflection spectra by the K-K transformation technique and they give information of electronic transitions in materials.

The measurements of reflection spectra are widely applied for semiconductors like Si in discussion of their electronic structures, but a few are done in oxide semiconductors. In order to obtain some information of the electronic structure in oxide semiconductors, reflection spectra of TiO_2(rutile) and $CaTiO_3$(perovskite) crystals were measured at the beam line 7B2 of UVSOR.

The plate shaped single crystals were set so that the incident angle of light is less than 10 degrees in order to simulate the normal incident reflection. The direction of the incident light to TiO_2 and $CaTiO_3$ crystals was normal to (110) and (100) planes, respectively. The photon energy was scanned from 2.0 to 20eV with the resolution smaller than 0.1eV. A simple correction was introduced in the present study because the reflection from the back surface of the crystal was included in the transparent region.

Reflection spectra of TiO_2 measured under E//c and E$\perp$c are shown in figure 1. The crystal structure of TiO_2 has large anisotropy that the spectra substantially differ between the polarization directions of the incident light. Each of the spectra was roughly divided into two parts, from 3.0 to 6.0-7.0 eV and from 6.0-7.0 to 15.0 eV. Considering participant orbitals of the component elements, it is supposed that the former part is related to an electronic transition from O2p band to Ti3d band and the latter one from O2p band to Ti4s band. Attribution of the structures in these parts requests precise calculations[1),2)].

Reflection spectrum of $CaTiO_3$ is shown in figure 2. The crystal structure of

$CaTiO_3$ is known as $GdFeO_3$ type derived from distorting the ideal cubic perovskite structure. Accordingly, anisotropy in the crystal structure is small and no apparent difference in spectra was detected from the polarizations of the incident light. The spectrum is also separable into two parts with the almost same energy regions in the case of TiO_2. The rough attribution of the low energy region is the same with the one in TiO_2, but that of the high energy region is a little different referring to the reflection spectra of $SrTiO_3$ and $BaTiO_3$[3]. Because Ca and Ti are near in the periodic table, energy levels of orbitals in these ions are similar. The high energy region is, therefore, supposed to be the transition from O2p band to Ti4s-Ca4s mixed band. This will be supported by the assumption that some peaks became weak and broad in the region because of the mixing of Ti4s-Ca4s bands and dilution of the Ti ion concentration per unit volume.

The theoretical background will be needed for more detailed discussion and some calculations will be performed soon. K-K transformation analysis is also in progress.

Reference

1)M.Cardona and G.Harbeke, Phys.Rev. 137 (1965) A1467
2)K.Vos and H.J.Krusemeyer, J.Phys.C 10 (1977) 3893
3)M.Cardona, Phys.Rev. 140 (1965) A651

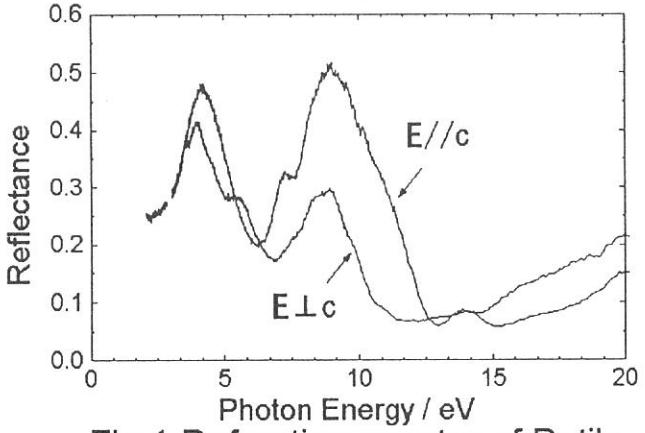

Fig.1 Refrection spectra of Rutile

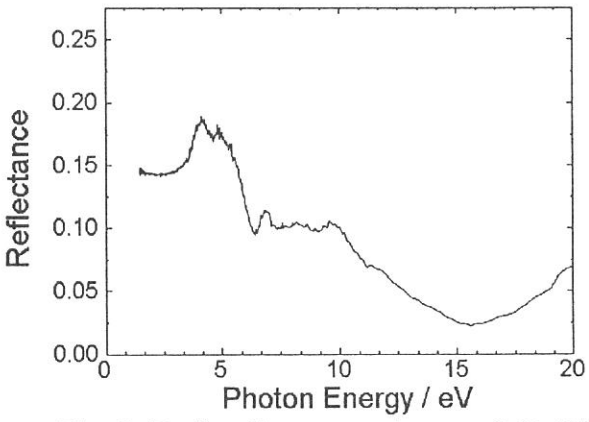

Fig.2 Reflection spectrum of $CaTiO_3$

(BL7B)

Spectral Sensitivity of a Bandpass Photon Detector in the Vacuum Ultraviolet Region

Naoki SATO, Ikuko KAWAMOTO and Sotaro ENDO

Institute for Chemical Research, Kyoto University, Uji, Kyoto 611

As a photon detector in the vacuum ultraviolet region for an inverse photoemission (IPES) measurement in the Bremsstrahlung isochromat spectroscopy (BIS) mode, we have fabricated a bandpass detector using a photomultiplier and optical windows with reference to that developed by Taniguchi et al. [1,2]. In this work we have examined a spectral sensitivity of the prepared detector, using a 1 m Seya-Namioka monochromator attached to the BL7B of UVSOR.

Our detector has been made of a commercially obtained Cu-BeO photomultiplier (Hamamatsu R-595) which has the first dynode working as a low-pass filter because of the threshold of its optical sensitivity. A 100 nm thick film of potassium chloride was vacuum deposited onto the surface of the first dynode to increase the sensitivity. In front of the first dynode optical crystal plates have been located to work as a high-pass filter due to their optical absorption edges. We have employed two kinds of crystals of alkali halides, i.e., calcium fluoride and lithium fluoride, both in the thickness of 2 mm. A 15 nm thick film of potassium chloride was vacuum deposited onto the surface of the lithium fluoride crystal and that of rubidium chloride onto the calcium fluoride one, to make the bandpass narrow and simple in its lineshape owing to characteristic absorption profiles of these crystals and overlayers. The thickness of the deposited films was monitored by a quartz crystal oscillator.

Experimental situation to observe spectral sensitivities of the detector above was as follows. A 1 m Seya-Namioka monochromator attached to BL7B of UVSOR, which permitted to use three concave gratings with different blaze angles, was used to cover the photon energy range from 8 to 13 eV. Signal intensities from the detector were normalized to the output light intensities from the monochromator monitored by fluorescence from sodium salicylate applied on the surface of the first dynode in place of that mentioned above. The bandpass characteristics of both the detector with double windows just mentioned above and that with a single window of lithium fluoride were examined.

Figure 1 depicts the optical sensitivity spectrum obtained for the detector fully equipped. As for this bandpass feature, the peak position at 9.80 eV is the same as the result by Namatame et al., the full width at half maximum (FWHM) of 0.65 eV is larger than their result [2]. This may be explained by a possible difference in the thickness of a potassium fluoride film deposited onto the surface of the first dynode from the thickness monitored by the quartz oscillator because of the concave surface of the dynode. On the other hand, although a small bump is examined at about 8.2 eV in the result by Namatame et al. [2], no such a feature has been observed in this work. This could be caused by a rubidium chloride film which has newly been overlaid onto the calcium fluoride window. Thus, it is concluded that our photon detector can be used as a detector for IPES measurements.

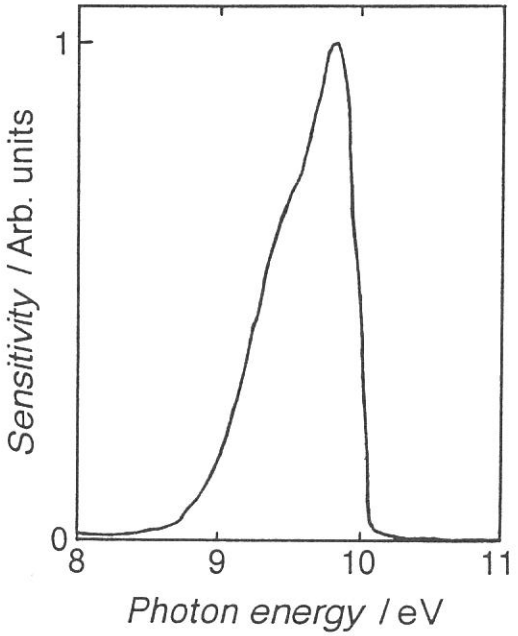

Fig. 1. Characteristics of the bandpass photon detector.

The authors are grateful to Prof. M. Taniguchi for providing them with valuable information on the detector and to Prof. T. Kinoshita for taking care of them when they carried out the measurement above at UVSOR.

References

[1] K. Yokoyama, K. Nishihara, K. Mimura, Y. Hari, M. Taniguchi, Y. Ueda and M. Fujisawa, *Rev. Sci. Instrum.* 64 (1993) 87.

[2] H. Namatame, M. Tamura, M. Nakatake, H. Sato, Y. Ueda and M. Taniguchi, *J. Elect. Spectrosc. Relat. Phenom.*, in press.

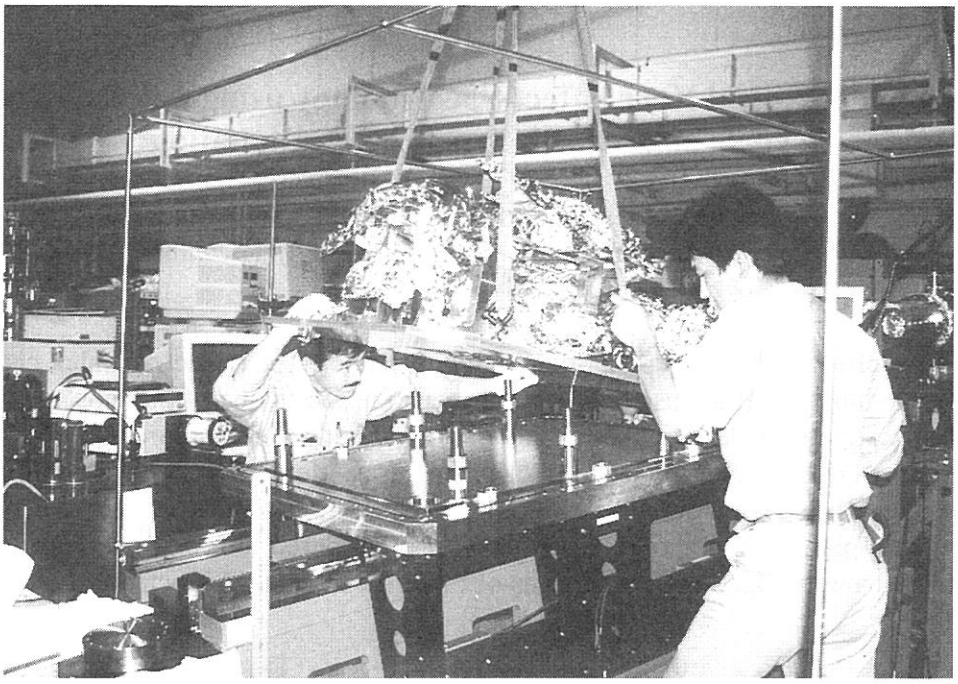

Messrs. T. Horigome (left) and N. Mizutani (right) are carefully setting an optical bench on the base flange of a grating chamber for construction of the SGM-TRAIN at BL5A.

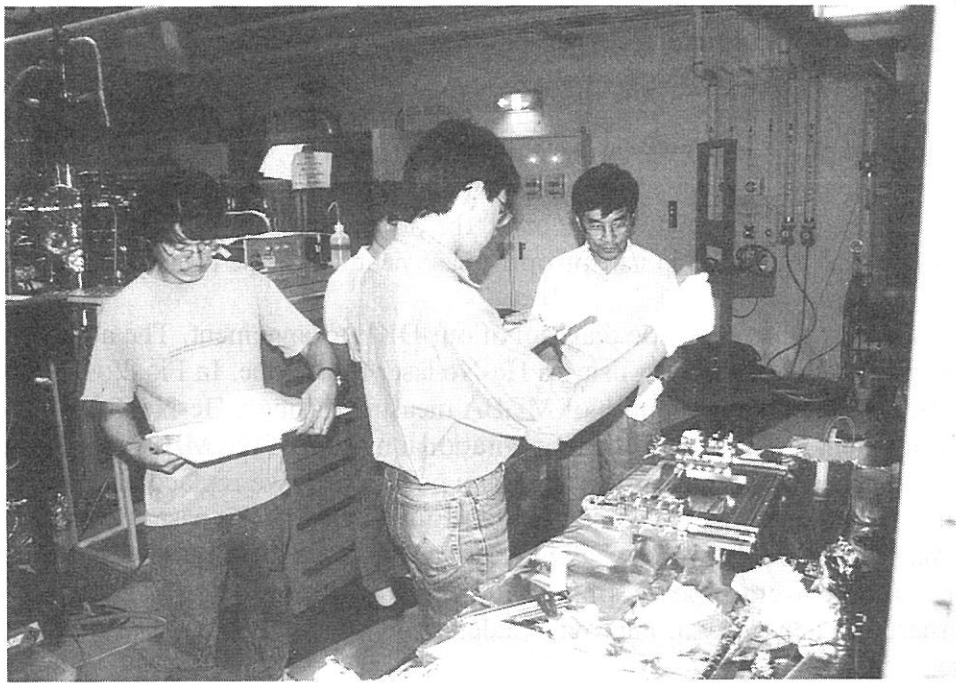

Prof. M. Kamada (right) and Dr. S. Kimura(middle) are installing gratings and mirrors on the exchange device of the SGM-TRAIN, with Dr. S.Hirose and Mr. M. Hasumoto (left).

(BL7B)

Resonance Optical Kerr Effect Spectroscopy using a Pulsed Laser synchronized with Synchrotron Radiation

Y.Shimada, N.Hashimoto, Y.Kanematsu and S.Kinoshita
Department of Physics, Faculty of Science, Osaka University, Toyonaka, Osaka 560, Japan

Optical Kerr effect (OKE) is a phenomenon which induces the refractive index change in materials by illumination of intense light and has been known as one of the most powerful methods to investigate the low frequency fluctuation and phonon structures. [1,2] If the exciting light for OKE is resonant with the electronic transition energy of the material, it is possible to probe the specific fluctuation which is coupled with the electronic transition through electron-phonon interaction. This method is considered to be very promising because we can discriminate the fluctuation by means of the difference in the electron-phonon interaction.

In the present study, we attempted the resonance OKE experiment using the synchrotron radiation (SR) at BL7B of UVSOR as a probe light. The SR is considered to be ideal for this study, because the light pulse is available for a wide wavelength range including the ultraviolet region. For the pump pulse, we used the fundamental light from a laser-diode pumped Q-switched Nd:YLF laser, whose width and pulse energy were 6 ns and 500 μJ, respectively. The Q-switch of this laser was triggred by the external pulse which was synchronized with the SR light pulse. The external trigger was supplied after the frequency division to 86Hz from the SR RF signal whose repetition rate was about 90MHz.

The sample employed was an organic liquid, 4'-methoxybenzylidene-4-n-butylaniline (MBBA), which shows a nematic-isotropic phase transition at 314.7K [3] and has an absorption band around 350nm. The probe light near this band is expected to show the resonance enhancement, while within the band, the probe light may be completely absorbed. The OKE signal was measured in its isotropic phase near the phase transition point.

In Fig.1, we show the schematic diagram of our OKE arrangement. The adjustment of the optical system was first carried out using a He-Ne laser as a probe. In Fig.2, we show the typical example of the OKE response of MBBA measured using a He-Ne probe. Very slowly decaying component is ascribed to the reorientational motion of the MBBA molecules whose rate becomes divergently slow near the transition point. Next, we replace the He-Ne laser with the SR light. Unfortunately the OKE signal was not observed in this case. Possible reason for this result may be ascribable to the weak intensity of the probe light per unit area and energy bandwidth, since the average power of the SR probe light is only one fifth of that of He-Ne laser. It is therefore necessary to improve the detection sensitivity. Further study is clearly needed.

References

[1] S. Kinoshita, Y. Shimada, W. Tsurumaki, M. Yamaguchi and T. Yagi, *Rev. Sci. Instrum.* **64**, 3384 (1993); *J. Opt. Soc. Am.* **B10**, 1017 (1993).
[2] S. Kinoshita, Y. Kai, M. Yamaguchi and T. Yagi, *Phys. Rev. Lett.* **75**, 148 (1995); *Chem. Phys. Lett.* **236**, 259 (1995).
[3] G.K.L.Wong and Y.R.Shen, *Phys. Rev.* **A10,** 1277 (1974).

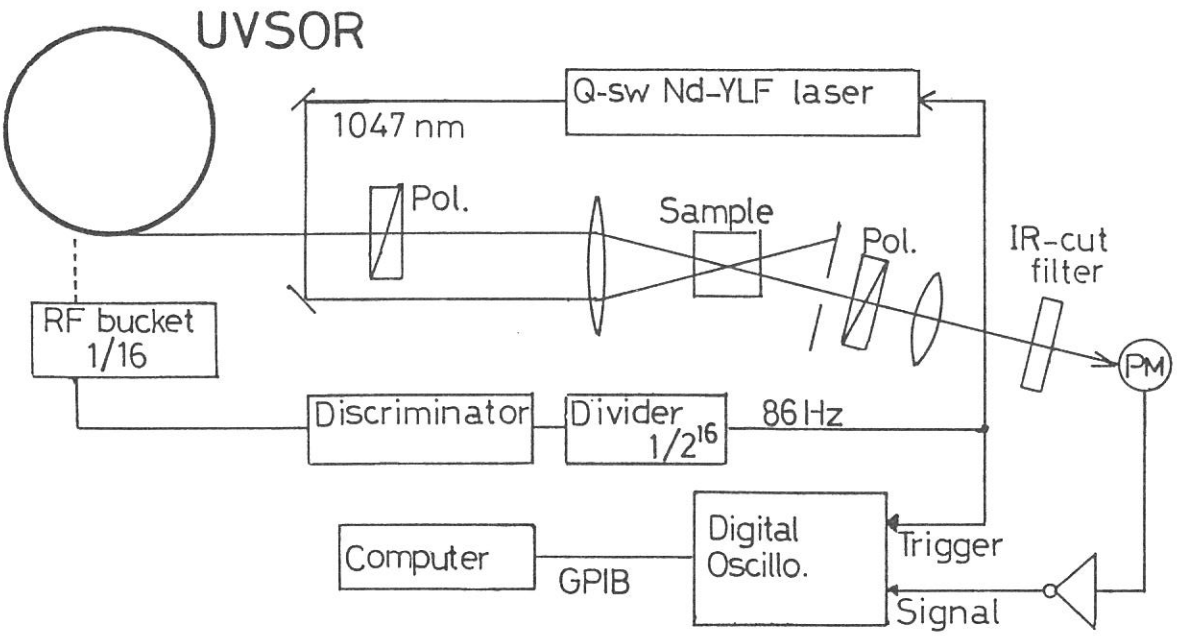

Figure 1. Schematic diagram of the OKE experiment.

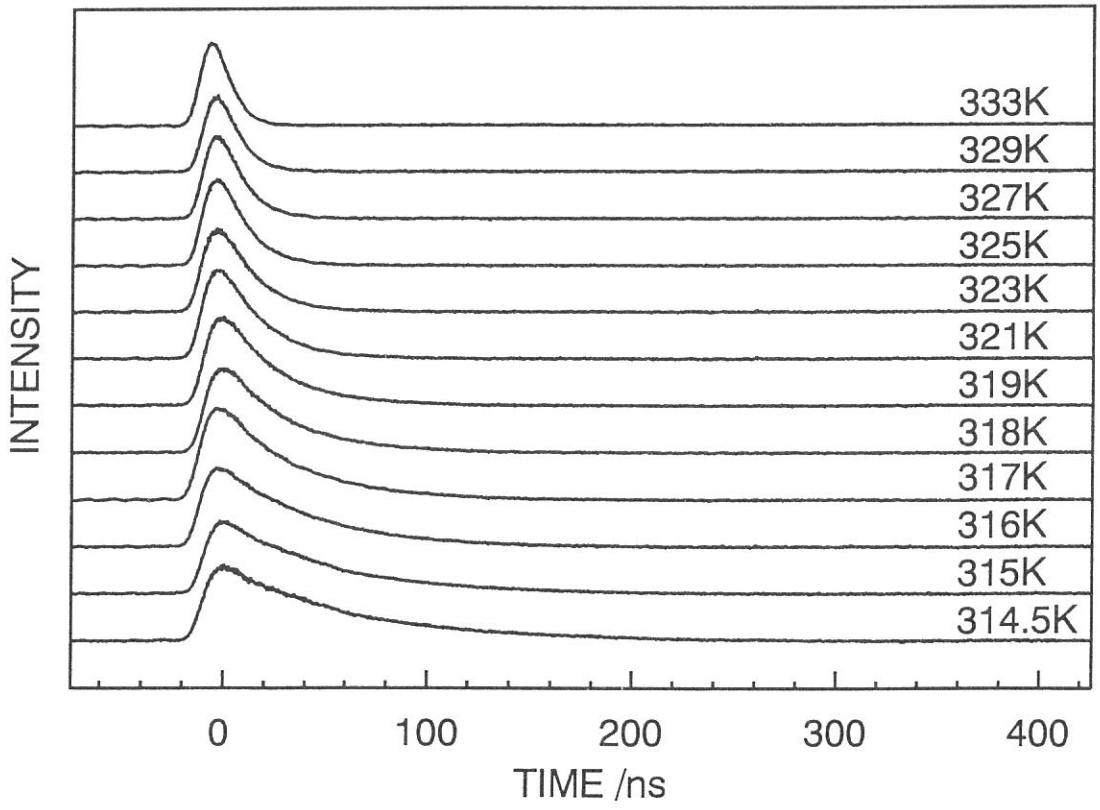

Figure 2. OKE response of MBBA measured using a He-Ne probe.

(BL7B)

Formation Process of Distributed Bragg Gratings in Optical Fiber

Junji Nishii, Kohei Fukumi, Naoyuki Kitamura and Hiroshi Yamanaka
Osaka National Research Institute, AIST, 1-8-31, Ikeda, Osaka 563

It has been generally accepted that the bleaching of oxygen deficient defect by irradiation with 5 eV light is an origin of the formation of Bragg gratings in Ge-SiO_2 glass fibers.[1] However, Albert et al. demonstrated that the Bragg gratings could be formed in the fiber by irradiation with ArF laser light(6.4eV).[2] In this study we investigated the dominant photochemical reaction channel related with the formation of Bragg gratings.

ArF(6.4eV) and KrF(5.0eV) excimer laser pulses were irradiated to $10GeO_2$-$90SiO_2$ optical fiber preforms at room temperature. Figure 1 shows the ESR spectra after irradiation with KrF laser(10mJ/cm^2/pulse) of 60 shots(curve a) and 3×10^4 shots(curve b). From the g values of the downward peaks(g=1.9933 and 1.9866), the signals between 347 and 350.5mT could be attributed to two kinds of electron trapped centers of four-fold coordinated Ge ions(GEC's)[3]. The g value of the weak signal around 345mT was very close to that of the self-trapped hole center(STH) of a bridging oxygen[4]. Figure 2 shows the relationship between the irradiated power densities of KrF and ArF laser pulses and the concentration of GEC's. The formation efficiencies of GEC's were same between the irradiations with ArF and KrF laser. The concentration of GEC's was increased with the second power of the power density, which means the GEC's and STH were formed via two-photon absorption process. Therefore, we propose that the following reaction path for the excimer laser irradiation:

$$-\overset{|}{\underset{|}{Ge}}- + \ddot{O} \text{ (bridging oxygen)} \xrightarrow{h\nu} \text{GEC} + \text{STH}.$$

Same photochemical reaction was observed by irradiation with XeCl laser(4.0eV) because the photon energy of XeCl laser is higher than the half of the band gap energy of the glass estimated by the Tauc plot of the VUV spectrum[5].

The curve c in figure 1 shows the difference spectrum between curve a and b, which could be attributed to the signal due to Ge E' center. The spin densities estimated from curve a and b were same. Thus we can conclude that the structural relaxation of GEC's to Ge E' proceeded during the continuous irradiation[6]. The refractive index change(efficiency of Bragg reflection) increased with the number of irradiated pulses, which might be closely related with the relaxation of GEC's to Ge E' center. Further quantitative study is now in progress.

References

1)H.Hosono, Y.Abe, D.L.Kinser, R.A.Weeks, K.Muta and H.Kawazoe, Phys. Rev. **B46**, 11445(1992), R.M.Atkins and V.Mizrahi, Electron. Lett., **28**, 1743(1992).

2)J.Albert, B.Malo, F.Bilodeau, D.C.Jhonson, K.O.Hill, Y.Hibino and M.Kawachi, Opt. Lett., 19, 387(1994).

3)H.Kawazoe, J.Non-Cryst. Solids, **71**, 231(1985).

4)D.L.Griscom, Phys.Rev. **B40**, 4224(1989).

5)J.Nishii, N.Kitamura, H.Yamanaka, H.Hosono and H.kawazoe, Opt. Lett., **20**, 1184(1995).

6)J.Nishii, K.Fukumi, H.Yamanaka, K.Kawamura, H.Hosono and H.Kawazoe, Phys. Rev. **B52**, 1161(1995).

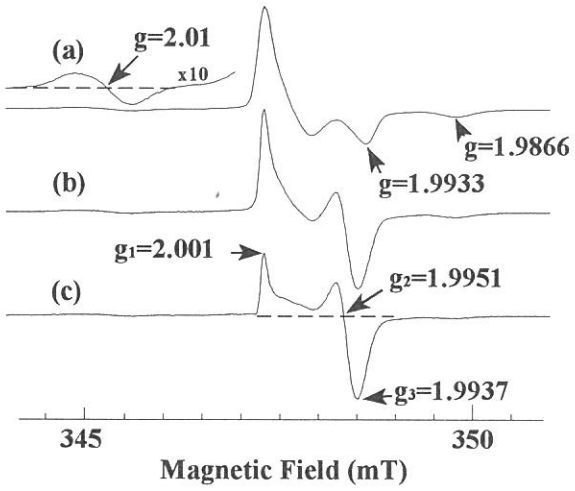

Fig.1. ESR signals of KrF laser(10mJ/cm^2 /pulse) irradiated 10GeO2-90SiO2 glasses.
(a)irradiated with 60 KrF laser pulses, (b)3x10^{4}pulses, (c)b-a.

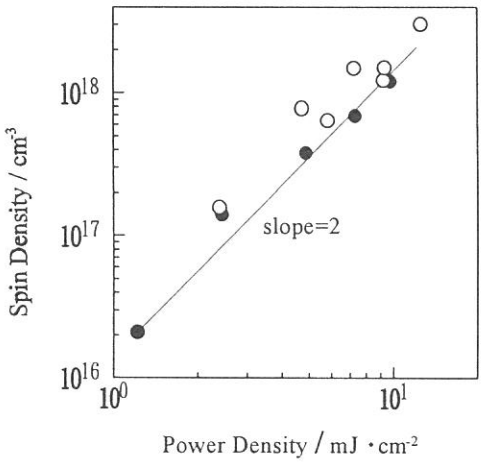

Fig.2, Relationship between power density of KrF(○) and ArF(●) lasers and the concentration of induced GEC's.

(BL7B)

Refractive Index Change in Al^+-ion-implanted Silica Glass.

Kohei FUKUMI, Akiyoshi CHAYAHARA, Naoyuki KITAMURA, Junji NISHII,
Kohei KADONO, Masaki MAKIHARA, Kanenaga FUJII and Junji HAYAKAWA.

Osaka National Research Institute, AIST, Midorigaoka, Ikeda, Osaka, 563

Ion implantation in silica glass is always accompanied with the formation of defects, resulting in optical absorption in the ultraviolet region.[1] The frequencies of absorption bands (the resonance frequencies of oscillators) due to the defects caused by ion implantation are lower than that of absorption edge of silica glass. In general, refractive index depends on the amount of oscillators in a unit volume, the resonance frequency of oscillators and the oscillator strength.[2] Therefore, it is expected that the formation of these defects increases the refractive index in the visible and infrared regions. In the present study, the refractive index of silica glass has been changed by Al^+-ion-implantation. The relationship between the refractive index change and the formation of defects has been discussed.

200keV Al^+ ions were implanted in silica glass plates (Nippon Silica Glass Yamaguchi Co.Ltd., direct method, OH=ca.1000wt.ppm) at doses of $1x10^{13}$-$1x10^{17}$ions/cm^2 at room temperature with an ion implantor at the Ion Engineering Center. The glasses implanted with $1x10^{15}$-$1x10^{17}Al^+$ions/cm^2 were heated up to 920 ℃ in an argon gas atmosphere. In addition, the glasses were heated up to 1000 ℃ in air. Vacuum ultraviolet (VUV) absorption spectra of as-implanted glasses were measured at the beam line BL7B of the UVSOR facility in the Institute for Molecular Science at Okazaki, Japan. Optical absorption spectra of the as-implanted and heat-treated glasses were also measured in ultraviolet(UV), visible(Vis) and near infrared(NIR) regions.

The absorption edge in the VUV region shifted toward lower energy side after ion implantation, as shown in fig.1. This edge shift is due to the formation of an absorption band at about 7.5eV, since an absorption band was observed at about 7.5eV in the difference absorption spectrum between $1x10^{16}$ions/cm^2-implanted glass and unimplanted glass, as shown in fig.1. It is known that the absorption band at 7.5eV is due to Si-Si homobonds and peroxy radicals.[3] Since the transmittance at 7.5eV was far below the detection limit of the measurement in the glasses implanted to doses of $5x10^{16}$ and $1x10^{17}$ions/cm^2, the absorbance at 6.5eV was adopted as a measure of the absorbance at 7.5eV. The ordinates in the right hand in fig.2 show the amounts of Si-Si homobonds and peroxy radicals corresponding to the absorbance at 6.5eV. The amounts of these defects were much larger than implantation dose in the glasses implanted to doses ranging from $1x10^{13}$ to $1x10^{15}$ions/cm^2. These defects diminished after heating in an argon atmosphere in the glass implanted with $1x10^{15}$ions/cm^2. These findings indicate that the defects causing the 7.5eV band is mainly produced through the collision process in the glasses implanted with Al+ions lower than $1x10^{16}$ions/cm2. In contrast, the amounts of these defects were comparable to implantation dose in the glasses implanted to doses ranging from $1x10^{16}$ to $1x10^{17}$ions/cm^2. In addition, the defects did not decrease after heating in an argon atmosphere in the glass implanted with $1x10^{17}$ions/cm^2. It was inferred that the 7.5eV band observed in the glass implanted with $1x10^{17}$ions/cm^2 is mainly attributed to Si-Si homobonds which is formed through chemical interaction between the implanted aluminum ions and oxygen ions in silica glass, since it has been shown that the implanted aluminum ions are mainly coordinated by oxygen ions of silica glass before and after heating in an argon atmosphere.[4]

Interference pattern was observed in the UV-Vis-NIR transmittance spectra of the $1x10^{17}$ions/cm^2-implanted glass before and after heating in an argon atmosphere. The presence of interference implies the presence of the layer which has refractive index different from silica glass. The interference pattern disappeared only when the absorption at 6.5eV diminished, indicating that

the change in refractive index is mainly caused by the 7.5eV band, presumably by Si-Si homobonds. On the other hand, it is deduced that the implanted aluminum ions, themselves, made minor contribution to the refractive index change, since the interference pattern disappeared in the glass after heating at 1000 ℃ in air. Refractive index of the implanted region was estimated from the amplitude of interference pattern observed in the UV-Vis-NIR transmittance curves. The refractive index at the maximum of the Al^{+}-ion distribution was larger than that of silica glass by 10% (at a wavelength of 600nm) - 8% (at a wavelength of 2500nm) .

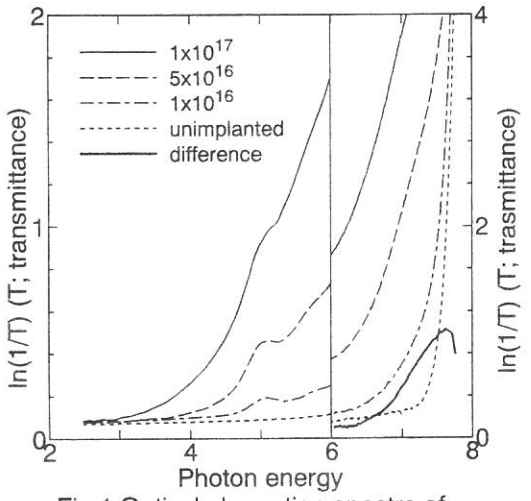

Fig.1 Optical absorption spectra of as-implanted glasses

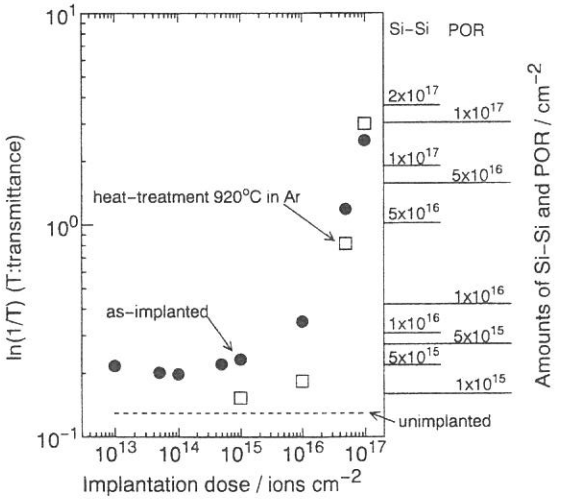

Fig.2 Absorbance at 6.5eV vs implantation dose

References

1) G.W.Arnold, IEEE Trans., Nucl.Sci., 20(1973)220
2) F.Wooten, "Optical Properties of Solids", Chap.3, p.42 (Academic Press, New York, 1972)
3) E.J.Friebele, "Optical Properties of Glass", p.205, edited by D.R.Uhlmann and N.J.Kreidl (Am.Ceram.Soc., Westerville, OH, 1991)
4) K.Fukumi, A.Chayahara, M.Makihara, K.Fujii, J.Hayakawa and M.Satou, J.Am.Ceram.Soc., 77(1994) 3019

(BL7B)

REFRACTIVE-INDEX DISPERSION AND VACUUM ULTRAVIOLET REFLECTION OF OXIDE GLASSES

Shigeru Fujino, Hiromichi Takebe and Kenji Morinaga

Department of Materials Science and Technology, Graduate School of Engineering Sciences, Kyushu University, Fukuoka 816

Refractive indexes as a function of wavelength are important properties for optical and optoelectronic glasses such as laser hosts, fibers for communications and photonic switches. We measured accurate refractive indexes of oxide glasses: silica, silicate, borate, aluminate, tellurite, antimonate and heavy metal gallate glasses in the wavelength range of 0.265 to 1.710 μm using the minimum-deviation method[1]. We discussed factors affecting the refractive index dispersion by using the single-oscillator model. Our previous study concluded that the values of refractive indexes were mainly affected by the effective resonance wavelength λ_0 all through the glass systems[1]. Since there are various oscillators such as bridging oxygens, nonbridging oxygens and cations in oxide glasses in the vacuum ultraviolet region[2], the wavelength λ_0 used in previous study[1] give an average feature of the oscillators. Therefore, the actual measurement of the resonance wavelengths in the vacuum ultraviolet region is inevitable for understanding of refractive index and its dispersion behavior in the visible region.

In this work we measured the reflection spectra of oxide glasses: silica, silicate, borate, aluminate, germanate, tellurite, antimonate and heavy metal gallate glasses in the spectral range of 2 to 20 eV using the synchrotron radiation. We determined the resonance wavelengths of various oscillators :Al^{3+}, Ge^{4+}, Te^{4+}, Sb^{3+}, Pb^{2+}, Tl^{+} in oxide glasses. We discuss the correlation between the measured resonance wavelength and effective resonance wavelength λ_0 calculated in terms of the single oscillator Drude-Voigt equation using the data of refractive-index dispersion.

Figure 1 shows the reflection spectra of oxide glasses:(a)silica and silicate, (b)tellurite, (c)antimonate and (d)heavy metal gallate glasses. These reflection spectra were normarized from refractive index data in the visible region. A downward arrow(↓) in Fig.1 denotes a resonance wavelength of a oscillator observed in oxide glasses. The peak energies of reflection bands due to the interionic transitions of high polarizable cations: Tl^{+}, Pb^{2+},Sb^{3+},Te^{4+} appear in the spectral range of 3.5 to 6.2 eV. A downward arrow (⇓) in Fig.1 denotes a caluculated effective resonance wavelength λ_0 based on the single oscillator model using refractive index data in the visible region[1].

Our results concludes that the refractive indexes of the silica and silicate glasses in the visible region are mainly affected by the average resonance wavelengths of the various oscillators observed in the reflection spectra. For the tellurite, antimonate and heavy metal gallate glasses, the refractive indexes in the visible region are mainly affected by the interionic transitions of high porarizable cations: Te^{4+}, Sb^{3+}, Pb^{2+}, Tl^{+}[3].

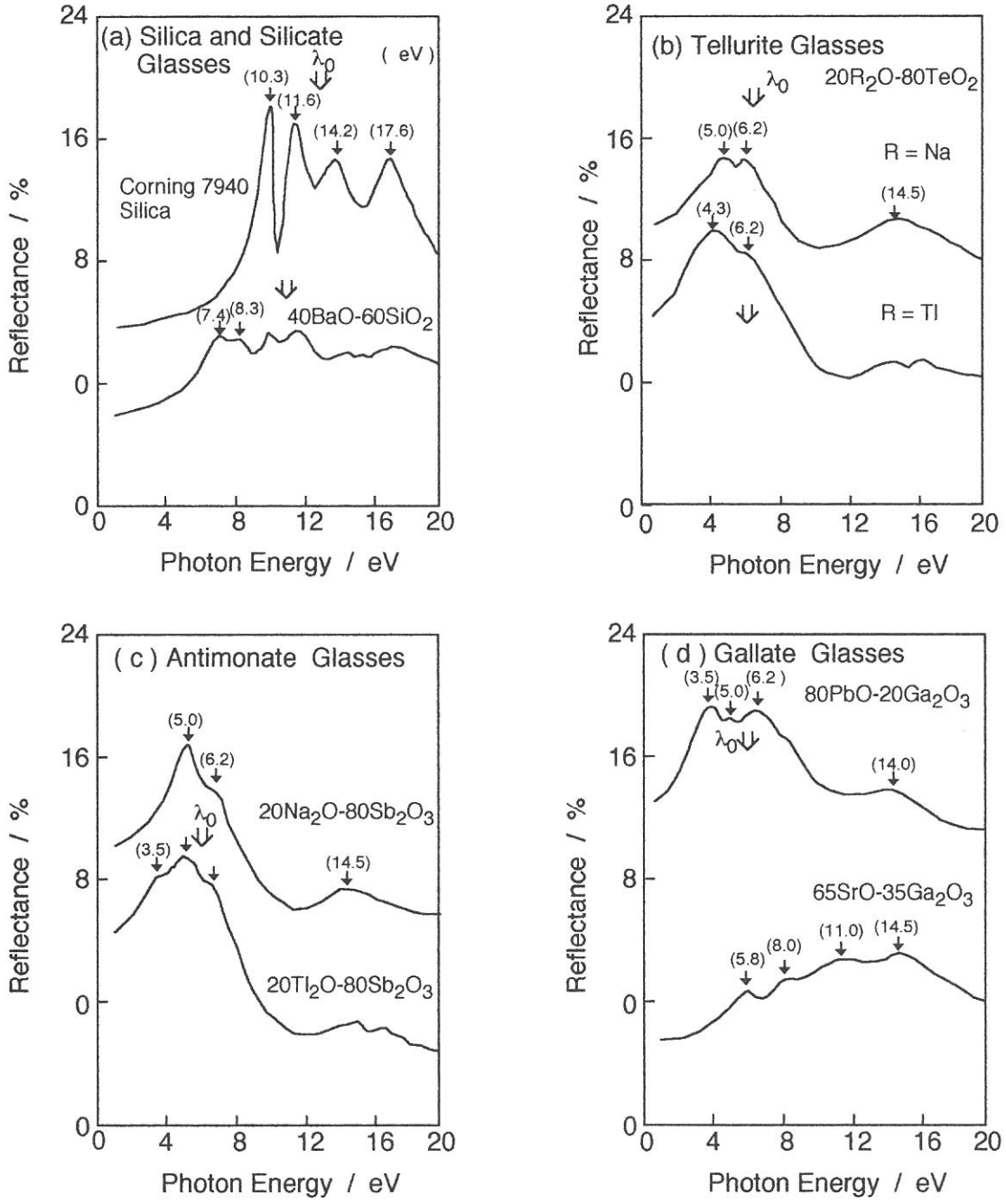

Fig.1 Reflection spectra of (a) silica and slicate, (b) tellurite, (c) antimonate and (d) gallate glasses.

References

[1] S.Fujino , H.Takebe and K.Morinaga , J. Am. Ceram. Soc. , 78[5]1179-84(1995).

[2] S.Hirota , T.Izumitani and R.Onaka , J. Non-Cryst. Solids, 39-50(1985).

[3] S.Fujino , H.Takebe and K.Morinaga ,Proc. XVII I. C. G., Beijin,163-168(1995).

(BL7B)

Reconstruction of BL7B for UV, VIS and IR Spectroscopy with a 3 m Normal Incidence Monochromator

Hideyuki NAKAGAWA, Kazutoshi FUKUI, Kazumichi NAKAGAWA*,
Takao NANBA** and Toyohiko KINOSHITA***

Department of Electrical and Electronics Engineering, Fukui University, Fukui 910
**Faculty of Human Development, Kobe University, Tsurukabuto, Nadaku, Kobe 657*
***Department of Physics, Faculty of Science, Kobe University, Kobe 657*
****Institute for Molecular Science, Myodaiji, Okazaki 444*

The beamline BL7B has been a powerful experimental station for the solid state spectroscopy with a 1 m Seya-type VUV monochromator, covering the wave-length region from 50 to 600 nm. This beamline is now under reconstruction aiming at the experimental station for the extended researches of the highest level with the higher resolution and intensity, the wider wave-length region available and the computer controlled operating system friendly to users, having possibilities to utilize the linear and circular polarization inherent in SR and to realize some combined experimental systems, for example, with the synchronized laser to the SR pulse or with the external field. It will be also taken account of to make possible the researches on gaseous, liquid and biochemical samples and at extremely low temperature in the conventional wavelength region.

An outline drawing of the new beam line is given in the figure which is not yet the final version. The total length from the light source point to the back end of the monochromator is of 870 cm. The experimental station is on the 2-nd floor at the hight of 175 cm from the ground level. The beam hight is 105 cm from the floor level. Main parts of the system are a pre-mirror focusing system, a 3-m normal incidence monochromator and a post-mirror focusing system. The pre-mirror system comprises two mirrors, M_0 and M_1. Parameters and specifications of this system are listed below.

acceptance angle	vertical: 10 mrad, horizontal: 50 mrad
M_0	plane mirror, 700×140 mm^2, incident angle: 87.5° water cooled, Au-coated SiC Computer cont.: pitch,roll and yaw
M_1	ellipsoidal mirror, 700×140 mm^2, incident angle: 87.5° Au-coated SiO_2, long semi-radius: 2650 mm, short semi-radius: 115.59 mm Computer cont.: pitch, roll, yaw, X and Z

In front of the pre-mirror system is installed a 2-jaw water cooled aperture component which chooses the SR beam in the vertical direction with the appropriate width to pass through selectively the linearly or circularly polarized light.

The main monochromator is of a upper grade model modified from the model 2253 UHV VUV normal incidence monochromator (McPHERSON) with 3 m focal length, vertical dispersion and the included angle of 15°. Wavelength coverage is from 50 to 1000 nm by changing three gratings. Entrance and exit slits are fixed on the Rowland circle. The grating rotates and linearly translates as wavelength is scanned. The grating translation is achieved automatically so as to compensate for changes of focal distance. Three gratings are mounted on a rotatable turret and are replaced one by one through rotation of the turret. Selection and scanning of grating, slit adjustment and initial setting are all controlled

by a computer. Both entrance and exit slits are adjustable for width between 5 μm and 3 mm and for hight from 0 to 30 mm. All spherical gratings are original laminar ones fabricated on SiO_2 and have the effective grooved area of 120×40 mm^2. Specifications of the gratings are listed in the following.

	Coverage nm	Grooves /mm	Dispersion nm/mm	duty factor	groove depth nm	coat(thickness) (nm)
G_1	50~150	1200	0.2	0.497	16.4	Au(75)
G_2	100~300	600	0.5	0.497	32.9	Al(52)
G_3	250~1000	300	1.0	0.497	73.3	Al(40)

The post-mirror focusing system comprises two troidal mirrors with long (M_4) and medium (M_5) focal length. The mirror dimension is 120×120 mm^2. They are interchanged manually with a turret and adjusted with mirror manipulators providing roll, pitch and yaw motions. The beam radius on the focal plane is expected to be smaller than 2 mm. The specifications of the post-mirrors are designed as,

M_4	focusing distance: 3150 mm, Au-coating, fused silica long semi-radius: 3380.7 mm, short semi-radius: 3323.2 mm
M_5	focusing distance: 4150 mm, Al+MgF_2 coating, fused silica long semi-radius: 3690.6 mm, short semi-radius: 3627.7 mm

For the beam adjustment are inserted two 4-blade beam monitors in front of the entrance slit of 3m-NIM and the post-mirror chamber and two beam intensity monitor just after the entrance and exit slits.

After the final adjustment and test run, which will be accomplished by the end of October (1996), this beamline will be used for absorption, reflection and fluorescence measurements on various materials of solid, liquid and gas phases including inorganic, organic and biochemical ones, presenting material scientists a powerful experimental station available to use the highly resolved, high brilliant, well polarized and short repetitive pulse light not only in the VUV region but also in the near UV, VIS and near IR region.

Fig.1 The outline of the side view of the new BL7B

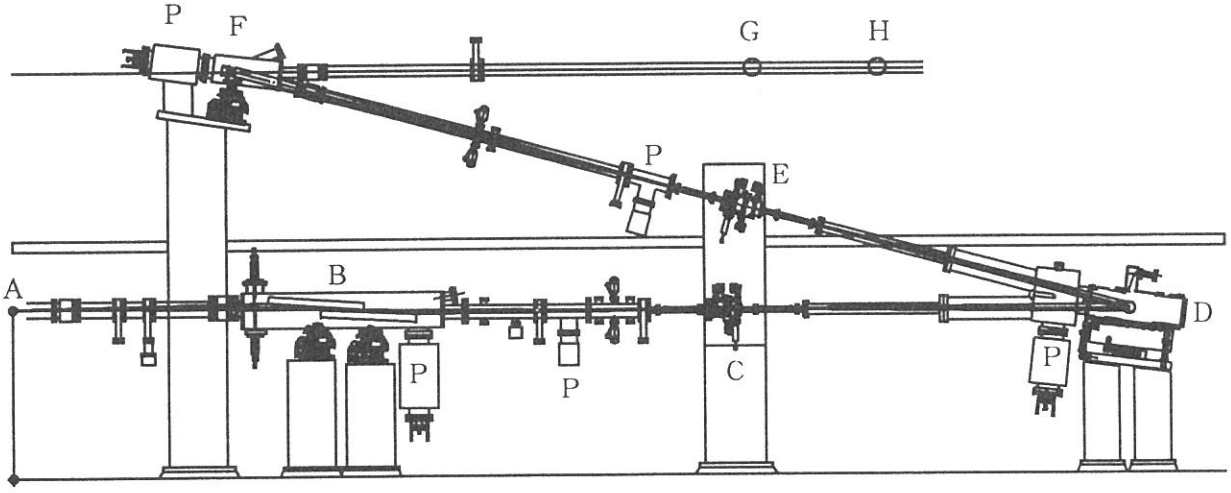

A: Light source point B: Pre-mirror chamber C: Entrance slit
D: Grating chamber E: Exit slit F: Post-mirror chamber
G: 1st focal point H: 2nd focal point P: Ionization pump

(BL－8A)

Temperature dependent dephasing time of the Aniline doped in PVA

Hiroshi Itoh, Shunsuke Nakanishi, Noriaki Tsurumachi[1)], Takao Fuji[1)], Hideyuki Inouye[2)], Hiroki Nakatsuka[1)] and Masao Kamada[3)]

Department of Physics, Kagawa University, Takamatsu 760
Institute of Applied Physics ,University of Tsukuba, Tsukuba 305[1)]
Hirao Active Glass project, ERATO[2)]
UVSOR, Institute of Molecular Science, Okazaki 444[3)]

We have investigated temperature dependence of accumulated photon echo signals of anorganic molecule(Aniline) doped in polyvinyl alcohol(PVA) in ultraviolet wavelength region.

The field autocorrelation trace of the excitation beam was recorded to determine the time resolution of the echo experiment. By inserting a quartz plate of 2 mm thickness between the PBS and one of the quartz corner cube prisms of the interferometer, the temporal width of the autocorrelation was drastically improved to about 35 fs.

Now we have measured temperature dependent dephasing time of the Aniline doped in PVA. The sample had the same concentration as the case of former investigation[1]. The dephasing time did not depend on the concentration of the Aniline in PVA, because the dephasing time remained 180 fs when the concentration of the Aniline in PVA was lowered. Figure 1 shows the temperature dependence f the dephasing time of the Aniline in PVA.

Next,we attempted to investigate the dephasing time of Polystyrene cast film at the center wavelength of 270 nm. The signals were obtained with the same manner as the case of the Aniline but the mirrors and bandpass filter were exchanged to suitable ones. But it was difficult to distinguish the signals from background noises, since the decay constant is too short to investigate and 2nd order component of the modulation frequency (2f) of the SR beam remains on the signal. To obtain shorter relaxation processes in this wavelength region, we have to compensated the dispersion in the Michelson interferometer. Moreover, shorter temporal resolution will be needed to distinguish the signal from noise components.

At last, we checked how short time resolution we could get with this interferometer which was slightly modified by changing mirrors and the PBS. The mirrors and the PBS were changed to uv enhanced Al coated ones and a metal coated cube type beam splitter which reflected about 30% and transmitted about 30 % in the wavelength region longer than 300 nm, so that a bandwidth of detection was limited by S1722-02(Hamamatsu Photonics

Inc.)PIN photodiode. After the dispersion of the interferometer was carefully compensated, we could successfully obtained the shortest autocorrelation trace as shown in Fig.2.

Reference

[1] H.Itoh et al, UVSOR ACTIVITY REPORT 1994.

Fig.1 Temperature dependence of dephasing time of the Aniline doped in PVA.

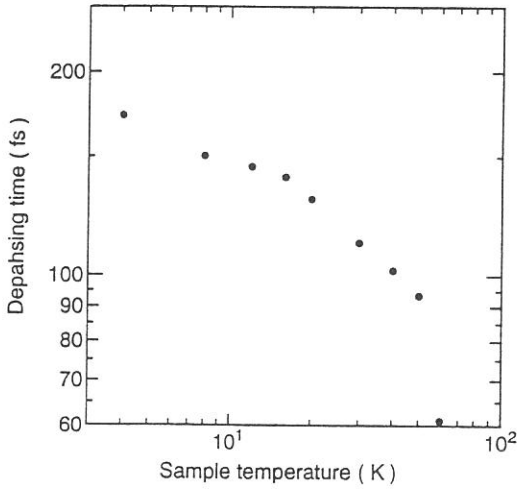

Fig.2 Autocorrelation trace of the beam trough the interferometer without bandpass filter. 1.5 mm thick quartz plates were inserted between the cube type beam splitter and the corner cube prisms in each arm of the interferometer,respectively.

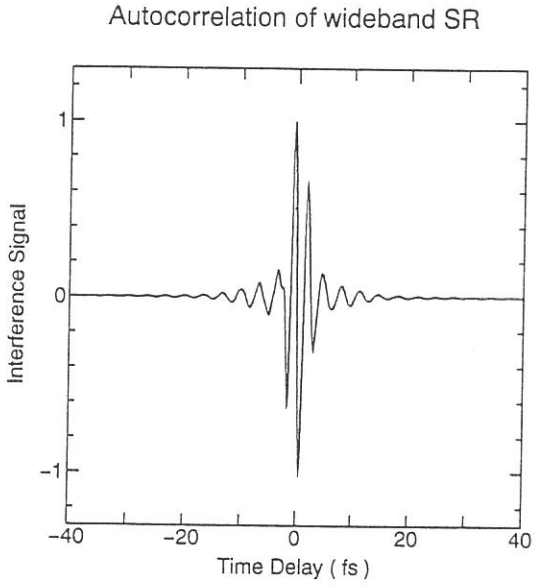

(BL-8A)

Imaging Soft X-ray Microscopy with Zone Plate, in Parallel Use of Optical Microscope for Wet Biospecimens in Air at UVSOR

A. Hirai[1], N. Watanabe[2], K. Takemoto[3], Y. Shimanuki[4], M. Taniguchi[5], E. Anderson[6], D.Attwood[6], D. Kern[7], S. Shimizu[8], H. Nagata[8], K. Kawasaki[4],S. Aoki[2],Y. Nakayama[1]and H. Kihara[3]

[1] *Department of Physics, Ritsumeikan University, Kusatsu, Shiga 525-77*
[2] *Institute of Applied Physics, Tsukuba University, Tsukuba 305*
[3] *Physics Laboratory, Kansai Medical University, Hirakata 573*
[4] *Department of Oral Anatomy, Tsurumi University, Yokohama 230*
[5] *Department of Physics, Naogoya University, Nagoya 464*
[6] *Lawrence Berkeley Laboratory, Berkeley, CA*
[7] *IBM Research Center, Yorktown Heights, NY*
[8] *Nikon Corp., Nishi-ooi, Shinagawa-ku, Tokyo 140*

We have been developing a soft X-ray microscope with zone plates at UVSOR BL8A[1]. This year, the system was improved at the following three points, which is, in principle, the same type as the Göttingen X-ray microscope at BESSY [2]. Figure1 shows the scheme of the soft X-ray microscope. First, a specimen stage was put in air gap, which was separated from condenser and objective chambers by SiN vacuum windows (thickness:0.1 μ m), as shown in Fig.2. This made possible to investigate a specimen without breaking the vacuum of the microscope. Second, an optical microscope was set to adjust and to prefocus a specimen. Third, a cooled CCD camera system (Astromed) was used as a detector.

The optical system was basically the same with the last type[1]. It consists of a filter (0.1 μ m SiN +55nm Ti), a central stop (2.4mm ϕ), a condenser zone plate (CZP, diameter: 4300 μ m, outermost zone width:0.25 μ m), a pinhole (20 μ m ϕ), a specimen, an objective zone plate (OZP, diameter: 50 μ m, outermost zone width:45nm) and a backside-illuminated CCD (SITe SI502A). The X-rays from the source was monochromatized and condensed at the pinhole by CZP. The first order radiation of CZP was adjusted at wave length of 3.8nm. However, as higher order radiations of CZP were detected more strongly, then imaging experiments were performed at 1.3nm (3rd order) or 0.94nm (4th order). Transmitted X-rays through a specimen were magnified by OZP and imaged at the CCD.

Resolution of 0.17 μ m was obtained at a wavelength of 1.3nm (Fig.3), whereas 0.47 μ m was obtained at 0.94nm. Both were estimated from rise widths of 25-75% intensities of Cu #2000 mesh image. A 0.14 μ m line and space pattern of a Ni Zone plate could be resolved at 0.94nm. These were worse compared with the theoretical resolution (55nm). This is probably due to low monochromaticity of illumination and the superposition of the higher order radiation images.

Several biospecimens, such as diatoms, collagen fibers, myofibrils, and blood cells, were observed. Wet biospecimens were put into the cell covered with thin polyimide foils supported by thick polyimide foils (Kapton tape). Figures 4 and 5 show images of a diatom and blood cells of ascidians in wet state at 0.94nm.

Acknowledgments

The authors are grateful for the help and encouragements from Prof. T.Kinoshita, Dr. A.Hiraya, Mr. K.Sakai, Mr. E.Nakamura and other staffs of the Institute for Molecular Science. We also thank to Dr.A.Yamamoto of Kansai Medical University and Dr.H.Michibata of Hiroshima University for their kind supply of ascidians.

References

[1] N.Watanabe et al., UVSOR Activity Report 1994, 194 (1995).

[2] P.Guttmann et al. Proc. SPIE 1741, 52 (1992).

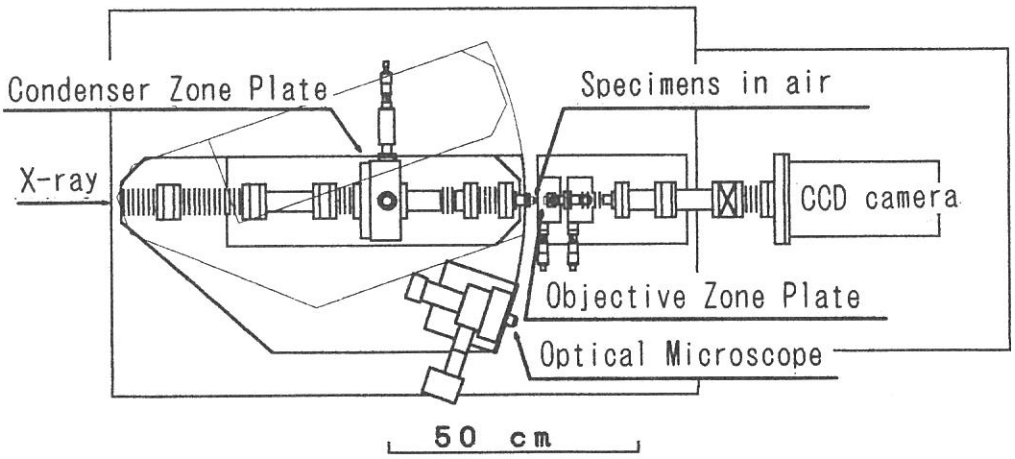

Fig1. Scheme of soft X-ray microscope.

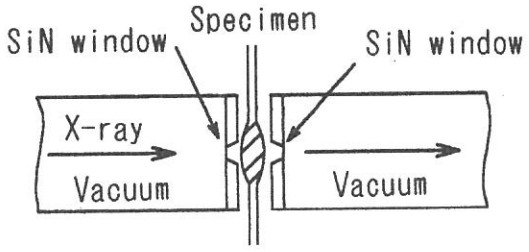

Fig.2 Vacuum camber around specimen.

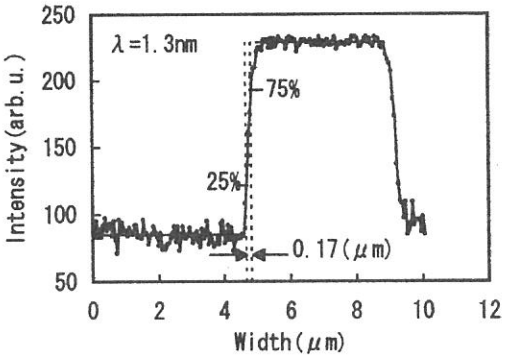

Fig3. Intensity distribution of Cu #2000 mesh at 1.3nm.

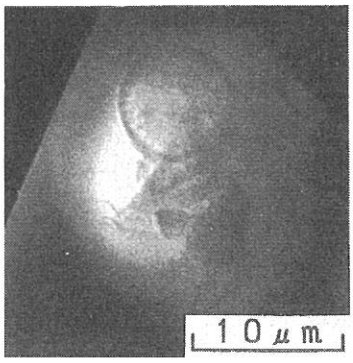

Fig.4 X-ray image of a wet diatom at 0.94nm (exposure time:10s).

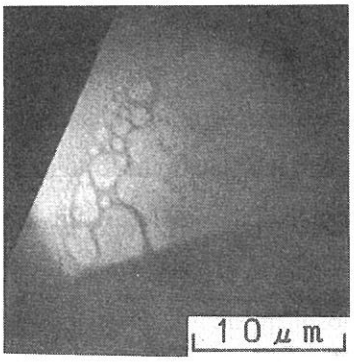

Fig.5 X-ray image of wet blood cells of ascidians at 0.94nm(exposure time:10s).

(BL8A)

Synchrotron radiation etching of diamonds

Eiji Ishiguro[a], Haruhiko Ohashi[b], Tomohiko Sasano[c], Takahiro Oguri[d] and Kosuke Shobatake[d]

[a]Physics Division, College of Education, University of the Ryukyus,
Senbaru, Nishihara-cho, Okinawa 903-01
[b]Institute for Molecular Science, Myodaiji, Okazaki 444
[c]Department of Applied Physics, Osaka City University, Sugimoto, Sumiyoshi-ku, Osaka 558
[d]School of Engineering, Nagoya University, Furo-cho, Chikusa-ku, Nagoya 464-01

Development of microfabrication technique for diamonds is important from a viewpoint of application of diamonds to electronic devices and micromachines. However, etching of diamonds is not easy, because of its high hardness and chemical inertness. We first observed the SR excitation etching of diamonds.

Synchrotron radiation emitted from a bending magnet of the 750 MeV UVSOR ring was used as an excitation source for etching. SR was concentrated on a sample in the reaction chamber by a toroidal mirror. The spot size of SR on the sample was about 2(vert.)mm × 4(hori.) mm. A nickel mesh with line spacing of 400 μ m and wire width of 40 μ m was used as a mask. It was located 5 mm away from the sample surface. Three different types of diamond; chemical vapor deposition(CVD), high pressure synthesized and natural diamonds were used as sample.

It is known that oxidation of diamonds starts at a temperature of about 500℃ in the atmosphere. In this study, experiments were performed below 400℃ to avoid the thermal oxidation. SR excitation etching of diamonds was found to occur even at a low temperature of -140℃ for the three types of diamonds. A micrograph of a surface etched at -140 ℃ was shown in figure 1. The pressure of O_2 was 0.1 torr and the dose 50,000 mA · min. We can see clearly the mask pattern on the surface. Figure 2 shows a profile of the etched surface measured with a surface profiler with a stylus of 12.5 μ m radius. We can see the line spacing of 400 μ m and the line width(FWHM) of 38 μ m. The slope of the line edges was fairly sharp and the height at the center of irradiated area was about 1.1 μ m. From the results shown above, it is obvious that only the surface irradiated by SR can be etched and therefore surface excitation plays an important role in SR etching of diamond in the O_2 atmosphere.

Irradiation of SR to diamond surfaces does not only give rise to etching but also graphitization, as seen from a dark portion in the irradiated surface in the photograph of figure 1. Probably an amorphous carbon layer might accumulate in this area. The carbon layer could be easily scraped away from the surface with something such as the tips of tweezers. In other words, carbon atoms of the diamond in the oxygen atmosphere are not always taken away as volatile products such as CO and CO_2 by SR irradiation, but a structural change to an amorphous carbon occurs under a circumstance. A graphitization was previously reported for ArF excimer laser etching of diamond in the vacuum[1]. In this case, a thermal

effect is considered to play an important role. On the other hand, the thermal effect can be neglected in our SR excited etching, because the photon flux is much smaller than that of the excimer laser. In fact, any changes were not observed in the diamond surface irradiated by SR in the vacuum. This suggests that existence of oxygen is essential to graphitization, as well as to etching in SR excitation and therefore the mechanism of etching and graphitization differs between the two processes of etching.

SF_6, XeF_2, and N_2 were also used as etchant, instead of oxygen gas. The samples irradiated in the atmosphere of these gases did not exhibit distinct evidences that etching occurred.

The authors would like to thank the staff of UVSOR for their support of our experiment.

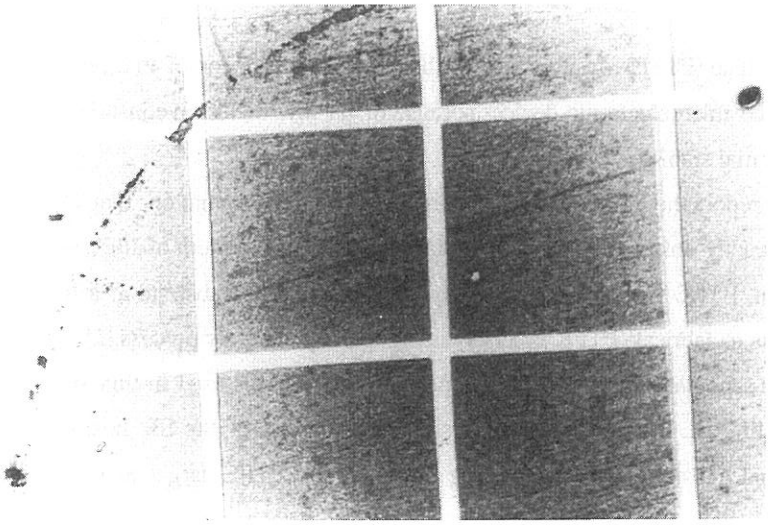

Figure 1. Micrograph of a diamond surface etched with the aid of SR excitation in O_2 atmosphere. The dark part around the center shows graphitization.

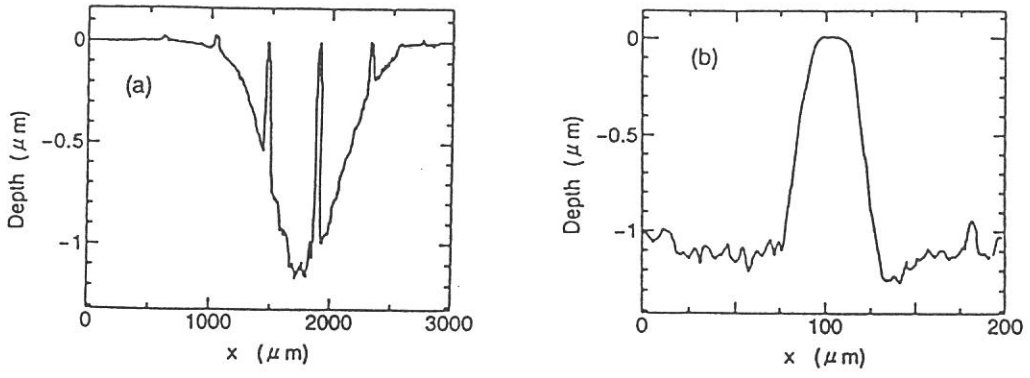

Figure 2. Profiles of the etched surface taken by a surface profiler with a stylus of 12.5 μm radius; (a) the whole profile of the etched surface and (b) a line profile in the center of the etched area.

REFERENCE

1.M.Rothschild,C.Arnone and D.J.Ehrlich, J.Vac.Sci.Technol.B4(1) (1988) 310.

(BL8A)

High-Rate Film Formation and micromachining of Polytetrafluoroethylene Using Synchrotron Radiation Ablation Process

Muneto INAYOSHI, Masanobu IKEDA, Masaru HORI, Toshio GOTO,
Mineo HIRAMATSU*and Atsunari HIRAYA**

Department of Quantum Engineering, School of Engineering, Nagoya University, Chikusa-ku, Nagoya 464-01
**Department of Electrical and Electronic Engineering, Meijo University, Tempaku-ku, Nagoya 468*
***Department of Material Science, Faculty of Science, Hiroshima University, 1-3-1 Kagamiyama, Higashihiroshima 739*

Polytetrafluoroethylene (PTFE) was expected as the parts for production of micromachine and as protective and insulating films in the microelectronic devices because of its low dielectric constant, high mechanical strength, and chemical and thermal stability.

In this study, we report the PTFE fabrication process using SR irradiation, that is, the SR ablation process. Heated PTFE was directly ablated by the SR irradiation with a fine pattern of high aspect ratio at an extremely high rate. In addition, PTFE film was successfully deposited on the substrate at a high rate. The SR ablation process will enable us to fabricate PTFE precisely using a completely dry process.[2]

Figure 1 shows a schematic diagram of the experimental apparatus used in this study. The experiments were carried out at beam line BL-8A of UVSOR. This system consists of the SR beam, an infrared (IR) lamp for heating the target and substrate, and a pumping system. The PTFE target and Si (100) substrate were set perpendicularly and parallel to the SR beam, respectively. The distance from the Si substrate to the SR beam was 5 mm. Micromachining and film formation of PTFE using SR ablation were carried out with the variation of PTFE target temperature in the range from 25 to 200 ℃.

PTFE was ablated by the SR irradiation effectively in vacuum. Figure 2 shows the ablation rate of PTFE as a function of target temperature. The PTFE can be ablated directly by the SR irradiation even at room temperature at a high rate of 14 μm/min·mA. The ablation rate of PTFE increases with increasing target temperature. At the target temperature of 200 ℃, the ablation rate reaches 35 μm/min·mA which is very high from a practical point of view.

Anisotropic ablation of PTFE was achieved by the SR irradiation. Figure 3 shows a photograph of a PTFE target of 5 mm thickness, in which a burr-free and smooth-edged hole has been produced by SR irradiation. The temperature of the PTFE target was 200 ℃. The ring current in this case was about 100 mA and it took less than 2 minutes to drill holes right through the target. Moreover, SR was irradiated above a 200-mesh of Ni as the contact mask set on the PTFE target at a dose of 200 min·mA and a PTFE temperature of 200 ℃. As a result, the shallow ablated pattern was produced in PTFE by SR irradiation. Area-selective ablation of PTFE applicable for micromachining was successfully achieved using SR ablation process.

A heated PTFE target was ablated by SR irradiation and PTFE thin films were deposited on a Si substrate placed normal to the target surface as shown in Fig. 1. The typical deposition rate of the PTFE film at the target and substrate temperatures of 100 ℃ was 2.6 μm/min for the typical ring current of 100 mA. This value is an

order of magnitude larger than that obtained using the conventional plasma polymerization method.[1] This indicates the usefulness of SR ablation process for high-rate deposition of PTFE thin films.

Figure 4 shows the FT-IR spectra of the PTFE target and the film deposited using SR ablation of PTFE at the dose of 50 min·mA and the target and substrate temperatures of 200 ℃. The absorption spectrum of the deposited film is similar to that of the PTFE target for the most part. As a result, the chemical structure of the deposited film was concluded to be similar to that of the PTFE target.

[1] L. Holland, H. Biederman and S. M. Ojha: Thin Solid Films 35 (1976) L19.

[2] M. Inayoshi, M. Ikeda, M. Hori, T. Goto, M. Hiramatsu and A. Hiraya:
Jpn. J. Appl. Phys. 34 (1995) L1675

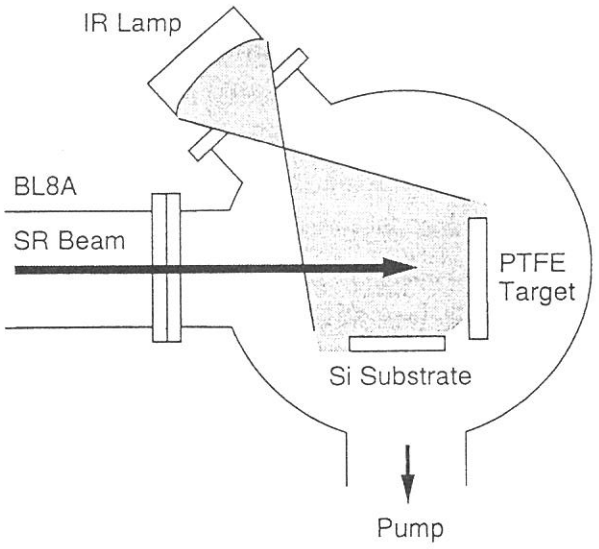

Fig. 1. Schematic diagram of experimental apparatus for the fabrication of PTFE by SR ablation.

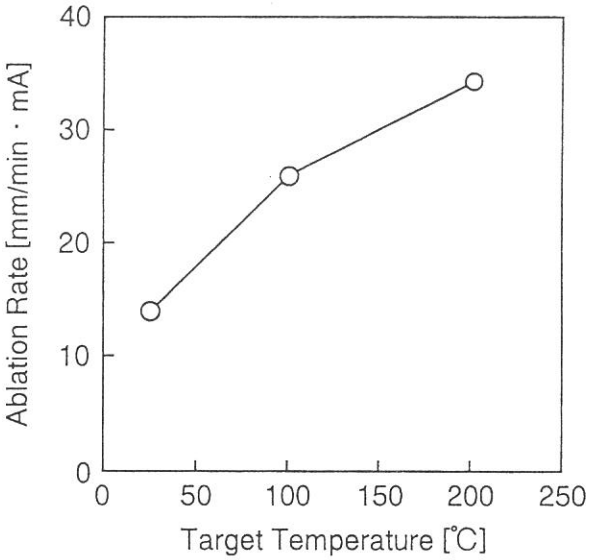

Fig. 2. Ablation rate of PTFE as a function of PTFE target temperature.

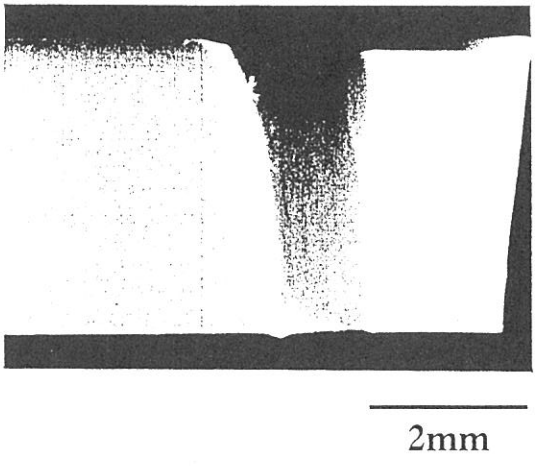

Fig. 3. Cross-sectional photograph of the PTFE target (5 mm thickness) ablated by SR irradiation at the PTFE temperature of 200℃ with a dose of 10000 min•mA.

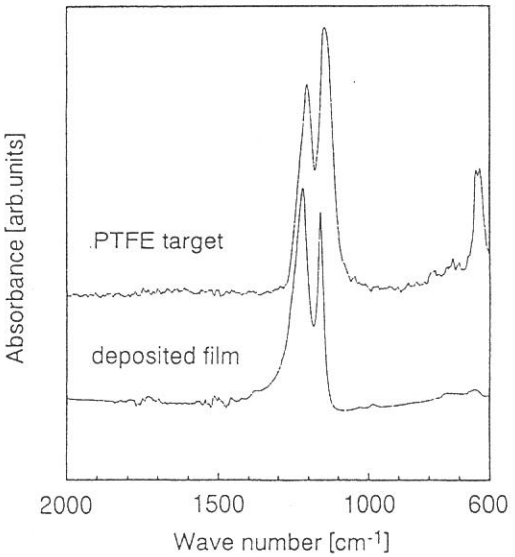

Fig. 4. FT-IR spectra of PTFE target and the film deposited using SR ablation at PTFE target and substrate temperatures of 200 °C.

(BL8A)

SOR Excited Etching of Si Wafer in CF_4 Gas Atmosphere

Shinzo Morita, Ryoichi Inanami and Toshihito Uchida
Nagoya university, CCRAST
Nagoya 464-01, JAPAN

There are several reports on fine pattern etching by SOR irradiation[1,2]. Although CF_4 gas are used generally in the etching process, it did not show any etching under the SOR irradiation perpendicularly to Si wafer. The reason why Si wafer was not etched under the SOR irradiation is not known. Recently, Nara *et.al.* reported the CF_4 gas was used for the etching under the negatively biased condition where the SOR was irradiated parallel to the surface of Si wafer[3]. But they did not explain the reason that Si wafer is not etched at positively biased conditions. In this experiment, the SOR was irradiated perpendicularly to the Si wafer in CF_4 gas and effect of bias on the process was discussed.

The apparatus used for the experiments is shown schematically in Fig. 1, which is equipped along the beam line of BL8A from UVSOR. The SOR was irradiated to the substrate perpendicularly through a channel with a hole of 3 mm diameter. CF_4 gas was introduced into the reaction chamber through a mass flow controller. The Si wafers used as a substrate were Sb doped n-type with (100) orientation and resistivity of 0.01 – 0.02 Ω·cm. After removing native oxide by dipping into HF solution, the Si wafer was mounted on a sample holder which is isolated electrically and a bias voltage was applied on the holder. A Cu mesh sheet of 100 lines/inch was placed on the Si wafer as a mask.

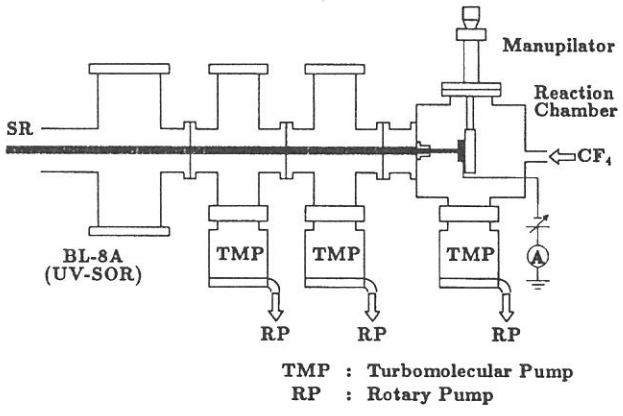

Fig.1 Experimental apparatus for SOR excited etching of Si wafer.

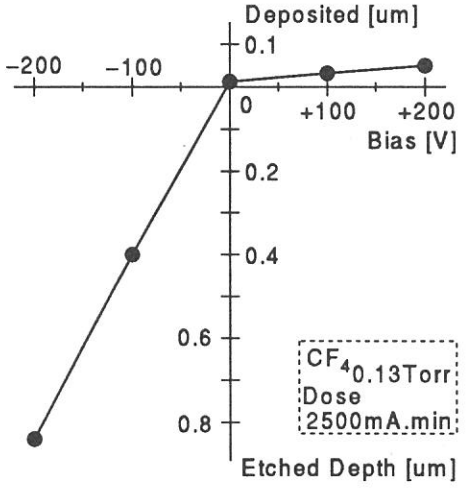

Fig.2 Etched depth and deposited thickness of film as a function of applied bias voltage on Si wafer.

The Si wafer was exposed to the SOR at a dose of 5561 mA·min, where CF_4 gas was introduced at a pressure of 0.16 Torr. The deposited structures on the Si wafer was observed by an optical microscope. When Si wafer was kept at the zero bias condition, convex deposited film structures were obtained at the Cu mesh windows. But the concave etched patterns were found under the −200 V bias condition. When a positive bias was applied on the Si wafer, the convex pattern became more clearer because of thicker film deposition. But the etching was observed when the bias voltage was changed from positive to negative.

The deposited film thickness and etched depth were plotted against the bias from −200 to +200 V at a dose rate of 2500 mA·min. and a pressure of 0.13 Torr in CF_4 gas atmosphere in Fig. 2. And the etched depth is increased with increasing of the CF_4 gas pressure. The deposited thickness and etched depth were also proportional to the bias voltage. These phenomena are caused on the fact that the process is referred to the total number of species.

It was confirmed that the main species of the deposited material were C and F atoms from an ESCA measurement. It will be concluded that carbonaceous film was deposited only at the positively biased condition. At the zero bias, the Si wafer was considered to be positively biased because of secondary electron emission by the excitation of SOR irradiation. The self biased positive voltage will be maintained by the resistivity of Si wafer and/or negative ion sheath near the surface even if the substrate is grounded. This suggests negative ion is predominant species for the deposition. It is known that the major negative ion is F^- in CF_4 plasma[4], which will not contribute for the deposition. In a low energy electron impact on CF_4, CF_4^- and CF_3^- are known as a stable ion species[5]. Therefore, CF_4^- and CF_3^- are possible candidates of negative ions for the deposition of carbonaceous film.

The etching is expected to be performed by a positive species. Several positive ions, mostly CF_3^+, reported to be formed in CF_4 gas under SOR irradiation[3]. Therefore, Si wafer etching will be referred to positive ion like as CF_3^+ and/or others.

In this experiment, the appropriate condition for the etching of Si wafer was found successfully, which was negatively biased condition. The deposition was occurred at the grounded and positively biased conditions, which suppress the etching process. At the next step, we will try to fabricate fine pattern below sub-micron width by using electron beam resist as an etching mask.

REFERENCES

[1] T.Urisu, H.Kyuragi: *J. Vac. Sci. Technol.*, **B5**, pp1436 (1987)

[2] N.Hayasaka, A.Hiraya, K.Shobatake: *Jpn. J. Appl. Phys.*, **26**, ppL1110 (1987)

[3] Y.Nara, Y.Sugita, K.Horiuchi, T.Ito: *J. Photopolymer Sci. Technol.*, **6**, pp617 (1993)

[4] A.Kono: *JSPS 153rd Committee on Plasma Science and Materials 17th Study Meeting*, pp2 (1992)

[5] G.J.Verhaart, W.J.Van Der Hart, H.H.Brongersma: *Chem. Phys.*, **34**, pp161 (1978)

Si-L Absorption Spectra of LiF/Si/LiF Multilayers

Takeo EJIMA, Katsumi OUCHI, and Makoto WATANABE
Research Inst. for Scientific Measurements, Tohoku Univ., Sendai 980-77, JAPAN

It is known that Si layers deposited on alkali halides have a non-crystalline structure except for NaCl, but it is unknown whether the structure is the usual amorphous type or not [1]. In this study, we investigated the structure of Si layers desposited on LiF by comparing their Si-L absorption with those of crystalline and amorphous Si previously reported [2]. The deposited Si layers studied here were overcoated with a 20 Å LiF film. The Si-L absorption spectra were obtained by total photoelectron yield measurements, changing the angle of incidence using the constant deviation monochromator on BL8B1.

A typical result is shown in Figure 1. The layer consisted of LiF(20Å), Si(20Å), and LiF(50Å), deposited on a Si wafer. At 0° angle of incidence, the Si-L absorption rises at 99.5eV. This spectrum is different from that of crystalline Si but similar to that of porous Si [3]. However, when the angle of incidence exceeds 60°, the profile changes remarkably and becomes similar to that of crystalline Si, showing clear spectral structure in comparison with that of crystalline Si. At present, we believe that the Si layers in this study are anisotropic, and the structure parallel to the LiF layer is similar to that of porous Si, but the structure perpendicular to the LiF layer is similar to that of crystalline Si.

The above result is preliminary, because we have yet to check the reproducibility of our results with different Si layers.

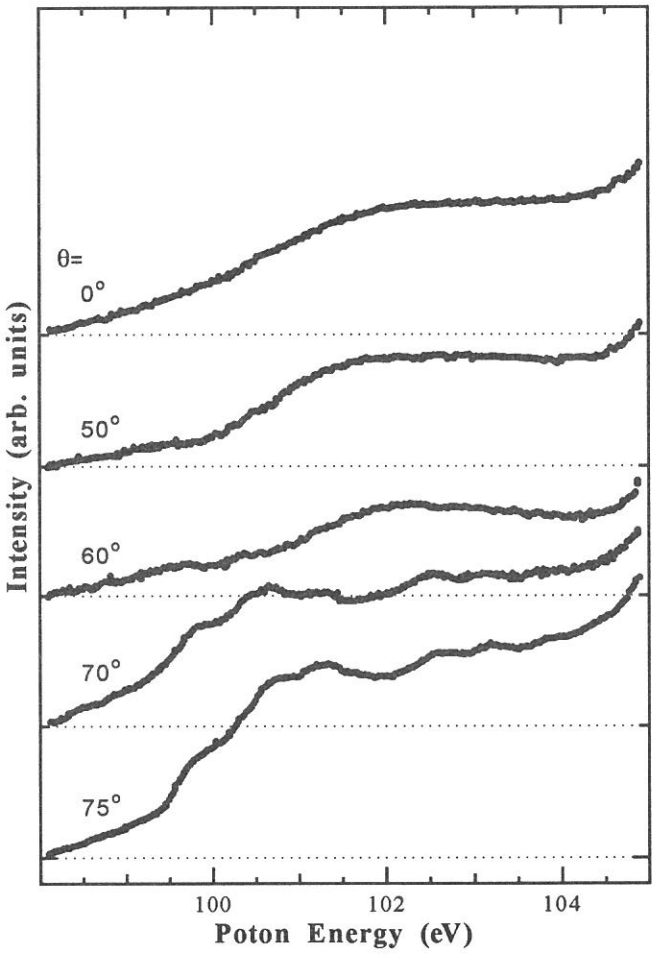

Figure 1. Si-L absorption spectra of LiF20Å/Si20Å/LiF50Å multilayers as a function of angle of incidence.

References

[1] for example; Y. Shiraki, J. Vac. Sci. Technol. B3(1985)725, G. Shimaoka and S. C. Chang, J. Vac. Sci. Technol. 9(1971)235.

[2] F. C. Brown, R. Z. Bachrack, and M. Skibowski, Phys. Rev. B15(1977)4781.

[3] K. Inoue, K. Maehashi, and H. Nakashima, Jpn. J. Appl. Phys. 32(1993)L361.

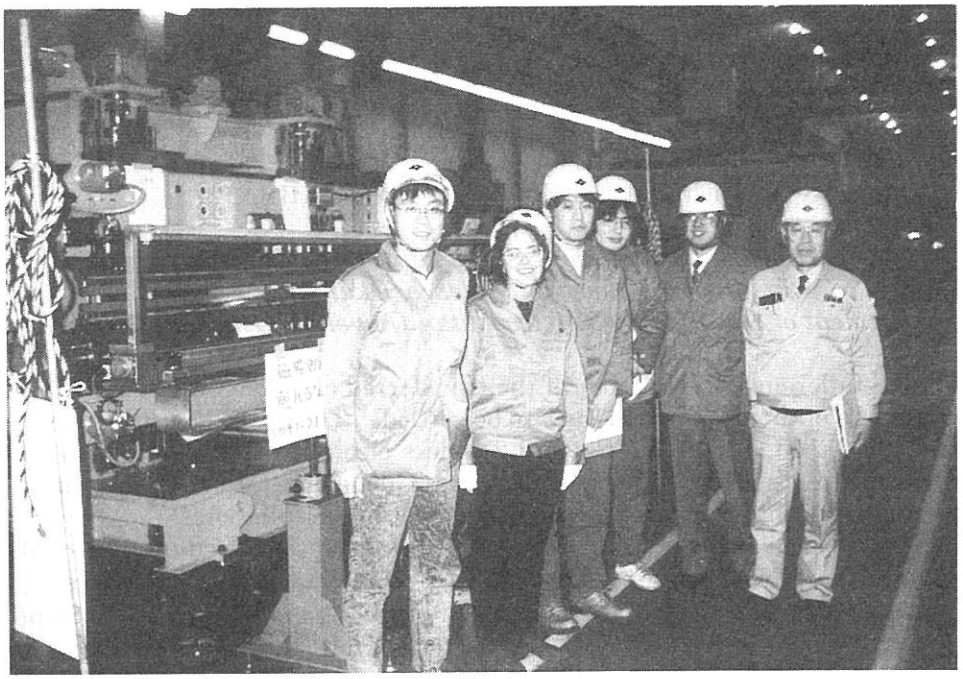

Prof. H. Hama, Mr. K. Kimura, and Dr. M. Hosaka (left to right) are standing beside a new helical undulator at the examination stage of the construction. Prof. M. E. Cuoprie (Lure in France) had a chance to join them during her stay in UVSOR.

Miss N. Onitake (secretary) is enjoying the welcome barbecue party together with Mr. J. Yamazaki.

PHOTOELECTRON SPECTRA OF METAL FULLERENES; GdC_{82} AND La_2C_{80}.

Shojun HINO, Kazunori UMISHITA, Kentaro IWASAKI, Takafumi MIYAZAKI*, Koichi KIKUCHI**, and Yohji ACHIBA**

Department of Engineering, Chiba University, Chiba,263 Japan
** Institute for Molecular Science, Okazaki 444 Japan*
*** Department of Science Tokyo Metropolitan University, Hachioji, Tokyo, Japan*

In metal fullerenes, the number of the transferred electrons from the metal atom to the fullerene cage is one of the important issues to be settled. Theoretical calculations [1] predicts 3 electron transfer in La@C_{82} and La_2@C_{80} and 2 or less electron transfer in Sc@C_{82}, Eu@C_{82} and Gd@C_{82}. Photoelectron spectra of metal fullerenes, GdC_{82} and La_2C_{80} have been measured to estimate the number of the transfered electrons in these metal fullerenes.

The UPS measurements on fullerenes were performed on vacuum deposited films. An attempt to obtain uniform evaporated films of GdC_{82} and La_2C_{80} was unsuccessful, since they won't sublime up to 750 ℃ even in an ultrahigh vacuum condition. It was found that they decomposed after heating at that temperature. Alternatively, the specimen films were prepared from solutions of the metal fullerenes. The solution was dropped on to a gold coated substrate disk and the solvent was allowed to dry to form films in an ambient atmosphere. The films were heat-treated in an ultrahigh vacuum preparation chamber attached to a photoelectron spectrometer to remove the contamination. After the heat treatment the amount of fast electrons has increased and that of the secondary electrons has decreased as is shown in Fig. 1. Heating at 200 ℃ is good enough to disclose the fast electrons of 10 -15 eV kinetic energy and 300 - 400 ℃ seems to be sufficient for obtaining the reasonable spectra. The spectra of GdC_{82} and La_2C_{80} shown in the following were recorded after 300 ℃ and 400 ℃ heat treatment, respectively.

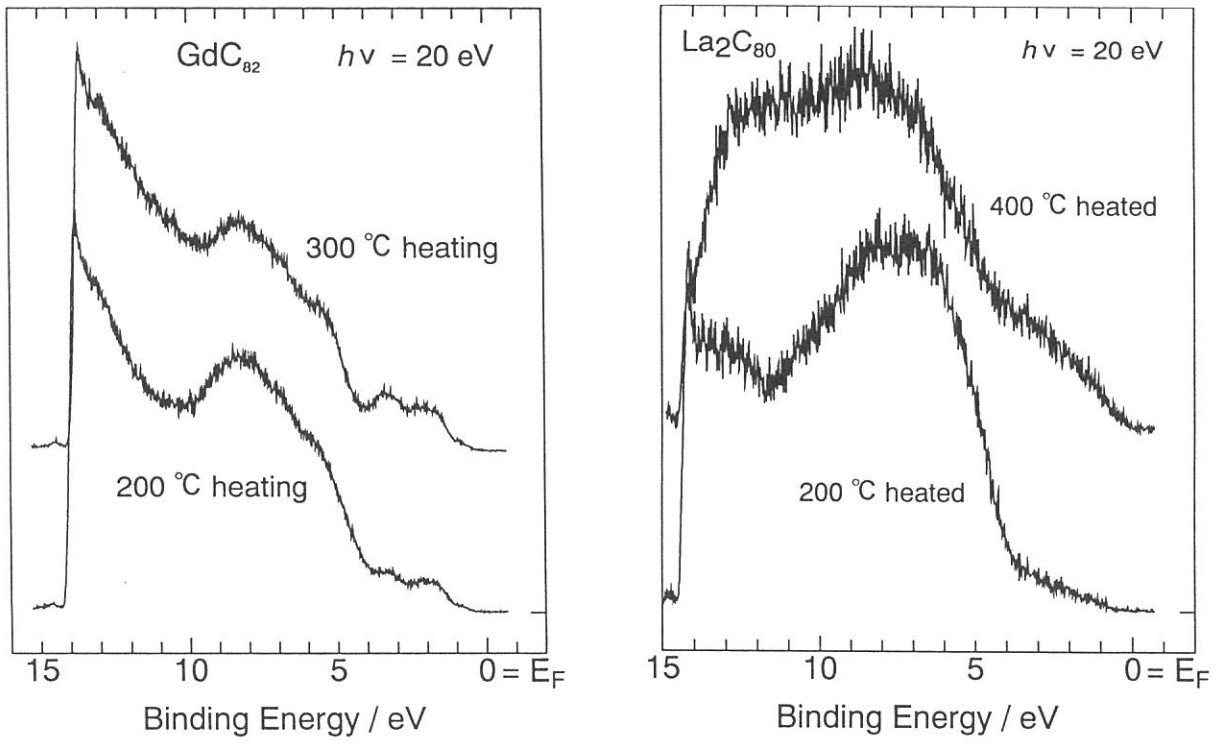

Fig. 1. The effect of heat-treatment of the UPS of metal fullerenes. The incident photon energy is 20 eV. The result of GdC_{82} (left) and the result of La_2C_{80} (right).

Figure 2 shows the UPS of GdC_{82} and La_2C_{80} obtained with the 20 eV incident photon energy. The spectra of C_{82} [2] and LaC_{82} [3] are also shown for comparison. The spectrum of GdC_{82} is rather dull compared with the spectra of LaC_{82} and C_{82}, which must be due to the secondary electrons induced by the contamination. Apart from this point the spectra of GdC_{82}, LaC_{82} and C_{82} are analogous. A difference among these spectra is an existence of structure N in the UPS of metal fullerenes. A difference spectrum between the UPS of GdC_{82} and C_{82} indicates 3 electron transfer from the metal atom to the fullerene cage, as is observed in LaC_{82}. That is, the electronic structure of GdC_{82} can be described formally as $Gd^{3+}C_{82}^{3-}$. This is against the theoretically predicted amount of the transferred electrons [1], but is for the number deduced from an ESR measurement [4].

The spectral edge of GdC_{82} and LaC_{82} locate at 0.3 eV. That is, they are not metallic but semi-conductive, although they are open shell molecules. This suggest an strong interaction between the adjacent metal fullerene molecules to form pairs or dimers so that the total energy of the solid becomes low. If the strong interaction is limited within the dimers, the contamination can be removed easily. Dimer formation is also able to explain low vapor pressure (small sublimation rate) at high temperature. From the deduction described above, LaC_{82} and GdC_{82} might have a relatively weak interaction force between the molecules (or rather dimers) in solid.

The spectrum of La_2C_{80} is quite different from those of other fullerenes or metal fullerenes, but resembles that of vitreous carbon [8]. The spectrum begins at the Fermi level and shows no sharp structure in whole valence band region that is characteristic to fullerene. This could be either due to its intrinsic electronic structure or due to the contamination of the film. The latter is able to be excluded from the reason, since the fastest electrons that is the most vulnerable to the contamination are observed clearly in the spectrum. Therefore, our present result seems to reflect the intrinsic electronic structure of La_2C_{80} with a high possibility. However, minute discussion on the number of the transferred electron is difficult because of the dullness of the spectrum.

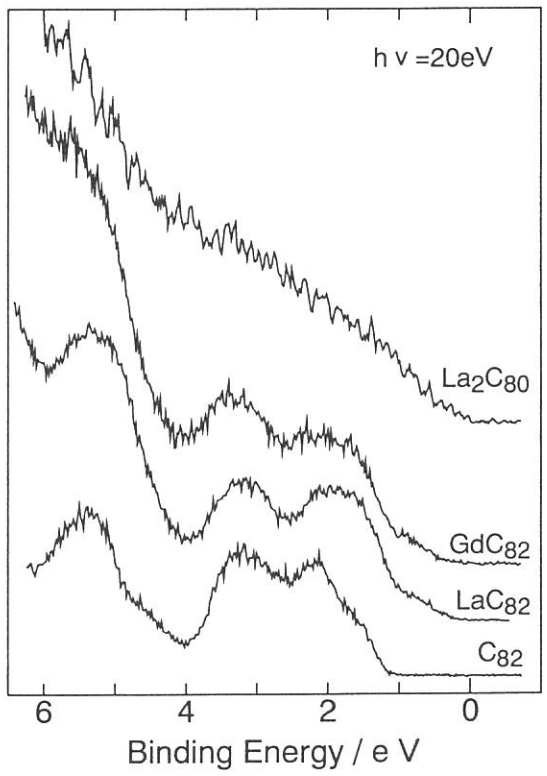

REFERENCES

1. S. Nagase et al., Proceedings of the Electrochemical Society, Reno, U. S. A., 1995 in press and references there in.
2. S. Hino et al., Phys. Rev., B48 (1993) 8418.
3. S. Hino et al. Phys. Rev. Lett., 71 (1993) 4261.
4. T. Kato, Proceedings of the Electrochemical Society, Reno, U. S. A., 1995, in press.
5. G. K. Wertheim and D. N. E. Buchman, Phys. Rev. B50 (1994) 11070.

Fig. 2. The hν = 20 eV spectra of metal fullerenes, LaC_{82} [2], GdC_{82}, and La_2C_{80}. The spectrum of C_{82} [2] is also shown for comparison.

BL8B2

Angle-resolved UPS of thin films of BTQBT on MoS_2: Determination of molecular orientation by quantitative analysis of photoelectron angular distribution and LEED

N. Ueno[a,b], K. Kamiya-Okudaira[a], A. Kitamura[a], T. Miyamae[b,c], Y. Harada[a], S. Hasegawa[c], H. Ishii[c], H. Inokuchi[c], T. Miyazaki[d] and K. Seki[e]

[a]*Department of Materials Science, Faculty of Engineering, Chiba University, Chiba 263*
[b]*Graduate School of Science and Technology , Chiba University, Chiba 263*
[c]*Institute for Molecular Science, Okazaki 444*
[d]*Department of Chemistry, Faculty of Science, Toyama University, Toyama*
[e]*Department of Chemistry, Faculty of Science, Nagoya University, Nagoya 464-01*

The angle-resolved ultraviolet photoelectron spectroscopy (ARUPS) using synchrotron radiation is useful to investigate the geometrical structure of the ultrathin films as well as the electronic structure. For the study of the geometrical structure of the thin films of functional organic molecules, ARUPS is very powerful, since it introduces much less radiation damages into organic thin films.

In the previous work, we demonstrated that the take-off angle (θ) dependencies of the photoelectron intensity from the second band of thin films of bis(1,2,5-thiadiazolo)-*p*-quinobis (1,3-dithiole) ($C_4H_4S_6N_4$) (BTQBT) on an cleaved HOPG graphite surfaces are excellently explained by calculated angular distributions using independent-atomic-center approximation [1] combined with molecular orbital calculation (IAC/MO) [2,3]. However, the observed θ dependence for the top valence band [highest occupied molecular orbital (HOMO)] showed insufficient agreement with the calculated results.

We recently realized to analyze observed photoelectron angular distributions from thin films of large organic molecules using the single scattering approximation [4] combined with molecular orbital calculation (SS/MO) [5,6]. In the present study, we analyzed the observed azimuthal angle (ϕ) dependence of the HOMO band of ultrathin films of BTQBT deposited on MoS_2 single crystal surface using the SS/MO method, and could determined the two-dimensional structure of the films.

ARUPS measurements were carried out at the beam line BL8B2 of the UVSOR at Institute for Molecular Science. The take-off angle (θ) and azimuthal angle (ϕ) dependencies of photoelectrons were measured at normal incidence [incidence angle of photon α=0°] and at hν=40 eV. The angle ϕ was measured from one of the three equivalent surface crystal axes ($[11\bar{2}0]$, $[1\bar{2}10]$ and $[\bar{2}110]$) of MoS_2

We used both the IAC/MO and SS/MO methods to calculate the photoelectron angular distribution. In the present calculations, the phase shifts and radial matrix elements were calculated using Muffin-tin potential [7]. The theoretical formula of the SS/MO approximation were described in Refs. 5 and 6.

Figure 1 shows the comparison between the observed and calculated θ dependencies for the HOMO band of BTQBT thin films (4 Å) grown on MoS_2 surfaces. The dotted and solid curves correspond to the calculated results with the IAC/MO and SS/MO, respectively. Both calculation were performed for flat-lie orientation of the molecules and using MNDO wave function for the initial state. Further, the calculations were carried out by averaging over the 6-hold rotation

of azimuthal angle owing to the rotational symmetry of MoS_2 surface. Although the IAC/MO does not reproduce the observed results, the SS/MO result agrees well with the observed θ dependence. Figure 2 shows the comparison between the observed and calculated ϕ dependencies of the HOMO band for flat-lie molecular orientation. In this calculation, we averaged ϕ patterns corresponding to six two-dimensional domains of BTQBT of different azimuthal orientations which were determined by LEED. Due to this averaging, the difference of the ϕ patterns calculated by the IAC/MO and SS/MO for the single domain disappeared. From these results, the two dimensional orientation of BTQBT molecules on MoS_2 single crystal surface was determined as shown in Fig. 3.

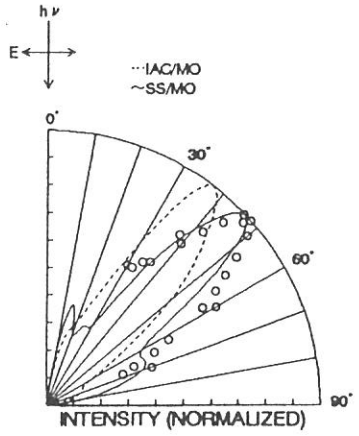

Fig. 1 Comparison between observed and calculated θ dependencies of the photoelectron intensity of the HOMO band of BTQBT(4Å) on MoS_2. ○; experimental results. ···; calculated by IAC/MO. −; calculated by SS/MO. The calculations were performed for flat-lie molecular orientation.

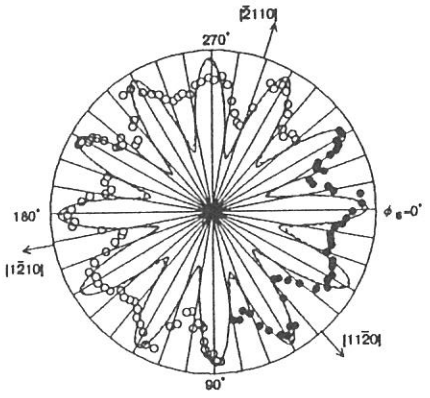

Fig. 2 Comparison between observed and calculated ϕ dependencies of photoelectron intensity of the top π band of BTQBT(4Å) on MoS_2. The experimental results for origin-al ϕ range (●), and the results shifted by 120° and 240° (○) are shown. Three arrows represent the three equivalent crystal axes of the MoS_2 surface. ···; calculated by IAC/MO. −; calculated by SS/MO. The calculations were performed for flat-lie molecular orientation.

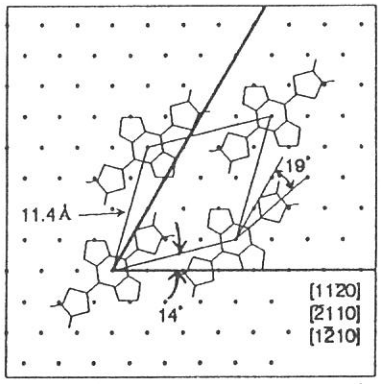

Fig. 3 Two dimensional structure of BTQBT molecules on MoS_2 determined by ARUPS and LEED.

REFERENCES

1. W. D. Grobman, Phys. Rev. B, **17** 4573 (1978).
2. S. Hasegawa, S. Tanaka, Y. Yamashita, H. Inokuchi, H. Fujimoto, K. Kamiya, K. Seki, and N.Ueno, Phys. Rev. B, **48** 2596 (1993).
3. N. Ueno, K. Suzuki, S. Hasegawa, K. Kamiya, K. Seki, and H. Inokuchi, J. Chem. Phys., **99** 7169 (1993) .
4. A. Liebsch, Phys. Rev. B, **13** 544 (1976).
5. S. Hasegawa, K. Seki, H. Inokuchi, and N. Ueno, J. Electron Spectr. Relat. Phenom. in press.
6. N. Ueno, *ibid* in press.
7. D. Dill and J. L. Dehmer, J. Chem. Phys., **61** 692 (1974).

(BL8B2)

ANGLE-RESOLVED ULTRAVIOLET PHOTOELECTRON SPECTROSCOPY OF ORIENTED FILM OF MODEL COMPOUND OF POLY(*p*-PHENYLENE): WAVE NUMBER(*k*)-CONSERVATION AND *k*-BLURRING IN A SYSTEM WITH SMALL NUMBER OF REPEATING UNITS

Hisao Ishii, S. Narioka[a], K. Edamatsu[b], K. Kamiya[c], S. Hasegawa, T. Ohta[d], N. Ueno[c], and K. Seki[a]

Institute for Molecular Science, Myodaiji, Okazaki 444, Japan
[a]*Department of Chemistry, Faculty of Science, Nagoya University, Chikusa-ku, Nagoya 464-01, Japan*
[b]*Department of Materials Science, Faculty of Science, Hiroshima University, Kagamiyama, Higashi-Hiroshima 724, Japan*
[c]*Department of Materials Science, Faculty of Engineering, Chiba University, Inage-ku, Chiba 263, Japan*
[d]*Department of Chemistry, Faculty of Science, The University of Tokyo, Hongo, Bunkyo-ku, Tokyo 113, Japan*

Recently short oligomers of various π conjugated polymers have attracted much attention because of their definite molecular weight, better crystallinity, and possibility of preparing well ordered oriented thin films by vacuum evaporation. The elucidation of the difference of the electronic structure between a polymer and its oligomer is indispensable for utilizing oligomers as device materials. The electron wave function of polymer can be regarded as 1-dimensional Bloch wave characterized by wave number (k) as a good quantum number. On the other hand, in oligomers, degradation of translational symmetry of the system due to small number of repeating units deviates the wave function from Bloch wave. So it is an interesting question how many repeating units are necessary for the validity of wave number as a good quantum number. This can be experimentally investigated, using angle-resolved ultraviolet photoelectron spectroscopy (ARUPS), by examining k-conservation rule in photoemission process where the value of k for the excited electron is conserved between the initial and final states. *p*-Sexiphenyl (6P), consisting of six benzene rings, is a suitable compound for examining whether k is a good quantum number even in a system with smaller number of repeating units.

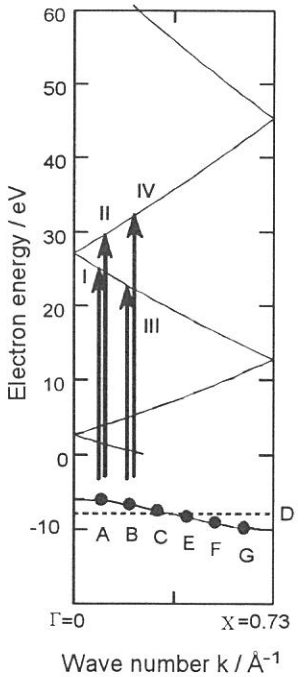

Fig.2. The energy-band dispersion along the molecular axis (Γ-X) for 6P and PPP.

We prepared oriented 6P thin films by vacuum evaporation on heated Ag substrates at about 423K. The results of Infrared reflection-absorption (IR-RAS) spectroscopy, x-ray diffraction, and selection rules of ARUPS indicated that 6P molecules are oriented with their molecular axes vertical to the substrate surface. The experimental details were reported elsewhere [1].

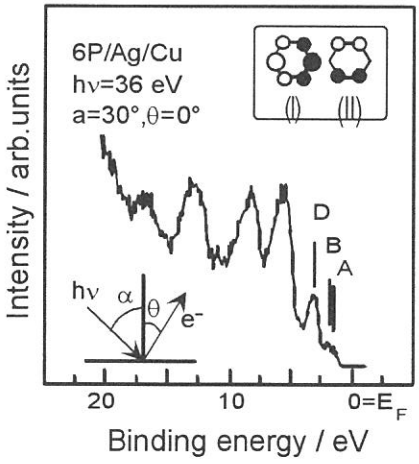

Fig.1 Normal emission UPS spectra of 6P film.

Figure. 1 shows normal-emission ARUPS spectra of 6P films. In the following we concentrate on the π -derived peaks in the lowest binding energy region of 0~4eV, since their assignments are well established[2] and suitable for examining k conservation rule. On the basis of Hückel approximation we plot the $E = E(k)$ relation in the Brillouin zone (Γ-X) for poly(*p*-phenylene)(PPP) (solid line) and 6P (filled circles A to G) in the lower part of figure 2. The split π states of 6P are on the way of forming the continuous $E(k)$ relation in PPP. The two uppermost states of 6P with $k=\pi/7a$ and $k=2\pi/7a$ (a: unit cell size) correspond to peaks A and B in Fig.1, respectively. In the upper part of Fig. 2, the dispersion relation for the vacant states is plotted assuming free-electron-like final states where we assumed a value of V_0=5.5eV. When we assume k-conservation at photoexcitation in Fig. 2, the transitions I-IV indicated by the arrows are expected,

with excitation energies hν=31.1eV and 35.7eV for A and hν=29.5eV and 38.8eV for B, respectively.

In Fig. 3, the constant-initial-state (CIS) spectra of normal emission for peaks A, B and D are shown in the photon energy region between 20 and 45eV. The normal emission of peaks A and B is enhanced at hν=28~40eV. On the other hand, the intensity of peak D gradually and almost monotonically decreases with hν. The expected enhancement of intensity at 30~40eV is consistent with the observed results of hν dependence of peak intensities of A and B in Fig.3, suggesting that the k-conservation rule still holds in 6P. This demonstrates that k vector serves as a reasonably good quantum number even for a system of only 6 repeating units. However, there remains a question: why are the peaks A and B continuously enhanced over a wide range of hν=28~40eV, in contrast to the expected enhancement only at specific photon energies mentioned above? For clarifying the above point, we formulate the photoemission intensity. We summarize the results because of the limit of space. The detailed derivation was described elsewhere [1]. The initial state wave function of the system consisting of n benzene rings $\Psi(\mathrm{k},\mathbf{r})$ can be expressed as Bloch states in tight binding approximation,

$$\Psi(k,\mathbf{r}) = \frac{1}{\sqrt{N}} \sum_{j=1}^{N} e^{ik\mathbf{R}_j} \phi(r - \mathbf{R}_j), \tag{4}$$

where ϕ is Wannier function, and $\mathbf{R}_j$ is position vector of each benzene ring. With this initial state wave function, photoemission intensity I can be expressed as

$$I \propto \eta^2 (\mathbf{A}_0 \cdot \mathbf{k}_f)^2 \left| s(k,\mathbf{k}_f) \right|^2 \left| f(\mathbf{k}_f) \right|^2 \tag{5}$$

Here $s(k,\mathbf{k}_f)$ is the structure factor corresponding to the arrangement of the repeating units expressed as

$$s(k,q) = \frac{1}{\sqrt{N}} \sum_{j=1}^{N} e^{i(\mathbf{k}-q)\mathbf{R}_j}, \tag{6}$$

and $f(\mathbf{k}_f)$ is the Fourier transformation of $\phi(\mathrm{r})$

$$f(\mathbf{q}) = \frac{1}{(2\pi)^3} \int e^{-i\mathbf{q}\cdot\mathbf{r}} \phi(\mathbf{r}) d\mathbf{r}. \tag{7}$$

For the present case of normal emission, k_f can be expressed as $\mathrm{k}_f=(0,0,\mathrm{k}_f)$, and $\mathrm{s}(\mathrm{k},\mathrm{k}_f)$ becomes, using $\Delta \equiv (\mathrm{k}-\mathrm{k}_f)a$ (a is the spacing between neighboring benzene rings),

$$\left| s(k,k_f) \right|^2 = \frac{1}{N} \frac{\sin^2\left[\frac{N\Delta}{2}\right]}{\sin^2\left[\frac{\Delta}{2}\right]} \tag{8}$$

For a large N, this becomes very small unless $\Delta=2\pi l$, where l is an integer. This corresponds to the wave number conservation rule in perfectly periodic system leading to the vertical transitions shown by the arrows in Fig. 2. In Fig. 4, we show the hν dependence of $\mathrm{q}^2|\mathrm{s}(\mathrm{k},\mathrm{q})|^2$ for N=6 and a=4.3Å in the range of the hν region in Fig. 3. The solid and broken lines are for the HOMO and the next-HOMO, respectively. We see that the position and the width of enhancement correspond well with the observed spectra in Fig. 3. The above discussion successfully gave qualitative description to the effect of k blurring. The detailed discussion including the physical meaning was described elsewhere [1].

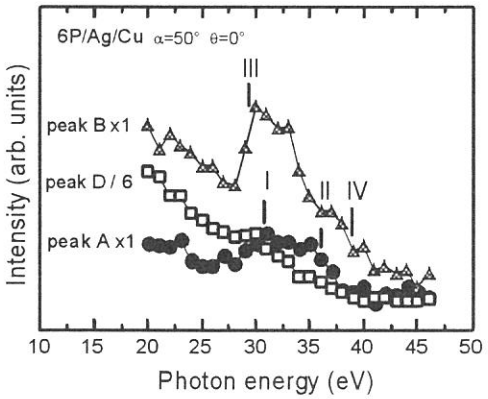

Fig.3. Constant-initial-state (CIS) spectra for normal emission of 6P for peaks A,B and D in Fig.1.

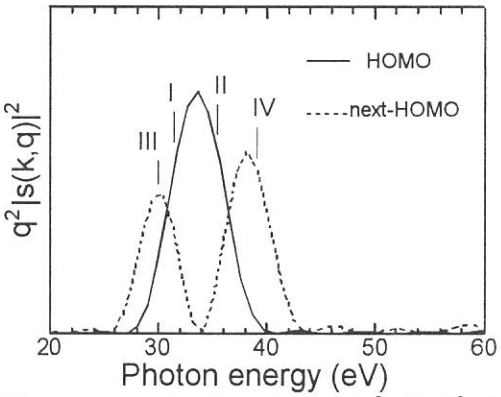

Fig.4. Photon energy hν dependence of $\mathrm{q}^2|\mathrm{s}(\mathrm{k},\mathrm{q})|^2$ of the HOMO (solid line) and next-HOMO (dashed line) of 6P by eq.(8), where N=6 and a=4.3 Å.

REFERENCES

1. S.Narioka, H.Ishii, K.Edamatsu, K.Kamiya, S.Hasegawa, T.Ohta, N.Ueno, and K.Seki, Phys. Rev. B, 52,2362(1995).
2. K. Seki, U.O.Karlsson, R.Engelhardt, E.E.Koch, and W.Schmidt, Chem. Phys. 91, 459 (1984).

(BL8B2)

THE ELECTRONIC STRUCTURE OF PORPHYRIN/METAL INTERFACES STUDIED BY ULTRAVIOLET PHOTOELECTRON SPECTROSCOPY

D. Yoshimura[a], H. Ishii[a,b], S. Narioka[a], M. Sei[a], T. Miyazaki[a], Y. Ouchi[a], S. Hasegawa[b]
Y. Harima[c], K. Yamashita[c] and K. Seki[a]

[a] *Department of Chemistry, Faculty of Science, Nagoya University, Chikusaku, Nagoya 464-01*

[b] *Institute for Molecular Science, Myodaiji, Okazaki 444*

[c] *Faculty of Integrated Arts and Sciences, Hirosima University, Kagamiyama, Higashi-Hiroshima 724*

Recently the applications of various organic-semiconductors to electric devices have been extensively studied. The study of electronic structure of organic-semiconductor/metal interface is indispensable for understanding and refining the performance of such devices. However, there have been few studies which directly observed the interfacial electronic structure. In most studies on organic devices, the interfacial electronic structure has been estimated with the traditional model assuming either that (a) vacuum level alignment occurs at the interface and energy levels in space charge layer bend to achieve Fermi level alignment (Mott-Schottky rule), as in the case of ideal inorganic-semiconductor/metal interface (Fig.1a), or that (b) vacuum level of organic layer coincides with that of metal without band bending, as in the case of ideal insulator/metal interface (Fig.1b). The latter model is often employed assuming a common vacuum level as the energy of a rest electron at the interface. However, the validity of these traditional models for organic-semiconductor/metal interface has not yet been well clarified. We reported the electronic structure of the interface between 5,10,15,20-tetraphenylporphynatozinc(ZnTPP, Fig.2: M=Zn, R=C_6H_5) and metals by ultraviolet photoelectron spectroscopy (UPS)[1]. These systems have been studied in connection with organic solar cell[2]. We found that the energy levels of ZnTPP are fixed to the vacuum level of the substrate metal with constant difference of vacuum level between ZnTPP and metal interface (Fig.1c).

In this work, we report the preliminary results of similar studies on 5,10,15,20-tetra(4-pyridyl) porphyrin (H_2T(4-Py)P, Fig.2: M=H_2, R=C_5H_5N)/metal systems and 5,10,15,20-tetraphenylporphyrin (H_2TPP, Fig.2: M=H_2, R= C_6H_5)/metal systems in order to discuss the validity of the above mentioned traditional models based on the observed energy level alignment at these porphyrin/metal interfaces.

The UPS spectra were measured using the angle-resolving UPS system at the beamline 8B2 of UVSOR at Institute for Molecular Science. We used three metals (Mg, Al and Au) as substrates, which were vacuum evaporated on a Mo plate. Then thin porphyrin films (5nm thick) were prepared on the metal substrates by vacuum evaporation in ultra high vacuum (UHV).

In Fig.3, we show the UPS spectra of H_2T(4-Py)P/metal(Mg, Al and Au) systems in low binding energy region. The abscissa is the binding energy relative to the Fermi level of the metal substrate (E_F^m). The peak A at the top of the valence states, which dominates the electric properties, is ascribed to the nearly degenerate two π orbitals delocalized over the central macrocycle. No difference is observed among the shapes of the UPS spectra of H_2T(4-Py)P/metal systems. This similarity indicates that the molecular electronic structure of H_2T(4-Py)P is not affected by the contact with metals. On the other hand, the peak positions and threshold energy

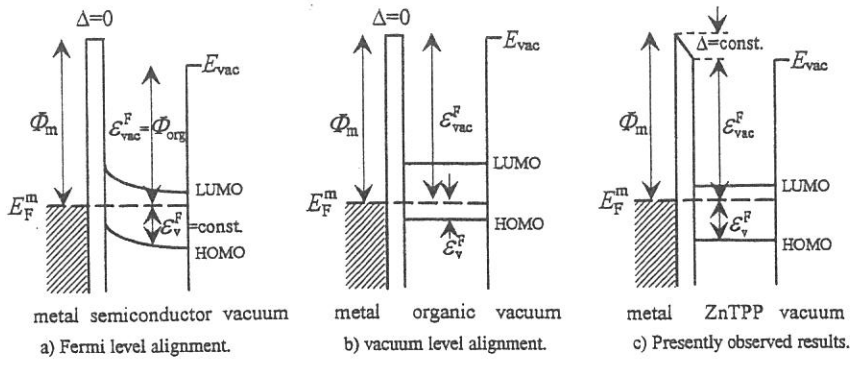

Figure 1. Three models of organic/metal interfaces.

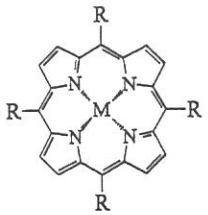

Figure 2.
The chemical structure of porphyrins.
ZnTPP: M=Zn, R=C_6H_5 M=H_2.
H_2T(4-Py)P: R=C_5H_5N.
H_2TPP: M=H_2, R=C_6H_5.

depend significantly on the substrate. Fig.4 shows the plot of the energy of the vacuum level (ε^F_{vac}) of $H_2T(4\text{-Py})P$ films and the threshold energy for the HOMO of $H_2T(4\text{-Py})P$ (ε^F_v) versus work function of the metals (Φ_m). At $H_2T(4\text{-Py})P$/metal interface, we found that ε^F_{vac} and ε^F_v are good linear function of Φ_m, but the slope of the plot is much smaller than unity. The lines by the least-squares fit in Fig.4 are $\varepsilon^F_{vac}=0.40\Phi_m+2.26$eV and $\varepsilon^F_v=0.37\Phi_m-3.65$eV, respectively. Since notable dependence of the UPS spectra on film thickness was not observed in the region of 1~5nm, the energy level shift near the interface due to band bending can be ignored. In the case of H_2TPP/ metal system, we also found that ε^F_{vac} and ε^F_v are good linear function of Φ_m and the slope of the plot is about 0.4.

Now we discuss the validity of the models of simple energy level alignments in Fig.1. If Fermi-level alignment occurs across the interface like Fig.1a, $\Delta\equiv\varepsilon^F_{vac}-\Phi_m$ is zero at the interface and band bending in the space charge layer occurs to achieve Fermi level alignment. This makes ε^F_{vac} and ε^F_v constant at the flat-band region, so the slope of these plots should be zero. On the other hand, vacuum level alignment like Fig.1b requires $\Delta\equiv\varepsilon^F_{vac}-\Phi_m=0$ at the interface and the bulk region of porphyrin. This means that the slope of these plots should be unity. In the case of the ZnTPP/metal interface, neither of these models hold. The energy levels of ZnTPP is fixed to the vacuum level of the substrate metal, with a constant energy shift Δ as shown in Fig.1c, so the slope of the plot is unity, and Δ is non-zero constant. The presently observed results show that the energy levels of $H_2T(4\text{-Py})P$ and H_2TPP are also fixed to the vacuum level of the substrate metal with an energy shift Δ. In contrast to the case of ZnTPP/metal systems, however, Δ is not constant, but a linear function of Φ_m.

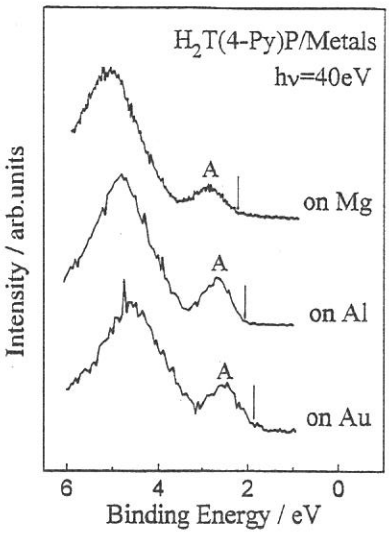

Figure 3. UPS Spectra of $H_2T(4\text{-Py})P$/Al.

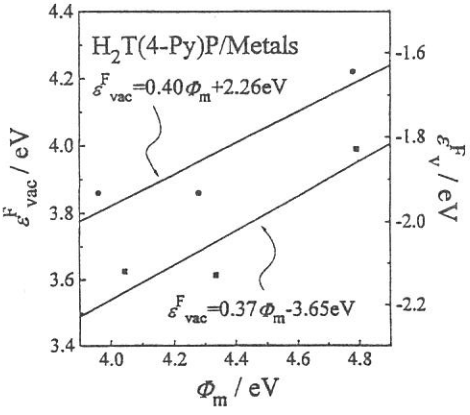

Figure 4. ε^F_{vac} and ε^F_v versus Φ_m plot.

Similar abrupt shift of vacuum level was also observed at inorganic semiconductor/metal systems[3] and organic/inorganic interfaces (merocyanine dyes /Ag halides[4]). This shift indicates the formation of an electric dipole layer. It may originate from the charge redistribution at the interfaces, which is due to the interaction between the first porphyrin layer and the metal surface. However, this needs further experimental examination.

In the case of inorganic-semiconductor/metal systems[3], a slope parameter is defined as $S\equiv d\phi_B/d\phi_m$, where ϕ_B is the Schottky barrier height. This corresponds to the slope of the ε^F_v versus Φ_m plot in our discussion. The value of S is unity when Mott-Schottky rule holds. The reported values of S in most inorganic-semiconductor/metal junction are less than unity. Bardeen attributed the discrepancy between the experimentally observed barrier heights and the Mott-Schottky rule to the interface states[5]. The small slope for $H_2T(4\text{-Py})P$ and H_2TPP /metals systems may be explained by similar effect of the interface states. A possible origin of such interface states is metal-induced gap state (MIGS)[3].

In conclusion, we found that the energy levels of $H_2T(4\text{-Py})P$ and H_2TPP are fixed to the vacuum level of metal substrate with an energy shift Δ. We also found that the magnitude of Δ depends on the work function of the substrate metal at $H_2T(4\text{-Py})P$/metal and H_2TPP/metal interfaces. This requires the modification of the traditional models of energy level alignment at the interface.

REFERENCES [1] S.Narioka, H.Ishii, D.Yoshimura, M.Sei, Y.Ouchi, S.Hasegawa T.Miyazaki Y.Harima, K.Yamashita, and K.Seki, Appl. Phys. Lett. 67 (1995) 1899

[2] K.Yamashita, Y.Harima, and T.Matsubayashi, J. Phys. Chem., 93 (1989) 5311.

[3] W.Mönch, Surf. Sci., 299/300 (1994) 928-944.

[4] K.Seki, H.Yanagi, Y.Kobayashi, T.Ohta, and T.Tani, Phys. Rev., B49 (1994) 2760.

[5] J.Bardeen, Phys. Rev., 71 (1947) 717.

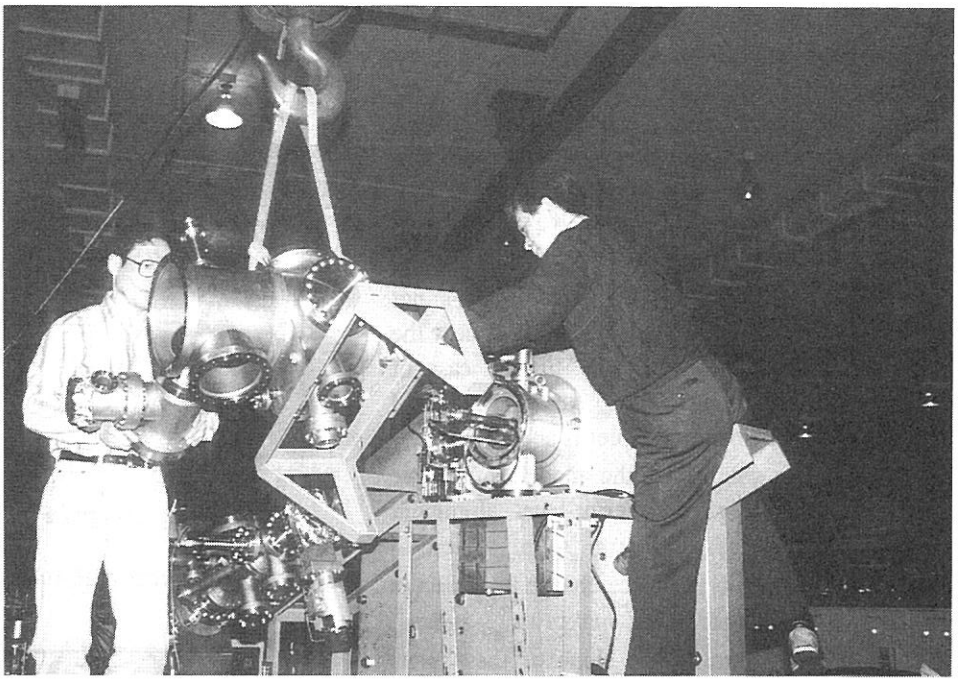

Profs. H. Nakagawa (Fukui Univ., right) and K. Nakagawa (Kobe Univ., left) are taking the oldest Seya-Namioka monochromator in UVSOR to pieces at the begining stage of a scrap and build project for BL7B.

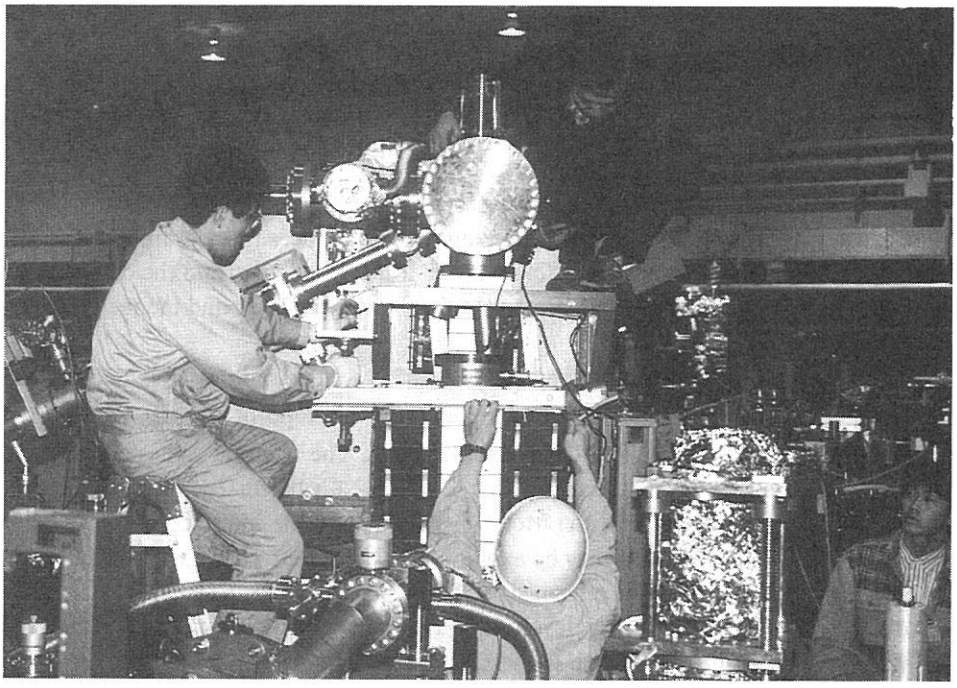

Prof. H. Nakagawa (Fukui Univ., top) and Dr. E. Okamura (Kobe Univ., left) are scrapping the Seya-Namioka monochromator at BL7B with students.